THE UNIVERSITY *of* EDINBURGH

SYNTHETIC CELL-BASED PATTERNING SYSTEMS AND THEIR APPLICATIONS IN STEM CELL DIFFERENTIATION

THE UNIVERSITY *of* EDINBURGH

Fokion Glykofrydis

College of Medicine & Veterinary Medicine

UK Centre for Mammalian Synthetic Biology

The University of Edinburgh

This dissertation is submitted for the degree of Doctor of Philosophy

September 2020

To my parents,

who gifted me the nature and nurture that has allowed me

to ask questions and pursue answers.

“Θηρεύοντας πράγματα αιώνια,

θ’ αφήσω να φύγουν τα χρόνια.

Θα φύγουν, και θα ’ναι η καρδιά μου

σα ρόδο που επάτησα χάμου.”

Κ. Γ. Καρυωτάκης, Σταδιοδρομία, Ελεγεία και Σάτιρες (1927)

“Pursuing things eternal,

I will let the years slip away.

They’ll slip away, and my heart will be

like a rose I stepped upon.”

K. G. Karyotakis, Career, Elegies and Satires (1927)

DECLARATION

This dissertation is the result of my own work and includes nothing that is the outcome of work done in collaboration except where specifically indicated in the text. It has not been previously submitted, in part or whole, to any university of institution for any degree, diploma, or other qualification.

In accordance with the Deanery of Biomedical Sciences guidelines, this thesis does not exceed 100,000 words, and it contains fewer than 150 figures.

Signed:___FOKION GLYKOFRYDIS_ _____

Date:____15th September 2020_____

Fokion Glykofrydis

Edinburgh

ABSTRACT

Pattern formation underpins cell specification, tissue organization, and morphogenesis during embryonic development. Tissue engineering strategies based on stem cell differentiation and organoid formation attempt to recapitulate developmental patterning, but suffer from variable efficiency, limited complexity, and anatomical disorganization. Whereas considerable research has focused on understanding patterning in vivo, bottom-up efforts in engineering synthetic niches to control patterning in vitro have been limited. This thesis explores a synthetic biology-based approach to create self-organizing mammalian cell systems, and use them as signalling centres for stem cell applications. The first half of the thesis explores whether integrin-ligand heterotypic adhesions can drive the formation of hyperuniform patterns. HEK-293 derivative cell lines were bio-engineered to overexpress heterophilic cell adhesion molecules in a drug-inducible manner using CRISPR genome editing. Transgenic systems were characterized in input sensitivity, output strength, adhesion properties, and their ability to form hyperuniform distributions. The second half of the thesis explores applications of self-organizing cell systems to control stem cell decisions. A pre-established phase-separation patterning system was modified to produce WNT3A from multicellular groups, which self-organize with mouse embryonic stem cells and elicit polarized signalling events. When differentiated in self-organizing co-cultures, embryonic stem cells exhibit enhanced and spatially controlled mesoderm induction in 2D and 3D conditions respectively, due to exogenous, localized Wnt signalling. WNT3A producers can also trigger nephrogenesis in mouse metanephric mesenchyme, demonstrating their wider applicability. This work provides novel prototype platforms and conceptual approaches to control developmental cell fate decisions and organization in vitro, contributing to the generation of synthetic niches.

LAY SUMMARY

The same events that operate in the development of embryos also occur when turning stem cells into useful cells, tissues and mini-organs. However, stem cell-derived tissues and mini-organs are not as ordered, detailed and realistic as true embryo development. Much research has focused on understanding how order emerges in embryos, and how stem cells are controlled by their environment. Having said that, not as much has been done in creating synthetic environments to improve the order in stem cell-derived tissues/organs. This thesis explores how we can engineer simple cells (not stem cells) to arrange in organized patterns (e.g. chessboard/polka dots), and how we can make some members of the pattern (e.g. only black squares) produce signals that control stem cell decisions. The first half of the thesis investigates how we can make cells arrange in new patterns. The idea is to engineer two cell types to strongly adhere to one another, so that when mixed together, “TypeA” cells are always surrounded by “TypeB” cells. Therefore, “TypeA” cells should arrange uniformly in space. To achieve this, I modified cultured cells to present different sticky proteins on their exterior surface when an antibiotic was added to the culture; these proteins should make connections between “TypeA” and “TypeB” cells. Experiments showed that high sticky protein levels were produced when the antibiotic was given to cells, and that these proteins were functional. Experiments were then performed to see whether “TypeA”-“TypeB” mixed cultures formed desired patterns. In the second half of the thesis, I used a different system in which two cell types arrange in patterns similar to cow-hides or water-oil mixtures. I modified the pattern so that one cell type produces the protein-signal WNT3A. Experiments showed that when this cell type was cultured together with stem cells, patterns again emerged. There, the stem cells responded to the WNT3A signal in both flat cultures and in 3D aggregates. In flat cultures, a lineage that gives rise to blood, muscles and kidneys (the mesoderm) emerged strongly when stem cells were cultured together with the WNT3A producers, but not as strongly when stem cells were cultured with the original cell type lacking WNT3A. In 3D aggregates, mesoderm appeared predominantly next to WNT3A producers, showing how stem cell decisions could be controlled locally. My final experiments show that the WNT3A-producing cells can stimulate aspects of kidney development, suggesting they can be used for more complex applications. Through this work, I wish to provide a conceptual advance to the scientific community, by illustrating that simple cells can be turned into organized signalling centres that can be used to control stem cell decisions with improved detail and order.

ACKNOWLEDGEMENTS

A heartfelt thank you to Jamie Davies, for giving me the opportunity to pursue such a pivotal chapter in my life, for sharing with me a different perspective on biology and science, and for all discussions about and beyond science that have cumulatively expanded my knowledge and perception.

A wholehearted thank you to Elaine Dzierzak, whom I consider my mother-in-science, and who throughout the years has stood as an inspiring role model in my eyes by radiantly projecting integrated traits of tenacity, pride and acumen.

My profound appreciation to Elise Cachat, for whenever we interacted I was left with a feeling of being enriched, deeply enjoying the natural communication flow in every little exchange of ideas (or plasmids).

I would be remiss to exclude those who throughout the years have built me up: Kostas Kampourakis, my first biology tutor who reinforced my passion and fascination for biology, science, rationalism and critical thinking. Kamil R. Kranc, the first investigator who opened his doors to me, and subsequently new doors, through his open-mindedness and generosity. Mari-Liis Kauts and Theano Panagopoulou, my first two bench-to-bench supervisors who gave me solid foundations for how to think about and conduct research in practice. Carmen Rodriguez-Seoane, Chris Vink, and Samanta Mariani, who have instilled in me habits that have improved me professionally and personally; habits that will continue to improve my life in the future.

I would like to acknowledge and thank the following people for specific contributions in this thesis:

Benjamin E. Reese and Patrick Keeley (Neuroscience Research Institute, University of California at Santa Barbara) for kindly gifting the custom MatLab script for cell coordinate analyses and extraction of hyperuniformity metrics (section 3.2.4).

Anna Popravko (Queen's Medical Research Institute, The University of Edinburgh) for assistance with MatLab and cell coordinate analyses using the aforementioned MatLab software (section 3.2.4).

Elise Cachat (UK Centre for Mammalian Synthetic Biology, The University of Edinburgh) for provision of *pCMV::mCherry-2A-Wnt3a* plasmid (section 3.3.3) and for provision of TREx-293$^{TOPflash::mCherry}$ (clone 1-13) cells (section 3.3.4).

Derk ten Berge (Erasmus MC, Rotterdam, Netherlands) for kindly donating Wnt/β-catenin reporter (*7xtcf/lef::eGFP*) mouse embryonic stem cells (sections 3.3.4-3.4.2).

The Dzierzak lab (Queen's Medical Research Institute, The University of Edinburgh), for providing *T-brachyury::eGFP* reporter mouse embryonic stem cells (sections 0-3.4.2), which were originally made by Hans Jörg Fehling.

Members of the Davies lab (Julia Tarnick, Mona Elhendawi, Jamie Davies) for kindly and patiently dissecting and providing metanephric mesenchyme from mouse embryos (section 3.4.3).

The Queen's Medical Research Institute flow cytometry and cell sorting facility (QMRI Flow), and confocal and advanced light microscopy (QMRI CALM) facility for technical assistance with flow cytometry and confocal imaging respectively.

CONTENTS

1 INTRODUCTION 1
1.1 DEVELOPMENTAL PATTERNING: COMPLEXITY & ORDER 1
1.1.1 Mechanisms of Patterning 3
1.2 PATTERNING IN VIVO 6
1.2.1 Cells: The pre-implantation embryo 6
1.2.2 Tissues: Gastrulation 10
1.2.3 Organs: Kidney Branching Morphogenesis 17
1.3 PATTERNING IN VITRO 21
1.3.1 Stem Cell Self-Organization 21
1.3.2 Synthetic Biology and Pattern Formation 25
1.4 AIMS OF THE PROJECT 32
2 MATERIALS & METHODS 33
2.1 METHODS RELATED TO SECTIONS 3.1 & 3.2 33
2.1.1 DNA Engineering 33
2.1.2 Bacteria Culture 37
2.1.3 Mammalian Cell Culture 39
2.1.4 Transfection and selection 39
2.1.5 Flow cytometry 40
2.1.6 Fluorescence-Activated Cell Sorting (FACS) 40
2.1.7 Titration of Tetracycline EC_{50} 41
2.1.8 Adhesion Assays 41
2.1.9 Cell Surface Area Measurement 42
2.1.10 Pattern formation co-cultures 42
2.2 METHODS RELATED TO SECTIONS 3.3 & 3.4 43
2.2.1 Cell Culture 43
2.2.2 Phase-separation pattern co-cultures 45
2.2.3 Mesoderm Assays 46
2.2.4 Kidney & Metanephric Mesenchyme processing 48
2.2.5 Image processing 48
3 RESULTS 50
3.1 PROGRAMMING PATTERN FORMATION 50
3.1.1 Integrin Biochemistry 53
3.1.2 Ligand-integrin pairs driving heterotypic adhesions 60
3.1.3 Strategy to program hyperuniform pattern formation 63
3.1.4 Molecular cloning of integrin receptor & ligand cDNA 65
3.1.5 Co-assembly of ICAM-1/MAC-1/LFA-1 mammalian expression cassettes .. 69

3.1.6 Construction of *ROSA26* transgene knock-in CRISPR systems 74
3.1.7 Genome editing of TREx-293 cells using CRISPR vectors 80
3.2 TESTING PATTERN FORMATION 84
3.2.1 Characterization of the *ROSA26* transgenic system 84
3.2.2 Adhesion properties of transgenic TREx-293 cells 87
3.2.3 Adhesion transgenes impart cell morphological changes 90
3.2.4 Evaluation of Hyperuniform Pattern Formation 95
3.2.5 Discussion 98
3.3 COUPLING SIGNAL PRODUCTION TO A SELF-ORGANIZING SYSTEM 101
3.3.1 Wnt ligands show limited diffusion and regulate fate decisions 102
3.3.2 Choice of Wnt ligand and patterning system 107
3.3.3 Establishment of TREx-293$^{Cdh3\text{-}Wnt3a}$ clonal lines 109
3.3.4 Using TREx-293$^{Cdh3\text{-}Wnt3a}$ to activate Wnt/β-catenin signalling 112
3.3.5 Self-organization and signalling events in mESCs-TREx-293$^{Cdh3\text{-}Wnt3a}$ co-cultures 116
3.4 CONTROLLING STEM CELL FATE DECISIONS 123
3.4.1 Augmenting and tracking mesoderm emergence in 2D differentiations 125
3.4.2 Specifying mesoderm organization in 3D embryoid bodies 134
3.4.3 Applying synthetic-signalling cells to higher systems 138
3.4.4 Discussion 140
4 FINAL DISCUSSION 144
5 REFERENCES 150

LIST OF TABLES

TABLE 1. LIST OF PRIMERS AND EXPECTED AMPLICONS PER PCR. 35
TABLE 2. THERMOCYCLER PROGRAMMES AND PRIMER SETS PER PCR. 36
TABLE 3. BACTERIAL TRANSFORMATION AND GROWTH CONDITIONS PER CONSTRUCT..... 38
TABLE 4. ANTIBODY DETAILS USED FOR FLOW CYTOMETRY ANALYSES AND SORTING. 41
TABLE 5. FORMULATION OF MEDIA USED FOR CELL AND TISSUE CULTURE..... 44
TABLE 6. ANTIBODY AND STAINING DETAILS USED FOR IMMUNOSTAINING..... 49
TABLE 7. HYPERUNIFORMITY METRIC VALUES EXAMPLES (KRAM ET AL., 2010). 51
TABLE 8. HETEROPHILIC LEUKOCYTE INTEGRINS AND THEIR LIGANDS..... 62

LIST OF FIGURES

FIGURE 1. PATTERNING OF THE PRE-IMPLANTATION MOUSE EMBRYO. 7
FIGURE 2. PATTERNING OF THE POST-IMPLANTATION MOUSE EMBRYO. 15
FIGURE 3. PATTERNING AND MORPHOGENETIC EVENTS DURING KIDNEY DEVELOPMENT. 19
FIGURE 4. OVERVIEW OF SYNTHETIC PATTERNING MECHANISMS IN BACTERIA. 27
FIGURE 5. OVERVIEW OF SYNTHETIC PATTERNING MECHANISMS IN MAMMALIAN CELLS. 29
FIGURE 6. OVERVIEW OF MAMMALIAN INTEGRIN RECEPTOR COMPOSITION. 53
FIGURE 7. STRUCTURAL COMPOSITION OF INTEGRIN RECEPTORS. 55
FIGURE 8. INFORMATION REGARDING CLONING OF INTEGRIN-SUBUNIT CDNA IN CARRIER VECTORS. 66
FIGURE 9 CLONING OF INTEGRIN SUBUNIT-ENCODING CDNA. 67
FIGURE 10. CLONING OF SYNTHETIC *ICAM-1* CDNA INTO *PTREX* VECTOR. 68
FIGURE 11. ASSEMBLY OF TETRACYCLINE-INDUCIBLE MAMMALIAN EXPRESSION CASSETTES DRIVING INTEGRIN RECEPTOR/LIGAND EXPRESSION. 71
FIGURE 12. MODIFICATION OF LFA-1 EXPRESSION CASSETTE TO REPORT TRANSGENE EXPRESSION THROUGH H2B-TAGBFP. 73
FIGURE 13. BIOINFORMATIC ANALYSIS OF *ROSA26* FOR CRISPR GENOME EDITING. 75
FIGURE 14. CLONING OF ROSA26-TARGETING GRNA IN *PSPCAS9-2A-EGFP* VIA GOLDEN GATE ASSEMBLY. 76
FIGURE 15. INFORMATION REGARDING *PHDR* CRISPR CONSTRUCT ASSEMBLY. 78
FIGURE 16. GENERATION OF *PHDRS* FOR INSERTION OF TRANSGENES IN THE *ROSA26* LOCUS. 79
FIGURE 17. CRISPR GENOME EDITING OF TREX-293 USING CRISPR VECTOR STRATEGY. 81
FIGURE 18. TRANSGENIC TREX-293 SCREENING FOR TRANSGENE EXPRESSION AND *ROSA26* INTEGRATION. 83
FIGURE 19. TRANSGENE CHARACTERIZATION IN INPUT SENSITIVITY AND OUTPUT LEVELS. 86
FIGURE 20. ADHESION ASSAYS FOR TRANSGENIC TREX-293. 88
FIGURE 21. DETAILS FOR MONOLAYER ADHESION ASSAY RESULTS SHOWN IN FIGURE 20B. 89
FIGURE 22. TREX-293^{MAC-1} SHOW INCREASED SPREADING IN ADHERENT CULTURES. 91
FIGURE 23. TETRACYCLINE-ACTIVATED TREX-293^{ICAM-1} DEMONSTRATE CYST-LIKE 3D GROWTH. 92
FIGURE 24. SPHEROID FORMATION CAPACITY OF TRANSGENIC TREX-293 LINES. 94
FIGURE 25. EVALUATION OF HYPERUNIFORM DISTRIBUTIONS IN TREX-293 CO-CULTURES. 97
FIGURE 26. OVERVIEW OF WNT SECRETION AND B-CATENIN ACTIVATION. 103

FIGURE 27. CHARACTERIZATION OF SELF-ORGANIZING, SIGNAL-PRODUCING TREX-293$^{CDH3\text{-}WNT3A}$. 111
FIGURE 28. USING TREX-293 TOPFLASH REPORTERS TO ASSAY WNT/B-CATENIN PATHWAY ACTIVATION. 113
FIGURE 29. USING MOUSE ESC *7XTCF/LEF::EGFP* REPORTERS TO ASSAY WNT/B-CATENIN PATHWAY ACTIVATION. 115
FIGURE 30. PHASE-SEPARATION 2D PATTERNING BETWEEN MESCS AND TREX-293^{CDH3} 117
FIGURE 31. PHASE-SEPARATION AND POLARIZED WNT/B-CATENIN ACTIVITY IN EB-293 CO-AGGREGATES. 119
FIGURE 32. OVERVIEW OF METHOD FOR EB-293 CO-AGGREGATION IN PHASE-SEPARATION, AND CHARACTERIZATION OF OUTPUT. 121
FIGURE 33. IMMUNOFLUORESCENCE SHOWS AUGMENTED T-BRACHYURY INDUCTION IN MESCS DIFFERENTIATED IN 2D PHASE-SEPARATION WITH TREX-293$^{CDH3\text{-}WNT3A}$. 126
FIGURE 34. FLOW CYTOMETRY GATING STRATEGY FOR *T-BRACHYURY::EGFP* DIFFERENTIATIONS IN PHASE-SEPARATION. 128
FIGURE 35. FLOW CYTOMETRY ANALYSIS OF *T-BRACHYURY::EGFP* DIFFERENTIATIONS IN 2D PHASE-SEPARATION ON DAY 4. 129
FIGURE 36. TIME-LAPSE MARKS MESODERM SPECIFICATION IN *T-BRACHYURY::EGFP* DIFFERENTIATIONS IN PHASE-SEPARATION. 131
FIGURE 37. DEFINITIVE MESODERM EMERGENCE IN PHASE-SEPARATION CO-CULTURES ON DAY 5. 133
FIGURE 38. TREX-293$^{CDH3\text{-}WNT3A}$ SPATIALLY SPECIFY MESODERM INDUCTION AND INDUCE PATTERN ELABORATION IN 3D EMBRYOID BODY DIFFERENTIATIONS. 136
FIGURE 39. TREX-293$^{CDH3\text{-}WNT3A}$ DO NOT AFFECT T-BRACHYURY PERCENTAGE YIELDS OR LEVEL INTENSITY DURING EBS DIFFERENTIATION. 137
FIGURE 40. TREX-293$^{CDH3\text{-}WNT3A}$ FACILITATE NEPHROGENESIS IN MOUSE EMBRYONIC METANEPHRIC MESENCHYME. 139

LIST OF ABBREVIATIONS AND ACRONYMS

AAVS1: Adeno-associated virus integration site 1

ActRIIA/B: Activin A receptor, type 2 A/B

Acvr2: Activin A receptor, type 2

ADMIDAS: Adjacent to MIDAS

AHL: Acyl-homoserine lactone

Akt: Protein kinase B

APC: Adenomatous polyposis coli protein

Arp2/3: Actin-related protein 2/3

ASC: Adult stem cell

AVE: Anterior visceral endoderm

BABB: Benzyl alcohol benzyl benzoate

BFP: Blue fluorescent protein

BMP4: Bone morphogenetic protein 4

BMPR1α: Bone morphogenetic protein receptor type 1 Alpha

bp: base pair

CD11a: Integrin subunit Alpha L

CD11b: Integrin subunit Alpha M

CD18: Integrin Beta 2

CD19: B-lymphocyte antigen CD19

CD54: ICAM-1

Cdc42: Cell division cycle 42

Cdh1: E-cadherin (Cadherin-1)

Cdh2: N-cadherin (Cadherin-2)

Cdh3: E-cadherin (Cadherin-3)

Cdx2: Caudal type homeobox 2

Cer1: Cerberus 1/Cerberus-related 1

CHAPS: 3-((cholamidopropyl)dimethylammonio)-1-propanesulfonate

cheZ: Protein phosphatase CheZ

Ck1: Casein kinase 1 Alpha 1

CMV: Cytomegalovirus

COS: CV-1 origin SV40 T-antigen transformed monkey fibroblast

Cres: Cystatin-related epididymal spermatogenic

DAPI: 4',6-diamidino-2-phenylindole

Dkk1: Dickkopf-related protein 1

DLL1: Delta-like canonical Notch ligand 1

DMEM: Dulbecco's modified Eagle's medium

(c)DNA: (complementary) DNA

DVE: Distal visceral endoderm

EB: Embryoid body

EBM: Embryoid body differentiation medium

ECM: Extracellular matrix

EDTA: Ethylenediaminetetraacetic acid

EGF: Epidermal growth factor

EMT: Epithelial-to-mesenchymal transition

Eomes: Eomesodermin

ERK: Extracellular signal-regulated kinase

(m/h)ESC: (mouse/human) embryonic stem cell

mESM: mouse embryonic stem cell maintenance medium

Esrrb: Estrogen related receptor Beta

Evi: Wnt ligand secretion mediator (Wntless)

ExE: Extraembryonic ectoderm

F-actin: Filamentous actin

FACS: Fluorescence-activated cell sorting

FAK: Focal adhesion kinase

Fat4: FAT atypical cadherin 4

FBS: Foetal bovine serum

FGF8: Fibroblast growth factor 8

FGFR1/2: Fibroblast growth factor receptor 1/2

FoxA2/D1/G1/H1: Forkhead box A2/D1/G1/H1

Frzb: Frizzled related protein (sFRP3)

Gal4: Regulatory protein Gal4

Gata6: GATA binding protein 6

GDF1/3: Growth differentiation factor 1/3

GDNF: Glial cell derived neurotrophic factor

(e/t)GFP: (enhanced/turbo) Green Fluorescent Protein

GFRα1: GDNF family receptor Alpha 1

GPR177: Wnt ligand secretion mediator (Wntless)

GRN: Gene regulatory network

GSK3: Glycogen synthase kinase 3

HBSS: Hank's Balanced Salt Solution

HDR: Homology-directed repair

HEK-293: Human embryonic kidney 293

Hes7: Hes family bHLH transcription factor 7

HGF: Hepatocyte growth factor

HUVEC: Human umbilical vein endothelial cell

ICAM-1: Intercellular adhesion molecule 1

ICM: Inner cell mass

IFNγ: Interferon Gamma

IL-1: Interleukin 1 Beta

IMDM: Iscove's modified Dulbecco's medium

IPTG: Isopropyl β-D-1-thiogalactopyranoside

IQR: Interquartile range

ISC: Intestinal stem cell

JAM-C: Junctional adhesion molecule 3

KCM: Kidney culture medium

LacI: Lactose operon repressor

$LacI_{M1}$: Hypomorphic lactose operon repressor

LAD: Leukocyte adhesion deficiency

$LB^{Amp/Kan}$: Luria-Bertani broth or agar with ampicillin/kanamycin

LEF: Lymphoid enhancer factor

LFA-1: Lymphocyte function-associated antigen 1

LGR5: Leucine rich repeat containing G protein-coupled receptor 5

LRP5/6: Low-density lipoprotein receptor-related protein 5/6

LuxI: Acyl-homoserine lactone synthase

LuxR: Transcriptional activator protein LuxR

MAC-1: Macrophage-1 antigen

MAPK: Mitogen-activated protein kinase

MEK: Mitogen-activated protein kinase kinase

MET: Mesenchymal-to-Epithelial Transition

MIDAS: Metal ion-dependent adhesion site

MM: Metanephric mesenchyme

Nkx2.1/2.2: Nk2 homeobox 1/2

NPC: Nephrogenic progenitor cell

Oct3/4; Oct6: Octamer-binding transcription factor 3; Octamer-binding transcription factor 6

OptiMEM: Reduced serum Eagle's minimum essential medium

Otx2: Orthodenticle homeobox 2

Pax6: Paired box 6

PBMC: Peripheral blood mononuclear cell

PBS: Phosphate-buffered saline

PBT: PBS with 0.5% Triton X-100

qRT-PCR: quantitative real time polymerase chain reaction

PFA: Paraformaldehyde

PMA: Phorbol myristate acetate

(i)PSC: (induced) pluripotent stem cell

Rac1: Ras family small GTPase 1

Rap1: Ras-related protein 1

Ret: Ret proto-oncogene

RFP: Red fluorescent protein

RIAM: Rap1-GTP-interacting adapter molecule

(g)RNA: (guide) Ribonucleic acid

rpm: Revolutions per minute

SD: Standard deviation

SEM: Standard error of the mean

sFRP: secreted frizzled related protein

SHH: Sonic hedgehog

SIX2: SIX homeobox 2

Smad2/3: Smad family member 2/3

SOST: Sclerostin

Sox2/17/21: SRY-box transcription factor 2/17/21

SPRY1: Sprouty RTK signalling antagonist 1

Src: Proto-oncogene tyrosine-protein kinase Src

SWI/SNF: Switch/Sucrose non-fermentable

SyMBS: Synergistic metal binding site

T7RNAP: T7 bacteriophage RNA polymerase

TAZ: Tafazzin

TCF: T-cell factor

TCM: TREx-293 culture medium

TE: Trophectoderm

TetO: Tetracycline operator binding site

TetR: Tetracycline repressor protein

Tenm4: Teneurin transmembrane protein 4

TGFα/β: Transforming growth factor Alpha/Beta

TNF-α: Tumor necrosis factor

TRE: Tetracycline response element

TREx-293: Tetracycline-regulated expression HEK-293 cell line

tTA: Tetracycline transactivator

UAS: Upstream activating sequence

UB: Ureteric bud

VP64: Four copies of transactivator viral protein 16

Wg: Wingless

WIF: Wnt inhibitory factor

Wnt: Wingless-type MMTV integration site family

WT1: Wilms Tumor 1

YAP: Yes-associated protein

YFP: Yellow fluorescent protein

μ: Mean

σ: Standard deviation

1 INTRODUCTION

1.1 Developmental Patterning: Complexity & Order

Embryonic development orchestrates the creation of a structured multicellular body through a process that generates complexity while creating order. In its simplest form, development is a series of progressive cell divisions followed by timely cell fate specifications, operating relatively simply at first and becoming more complicated as cross-regulating cell states and systems emerge. New cell fates (specialized cells) or cell states (different expression profile, but not terminally specialized) do not emerge at random, but rather in statistically non-random distributions (patterns) through a process termed pattern formation or patterning (Kicheva & Briscoe, 2015). Patterning underpins the orderly emergence of complexity that defines development, operating at different scales, dimensions, and with distinct biological and phenotypic outputs (Lander, 2011). Delineating the molecular mechanisms underlying patterning provides insights into how specialized cells emerge, how different cells self-organize into higher structures, and how evolutionary novelty might arise through development (Salazar-Ciudad et al., 2003). Manipulating and/or recreating such mechanisms can aid tissue engineering, where attempts to generate functional cells, organized tissues and physiological organs currently fall short. For these reasons, understanding the nature of patterning becomes essential in the context of developmental biology and regenerative medicine.

Pattern formation as a concept originates through the marriage of embryology and theoretical modelling. Early grafting experiments in *Xenopus laevis* embryos demonstrated that developmental cell fates were acquired based on information relayed by localized cell groups termed organizers, illustrating that fate specification was plastic and controlled through cell-cell interactions in a process termed induction (Nieuwkoop, 1967, 1973; Spemann & Mangold, 1924). In 1953, Alan Turing applied mathematical modelling to suggest that complex anatomical patterns, such as limb features and coat colouration, can be explained from underlying chemical and physical laws (Turing, 1990). Lewis Wolpert bridged induction to patterning, by postulating that developmental cell fates are specified through cells differentially responding to positional information, conveyed as dosages of diffusive signalling molecules termed morphogens (Wolpert, 1969). Models such as the French Flag (Wolpert, 1969) and the Epigenetic Landscape

(Waddington, 1940) provided significant concepts for how organizer-derived signalling patterns cell fate in space. Simulations by Gierer and Meinhardt led to the Reaction-Diffusion model (analogous to Turing's propositions), where interactions between a local activator and a diffusive inhibitor molecule can generate equilibrated patterns of "activated cell" locales separated by "non-activated cell" areas (Gierer & Meinhardt, 1972; Meinhardt & Gierer, 2000). By changing parameters such as activation threshold and diffusion rates, a variety of patterns comparable to in vivo counterparts could be generated. These models brought forth the idea that genetic and molecular networks could, in theory, mediate developmental patterning, and without the requirement of dedicated organizers. Empirical evidence came from Edward Lewis through his work on homeotic mutations in *Drosophila melanogaster*, leading to the discovery of Hox genes and their involvement in patterning the body plan (E. B. Lewis, 1978). This demonstration of the genetic basis of patterning initiated the investigation on genetic and molecular mechanisms mediating pattern formation in different developmental time points, scales and contexts.

Patterning has since been studied in the context of embryonic development (Q. Chen et al., 2018; Costantini & Kopan, 2010), stem cell-derived organoids (Renner et al., 2017; Serra et al., 2019; van den Brink et al., 2020), and stem cell niches (Inaba & Yamashita, 2012). It can be assumed that the aim of such studies is to understand the mechanisms through which specialized cells, organized tissues, and structured organs emerge in the developing embryo, in order to facilitate their reconstruction for purposes of regenerative medicine and to answer biological and evolutionary questions. When knowledge is acquired from in vivo embryo experiments, it is traditionally applied to in vitro systems that show unsophisticated organization and patterning, and usually in crude ways. For example, upon discovering that the specification of a developmental lineage depends on high activity of *PathwayX*, which is activated by *SignalX*, stem cell differentiation protocols aiming for derivation of that lineage are modified to contain high levels of *SignalX* in the culture medium. However, this approach does not take into consideration the temporal dynamics of autoregulatory signalling pathways, or the provision of signalling ligands from spatially localized cell populations (for an example, see the NODAL-SMAD2 signalling axis (Funa et al., 2015; Heemskerk et al., 2019)). As a result, this approach does not allow for the accurate reconstruction of biological organization specified via controlled, dose-sensitive, cell-based signal production. There are certain exceptions to this mode, which will be presented herein. To this end, coupling mechanisms of patterning to signal production, i.e. reconstructing developmental organizers, could offer novel advances in improving tissue and organoid self-organization and realism, thus assisting biological research and biomedical applications.

1.1.1 Mechanisms of Patterning

Developmental patterning can arise via different general mechanisms (Salazar-Ciudad et al., 2003). The aim of this section is to provide a basic conceptual framework for how a population of units/entities (in this case cells) self-organize into ordered patterns. While pragmatic examples are provided to illustrate various mechanisms, the use of thought experimentation and logic helps to understand the basic rules behind pattern formation.

Patterning can emerge via cell-autonomous mechanisms, whereby asymmetric inheritance of cell state-defining components, or internal cell state oscillators, take advantage of cell divisions to organize cell states over a multicellular field. On asymmetric inheritance, the pre-implantation mouse embryo exhibits heterogeneity in the distribution of the pluripotency factor SOX21 across cells of the 4-cell and 8-cell stage embryos, with cells inheriting SOX21 being less likely to contribute to extra-embryonic trophectoderm (Goolam et al., 2016). On the other hand, most trophectoderm cells divide asymmetrically, with outside-positioned cells inheriting determinants of cell polarity and the transcription factor CDX2 that maintain trophectoderm fate (Korotkevich et al., 2017; Skamagki et al., 2013). It is not uncommon for asymmetric inheritance to be related to small-scale positional information, whereby cells exhibiting a degree of polarity based on contact to localized extracellular matrix components or cell neighbours, adopt different fates compared to their sister cell following division. This is illustrated in aforementioned trophectodermal cells, in which CDX2 expression and inheritance is interlinked to cell polarity and outside position with respect to the blastocyst (Korotkevich et al., 2017; Skamagki et al., 2013). It is also evident in numerous other contexts, such as in *Drosophila* gametogenesis, in which germline stem cells that remain juxtaposed to the germarium tip following division retain self-renewal capacity, whereas the sister cell that exits the niche undergoes differentiation (Inaba & Yamashita, 2012). Control of cell fate by means of asymmetric divisions is observed across different kingdoms and phyla of life, and is therefore a deeply conserved biological mechanism (Inaba & Yamashita, 2012). On internal state oscillators, the somite segmentation clock is perhaps one of the best examples to illustrate how oscillation in internal gene expression (e.g. the Notch target *Hes7*) is interrelated with cell fate specification. Given that oscillation parameters and fate acquisition are dependent on signalling cascades (FGF8/ERK, Wnt/β-catenin, YAP/TAZ), the somite segmentation clock demonstrates that cell-autonomous mechanisms are usually intertwined with inductive interactions, through which intercellular communication networks equilibrate into a cell state pattern over a geometric field (Diaz-Cuadros et al., 2020). Logically, this field should be defined by the range in which the intercellular communication signals operate, in terms of protein diffusion and subsequent cell responses which can relay, extend or limit signal propagation.

The nature of these communication networks define patterns, not only in distribution of cells, but also in properties such as range of patterning field, signal response sensitivity, and potential evolvability (Bier & De Robertis, 2015; Salazar-Ciudad et al., 2003). For example, hierarchic induction defines signal-and-response relationships that are uni-directional (i.e. the response of receiver cells does not affect signalling from producer cells), which should limit the patterning field to approximate protein diffusion/transport dynamics. One of the most robust demonstration of hierarchical induction is the patterning of gap gene expression through maternal morphogen gradients in the early *Drosophila* embryo (Grimm et al., 2010). Emergent induction describes bi-directional communication loops, through which receiver cells regulate the production or diffusion of signalling ligands from producer cells. This can fine-tune patterning and expand the field beyond that of protein diffusion (e.g. modulation of Wnt ligand diffusion, see section 3.3.1). Turing-type reaction-diffusion systems are great examples of emergent induction operating in the same cells that lead to large-scale patterning (Karig et al., 2018; Sekine et al., 2018; Turing, 1990). The precise architecture of communication networks is what discriminates general mechanisms from specific ones. Cell-autonomous and inductive mechanisms mediate patterning by changing cell states de novo, but patterning can also emerge through changes in spatial distributions of already specified cells, achieved via cell behaviours affecting shape/form (morphogenetic). For example, if specified cell states of a two-dimensional plane undergo migration and/or directional growth perpendicular to that plane, the geometrical pattern will extend from 2D to 3D without changes in cell-states (Salazar-Ciudad et al., 2003). These basic mechanisms are often interlinked as parts of higher developmental networks themselves.

Patterning accommodates developmental dynamics through close interlink with two further embryological processes: growth and morphogenesis (the birth of shape and form) (Thompson, 1992). Growth of a patterned tissue expands the field over which patterning can occur, in terms of geometry and cell numbers. Theoretically, this generates new patterning fields and in effect further sub-patterning within the organized tissue, adding detail and elaboration. Signalling protein diffusion/transport kinetics themselves can be subjected to modulation in various ways, such as ligand post-translational modifications, secretion method, ligand co-aggregation, ligand-trapping, or facilitated diffusion (see section 3.3.1 for detailed example). This gradient modulation allows pattern formation or elaboration to occur over greater distances (scaling) or finer detail respectively (Bier & De Robertis, 2015). Patterning is coupled to morphogenesis in a manner parallel to hierarchical-versus-emergent inductions: pattern formation can lead to morphogenesis linearly/directionally (morphostatic mechanism, e.g. *Drosophila*

microchaete patterning (Corson et al., 2017; Couturier et al., 2019)), or morphogenesis can create new patterning fields and form a feedback loop between patterning and morphogenesis (morphodynamic mechanism). The latter process can generate repetitive or fractal patterning/morphogenesis locales over a large physical scale as typically seen in organogenesis (the example of kidney development is presented in section 1.2.3). Together, connecting pattern formation to growth and morphogenesis can explain exponential increase in complexity (Waites & Davies, 2019), considering that these processes operate over four dimensions (2D and 3D fields over time).

The theme of networks recurs at different scales and hierarchical dimensions. Evolutionarily speaking, development can be considered as a selected and elaborated system/process emerging from networks of patterning, growth and morphogenesis. It is conceivable that evolutionary/developmental novelty might arise by changing the interconnections of these processes within developmental networks (Salazar-Ciudad et al., 2003). Analogously, organ/tissue morphogenesis and collective cell behaviour emerge from individual cell morphogenetic behaviours, coordinated via patterning (illustrated in forthcoming sections). After all, patterning itself is an emergent property of communication networks whose output is the distribution of cell states, similar to how the sophisticated control of gene expression is a result of integrative protein/gene regulatory networks. The theme continues deeper, as in chemical oscillations in purely inorganic reactions; in the famous Belousov-Zhabotinsky reaction, a pattern of travelling waves of alternating blue/brown colours emerges from oscillations in bromine reduction/oxidation states, resulting from feedback loops and the overall instability of the reaction (Zaikin & Zhabotinsky, 1970). This is perhaps the most direct illustration of Turing's idea that interacting chemical reactions could create pattern formation (Turing, 1990). The recurrent theme of cross-interactions among similar entities (molecules/genes/cells) creating more complex phenotypes at different scales (auto-regulatory systems/patterning) places network theory at the heart of developmental biology. It also implies that developmentally complex behaviours can be achieved via genetic engineering, by interconnecting morphogenetic cell behaviours or state-defining gene regulatory networks (GRNs) to intercellular communication. Such gene networks could be synthesized bottom-up and elicit developmental events when successfully implemented in naïve cells in vitro. Design of such networks, just like pattern formation, is based on theoretical modelling and insights from developmental systems.

1.2 Patterning in vivo

Cell specification, tissue organization, and organ morphogenesis proceed by setting patterning fields at respective biophysical scales, or resetting patterning fields of a constant scale following growth and morphogenesis. Molecular compartmentalization (either intracellularly or across a multicellular population) is typically coupled to cell fate specification and/or morphogenetic events that underpin multicellular organization over given patterning fields (Bier & De Robertis, 2015; Q. Chen et al., 2018; Costantini & Kopan, 2010; Grimm et al., 2010). In this section, examples from in vivo development are presented to illustrate how cells, tissues and organs self-organize in relation to mechanisms of patterning. The purpose of this analysis is to illustrate how concepts of pattern formation, growth, pattern elaboration, and symmetry breaking recurrently emerge throughout different contexts, and how they drive self-organization. Because the literature across developmental model systems is extensive, examples are drawn primarily from mouse embryos, supplemented with relevant findings from equivalent in vitro stem cell-related counterparts. The choice of the mouse embryo stems from the fact that it has been widely studied and used as a model system for mammalian development, and similarly, mammalian stem cell research is often based on murine stem cells.

1.2.1 Cells: The pre-implantation embryo

In early mouse development, blastocyst patterning occurs at a scale of few compacted cells (80-90μm) which yield the trophectoderm (TE) or the inner cell mass (ICM), which generate the placenta and embryo respectively (Johnson & Ziomek, 1981). Lineage segregation occurs via competing gene regulatory networks (GRNs) each promoting TE/ICM identities (Figure 1A). ICM is specified through a pluripotency GRN involving *Oct3/4*, *Sox2* and *Nanog*, that establishes epiblast identity through broad transcriptomic changes (Gagliardi et al., 2013), of which *Esrrb* upregulation is a primary mediator (Festuccia et al., 2012). OCT4 acts cooperatively with SOX2 to autoregulate *Oct4* and *Nanog* expression, while OCT4 and its targets repress TE-defining *Cdx2*. CDX2 amplifies itself and represses *Oct4* (Niwa et al., 2005) and its targets (Huang et al., 2017). This system of self-amplifying, mutually inhibiting GRNs amplifies divergence of fate specifications: early TEvsICM decisions are metastable (i.e. cells can stochastically shift to either state), but acquisition of any one fate likely results in commitment. This is accentuated by virtue of OCT4/SOX2 targets (e.g. *Sox21*) repressing *Cdx2* (Goolam et al., 2016), which locks ICM cells into pluripotency and prevents them from reverting to TE. This network logic illustrates how TE/ICM fate decisions are stabilized, but does not explain how these fates are patterned such that the ICM core is engulfed by the TE layer.

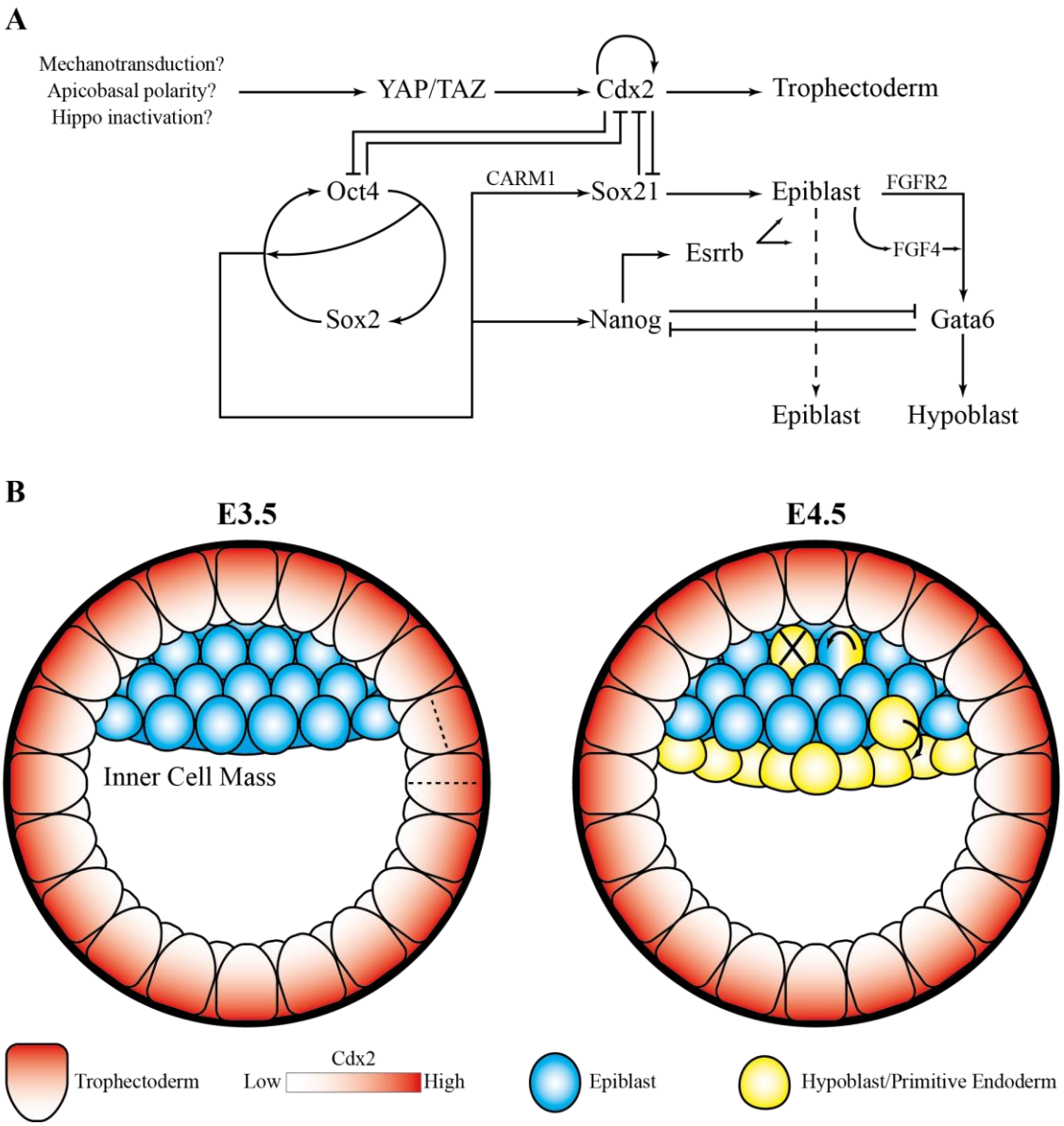

Figure 1. Patterning of the pre-implantation mouse embryo.

(A) Gene-regulatory networks (GRNs) controlling fate-segregation in the early embryo. A pluripotency GRN (Oct4, Sox2, Nanog) maintains epiblast pluripotency (partly via Esrrb) and represses tropgectoderm-defining Cdx2 directly (Oct4) or indirectly (Sox21). Cdx2 expression is is maintained autonomously, and initially induced via YAP/TAZ that lies downstream cell adhesion mechanics and the Hippo pathway. Within the epiblast, Nanog/Esrrb maintains pluripotency, whereas FGF-dependent Gata6 supports hypoblast/primitive endoderm fate. **(B)** Cellular mechanisms in early embryo patterning. In the E3.5 embryo (left), trophectoderm cells divide in two planes (dotted lines), yielding two trophectoderm cells via symmetric divisions, or one trophectoderm/Cdx2High cell and one epiblast/Cdx2Low cell via asymmetric divisions. This is achieved due to intracellular apical localization of Cdx2 transcripts (red gradient). In the E4.5 embryo, primitive endoderm segregates from the epiblast via adhesion-based sorting (arrow), and ectopic epiblast undergoes apoptosis (cross) or transdifferentiation (arrow in gradient), leading to early embryo patterning. Collectively adapted from references in text.

In such small scales (<100μm) where protein diffusion presumably cannot precisely induce distinct regions (compare to 500μm *Drosophila* embryo (Grimm et al., 2010)), patterning proceeds mainly via cell-autonomous mechanisms coupled to established bias. The compact morula appears radially symmetrical, but inside-out asymmetry occurs at the molecular and cellular level (Figure 1B). Peripheral "outside" cells depict apical-basal polarity and fewer intercellular adhesions (Johnson & Ziomek, 1981). In these cells, *Cdx2* transcripts are localized to apical poles; cells dividing parallel to the apico-basal axis generate symmetric $CDX2^{High}$ daughter TE cells, whereas perpendicular divisions are asymmetric, generating one $CDX2^{High}$ outside cell that will yield TE and one $CDX2^{low}$ cell that will contribute to the ICM (Figure 1A-B) (Skamagki et al., 2013). This mechanism reinforces patterning of the early embryo, through spatial segregation between ICM and TE cells. Most divisions are asymmetric, dictated by the apical domain that regulates mitotic spindle orientation and, autonomously, YAP/TAZ nuclear localization, *Cdx2* expression and TE specification (Korotkevich et al., 2017). YAP/TAZ-mediated *Cdx2* expression is implicated in TE specification (Nishioka et al., 2009; Strumpf et al., 2005), and given the mechanosensitive nature of Yap/Taz (Chang et al., 2018), "outside" cells might be biased towards TE specification by virtue of position and different adhesion mechanics. Additionally, the early embryo demonstrates molecular (Goolam et al., 2016) and developmental heterogeneity at the 4-cell stage and earlier, which might underpin TE/ICM specification and self-organization (e.g. by asymmetrical inheritance of cell adhesion molecules). The emerging view is that the early embryo possesses an initial asymmetry bias, defined either by site of sperm entry, intracellular polarization of RNA and proteins, or random inheritance during the first division (Q. Chen et al., 2018).

Following expansion of the patterning field through growth, FGF from pluripotent epiblast promotes specification of primitive endoderm in FGFR2-expressing ICM cells (Kang et al., 2017; Mistri et al., 2018; Nichols et al., 1998). Similarly to competing GRNs in ICM/TE specification, reciprocal repression between *Gata6* and *Nanog* drives divergence between primitive endoderm and epiblast fates respectively (Lavial et al., 2012). FGF signalling events might cooperate with intrinsic noise/fluctuations in transcript levels to bias decisions in a dose-dependent manner, such as $OCT4^{OFF}$ yields TE, $OCT4^{MEDIUM}$ epiblast, and $OCT4^{HIGH}$ primitive endoderm (Karwacki-Neisius et al., 2013; Niwa et al., 2000). This represents an important paradigm in developmental and stem cell biology, which is that signalling events influence cell responses in a context-specific manner. Primitive endoderm/epiblast decisions are translated into pattern formation through cellular mechanisms: $GATA6^{+}$ cells emerging in the epiblast can undergo transdifferentiation back to epiblast, apoptosis, or adhesion-based sorting

(Chazaud et al., 2006). This generates two separated primitive endoderm/epiblast phases surrounded by the TE layer, representing the first event of multicellular pattern elaboration in development (Figure 1B). These events are concurrent with blastocyst cavitation, which represents the first multicellular morphogenetic event that also leads to symmetry breaking through the polarization of the ICM to one side of the cavity. Despite its small size, the preimplantation embryo demonstrates all events of pattern formation, elaboration, and morphogenesis.

Therefore, the pre-implantation mouse embryo demonstrates that small scale patterning with limited information can emerge via cell-autonomous mechanisms (e.g. asymmetric divisions) coupled to single-cell morphogenetic mechanisms (polarization, adhesion-based sorting). Importantly, the early embryo highlights that the patterning field can be the intracellular volume itself, where asymmetric localization of components can form biochemical, inheritable locales that are critical for cell fate acquisition. In such cases, information controlling asymmetric divisions might be conveyed by means of the extracellular matrix and adhesion-based mechanics, events that are difficult to dissect. It will be interesting to see whether such patterning mechanisms are re-invoked later in development where cell fate-acquisition occurs at small scales involving few tens of cells. It should be restated that the point of this analysis of mouse embryonic development is to illustrate and understand how general patterning mechanisms, operating through specific molecular machinery, control facets of mammalian self-organization. Understanding the mechanisms through which cellular components and signalling events become organized during embryonic development is integral to improving self-organization in contemporary stem cell differentiation regimes.

1.2.2 Tissues: Gastrulation

Shortly following implantation to the uterine wall, the mammalian embryo acquires aspects of anteroposterior patterning and sets out the basic body plan. The pluripotent epiblast forms a structure known as the primitive streak (Box 1) and segregates into three germ layers (ectoderm, mesoderm, endoderm) in a process known as gastrulation. These germ layers possess distinct developmental potentials and form the precursors of adult tissues and organs. In the mouse embryo, the steps between uterine implantation at E4.5 and epiblast priming for differentiation at E5.5 are not clear, but a recent study shows that downregulation of the Wnt/β-catenin pathway converts naïve epiblast into a "rosette-state" at E4.9-E5.1 through expression of *Otx2*, followed by FGF-ERK-mediated conversion into $OCT6^{+}$ primed epiblast by E5.5 (Neagu et al., 2020). Around that time, signalling activities (TGFβ, Wnt/β-catenin, FGF) start becoming asymmetrically distributed across what will form the anteroposterior body axis (Bardot & Hadjantonakis, 2020). This signalling organization occurs via long-range and short-range inductive interactions among mid-gastrulation embryonic domains (Box 1) and can be broken down to: i) symmetry breaking through establishment of the anterior visceral endoderm (E5.5-E6.5) and ii) anteroposterior patterning and primitive streak induction (E5.75-E6.0). These processes underpin streak maintenance and gastrulation (E6.5-E8.5).

Box 1. Anatomical domains of mid-gastrulation mouse embryos.

Extra-embryonic ectoderm (ExE): Trophectoderm derivative that forms the ectoplacental cone and provides inductive cues to the embryo proper. Eventually yields the placenta.

Visceral Endoderm: Extra-embryonic tissue deriving from primitive-endoderm that encapsulates the embryo and coordinates its development through signal cross-talk.

Anterior Visceral Endoderm (AVE): Specialized domain that localizes to and specifies the embryo's anterior, secreting long-range inhibitors of the TGFβ and β-catenin pathways.

Primitive Streak: Embryonic tissue that arises at the posterior pole, opposite to the AVE, from which mesendoderm emerges during gastrulation. Extends towards the distal embryonic cylinder as the primitive node migrates, forming a crescent shape. Emerging definitive endoderm displaces the underlying visceral endoderm, and mesoderm fills the epiblast-endoderm space, generating a tri-layered embryo.

Primitive Node: Anterior-most front of the primitive streak that forms a concave groove. Migrates to the distal tip of the embryonic cylinder, extending the primitive streak along its course. Undergoes morphogenetic changes such as tissue involution and epithelial-to-mesenchymal transition, shedding mesendoderm until E8.5.

1.2.2.1 Symmetry breaking

Symmetry breaking across the proximodistal axis of the egg cylinder proceeds via specification of a "counter-organizer" at the visceral endoderm. At E5.5, a specified part of the distal visceral endoderm (DVE, expressing *hex* and TGFβ inhibitors *Lefty1, Cerberus-like/Cer1*) begins migrating towards the prospective anterior embryonic pole, establishing the anterior visceral endoderm (AVE) by E6.25 (Yamamoto et al., 2004). DVE specification is thought to rely on Gdf1/Gdf3, expressed in the epiblast throughout E4.5-E6.0, potentiating early Nodal/TGFβ activity through Cripto-dependent ActRIIA/ActRIIB interactions (Andersson et al., 2007; C. Chen et al., 2006). Given that *Bmpr1a* deletion leads to DVE expansion (Miura et al., 2010), BMP4 from the extraembryonic ectoderm (Andersson et al., 2007; Waldrip et al., 1998) might restrict DVE emergence and thus represent one facet of proximo-distal patterning of the embryonic cylinder. However, β-catenin$^{-/-}$ embryos lack AVE markers *Lefty1* (Kelly et al., 2004) and *Hex,* and a *Cer1*-expressing remnant region remains distally (Huelsken et al., 2000), suggesting that Wnt/β-catenin pathway is also implicated in DVE specification. Embryo manipulation experiments show that DVE migrates away from Nodal or Wnt3a sources, and towards areas of *Cer1/Lefty1* expression and low Wnt/β-catenin activities (Kimura-Yoshida et al., 2005; Yamamoto et al., 2004). Asymmetry in Wnt/β-catenin activity is set through the receptor antagonist DKK1, which is symmetrically expressed along the proximal epiblast at E5.25 before localizing to the prospective anterior and in front of migrating DVE by E5.75 (Kimura-Yoshida et al., 2005; S. L. Lewis et al., 2008). However, *Dkk1*$^{-/-}$ embryos with expanded β-catenin activity are normal in terms of AVE/streak/gastrulation specification processes, and only show later defects such as limb-bud development and head truncations (S. L. Lewis et al., 2008; Mukhopadhyay et al., 2001). Localization of the AVE and associated antagonists (*Dkk1, Lefty1, Cer1*), patterns signalling and proliferative activities along the embryonic cylinder (Kimura-Yoshida et al., 2005; S. L. Lewis et al., 2008; Yamamoto et al., 2004).

AVE dictates the opposite embryonic pole to become the posterior, marked by expression of Wnt3 and T-brachyury (primitive streak and nascent mesoderm marker) (Kimura-Yoshida et al., 2005). Abrogating the AVE, either in activity through *Cer1;Lefty1* co-deletion (Perea-Gomez et al., 2002), or specification/localization through *Gdf1*$^{-/-}$*;Gfd3*$^{-/-}$ co-deletion (Andersson et al., 2007), leads to anteroposterior mispatterning (anterior streak *Foxa2* domain expanded; *T-brachyury* restricted; posterior streak *Wnt3* expressed uniformly) or primitive streak duplication. Streak duplications are also observed in contexts where β-catenin degradation is hampered (L. Zeng et al., 1997), suggesting that controlled downregulation of Wnt/β-catenin signalling is involved in specification of the posterior pole. Together, these studies suggest that the embryo detects early

asymmetries in signalling and proliferative activities, and reinforces them through DVE migration to form the AVE. This asymmetry reinforcement, via long-range TGFβ (*Cer1, Lefty1*) and β-catenin (*Cer1, Dkk1*) pathway antagonists, tightens signalling activities across the egg cylinder to pattern the antero-posterior axis and induce localized primitive streak induction.

1.2.2.2 Anteroposterior Patterning

Activation of patterning and gastrulation programmes largely depends on the TGFβ pathway. The primary ligand is Nodal, named after its localized expression around the E7.5 mouse primitive node (Zhou et al., 1993). *Nodal*$^{-/-}$ mutants lack a primitive streak and express no posterior-defining markers (*Wnt3, Cripto*). These mutants also lack Nodal-inhibiting transcripts at the AVE (*Cer1, Lefty1*) and anterior primitive streak (*Lefty2*), while anterior streak markers (*Foxa2*) are uniformly expressed in the epiblast (Brennan et al., 2001; Conlon et al., 1994), resembling AVE mutants (Andersson et al., 2007; Perea-Gomez et al., 2002). In a *Smad2*$^{-/-}$ background, embryos similarly show defects in visceral endoderm and primitive streak formation; however markers of anterior (*Foxa2*) and posterior (*Wnt3, Cripto*) streak are broadly expressed (Brennan et al., 2001; Waldrip et al., 1998). *Nodal*^{lacZ} reporters reveal Nodal activity in both epiblast and visceral endoderm; in *Smad2*$^{-/-}$ embryos, responses in the visceral endoderm are compromised, but expanded in the epiblast (Brennan et al., 2001). Hence, Nodal signalling initiates primitive streak induction programmes in the epiblast, whose spatial patterning is mediated through emergent interactions with the Nodal-Smad2-activated AVE (*Cer1, Lefty1*) and peri-streak populations (*Lefty2*).

Posterior fates are largely specified through the Wnt/β-catenin pathway. Wnt/β-catenin asymmetry is established via aforementioned *Dkk1* anterior localization at E5.75 (Kimura-Yoshida et al., 2005). Concurrently, *Wnt3* begins being expressed at the prospective posterior at E5.75 (Rivera-Pérez & Magnuson, 2005), where it is required for loss of pluripotency (*Oct4*) and primitive streak establishment (*T-brachyury*, *Fgf8, Goosecoid*, *Nodal*) at E7.5, and continues to be expressed at the posterior streak until late stages of gastrulation (P. Liu et al., 1999; Tortelote et al., 2013). Its close relative, *Wnt3a*, is also expressed in the streak where it directly upregulates *T-brachyury* (Yamaguchi, Takada, et al., 1999). Co-deletions of Lrp5/6, essential Wnt/Dkk1 co-receptors with largely redundant functions (Mao et al., 2002), phenocopy *Wnt3* mutants in loss of *Wnt3, T-brachyury, Fgf8*, and persistence of *Oct4* expression in the epiblast (Kelly et al., 2004). In these models, AVE is specified correctly in terms of *Hex* and *Cer1* expression (Kelly et al., 2004; P. Liu et al., 1999), but while *Wnt3* mutants completely

lose *Nodal* expression (P. Liu et al., 1999), *Lrp5*$^{+/-}$;*Lrp6*$^{-/-}$ embryos show reduced *Lefty2* in the primitive streak coupled to prominent *Nodal* and *Foxa2* expression (Kelly et al., 2004). Microarray analyses comparing E6.0-6.5 embryos of β-catenin$^{-/-}$ and *Wnt3*$^{-/-}$ backgrounds corroborate that genes involved in gastrulation are downregulated in the epiblast (*T-brachyury, Eomes, Fgf8*), but so are components of the TGFβ pathway (*Cripto* (direct target)*, Tgfa, Acvr2,* but not *Nodal*) (Morkel et al., 2003). These studies reveal that the Wnt/β-catenin pathway is indispensable for epiblast differentiation towards posterior embryonic states, and that is also regulates TGFβ-dependent programmes. Given *Nodal* is expressed in the primitive streak of E6.0 β-catenin$^{-/-}$ (Morkel et al., 2003), but not E7.5 *Wnt3*$^{-/-}$ embryos (P. Liu et al., 1999), the Wnt-β-catenin pathway is likely required for the sustenance, but not induction, of Nodal-dependent programs (Ben-Haim et al., 2006; Tortelote et al., 2013).

The FGF-MEK-ERK pathway contributes to Wnt-mediated gastrulation effects. *Fgf8* is expressed in a subset of the *Wnt3*-expressing posterior embryonic domain (Di-Gregorio et al., 2007). *Fgfr1*-deficient embryos seem normal until E7.5, wherefrom onwards they appear smaller and morphologically defunct due to an enlarged primitive streak that fails to gastrulate (Ciruna & Rossant, 2001; Yamaguchi et al., 1994). Chimeric embryos reveal faint T-brachyury expression in *Fgfr1*$^{-/-}$ cells compared to wild-type, attributed to compromised *Fgfr1*-dependent *Snail* expression and subsequent E-cadherin downregulation (Ciruna & Rossant, 2001), events involved in epithelial-to-mesenchymal transition (EMT) (Cano et al., 2000; Carver et al., 2001). Notably, β-catenin co-localized to membrane E-cadherin staining in *Fgfr1*$^{-/-}$ cells, and antibody-mediated E-cadherin downregulation in primitive streak explants restored T-brachyury expression (Ciruna & Rossant, 2001). Depleted Wnt/β-catenin activity and E-cadherin downregulation is also reported in *Tenm4* loss-of-function/hypomorph mutants, and given the protein contains EGF-like repeats, it supports a role for EGF/FGF-family ligands in potentiating Wnt/β-catenin activity during gastrulation (Nakamura et al., 2013).

Lastly, various genes of aforementioned pathways are expressed and involved in physiological post-implantation development. Firstly, *Bmp4* is expressed at the distal extraembryonic ectoderm (Andersson et al., 2007; Waldrip et al., 1998), and deletion of its receptor *Bmpr1a* leads to premature epiblast differentiation towards the default neuronal fate (Di-Gregorio et al., 2007). The extraembryonic ectoderm is also involved in proteinase-dependent maturation of Nodal pro-peptides, hence their subsequent activities (Beck et al., 2002; Ben-Haim et al., 2006). Heterozygous *Smad2*$^{+/-}$ mutants display restricted posterior T-brachyury expression, with surviving newborns showing facial malformations (Nomura & Li, 1998). These anterior malformations are compounded in *Nodal*$^{+/-}$;*Smad2*$^{+/-}$ mice, which also show posterior-arrested node, severe

head truncations and irregular left-right organ patterning (Nomura & Li, 1998). Milder cranial-facial anterior defects are also present in activin receptor type II mutant mice (Matzuk et al., 1995) or *Smad2*$^{+/-}$*;Smad3*$^{+/-}$ mice (Dunn et al., 2004). Given that expansion of β-catenin activity also leads to craniofacial truncations (S. L. Lewis et al., 2008; Mukhopadhyay et al., 2001), anterior fates depend on tight regulation of TGFβ signalling, either in levels or different receptors-transducers, that are cross-regulated by β-catenin. Additional Wnt ligands, such as Wnt5a and Wnt11, form posterior-strong/anterior-weak gradients and are involved in post-gastrulation processes such as paraxial mesoderm specification, somitogenesis, limb bud and notochord development (Andre et al., 2015; Martin & Kimelman, 2012; Yamaguchi, Bradley, et al., 1999). Most of these events occur post-gastrulation, after growth has established new patterning fields within which the same pathways/circuits act to add pattern elaboration. Consequently, patterning of the post-implantation embryo depends on tight signalling thresholds set by the anterior "counter-organizer", localized signalling sources emanating from the posterior (Wnt3/Fgf8), and reinforcement from the extraembryonic ectoderm (Figure 2A). The emergent interactions occurring at the anterior primitive streak and the underlying visceral endoderm, while less understood, should also be noted in the sense that they might self-regulate signalling activities analogous to the AVE vs the posterior primitive streak.

1.2.2.3 Understanding Gastrulation Gene Regulatory Networks

Signalling pathways and their effectors are highly interconnected throughout development, and cannot be sufficiently understood through conventional knock-out studies. While hierarchical and emergent networks can be drawn by cross-examining which gene deletions affect expression of which other genes and applying logical inference, the accuracy of presumptive networks is hindered by the number of genes/nodes and the number of interactions/interconnections. Adding mechanistic insight partially delineates the uncertainty, e.g. both *Nodal*$^{-/-}$ and *Wnt3*$^{-/-}$ mutants lack expression of *Cripto* (Brennan et al., 2001; Morkel et al., 2003), and given that β-catenin directly upregulates *Cripto* (Morkel et al., 2003), *Nodal* upregulates *Cripto* at least via β-catenin. In the context of numerous genes and cross-regulatory interactions, while presumptive GRNs can be drawn (Figure 2B), the task becomes increasingly difficult and the probability of flow-charts being inaccurate increases. In such cases, GRN quality can be increased through computation, to translate a tabular input of "*Row*: *GeneX*; *Column*: Present/Absent in *GeneY-null*" into possible GRNs, and through modelling on ICM-derived embryonic stem cells (ESCs), followed by verification in the embryo.

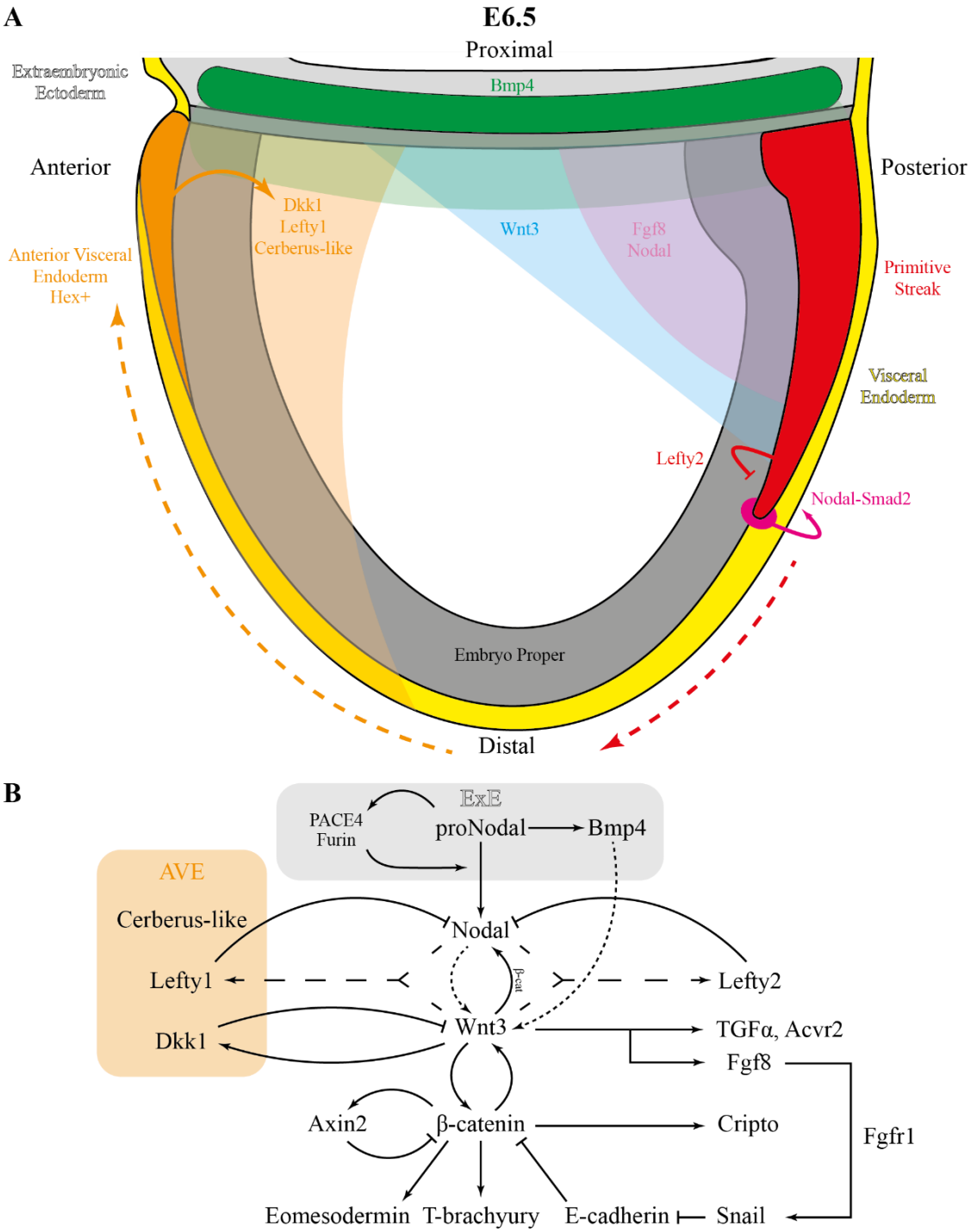

Figure 2. Patterning of the post-implantation mouse embryo.

(A) Schematic representation of patterning events in the early-primitive streak stage E6.5 embryo. The anterior visceral endoderm (orange) establishes gradients of Nodal and Wnt antagonists and the prospective embryo anterior. The posterior emerges to the opposite, in which posterior-based gradients of Wnt3 (blue) and Fgf8/Nodal (magenta) establish the T-brachyury+ primitive streak (red). The extraembryonic ectoderm (ExE, light gray) provides Bmp4 signalling to the streak (green) and facilitates maturation of Nodal pro-peptides. **(B)** Presumptive gene regulatory network summarizing inductive interactions in the primitive streak. Dotted lines represent questionable interactions, which could be attributed to different signals, and resolution of which requires mechanistic data. Collectively adapted from references in text.

Significant mechanistic insights have recently come from molecular studies and single-cell transcriptomics. In human ESCs, β-catenin forms complexes with SMAD2/SMAD3 to directly and collaboratively upregulate primitive streak-related genes (*T-BRACHYURY, EOMES, NODAL, LEFTY*), with co-occupancy of OCT4 in one-third of β-catenin-occupied genes (Funa et al., 2015). In such conditions, exogenous ACTIVIN-A promotes endoderm differentiation instead of mesoderm, whereas abrogating the *NODAL-SMAD2* axis entirely allows β-catenin to promote expression of neural crest-related genes (Funa et al., 2015). This provides a possible mechanistic link between developmental patterning and fate decisions for the mouse embryo, whereby i) posterior cells are induced to primitive streak via co-expression and collaborative activity of Nodal and Wnt3/β-catenin, ii) streak cells subjected to higher TGFβ activities from pre-patterned expression of activins and other ligands are converted to endoderm, iii) Wnt-dominant/TGFβ-low streak cells are converted to mesoderm and iv) Wnt-active/TGFβ-inactive cells are specified to non-mesendodermal fates. The study highlights that signalling effectors converge, and their interactions could depend on cell/tissue-specific enhancers, epigenetics, and/or expression of co-factors. Recent single-cell transcriptomic analyses are able to link known transcriptomic fate-signatures and expressed pathway components to deduced position in the developing gastrula, such as Bmp signalling to lateral mesoderm identity (Scialdone et al., 2016), anterior primitive streak signatures to definitive endoderm, and far-posterior streak to primitive haematopoietic cells (Pijuan-Sala et al., 2019). The ability to link transcriptomic fate-signatures (Pijuan-Sala et al., 2019) and epigenetic states (Argelaguet et al., 2019) to bona fide positions in the developing embryo through novel high-resolution imaging techniques (McDole et al., 2018), as has been achieved in certain systems (Lindström et al., 2018), will illuminate how fate-acquisition is linked to embryonic patterning.

In summary, patterning of the post-implantation embryo begins with symmetry breaking through the localized specification of the DVE, which migrates to the anterior and sets the AVE. The AVE secretes Nodal/TGFβ and Wnt/β-catenin pathway inhibitors. The posterior pole of the embryo expresses Nodal, Wnt3 and Fgf8 early on, and Wnt3 and Fgf8 later. These opposing/antagonistic gradients of pathway activators vs inhibitors set tight signalling activities that pattern the embryonic anteroposterior axis. Notably, the DVE-AVE migration transforms the proximodistal axis to an anteroposterior axis, and the Nodal-expressing primitive node migrates towards the distal pole while shedding mesendoderm, illustrating how migration of signalling centres can lead to large-scale patterning and subsequently morphogenesis. This forms a paradigm for developmental and stem cell self-organization, and is perhaps best illustrated during organogenesis of the developing kidney.

1.2.3 Organs: Kidney Branching Morphogenesis

Kidney development provides a suitable system to investigate how large-scale three-dimensional complexity emerges through a relatively limited set of interactions/events. Between E8.5 and E9.5, the intermediate mesoderm splits into the dorsal nephric duct and the ventral nephrogenic cord, which eventually give rise to the definitive kidney (metanephros) collecting duct and filtration systems respectively (reviewed by (Costantini & Kopan, 2010)). This is achieved through a repeating morphodynamic programme, initiated when the nephrogenic cord-derived metanephric mesenchyme (MM) induces the nephric duct to invade the mesenchyme at E10.5, forming the ureteric bud (UB). The single UB protrusion bifurcates at E11.5, and each branch continues to grow and migrate away from the bifurcation site until the next bifurcation event. At each event, MM surrounding the bifurcation point undergoes mesenchymal-to-epithelial transition (MET), forming an epithelial population that generates the blood-filtering nephron unit. This cycle is repeated multiple times, and together with contributions from stromal cells, the UB, MM and stromal lineages develop the functional kidney.

The UB comprises cell populations at the tips and the trunk, each with distinct functional properties. UB demonstrates active migration, based on GDNF provided by the MM (Pepicelli et al., 1997), and GFRα1/RET co-receptor complexes localized in highly proliferating and migrating tip cells (Chi et al., 2009; Sakurai et al., 2005), that activate the MAPK/ERK pathway (Fisher et al., 2001). UB outgrowth/migration is tightly directed by negative regulators of GDNF-RET activity, primarily SPRY1 present in the UB trunk, mutation of which results in multiple UB outgrowths (Basson et al., 2005). Co-deletion of *Spry1* and *Gdnf/Ret*, while leading to minor nephron patterning defects, is tolerated in terms of kidney development due to FGF10 (Michos et al., 2010) likely compensating for lack of GDNF in downstream ERK/MAPK activation (Fisher et al., 2001). Some contribution to branching is also provided by the HGF-MET axis that converges to the MAPK cascade (Ishibe et al., 2009).

The primary GDNF-RET axis triggers an auto-regulatory network, amplifying expression of *Ret*, the negative regulator *Spry1* (Basson et al., 2005), and *Wnt11* at the UB tips (Majumdar et al., 2003; Sweeney et al., 2008). Wnt11 stimulates the surrounding metanephric mesenchyme to upregulate *Gdnf* (Majumdar et al., 2003), forming an auto-regulatory circuit that possibly maintains high GDNF-RET activity in UB tip cells (Figure 3A). It is tempting to hypothesize that UB migration proceeds via a “carrot-on-a-stick” model, whereby GDNF/RET-active UB tips migrate into the MM, stimulating it to upregulate *Gdnf* based on the range of Wnt11 diffusion, causing further UB migration to the new GDNF wavefront, at which point the cycle is repeated. The UB trunk also expresses Wnt9b, which acts in an autocrine manner to coordinate planar cell polarity

and oriented divisions, thereby extending the ureteric bud in length rather than width (Karner et al., 2009). Excessive branching is restricted primarily through BMP4 which is expressed in the MM and the mesenchyme surrounding the nephric duct; this is locally antagonised by Gremlin expression which allows UB outgrowth and branching (Michos et al., 2007; Nie et al., 2011). The negative effect of the TGFβ pathway in branching is also illustrated in the higher branching rate of *Tgfβ2*$^{+/-}$ mice (Sims-Lucas et al., 2008). The UB branching system is plastic, in the sense that branching can be ectopically re-induced upon MM transplantation (Sweeney et al., 2008), or inhibited through exogenous application of localized BMP4 (Mills et al., 2017). Collectively, the compartmentalization of high MAPK/ERK activity in tips and high BMP/SMAD activity in trunk, combined with planar cell polarity, increases the efficiency of UB elongated growth and branching and associated nephrogenesis from the MM pool (Figure 3).

Nephrogenesis is induced from nephrogenic progenitor cells (NPCs) that reside in the MM. NPCs express WT1 (Hartwig et al., 2010) and SIX2, the latter required for self-renewal and prevention of premature differentiation that exhausts the NPC pool (Kobayashi et al., 2008; Self et al., 2006). Induction of nephrogenesis requires UB and stroma-derived Wnt9b activating β-catenin in NPCs (Carroll et al., 2005; Karner et al., 2011), which interacts with SIX2 to control NPC differentiation (Kobayashi et al., 2008; Park et al., 2012). Activation of β-catenin is required and sufficient to induce NPC differentiation, but completion of MET and nephrogenesis requires downregulation of β-catenin (Park et al., 2007). Induced NPCs differentiate into Wnt4-expressing progenitors localizing exclusively inside UB bifurcation corners (Mugford et al., 2009). This suggests that induction is tightly restricted, either at the level of niche-derived signals (Ramalingam et al., 2018) or cell-autonomously in the NPCs (Mugford et al., 2009). Downregulation of the Wnt/β-catenin pathway is thought to be achieved, at least partially, through Hippo pathway activation that leads to phosphorylation and cytoplasmic retention of TAZ, which sequesters Dishevelled and restricts β-catenin stabilization (Varelas et al., 2010). Further to nephrogenesis, nephron polarity and attachment to the UB depends on Wnt11 (O'brien et al., 2018). The developing nephron is patterned across the proximo-distal axis, through a distal-strong/proximal-weak β-catenin gradient, antagonized by medial BMP4, and absent in the proximal DLL1-Notch2-dependent domain (Cheng et al., 2007; Lindström et al., 2014; Surendran et al., 2010). The proximal domain also expresses *Dkk1* and *Bmp2* (Georgas et al., 2009), suggesting further proximal inhibition of Wnt/β-catenin activity. In summary, nephron induction, polarization, and proximo-distal patterning heavily relies on the Wnt/β-catenin pathway, with additional contributions from the BMP and Notch pathway adding pattern elaboration during late nephron development (Figure 3).

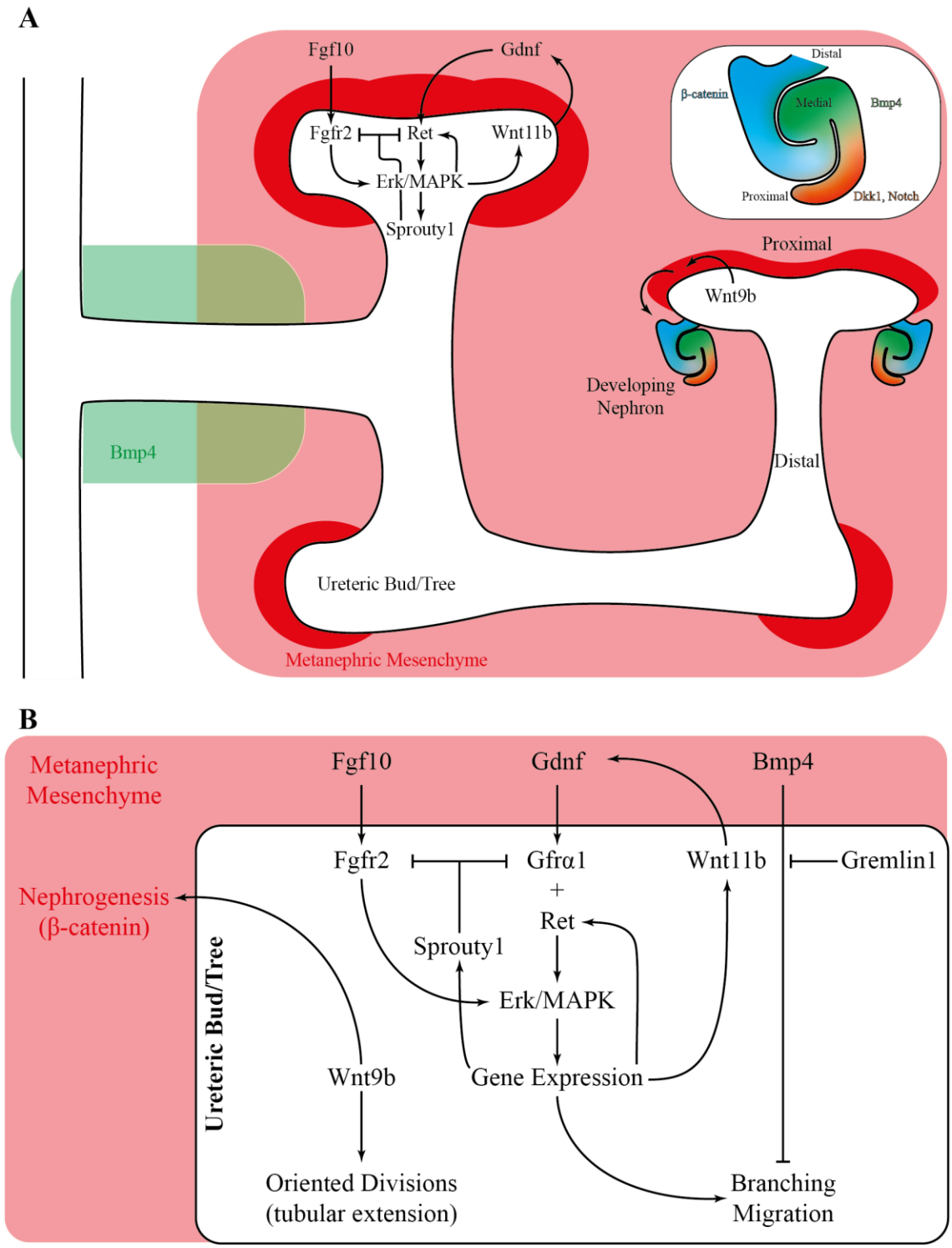

Figure 3. Patterning and morphogenetic events during kidney development.

(A) Schematic representation of branching morphogenesis. The ureteric bud (UB) invades the metanephric mesenchyme (MM, light red) while branching is inhibited due to peri-Wolffian mesenchyme-derived Bmp4 (green). Branching and migration is maintained by a positive, self-regulated loop between UB tips and the MM. Nephrogenesis is stimulated by Wnt/β-catenin induction of the cap mesenchyme (red), and developing nephrons (top right inlet) show proximo-distal patterning in β-catenin (blue), Bmp4 (green), and Notch and Dkk1 (orange) activities. **(B)** Gene regulatory network of UB-MM inductive interactions that drive kidney branching, tubular extension and nephrogenesis. Collectively adapted from references in text.

Lastly, the stroma plays supportive roles in coordinating interactions between UB and MM. Kidneys developing with compromised stroma end up malnourished, close to the body midline, underbranched and with compromised nephrogenesis (Hatini et al., 1996; Levinson et al., 2005). Stromal cells (FoxD1+) coordinate nephrogenesis by activating the Hippo pathway (thus promoting cytoplasmic YAP/TAZ) in the MM via juxtacrine presentation of the ligand Fat4, modulating Wnt9b activity and converting stem-like progenitors to differentiating nephron progenitors (Das et al., 2013). Whether YAP/TAZ regulates β-catenin activity purely in levels (quantitative), or also by modulating β-catenin DNA binding occupancy (qualitative), is unclear. In a striking tissue recombination experiment, kidney UB and lung stroma chimeras demonstrate lung-type branching morphogenesis, highlighting the importance of the niche in patterning and morphogenesis (Vainio et al., 2003). It is unknown whether the stroma itself is pre-patterned, or whether it acts as a relay mediator that coordinates emergent interactions between the UB and MM. There are many open questions in the field of kidney development, such as whether developed nephrons provide feedback to UB branching, how do stromal cells coordinate UB-MM interactions, and what causes the termination of kidney development.

The developing kidney provides a fine example of how short-scale signalling circuits, when repeated over a large scale and are coupled to directed migration, can lead to fractal-type, highly complex patterning and morphogenesis. In kidney development, symmetry breaking precedes pattern formation, as the UB initially invades the MM from a single polarized entry; this original invading tubule will later form the ureter (Basson et al., 2005; Chi et al., 2009; Nie et al., 2011). Following UB dichotomy, each branch autonomously interacts with the MM on a small-scale, which drives morphogenesis through UB migration and nephron induction (Carroll et al., 2005; Karner et al., 2011; Majumdar et al., 2003). Because these events occur repeatedly over the MM scale, an overall pattern emerges as morphogenesis ensues. Nephrons also show proximodistal patterning, which can be considered as a form of pattern elaboration within the developing kidney (Lindström et al., 2014; O'brien et al., 2018). It is clear that developmental self-organization, whether it concerns a few cells, tissues or organs, is complex and challenging to study in vivo, which is why increasing effort has focused on trying to model and recapitulate it in vitro.

1.3 Patterning in vitro

The 1960s marked the discovery of adult stem cells, which possessed multi-lineage potential and the capacity to renew themselves (Becker et al., 1963; McCulloch & Till, 1960). This was followed by the isolation and culture of murine and human embryonic stem cells (mESCs/hESCs), pluripotent stem cells harvested from the embryo inner cell mass that could differentiate into any cell type of the adult body (Bradley et al., 1984; Evans & Kaufman, 1981; Nagy et al., 1993; Thomson, 1998). The bioethical implications surrounding human ESC derivation and embryo destruction were resolved by converting human fibroblasts into induced pluripotent stem cells (iPSCs) by means of transcription factor-mediated reprogramming (Takahashi & Yamanaka, 2006), adding a new dimension into how cell fate could be specified in vitro. Pluripotent stem cells (PSCs) and tissue-specific adult stem cells (ASCs) are used to generate specialized cells, tissues and mini-organs for basic research, pharmacological screening, disease modelling, and eventually biomedical transplantations, establishing the basis of regenerative medicine.

1.3.1 Stem Cell Self-Organization

The inherent challenge with PSC differentiation regimes is the attempt to recapitulate complex developmental events in a simplified in vitro microenvironment. The status quo for addressing this limitation is culturing PSCs in suspension, forming 3D aggregates termed embryoid bodies (EBs) that demonstrate elements of developmental patterning. T-brachyury^{+} nascent mesoderm emerges in proximity to or overlapping β-catenin^{+} cells, and undergoes Wnt-dependent EMT (ten Berge et al., 2008). EB stimulation with a pulse of CHIRON-99021 (β-catenin agonist) between 48-72h of differentiation elicits EB elongation in a size-dependent manner; small EBs (200-400 seeded mESCs) undergo unidirectional elongation, whereas larger EBs (>600 mESCs) demonstrate symmetrical growth or multiple elongation protrusions (Van Den Brink et al., 2014). Axial elongation marks EB symmetry breaking, as Wnt/β-catenin-active T-brachyury+ nascent mesendoderm and/or Activin-A-dependent endoderm reside polarized within the elongated protrusion. This polarized expression occurs between 84-96h of differentiation (Van Den Brink et al., 2014). Wnt3a can substitute for CHIRON-99021 in polarizing T-brachyury, and Wnt-dependent T-brachyury expression requires upstream Nodal activity (Turner et al., 2017). Extending these aggregates to 7 days of differentiation reveals impressive similarities to gastrulating embryos, such as Wnt3a/T-brachyury posterior localization, further anterior Nodal expression, and Hox gene co-linearity (Beccari et al., 2018). Developmental programmes, such as the somitogenesis segmentation clock, can be recapitulated when gastruloids are embedded in extracellular matrix formulations,

recreating remarkable axial patterning (van den Brink et al., 2020). However, gastruloids show limitations including slower differentiation rates marked by prolonged expression of pluripotency factors, absence of extraembryonic tissues, posteriorization due to absence of anterior-most neuronal markers, and limited morphogenesis (Beccari et al., 2018; Turner et al., 2017). To date, gastruloids offer the most sophisticated in vitro model of anteroposterior embryonic patterning, and the derivation of human gastruloids from hESCs has been recently achieved (Moris et al., 2020).

Similar to gastruloids, three-dimensional mini-organs (organoids) can be generated from PSCs and ASCs. Depending on initial EB differentiation conditions, anterior-type neuronal organoids, such as optic-cup organoids from mouse (Eiraku et al., 2011) or human ESCs (Nakano et al., 2012) or hESC-derived cerebral organoids (Renner et al., 2017) can be generated from PSCs. These aggregates undergo autonomous patterning, morphogenesis and tissue stratification via intra-organoid inductive interactions. Organoid generation from ASCs is best illustrated through Lgr5+ intestinal stem cells (ISCs), which can generate self-organizing intestinal organoids from a single cell input (Sato et al., 2009). Development of intestinal organoids requires symmetry breaking, whereby transient YAP1 activation in early-stage aggregates converts Lgr5+ stem cells into niche Paneth cells, which support ISC maintenance by providing short-range Wnt3 and Notch signalling ligands (Farin et al., 2016; Sato et al., 2011; Serra et al., 2019). Interestingly, intestinal organoid development parallels many themes from pre-implantation embryo patterning: Both structures emerge from a clonal outgrowth; transient YAP/TAZ activation converts stem cells (epiblast/intestinal) into niche/supporting cells (trophectoderm/Paneth); this conversion occurs in multicellular aggregates of a few tens of cells; and this fate-segregation precedes symmetry breaking and morphogenesis (morula cavitation/organoid budding). Altogether, these points highlight the power of stem cells as systems for modelling developmental processes.

While gastruloids/organoids encompass histological domains that are interdependent, bear physiological immunophenotypic profiles, and demonstrate impressive levels of self-organization, they are limited in more sophisticated elements of patterning, such as spatial control of cell/tissue emergence, symmetry breaking at different scales, and multi-component integration (e.g. organoid vascularization). On the other hand, the current degree of self-organization emerges at complex, rapid and heterogeneous rates, hindering attempts for deep mechanistic dissection. Engineering self-organization can therefore assist both in producing more realistic/physiological organoids (reviewed in (Brassard & Lutolf, 2019)), and bolster our understanding of basic developmental mechanisms. The first steps in this field have focused on combining highly-defined ESC micropatterning to differentiation under microfluidics-induced flow.

Micropatterning yields hESC monolayer colonies showing symmetrical roundness, defined radius and geometrical confinement. BMP-induced differentiation leads to concentric domains, with an outer rim of $CDX2^+$ cells followed by successive rings of $CDX2^+SOX17^+$, $CDX2^+$T-$BRACHYURY^+$ and an inner centre of $SOX2^+$ cells, representing presumptive trophectoderm, endoderm, mesoderm and ectoderm fates respectively (Deglincerti et al., 2016; Warmflash et al., 2014). Signalling events become organized such that BMP/pSMAD1 activation occurs in the outer rim, followed by a short travelling NODAL/SMAD2 outside-in gradient (high in $CDX2^+SOX17^+$, low in $CDX2^+$ T-$BRACHYURY^+$, absent in $SOX2^+$ equivalent regions) which is required for downstream T-BRACHYURY emergence (Heemskerk et al., 2019; Warmflash et al., 2014). Notably, T-$BRACHYURY^+$ cells are also active in pERK/FGF and undergo EMT to yield two-three stacked cell layers (Warmflash et al., 2014). Peripheral restriction of BMP4/pSMAD1 activation can be explained by cell density-dependent sensitivity and Turing-like Reaction-Diffusion: cell confinement lateralizes BMP receptors and is thought to reduce BMP4/pSMAD1 activation sensitivity, while early homogeneous BMP4/pSMAD1 activation induces expression of its own inhibitor NOGGIN. These factors set tight pSMAD1 activation thresholds, exceeded only in peripheral cells presenting receptors apically and located away from the central NOGGIN mass/gradient, or when BMP4 dosages exceed density-depend insensitivity (Etoc et al., 2016; Tewary et al., 2017). Notably, pattern formation requires BMP4 dosages to scale according to the colony size (Tewary et al., 2017), and ectodermal differentiation experiments reveal that fate patterning depends on carefully timed integration of relative BMP and WNT signalling activities following NODAL inhibition (Britton et al., 2019). Symmetry breaking can occur when micropatterned hESCs are differentiated under microfluidics, where polarized BMP4 shifts $CDX2^+$ and mesendoderm lineages near the source, while NOGGIN emanating from the opposite pole further refines expression patterns (Manfrin et al., 2019). These experiments illustrate that PSC differentiation entails hard-wired Reaction-Diffusion networks that autonomously generate and integrate Wolpert-style signalling gradients to drive pattern formation, in conjunction to biophysical properties such as density-dependent receptor localization and colony size/patterning field (Britton et al., 2019; Etoc et al., 2016; Tewary et al., 2017). The findings highlight the importance of starting conditions in emerging fate patterning, providing insights as to how EB elongation relates to starting cell density and EB size (Van Den Brink et al., 2014). Defining organoid homogeneity through microfabrication of hydrogel-moulded microcavities represents early steps in transferring principles of micropatterning to 3D culture conditions (Brandenberg et al., 2020).

In summary, ESCs constitute powerful tool to model developmental processes due to their inherent autonomous self-organization properties. When high complexity is desired, ESCs are cultured as suspension aggregates to yield self-organizing EBs, gastruloids or organoids, which suffer from poor user-defined control, limited symmetry breaking, and absent integration of physiological components. When control and close mechanistic dissection is desired, ESC micropatterning permits the study of early inductive interactions and pattern formation events, but lacks complexity and is limited to restricted two-dimensional growth. Studying and controlling high-order patterning events in both two- and three-dimensional developmental systems in vitro, is currently an unfilled gap in stem cell research, which can be addressed via synthetic biology.

1.3.2 Synthetic Biology and Pattern Formation

Synthetic biology approaches biological phenomena from a systems and engineering perspective: biological mechanisms constitute a hierarchical complex composed of sub-systems, devices and units that are amenable to change or re-design de novo, to execute desirable functions. Inspired by electrical engineering, synthetic and/or wild-type cross-interacting genes (modules) can be assembled into genetic circuits (devices) to execute a cellular operation in a predictable manner. Synthetic gene circuits have been able to produce desirable outputs with unprecedented precision, timing and efficiency, such as oscillating gene expression (circadian rhythms) and Boolean logic gates (multifactorial control of gene expression), and their applications include production of metabolites and next-generation therapeutics (reviewed in (Xie & Fussenegger, 2018)). In this spirit, synthetic biology can be used to engineer genetic systems driving pattern formation for two main reasons: i) trying to (re)create patterning systems by engineering the underlying molecular logic allows scientists to interrogate current views surrounding the mechanisms through which self-organization emerges during development and ii) successfully produced synthetic patterning systems might be used as tools for future tissue engineering (reviewed in (Davies & Glykofrydis, 2020)).

Pattern formation has been largely engineered in bacteria due to relative host simplicity, ease of engineering, and defined molecular tools. Early experiments focused on engineering bacteria to detect intermediate levels of a diffusive metabolite (acyl-homoserine lactone; AHL): GFP was put under the control of two repressors: *lacI*, expressed constitutively, and its hypomorphic derivative $lacI_{M1}$. The circuit behaved as follows: AHL activates LuxR to indirectly repress *lacI* expression, and directly upregulate $lacI_{M1}$. At AHL concentrations too low to activate LuxR, constitutive LacI represses GFP. High AHL concentrations, while repressing *lacI*, produce high levels of $LacI_{M1}$ that sufficiently repress GFP. Only at intermediate concentrations, which repress *lacI* and express subpar $lacI_{M1}$, is GFP expressed, acting as a band-pass filter. When a disc of AHL sender cells was co-cultured on a lawn of receivers, a GFP bullseye pattern was generated (Basu et al., 2005). In a different configuration, both AHL production (*luxI*) and detection (*luxR*) were configured to repress a flagella motility factor (*cheZ*). This creates a quorum-sensing-based motility device, whereby low cell density permits free bacteria motility, whereas high density ($4x10^8$cells/ml) causes bacteria to continuously tumble and remain effectively stationary. When the centre of an agar plate is inoculated, bacteria migrate radially while proliferating; the central spot becomes high-density, forming an immobilization trap for bacteria either contained within or migrating into the zone. As the migratory front expands radially, and proliferation increases cell density behind it, a net accumulation of AHL sets new radial immobilization zones. This system generated

bullseye patterns of bacteria cell densities (C. Liu et al., 2011). In a different approach, a transgenic bacterial library was produced, each strain expressing one membrane-tethered camelid-derived nanobody variant, or one of many potentially corresponding antigens. The library was screened to identify bacteria pairs that co-aggregate based on nanobody-antigen interactions, and different adhesion-based multicellular patterns (rosettes, separated population phases, enveloped multicellular core) could be rationally assembled (Glass & Riedel-Kruse, 2018). These examples (Figure 4A-B) illustrate how self-organization can emerge through relatively simple rules that dictate interactions on the level of gene circuit logic (band-pass filter), morphogenetic behaviours (differential adhesion), or the combination of the two (density-dependent motility). Importantly, they provide insights to potential mechanisms that might instruct development; e.g. responses to intermediate morphogen concentrations could rely on band-pass logic, and cell adhesion interactions might be implicated in tissue self-organization.

Composite devices integrating independent circuits have been able to produce more complex behaviours. One such device has been described (Boehm et al., 2018), whereby distinct homoserine lactone metabolites orthogonally drove expression of i) YFP and the T7 polymerase N-terminus ($T7RNAP_{1-179}$) or ii) CFP and the T7 polymerase bulk region ($T7RNAP_{180-880}$). Expression of a third RFP module was induced through co-expression of $T7RNAP_{1-179}$ and $T7RNAP_{180-880}$, but not of each alone, forming an AND logic gate. When bacterial colonies were micropatterned and exposed to opposing localized sources of inducer metabolites, sequential YFP, RFP and CFP domains emerged as they received either of each inducers near the poles or both around the middle (Boehm et al., 2018). This single population was split in two derivatives, each engineered to autonomously produce one of two inducer metabolites, and then micropatterned so that each population occupied half of the culture vessel; an RFP population similarly emerged at the co-culture interface (Boehm et al., 2018). These composite models (Figure 4C) are reminiscent of developmental concepts: the experiment of opposing inducer sources demonstrates how morphogens from differentially localized organizers integrate, according to gene regulatory networks, to drive pattern formation. On the other hand, the two-population co-culture in which a third fate emerges approximates inductive interactions that emerge along differentiation trajectories, which add pattern elaboration. Altogether, these synthetic systems demonstrate that pattern formation can be produced by programming interpretation of exogenous signalling ligands (Basu et al., 2005; Boehm et al., 2018), or autonomously (self-organization) through custom morphogenetic behaviours and dynamic population interactions (Boehm et al., 2018; Glass & Riedel-Kruse, 2018; C. Liu et al., 2011).

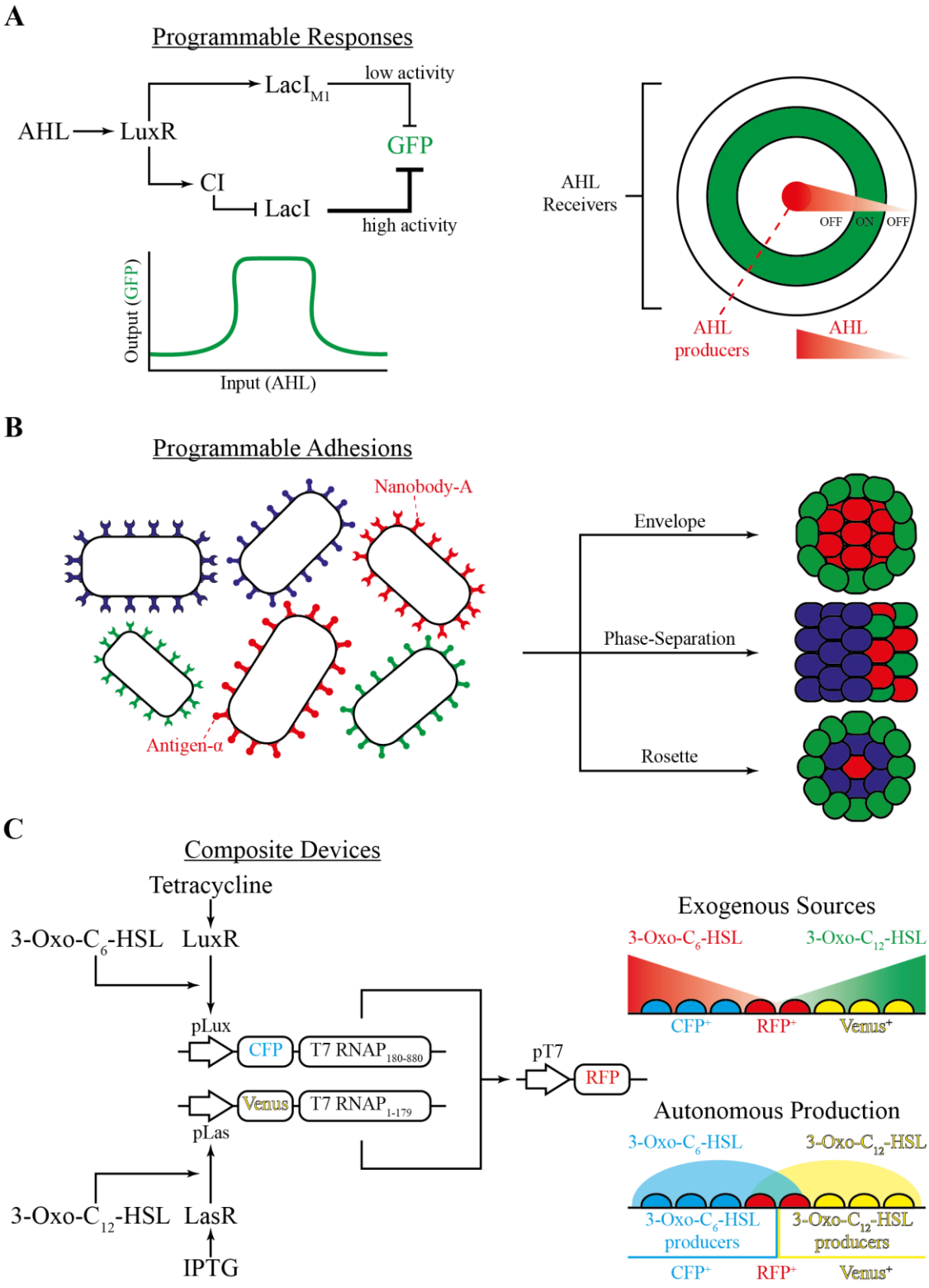

Figure 4. Overview of synthetic patterning mechanisms in bacteria.

(A) Band-pass circuit that mediates cell-state response at intermediate levels of input signal. **(B)** Custom nanobody-antigen interactions allow rational assembly of adhesion-based patterns. **(C)** Integration of independent orthogonal circuits into a composite device, whereby co-activation of circuits elicits a third state. When signals are localized, cell-responses are translated into patterns. For detailed explanation, refer to text in section. Adapted from (Basu et al., 2005; Boehm et al., 2018; Glass & Riedel-Kruse, 2018).

Programmed pattern formation in bacteria has provided substantiating evidence that engineering patterning is possible and potentially applicable in mammalian systems. Early steps in engineering pattern formation in mammalian cell lines built on the differential adhesion hypothesis. This concept postulates that differences in intercellular adhesiveness propagate into differences in tissue surface tensions, which in turn leads to morphogenetic events such as segregation or enveloping between distinct cell populations (Foty & Steinberg, 2005). By modifying mouse fibroblasts to variably express *Cdh2* (a homophilic cell adhesion molecule), it was shown that the propensity of multicellular aggregation and aggregate surface tension was directly proportional to cadherin expression levels (Foty & Steinberg, 2005). This cadherin-driven manipulation of intercellular adhesiveness led to adhesion-based cell sorting (Foty & Steinberg, 2005). Mouse fibroblasts expressing different cadherins (*Cdh1* or *Cdh3*) also form segregated population phases, in which distinct cell types preferentially self-aggregate homotypically rather than intermingling heterotypically due to differential adhesion affinities (Nose et al., 1988). When distinct cadherins (*Cdh1; Cdh3*) were separately introduced into HEK-293-based cells, transgenic populations (TREx-293^{Cdh1}; TREx-293^{Cdh3}) segregated into phase-separation patch-like patterns in 2D and 3D co-cultures, in an autonomous self-organizing manner (Cachat et al., 2016). This mechanism is semi-synthetic, in the sense that cadherin-mediated phase-separation was wholly adapted from in vivo development to in vitro cell culture, with minimal reconfiguration.

One synthetic tool includes the *SynNotch* system, in which the extracellular ligand binding and intracellular transcription factor domains of the Notch receptor were replaced by custom sensor and actuator domains, allowing cells to elicit desired genetic responses following juxtacrine detection of defined signals (Morsut et al., 2016). Using this system, receiver cells were programmed by engineering the following circuit: upon SynNotch-based detection of extracellular GFP, release of SynNotch-sequestered tTA allows induction of a *TRE::CD19-mCherry* module from which CD19 traffics to the cell surface. Receivers also harbour an antiCD19-SynNotch-Gal4-VP64 module, which analogously induces expression of *UAS::tagBFP* following juxtacrine CD19 detection; Notch-based receptors are activated only when ligands are presented from neighbouring cells (in trans) and not in an autocrine fashion (in cis). Hence, when programmed receivers were co-cultured amidst membrane-tethered GFP sender colonies, antiGFP-SynNotch-tTA activated a first layer of *CD19-mCherry* response, followed by a second layer of BFP expression via antiCD19-SynNotch-Gal4-VP64, leading to GFP-mCherry-BFP two-dimensional radial patterns (Morsut et al., 2016). This work has marked the construction and implementation of native (cadherin-driven) or synthetic (SynNotch-based) circuits to drive pattern formation in mammalian systems (Figure 5A-B).

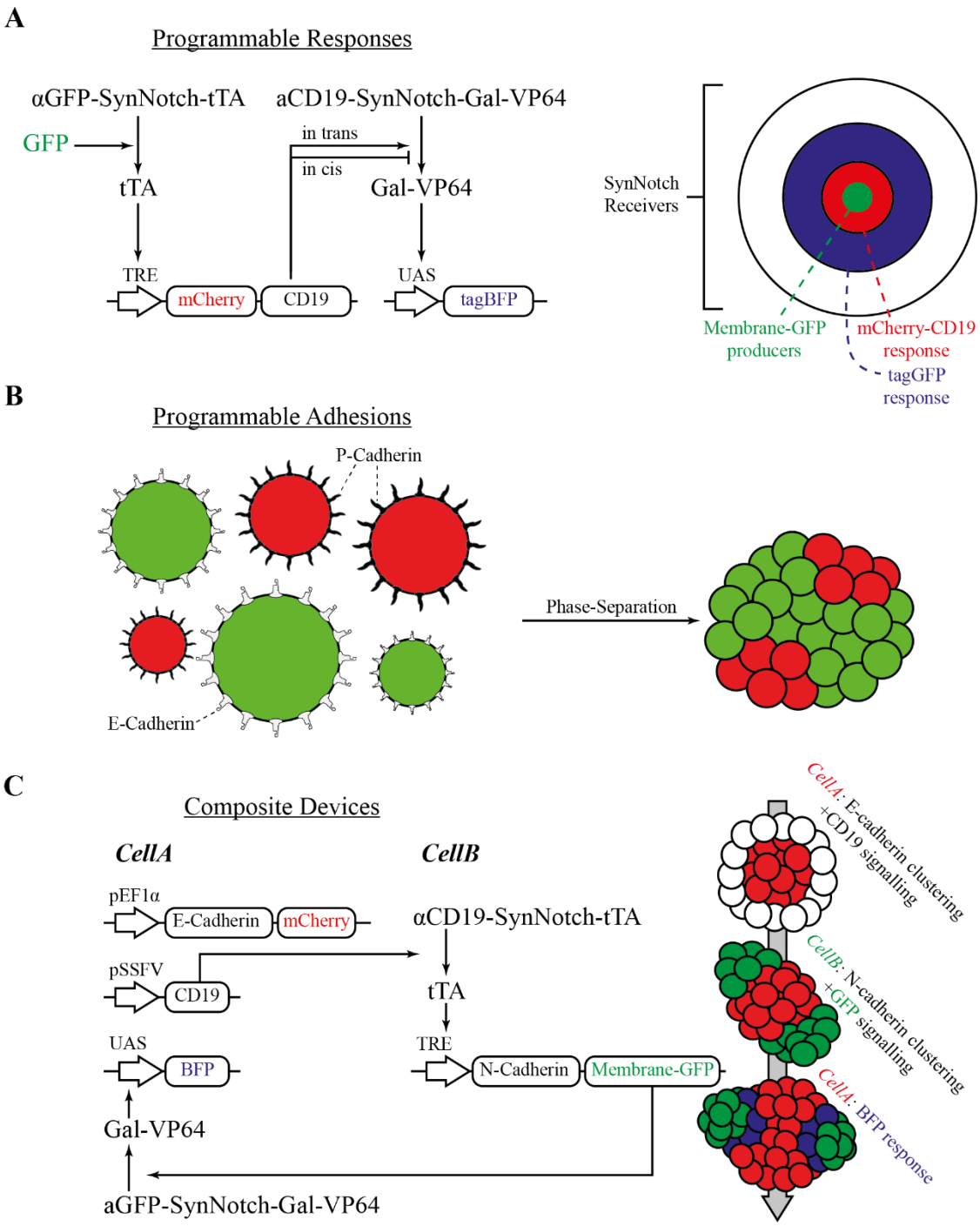

Figure 5. Overview of synthetic patterning mechanisms in mammalian cells.

(A) Programmable sensing and response via SynNotch allow the step-wise elicitation of state changes. The circuit depicts a first layer of juxtacrine interactions that specify mCherry^{+} cells, which propagates into a second layer of interaction that specifies tagBFP^{+} cells. **(B)** Adhesion engineering allows control of cell-cell interactions, as illustrated by distinct cadherin-cadherin homophilic interactions that drive phase-separation of entailed cell populations. **(C)** Integration of cadherin-based phase-separation into SynNotch custom circuits allows autonomous stepwise patterning and morphogenesis in three-dimensional aggregates comprising a few tens to a few hundred cells. For detailed explanation, refer to text in section. Adapted from (Cachat et al., 2016; Morsut et al., 2016; Toda et al., 2018).

The integration of cadherin-based phase-separation into SynNotch circuit configurations has allowed user-defined generation of various patterns (Toda et al., 2018). For example, *CellA* was engineered to express CD19, mCherry and Cdh3 constitutively, and BFP under antiGFP-SynNotch control. *CellB* was engineered to express antiCD19-SynNotch constitutively, activation of which induced expression of Cdh2 and membrane-tethered GFP. When *CellA* and *CellB* were co-aggregated, *CellA*-derived CD19 activated *CellB* antiCD19-SynNotch to begin expression of Cdh2 and membrane-tethered GFP, while forming a Cdh3-dependent intracellular core. This led to phase-separation pattern formation between a $CellA^{Cdh3\text{-}mCherry}$ core and $CellB^{Cdh2\text{-}GFP}$ side-groups. In turn, induced membrane-tethered GFP from *CellB* signalled back to *CellA*, activating antiGFP-SynNotch to upregulate BFP at the *CellA*-*CellB* interface, adding pattern elaboration (Toda et al., 2018). The critical message here is that independent pattern formation circuits can be successfully integrated into composite devices (Figure 5C), through which predictable, programmed emergent interactions drive pattern formation and elaboration, based on signalling feedback loops and morphogenetic mechanisms.

Autonomous circuits that utilize exclusively signalling to organize cell states over a multicellular field have also been reported. In mammalian cells, the first successful Turing-like Reaction-Diffusion system has been built using a Nodal-Lefty2 activator-inhibitor circuit (Sekine et al., 2018). By introducing the activator *Nodal*, whose diffusion is limited to a few cell diameters, the inhibitor *Lefty2*, whose diffusion is 3.5-fold wider than Nodal, receptor components *Acvr2b* and *Cryptic*, and the downstream Smad2/3 co-transducer *FoxH1*, cultured HEK-293 cells adopted periodic distributions of high Nodal activity separated by low/absent activity zones. Notably, these distribution were sensitive to genetic alterations that modified diffusion rates (Sekine et al., 2018). Although the authors reported characteristics regarding width and periodicity of Nodal-active domains, the metrics describing pattern formation were limited and not compared to any reference control, perhaps because cell-state distributions seemed more continuous than binary (ON/OFF). In contrast, a complex quorum sensing-based Reaction-Diffusion system led to tightly cut-off distributions in bacteria (Karig et al., 2018). A different autonomous lateral inhibition signalling circuit, whereby juxtacrine Delta-Notch signalling facilitated a $Notch^{ON}$/$Delta^{OFF}$ state conversion in net receivers versus $Delta^{ON}$ state in net senders, led to robust cell state bifurcation (1:2 ratio of $Delta^{ON}$:$Delta^{OFF}$) from single-sorted outgrowths, showing bifurcation potential even at the 2-cell stage (Matsuda et al., 2015). Although no apparent patterning was observed, the study interestingly highlights that aspects of cell geometry that are influenced by morphogenetic modules (in the study, intercellular interface area that was increased by N-cadherin expression) have the

capacity to change cell fate/state specification propensities, presumably by influencing downstream signalling events (Matsuda et al., 2015). This engineering of self-regulated circuits that autonomously bifurcate cell states over two-dimensional multicellular fields marks our advances in understanding, modelling and recreating complex signalling events that potentially organize cell fate specification events during development.

Implementations of synthetic biology in improving self-organization and pattern formation in stem cells have been limited. One case described the construction and lentiviral delivery of a doxycycline-inducible GATA6 overexpression module in iPSCs. Monolayer differentiation of mixed iPSC populations under doxycycline provision led to phase-separation-type patterning between $GATA6^{High}$ and $GATA6^{low}/GATA^{-}$ cells, followed by asynchronous and multi-lineage differentiation (Guye et al., 2016). This experiment is highly reminiscent of patterning events in the pre-implantation embryo (Figure 1). While this platform offers a pilot to study inductive interactions between self-organizing motifs during two-dimensional co-differentiation of hPSCs, it suffers from high heterogeneity and complexity. In one particular experiment, iPSCs engineered to express Sonic Hedgehog (SHH) in a doxycycline-inducible manner were aggregated (10^3 cells) and sequentially layered with wild-type iPSCs (10^4 cells), generating chimeric EBs in which SHH could be produced from a localized source (Cederquist et al., 2019). Long-range signalling activity of SHH, extending around 300μm from the polarized "organizer" iPSCs, was able to break symmetry in cerebral organoids, specifying a posterior-ventral forebrain fate ($OTX2^{+}$,$NKX2.1^{+}$) with hypothalamic markers ($NKX2.2^{+}$) proximal to the SHH source, while anterior-dorsal markers ($PAX6^{+}$,$FOXG1^{+}$) appeared distally. In contrast, chimeric organoids differentiated without doxycycline-SHH induction wholly comprised anterior-dorsal markers (Cederquist et al., 2019). Unfortunately, "organizer" iPSCs were frequently (25%) separated and intermingled with wild-type iPSCs following aggregate fusion, compromising morphogen polarization and overall strategy efficiency. Similarly, when cell lines were used to provide signals that skew fate specification in EBs, they lacked self-organization in conjunction to mESCs (Sagy et al., 2019). Hence, the contribution of synthetic biology to stem cell self-organization through the engineering of transcription factor networks or organized signalling events, while proven possible is still in its infancy.

1.4 Aims of the Project

This thesis argues that synthetic biology can be used to improve self-organization in contemporary PSC differentiation regimes by engineering synthetic stem cell niches or organizers. This can be achieved by converting simple cell lines into self-organizing patterning systems. A second round of engineering can be used to program user-defined release of signalling ligands from desired components/members of the pattern, converting a non-random cell distribution to a non-random signalling distribution. This presupposes that the signalling ligand diffusion rate does not exceed pattern periodicity. If the patterning system retains self-organization capacity with PSC-derived systems, then pattern formation between synthetic producers and recipient PSCs will lead to organized, user-defined signalling events. If these signalling events influence stem cell fate-decisions, then patterning of signalling events might imprint patterning of stem cell fate decisions. The synthesis of such prototypic platforms could seed future work in tissue engineering and assist in producing highly-ordered “designer tissues”, more physiological organoids, or acquisition/expansion of therapeutically important cell types.

The aim of this project is to construct prototypic self-organized multicellular signalling systems that elicit cell signalling events in an organized manner, and apply them to direct stem cell fate-decisions with control over self-organization and demonstrate proof-of-concept. These aims are listed below and elaborated into specific hypotheses at the beginning of corresponding *Results* sections.

1. Program Pattern Formation

Construction of genetic circuits/systems that, when introduced into mammalian cells, drive the formation of statistically non-random multicellular distributions (patterns).

2. Couple Signal Production

Second-stage genetic engineering of an established patterning system. Self-organizing multicellular systems will be engineered so that signalling ligands are produced and secreted only from specific topological domains of the pattern. This should translate the patterned multicellular arrangement into an organized presence of signalling ligand(s).

3. Control Stem Cell Fate-decisions

Utilization of multicellular patterning-signalling platforms to control stem cell fate-decisions via co-culture methods. If successful, lineage specification during stem cell differentiation should proceed in an organized fashion, according to the position of stem cells with respect to the self-organizing signal senders. This will provide proof-of-concept for using synthetic biology to engineer synthetic stem cell niches and/or organizers.

2 MATERIALS & METHODS

2.1 Methods related to Sections 3.1 & 3.2

2.1.1 DNA Engineering

2.1.1.1 Polymerase Chain Reaction (PCR)

For cloning purposes, DNA was amplified using Q5 Hot Start High-Fidelity Master Mix (NEB #M0494S), primers at 0.5μM each, template DNA at 1-3ng (plasmids) or 12.5-20ng (genomic DNA/cDNA), in 25μl reactions. Post-PCR reactions were mixed with 5μl Gel Loading Dye, Purple (NEB #B7024S) and resolved in TAE-based 0.8% agarose gels incorporating SYBR Safe DNA Gel Stain (Invitrogen #S33102) for 40-60 minutes at 120V. Gels were imaged using UGenius-3 platform (Syngene) and products purified using the Monarch DNA Gel Extraction Kit (NEB #T1020S) with protocol modifications (1xDNA wash; elute with 26-41μl H_2O depending on band intensity).

For genotyping purposes, DNA was amplified using GoTaq G2 DNA Polymerase (Promega #M7822), primers at 0.5μM each, in 20μl reactions. For bacterial colony PCR, colonies were resuspended in 20μl H_2O, 3μl of which were flash-frozen at -80^{o}C for 5-10 minutes, and PCR master-mix was directly added after thawing. For mammalian genotyping, genomic DNA was extracted using the DNeasy Blood & Tissue Kit (Qiagen #69504) according to the manufacturer's instructions, and 150ng DNA was used as input. Primers are listed in Table 1 and thermocycler programmes in Table 2.

2.1.1.2 T/A Ligation

A-tailing was performed by mixing 7μl Q5-generated insert DNA with 5U Taq polymerase (NEB: M0273S) in 10μl reactions containing Taq Buffer (NEB #B9014S) and 0.2mM ATP (Thermo Scientific #R0441), and incubating at 70^{o}C for 30 minutes. A-tailed insert and *pGEM-T* Easy Vector (Promega #A137A) were mixed at 3:1 molar ratio respectively (24-36fmol:8-12fmol), and ligated using 3 Weiss Units of T4 DNA ligase (Promega #M180A) in 10μl reactions containing Rapid Ligation Buffer (Promega #C671A), at 4^{o}C overnight. For *pGEM* blue/white screening, transformants were plated on LB^{Amp} agar with 100μM IPTG (Invitrogen #15529-019) and 40μg/ml X-gal (SIGMA #X3753-4ML).

2.1.1.3 Gateway Recombination

Equimolar amounts of *attB*-adapted insert and *pDONR-221* vector (25fmol each) were mixed in 5µl reactions containing 1.0µl BP ClonaseII (Invitrogen #11789-020) and incubated on the benchtop overnight. The reaction was stopped by adding 0.5µl Proteinase K and incubating at 37ºC for 10 minutes.

2.1.1.4 Gibson Assembly

Assemblies comprised 50fmol/fragment and NEBuilder HiFi DNA Assembly Master Mix (NEB #M5520A) in 20µl reactions; if fragment concentrations were high enough (total fragment volume ≤5µl), then 10µl reactions were set instead. Reactions were incubated at 50ºC for 1 hour. For constructs larger than 13kb, 1.5µl of the assembly (18.75fmol) was used for electroporation (Table 3); for everything else, standard heat-shock using one-tenth of the assembly mixture was used (25fmol).

2.1.1.5 Golden Gate Assembly

Insert oligos (100pmol each) were mixed in 10µl reactions containing 10U T4 polynucleotide kinase (NEB #M0201S) in T4 buffer (NEB #B0201S), incubated at 37ºC for 30 minutes, 95ºC for 5 minutes, and cooled to 25ºC at a ramp of -0.1ºC/sec. Assembly mixtures (20µl) comprised 100fmol DNA duplex, 100ng (17.5fmol) *pSpCas9-2A-eGFP* (Addgene #48138), 0.5mM DTT, 0.5mM ATP (Thermo Scientific #R0441), 1µl FastDigest BbsI (Thermo Scientific #FD1014), 1.5 Weiss Units T4 DNA Ligase (Promega #M180A) and NEBuffer 2.1 (NEB #B7202S). Reactions were incubated at 37ºC for 5 minutes followed by 21ºC for 5 minutes, for a total of 6 cycles.

2.1.1.6 Diagnostic Restriction Digestion

Digestions were performed in 10µl reactions containing 500ng purified plasmid, FastDigest Buffer and 10U appropriate FastDigest restriction enzyme(s) (Thermo Scientific) for 15 minutes; the temperature was chosen according to the manufacturer's specifications for each enzyme.

2.1.1.7 Sanger Sequencing

Plasmid DNA (500ng) and sequencing primer (6.5pmol) were mixed with H_2O to produce a total volume of 6µl and sent to a sequencing service provider (Edinburgh Genomics) for BigDye reaction-based Sanger Sequencing on an ABI 3730XL DNA analyzer.

Table 1. List of primers and expected amplicons per PCR.

PCR Target	Primer	Sequence (5'-3')	Amplicon (bp)
		cDNA Cloning	
CD11a T/A	*CD11a* forward	ATGAAGGATTCCTGCATCACTGTGATGGCC	3558
	2A-CD11a reverse	CACGTCGCCGGCCTGCTTCAGCAGGCTGAAGTTGGTGGCGCCGCTGCCGTCCTTGCCACCACCACTCTCAGAGTCCTTC	
CD11b T/A	*CD11b* forward	ATGGCTCTCAGAGTCCTTCTG	3507
	2A-CD11b reverse	CACGTCGCCGGCCTGCTTCAGCAGGCTGAAGTTGGTGGCGCCGCTGCCCTGGGGTTCGGCCCCCGGGGGACCCCCTTC	
CD18 Gateway	*attB-CD18* forward	GGGGACAAGTTTGTACAAAAAAGCAGGCTTCATGCTGGGCCTGCGCCCCCCACTGC	2371
	attB-CD18 reverse	GGGGACCACTTTGTACAAGAAAGCTGGGTACTAACTCTCAGCAAACTTGGGGTTCATGAC	
		***pTREx-mCherry-2A-hICAM-1* Assembly**	
ICAM-1	*ICAM-1* forward	ATGGCTCCCAGCAGCCCCCG	1599
	ICAM-1 reverse	TCAGGGAGGCGTGGCTTGTGTGTTCG	
pTREX	*ICAM-1-pTREX* forward	AAACCGAACACACAAGCCACGCCTCCCTGAACCCAGCTTTCTTGTACAAAGTGGTTGATG	6734
	ICAM-1-pTREX reverse	CAGCGCGGGCCGGGGGCTGCTGGGAGCCATTGGGCCAGGATTCTCCTCCACGTCACC	
		***pTREx-tGFP-2A-hMAC-1* Assembly**	
CD11b-2A		Same as cDNA cloning	
2A-CD18 (*LFA-1/MAC-1*)	*2A-CD18* forward	TTCAGCCTGCTGAAGCAGGCCGGCGACGTGGAGGAGAACCCCGGCCCCATGCTGGGCCTGCGCCCCCCACTGCTCGCC	2358
	CD18 reverse	CTAACTCTCAGCAAACTTGGGGTTCATGAC	
pTREX	*CD18-pTREX* forward	GTCATGAACCCCAAGTTTGCTGAGAGTTAGACCCAGCTTTCTTGTACAAAGTGGTTGATG	6756
	CD11b-pTREX reverse	GGCTGTTAACAGAAGGACTCTGAGAGCCATTGGGCCAGGATTCTCCTCCACGTCACC	
		***pTREx-tGFP-2A-hLFA-1* Assembly**	
CD11a-2A		Same as cDNA cloning	
2A-CD18 (*LFA-1/MAC-1*)	*2A-CD18* forward	TTCAGCCTGCTGAAGCAGGCCGGCGACGTGGAGGAGAACCCCGGCCCCATGCTGGGCCTGCGCCCCCCACTGCTCGCC	2358
	CD18 reverse	CTAACTCTCAGCAAACTTGGGGTTCATGAC	
pTREX	*CD18-pTREX* forward	GTCATGAACCCCAAGTTTGCTGAGAGTTAGACCCAGCTTTCTTGTACAAAGTGGTTGATG	6756
	CD11a-pTREX reverse	GGCCATCACAGTGATGCAGGAATCCTTCATTGGGCCAGGATTCTCCTCCACGTCACC	
		Modified *pTREx-H2B-TagBFP-2A-hLFA-1* Assembly	
H2B-BFP	*ptrex-H2B-BFP* forward	ACAAGTTTGTACAAAAAAGCAGGCTTCACCATGCCAGAGCCAGCGAAGTCTGCTCCC	
	2A-H2B-BFP reverse	CACGTCGCCGGCCTGCTTCAGCAGGCTGAAGTTGGTGGCGCCGCTGCCATTAAGCCCCAGTTTGCTAGGGAG	
	cd11a-2A-H2B-BFP reverse	CACAGTGATGCAGGAATCCTTCATGGGGCCGGGGTTCTCCTCCACGTCGCCGGCCAGCAGGC	
Modified *pTREx*	*CD18-pTREX* forward	GTCATGAACCCCAAGTTTGCTGAGAGTTAGACCCAGCTTTCTTGTACAAAGTGGTTGATG	
	pTREx reverse	GGTGAAGCCTGCTTTTTTGTACAAACTTGTCC	
		***pTREx* Construct Screening**	
LFA-1/MAC-1	*CMV Forward*	CTGGCTGACCGCCCAACG	
LFA-1	*CD11a Reverse*	TTCTGGCGGAAGAGGTAACA	1897
MAC-1	*CD11b Reverse*	GAGACAAACTCCTTCATCCGCC	2014
LFA-1	*CD11a Forward*	TGCTGAAGCCCCATAGC	1564
MAC-1	*CD11b Forward*	CCTACCGGAAGGTGTCCACG	1531
LFA-1/MAC-1	*CD18 Reverse*	GACTCGGTGATCTCGTTGAG	
LFA-1/MAC-1	*CD18 Froward*	ATGTCCCGATCACCTTCCA	1226
	M13 Reverse	GTAAAACGACGGCCAGT	
		***pHDR-hROSA26* Assembly**	
Backbone	*pUC* forward	GTCAGCGATCTTCAGGCCTCCTTTTCCATAGGCTCCGCCCCCCTGACG	1779
	pUC reverse	CTCTCTGAGGAGCCGCTTTTCGGGGAAATGTGCGCGGAACCC	
ROSA26 5' Homology Arm	*5' Homology Arm* forward	CATTTCCCCGAAAAGCGGCTCCTCAGAGAGCCTCGGCTAGGTAGGG	1201
	5' Homology Arm reverse	GCCTCGTACTACGCCGCGACTCGACATGGAGGCGATGACG	
ROSA26 3' Homology Arm	*3' Homology Arm* forward	GTAACTTTAAATAATTGGCATTATTTAAAGTTAGGCGCGCTTCTCGATTATGGGCGGGATTCTTTTGCC	2788
	3' Homology Arm reverse	GGGGGCGGAGCCTATGGAAAAGGAGGCCTGAAGATCGCTGACATAAGGG	
Puromycin Cassette	*Puromycin* forward	TTAATTAATGATCATAATCAGCCATATCAC	2824
	Puromycin reverse	GCGCGCCTAACTTTAAATAATG	
Transgene Cassette	*pHDR-CMV forward*	TCGCCTCCATGTCGAGTCGCGGCGTAGTACGAGGCCCTTTCACTCATTAG	7889 (LFA-1)
	pHDR-CD18 reverse	GTGATATGGCTGATTATGATCATTAATTAACTAACTCTCAGCAAACTTGGGGTTCATGACC	7445 (MAC-1)
	pHDR-ICAM-1 reverse	GTGATATGGCTGATTATGATCATTAATTAATCAGGGAGGCGTGGCTTGTGTGTTCG	3187 (ICAM-1)
		Genotype *ROSA26* cells	
ROSA26 wild-type	*ROSA26 wild-type* forward	GACCTGCTACAGGCACTCGT	693
	ROSA26 wild-type reverse	GTGAGGGAGGGAAGCACTGG	
Puromycin - 3' ROSA26 genomic	*Puromycin* forward	GCAACCTCCCCTTCTACGAGC	3964
	ROSA26-3' reverse	TGGGACCCTGAAGTCTCTCC	

Table 2. Thermocycler programmes and primer sets per PCR.

PCR Description	Primers	Programme
Amplification *CD11a/CD11b/CD18*	See Table 1	1. 98ºC, 0:30' 2. 98ºC, 0:15' 3. 66ºC, 0:20' 4. 72ºC: 2:45' 5. Go to 2 (x39) 6. 72ºC, 2:00'
Amplification *ICAM-1*	*ICAM1* forward *ICAM1* reverse	1. 98ºC, 0:30' 2. 98ºC, 0:15' 3. 72ºC, 0:20' 4. 72ºC, 1:05' 5. Go to 2 (x39) 6. 72ºC, 2:00'
Amplification *pTREx* backbone	See Table 1	1. 98ºC, 0:30' 2. 98ºC, 0:15' 3. 60ºC, 0:20' 4. 72ºC, 4:45' 5. Go to 2 (x39) 6. 72ºC, 2:00'
Amplification *pHDR* Fragments 3' *ROSA26* Homology Arm; Puromycin resistance cassette	See Table 1	1. 98ºC, 0:30' 2. 98ºC, 0:10' 3. 62ºC, 0:20' 4. 72ºC, 2:30 5. Go to 2 (x39) 6. 72ºC, 2:00'
Amplification *pHDR* Fragments Backbone; 5' *ROSA26* Homology Arm; *ICAM-1* transgene cassette	See Table 1	1. 98ºC, 0:30' 2. 98ºC, 0:10' 3. 72ºC, 0:20' 4. 72ºC, 2:30 5. Go to 2 (x39) 6. 72ºC, 2:00'
Amplification *pHDR* Fragments *MAC-1/LFA-1* transgene cassette	*pHDR-CMV forward* *pHDR-CD18 reverse*	1. 98ºC, 0:30' 2. 98ºC, 0:10' 3. 72ºC, 0:20' 4. 72ºC, 6:00' 5. Go to 2 (x39) 6. 72ºC, 2:00'
Colony PCR *pGEM-hCD11a* Colony PCR *pGEM-hCD11b*	T7; SP6	1. 95ºC, 1:30' 2. 95ºC, 0:20' 3. 44ºC, 0:20' 4. 72ºC, 3:45' 5. Go to 2 (x24) 6. 72ºC, 2:00
Colony PCR *pENTR-hCD18*	M13F; M13R	1. 95ºC, 1:00' 2. 95ºC, 0:20' 3. 47ºC, 0:20' 4. 72ºC, 3:00' 5. Go to 2 (x29) 6. 72ºC, 2:00'
Colony PCR *pTREx-hCD11a* Colony PCR *pTREx-hCD11b* Colony PCR *hCD11a-hCD18* Colony PCR *hCD11b-hCD18* Colony PCR *hCD18-pTREx*	CMV_F; CD11a_580R CMV_F; CD11b_SEQ1R CD11a_2672F; CD18_721R CD11b_SEQ6F; CD18_721R CD18_1450F; M13F	1. 95ºC, 1:00' 2. 95ºC, 0:20' 3. 55ºC, 0:20' 4. 72ºC, 2:00' 5. Go to 2 (x34) 6. 72ºC, 2:00'
Genotype *ROSA26* Wild-type	*ROSA26 wild-type* forward *ROSA26 wild-type* reverse	1. 95ºC, 1:30' 2. 95ºC, 0:20' 3. 66ºC, 0:20' 4. 72ºC, 0:45' 5. Go to 2 (x29) 6. 72ºC, 1:00
Genotype Puromycin - 3'*ROSA26* Genomic	*Puromycin* forward *ROSA26-3'* reverse	1. 95ºC, 1:30' 2. 95ºC, 0:20' 3. 58ºC, 0:20' 4. 72ºC, 4:00' 5. Go to 2 (x34) 6. 72ºC, 1:00
Oligo Duplex Annealing	N/A	1. 37ºC, 30:00' 2. 95ºC, 5:00' 3. 25ºC, 0:00' at 0.1ºC/sec
Golden Gate Assembly	N/A	1. 37ºC, 5:00' 2. 21ºC, 5:00' 3. Go to 1 (x5)

2.1.2 Bacteria Culture

2.1.2.1 Heat-shock Transformation

Ten nanograms of vector were added to 50μl of NEB-5-α chemically competent bacteria (NEB #C2987H) thawed on ice, and gently mixed by tapping lightly. Mixtures were incubated still on ice for 30 minutes, immersed in a 42°C water bath for 30 seconds, and returned to ice for 3-5 minutes. After addition of 250-550μl SOC medium, transformants were incubated on an orbital shaker at 37°C, 300 revolutions per minute (rpm) for 45 minutes, and one-eighth to one-third of the suspension was plated on LB^{Amp}/LB^{Kan} agar depending on the construct (Table 3).

2.1.2.2 Electroporation Transformation

NEB-10-β electrocompetent bacteria (NEB #C3020K) were thawed on ice, gently mixed once with 18.75fmol plasmid (DNA volume being less than 5% of final volume) and immediately electroporated in pre-chilled 0.1cm-gap cuvettes (Thermofischer #P41050) using an Multiporator (Eppendorf #4308805005) at ~1600V for 5ms. Warm 450μl SOC medium were immediately added, the mixture was transferred to an Eppendorf tube using a fine-tip pastette, incubated on an orbital shaker at 37°C, 300rpm for 60 minutes, and one-quarter of the suspension was plated on LB^{Amp} agar (Table 3).

2.1.2.3 Low-yield plasmid purification

Single colonies were picked and resuspended in 3ml LB^{Amp}/LB^{Kan} broth and incubated overnight on an orbital shaker at 300rpm, 37°C. When colony PCR was desired, colonies were resuspended in 20μl H_2O, 3μl of which were flash-frozen at -80°C and used as PCR input, and the rest used as broth inoculum. From the culture, 1.5ml was used for DNA extraction using the Monarch Plasmid Miniprep Kit (NEB #T1010S) according to the manufacturer's instructions.

2.1.2.4 High-yield plasmid purification

One-third of the low-yield bacterial culture was added to 200ml LB^{Amp}/LB^{Kan} broth and incubated overnight on an orbital shaker at 300rpm, 37°C. Plasmid was purified using a Plasmid Maxi Kit (Qiagen #12663) according to the manufacturer's instructions, eluting twice with 300μl H_2O.

Table 3. Bacterial Transformation and Growth Conditions per Construct.

Cloning Method	Constructs	Transformation Method		Growth Agar
		Heat-shock	Electroporation	
T/A Ligation	*pGEM-CD11a*	✓		LB^{Amp}, 100μM IPTG, 40μg/ml X-gal
	pGEM-CD11b	✓		
Gateway	*pENTRY-CD18*	✓		LB^{Kan}
Gibson Assembly	*pTREx-hICAM-1-IRES-mCherry*	✓		LB^{Amp}
	pTREx-mCherry-2A-hICAM-1	✓		
	pTREx-tGFP-2A-hMAC-1	✓		
	pTREx-tGFP-2A-hLFA-1	✓		
	pTREx-H2B-TagBFP-2A-hLFA-1	✓		
	pHDR-mCherry-2A-hICAM-1	✓		
	pHDR-tGFP-2A-hMAC-1		✓	
	pHDR-H2B-TagBFP-2A-hLFA-1		✓	
Golden Gate Assembly	*pSpCas9-2A-eGFP-gRNA*	✓		LB^{Amp}

Heat-shock: NEB-5-α.
Genotype: *fhuA2 a(argF-lacZ)U169 phoA glnV44 a80a(lacZ)M15 gyrA96 recA1 relA1 endA1 thi-1 hsdR17*

Electroporation: NEB-10-β.
Genotype: *Δ(ara-leu) 7697 araD139 fhuA ΔlacX74 galK16 galE15 e14- φ80dlacZΔM15 recA1 relA1 endA1 nupG rpsL (StrR) rph spoT1 Δ(mrr-hsdRMS-mcrBC)*

LB^{Amp}: Luria-Bertani with 100μg/ml ampicillin
LB^{Kan}: Luria-Bertani with 50μg/ml kanamycin
Luria-Bertani: 10g/L NaCl, 10g/L tryptone, 5g/L yeast extract (+15g/L agar) in H_2O

2.1.3 Mammalian Cell Culture

2.1.3.1 Harvesting cells

This general method applies for sub-passaging of all adherent cell cultures listed herein. Medium was aspirated, culture wells were washed with Ca^{2+}/Mg^{2+}-free PBS, and adherent cells incubated in trypsin-EDTA (0.05%) for 5 minutes. Cells quenched with double the amount of culture medium were centrifuged at 400g for 4 minutes, resuspended in fresh culture medium, and sub-cultured in appropriate ratios.

2.1.3.2 TREx-293 cells

TREx-293 cells were cultured in high-glucose DMEM (Gibco #41966-052) with 10% FBS, L-Glutamine (Gibco #25030-024), Pen/Strep (Gibco #15140-122), blasticidin (6µg/ml) abbreviated TREx-293 culture medium (TCM). For TREx-293^{ICAM-1}/TREx-293^{LFA-1}/TREx-293^{MAC-1}, puromycin (10µg/ml) was additionally supplemented. TREx-293 were seeded at 0.2x10^6 cells/6-well and at 80-90% confluence, sub-cultured in a 1:12 ratio every 3-4 days. For 3D culture, 5-10x10^3 tetracycline-induced cells were plated in 50-100µl tetracycline-supplemented TCM per low-adhesion/cell-repellent U-bottom 96-well for 24 hours.

2.1.3.3 Human Umbilical Vein Endothelial Cells

Mixed donor pool Human Umbilical Vein Endothelial Cells (HUVECs) were cultured in Endothelial Cell Growth Medium 2 (EGM2; PromoCell #C-22011). HUVECs were seeded at a density of 5 – 6.25x10^3 cells/cm^2 (12.5x10^4 cells/T-25 flask; 6x10^4 cells/6-well) and at 80-90% confluence, sub-cultured in a 1:4-1:6 ratio every 2-4 days.

2.1.4 Transfection and selection

TREx-293 cells were grown in 6-well plates to 75-80% confluence before transfecting with Lipofectamine 3000 (ThermoFisher #L3000001). *pHDR* construct (3µg), *pSpCas9-2A-eGFP* (1µg) and P3000 reagent (5µl) were mixed in OptiMEM (125µl). The DNA mixture was gently mixed into a vortex-mixed solution of OptiMEM-Lipofectamine 3000 (125µl-5µl) and incubated on site for 15-20 minutes. Culture medium was replaced with OptiMEM (1ml) and transfection mixture was distributed drop-wise while gently rocking the plate. Cells were returned to the incubator and, after 7 hours, medium was replaced with culture medium. Two days post-transfection, medium was refreshed with puromycin-supplemented (10µg/ml) culture medium, refreshing every 2 days for 8 days, with tetracycline (10µg/ml) additionally supplemented on day 8.

2.1.5 Flow cytometry

2.1.5.1 TREx-293 cells

Twenty-four hours before processing, $0.5x10^6$ cells were seeded in a 6-well plate in TCM with or without tetracycline (10μM). Cells were harvested using accutase (ThermoFisher #A1110501).

2.1.5.2 HUVECs

HUVECs ($0.25x10^6$) were seeded in a 6-well plate in EGM2. After 4 hours, media was replaced with EGM2 with/without TNF-α (150ng/ml; Sigma #H8916), and cells were harvested using accutase after 16-18 hours of incubation.

2.1.5.3 Peripheral Blood Mononuclear Cells

Components from 15ml of blood extracted from a healthy volunteer (Centre for Inflammation Research Blood Resource, project CIRBRP037) were separated on Lymphoprep (STEMCELL Technologies #07801) according to the supplier's instructions. The buffy coat, which is the collection of mononuclear cells that forms at the interphase between the top yellow phase (plasma and platelets) and transparent centrifugation medium (followed by sediment of erythrocytes and granulocytes), was isolated, washed, resuspended in PBS-2% FBS, and cells counted.

2.1.5.4 Staining and Analysis

Accutase-harvested/isolated cells ($0.5x10^6$) were stained in 200μl PBS-10% FBS containing appropriate antibodies (Table 4), for 30 minutes, on ice, in the dark. Samples were washed in excess PBS, resuspended in 600μl PBS-5% FBS, filtered through flow cytometry tube cap strainers (Falcon/Corning #352235) and kept on ice protected from light. Analysis was performed on a BD 5Laser LSRFortessa analyser; Hoechst viability stain was added to samples immediately before processing.

2.1.6 Fluorescence-Activated Cell Sorting (FACS)

After 9 days of puromycin selection and 24 hours of tetracycline induction, transgenic TREx-293 cells were harvested and stained as described above, resuspended in 0.8ml PBS-5% FBS and filtered through flow cytometry tube caps (Falcon/Corning #352235). Fluorescent cells ($0.1\text{-}0.5x10^6$) were sorted in PBS-50% FBS using a BD FACSAria Fusion sorter equipped with a 100μm nozzle, resuspended in culture medium and seeded on 6-well/12-well plates depending on yield.

Table 4. Antibody details used for flow cytometry analyses and sorting.

Antibody	Sample	Stain Concentration (Dilution factor)	Clonality (specification)	Supplier (Cat. Number)
Mouse anti-human CD54 – FITC	HUVECs; TREx-293^{ICAM-1}	2µg/ml (1:200)	Monoclonal (HA58)	BioLegend (#353107)
Mouse anti-human CD11a – PE	PBMCs; TREx-293^{LFA-1}	12.5ng/ml (1:4000)	Monoclonal (TS2/4)	BioLegend (#350605)
Rat anti-mouse/human CD11b – PE	PBMCs; TREx-293^{MAC-1}	50ng/ml (1:4000)	Monoclonal (M1/70)	BioLegend (#101207)
Mouse anti-human CD18 – PerCP/Cy5.5	PBMCs; TREx-293^{LFA-1}; TREx-293^{MAC-1}	1µg/ml (1:200)	Monoclonal (TS1/18)	BioLegend (#302119)

2.1.7 Titration of Tetracycline EC_{50}

Nine-hundred-thousand TREx-293^{ICAM-1} cells were resuspended in 900µl medium and distributed over 18 wells of a 96-well plate. After 4 hours, medium was replaced with medium containing different tetracycline concentrations in triplicates (1nM-10µM). Fluorescence was recorded on a FlexStation plate reader (bottom reads, 15 reads/well, excitation/emission spectra 584/612nm) 24 hours after tetracycline supplementation.

2.1.8 Adhesion Assays

2.1.8.1 Immobilized ICAM-1

This adhesion assay was adapted from a method described to assay leukocyte integrin activation (Strazza et al., 2014). TREx-293 cells ($0.7x10^6$) were cultured in tetracycline-supplemented TCM for 24 hours; PBMCs were Lymphoprep-purified and serum-starved for 2 hours at 37°C, 5% CO_2. Triplicate 96-wells were coated with 50µl PBS (0.5mM $MgCl_2$, 1mM $CaCl_2$) containing recombinant human ICAM-1 (10µg/ml, BioLegend #552904) for 1 hour at 37°C. Harvested cells ($1x10^6$) were stained in 0.2ml PBS containing CellTracker Green CMFDA (5µM, ThermoFisher #C7025) in suspension for 8 minutes, washed and resuspended in 0.5ml PBS (10mM $MgCl_2$, 1mM $CaCl_2$, 0.5% BSA). For PBMCs, PMA (25ng/ml; 40nM) was added to activate integrins. Labelled cells were seeded on coated 96-wells (50µl; $0.1x10^6$ cells/well) for 20 minutes at 37°C, 5% CO_2, washed four times (PBS 10mM $MgCl_2$, 1mM $CaCl_2$). The well was imaged near-centre using a Zeiss AxioVert 200 inverted microscope (one frame/well). Images were processed on ImageJ/FiJi: GFP threshold was set manually (Image, Adjust, Threshold), adjacent cells from 8-bit binary images separated (Process, Binary, Watershed) and counted (Analyze, Analyze Particles).

2.1.8.2 Monolayer Co-culture

Monolayers were prepared by seeding TREx-293^{ICAM-1}/TREx-293 cells in 96-wells ($0.1x10^6$ cells/well) in tetracycline-supplemented TCM for 24 hours. PBMCs were treated as in the immobilized ICAM-1 assay, but resuspended in TCM with PMA (40nM) at $1x10^6$ cells/ml. Each 96-well monolayer was overlaid with $0.1x10^6$ stained cells and incubated at 37°C, 5% CO_2 for 60 minutes. Medium was aspirated, wells washed with PBS, and fluorescence measured in 100µl PBS on a FlexStation plate reader (top read, 15 reads/well).

2.1.8.3 Suspension Co-culture

TREx-293 cells were cultured in tetracycline-supplemented 6-well cultures for 24 hours. $2x10^7$ lymphoprep-purified, CellTracker-labelled PBMCs were resuspended in 1.0ml HBSS-50% FBS with PMA (40nM). Half the suspension ($1x10^7$ PBMCs) was used to resuspend $0.5x10^6$ accutase-harvested TREx-293^{ICAM-1}/TREx-293 cells filtered through a 40µm strainer. Mixtures were incubated at 25°C for 1 hour, gently resuspended, 50µl samples were loaded on histology slides and imaged on a fluorescence microscope. Aggregates were scored based on a minimum of 4 co-aggregated cells, of which at least one is TREx-293.

2.1.9 Cell Surface Area Measurement

TREx-293 cells cultured for 24 hours in tetracycline-free/supplemented conditions were imaged on a Zeiss AxioVert 200 inverted microscope. Images were analysed on ImageJ/FiJi (https://fiji.sc), custom-drawing around single-cell outlines with freeform selection on magnified sections, and measuring area (Analyze, Set Measurements, Area; Analyze, Measure).

2.1.10 Pattern formation co-cultures

TREx-293 cells were cultured in tetracycine-supplemented TCM for 24 hours and harvested using accutase. TREx-293$^{Wild-type}$/TREx-293^{MAC-1}/TREx-293^{LFA-1} cells were stained using CellTracker CMFDA as described previously and mixed with TREx-293^{ICAM-1} at 6:1 ratio respectively. Cells were resuspended in Ca^{2+}-free DMEM supplemented with tetracycline, 5% FBS, 0.5mM $CaCl_2$ and 10mM $MgCl_2$ and cultured at $0.5x10^6$ cells/24-well. Cultures were imaged after 24 hours and at near confluence. Centre-of-mass cell co-ordinates were recorded on FiJi from the mCherry channel, and analyses for extraction of hyperuniformity metrics (as described in section 3.2.4) were performed on MatLab using a custom software script kindly provided by Patrick Keeley and Benjamin Reese (University of California at Santa Barbara). MatLab analyses were performed with the help of Anna Popravko (The University of Edinburgh).

2.2 Methods related to Sections 3.3 & 3.4

2.2.1 Cell Culture

2.2.1.1 Mouse Embryonic Stem Cells

Mouse embryonic stem cells (mESCs) were maintained on irradiation-inactivated mouse embryonic fibroblasts (MEFs; Amsbio #ASF-1201) seeded on 0.1% gelatin-coated 12-well plates in mESC medium (mESM, Table 5). When colonies grew to medium-large sizes (empirically judged), cells were harvested by aspirating the medium, washing the wells with PBS, adding 0.4-0.5ml trypsin-EDTA (0.05%) and incubating at 37^{o}C for 5 minutes (trypsinization). Cells were quenched with fresh mESM, centrifuged at 400g for 4 minutes, resuspended in fresh mESM, and sub-cultured on MEFs at a ratio of 1:8-1:10 every other day, or 1:10-1:12 every three days, adjusting ad hoc depending on the line and its growth rate. For differentiation purposes, mESCs were resuspended in 5ml IMDM supplemented with HyClone FBS (20%) and Pen/Strep (100U/ml; 100μg/ml), plated on 6cm-diameter dishes (Greiner Bio-One #628160), and incubated at 37^{o}C, 5% CO_2 for 30-40 minutes to deplete MEFs (which rapidly attach to the culture surface). The supernatant was collected and mESCs counted for use in differentiations according to section *Phase-Separation pattern co-cultures*.

2.2.1.2 Mouse Kidneys & Metanephric Mesenchyne

One day prior to dissections, 6-well transwell inserts (10μm thick, 0.4μm pore size, clear polyester; Scientific Laboratory Supplies #3450) were seeded with 0.12x10^{6} TREx-293^{Cdh3}/TREx-293$^{Cdh3\text{-}Wnt3a}$ cells in tetracycline-supplemented TCM. For TREx-293 culture, see section [2.1.3.2]. Metanephric mesenchyme or whole kidneys were dissected from E11.5 embryos by various members of the Davies lab. Metanephric mesenchyme was trypsinized for 45 seconds, and cells from 5 or 10 kidney mesenchymes (depending on embryo yield) were pooled and centrifuged at 300g for 3 minutes. Pre-seeded transwells were aspirated and washed of medium, and metanephric mesenchyme aggregate pellets were gently lifted in solution and transferred onto transwells in 50μl Kidney Culture Medium (Table 5). Kidneys were also placed on non-seeded transwells. The bottom chamber was filled with 1.5ml KCM supplemented with tetracycline (10μM), and cultures were incubated at 37^{o}C, 5% CO_2 for 72 hours.

2.2.1.3 Wnt/β-catenin pathway reporters

Transgenic reporter cell lines were grown normally in replicate cultures. At intermediate confluence (TREx-293: 40-50% plate area covered; mESCs: small-medium sized colonies), medium was replaced with culture medium containing CHIRON-99021 (5μM), recombinant human WNT3A (0.01-10μM) (R&D systems #5036-WN-010), or normal

culture medium. For conditioned media experiments, TCM from TREx-293^{Cdh3}/TREx-293$^{Cdh3\text{-}Wnt3a}$ cultures at the time of passage (conditioned over 4-5 days), was mixed 50-50 with mESM (adjusting LIF concentration), and used to refresh *7xtcf/lef* mESC cultures. Fluorescence was evaluated after 24 hours of exposure.

Table 5. Formulation of Media used for Cell and Tissue Culture

Medium	Cell Type	Components (Supplier & Cat. Number)	Working Concentration
TCM	TREx-293	Dulbeco's Modified Eagle Medium; DMEM (Gibco #41966-052)	
		Foetal Bovine Serum; FBS (various, American origin)	10%
		L-Glutamine (Gibco #25030-024)	2mM (1%)
		Penicillin/Streptomycin (Gibco #15140-122)	100U/ml; 100µg/ml (1%)
		Blasticidin	5-6µg/ml
EGM2	HUVEC	Endothelial Growth Medium 2 (PromoCell #C-22011)	
		Supplement Mix (PromoCell #C-39216)	
mESM	mESC	DMEM high glucose (Lonza #BE12-604F/U1)	
		HyClone FBS (GE Healthcare #10309433, SV30160.03, Lot RB35954)	15%
		GlutaMAX (Gibco #35050-038)	2mM (1%)
		Sodium Pyruvate (Gibco #11360-039)	1mM (1%)
		Non-essential amino-acids (Lonza #BE13-114E)	0.1mM (1%)
		B-mercaptoethanol (Gibco #31350-010)	0.1mM (0.2%)
		Penicillin/Streptomycin (Gibco #15140-122)	100U/ml; 100µg/ml (1%)
		Leukaemia Inhibitory Factor (Santa Cruz Biotechnology #sc-4989A)	1000U/ml
EBM	mESC 3D differentiation	IMDM (no phenol red) (Gibco #21056-023)	
		Penicillin/Streptomycin (Gibco #15140-122)	100U/ml; 100µg/ml (1%)
		HyClone FBS (GE Healthcare #10309433, SV30160.03, Lot RB35954)	15%
		GlutaMAX (Gibco #35050-038)	2mM (1%)
		Ascorbic Acid (Sigma #A4544-25G)	50µg/ml
		Transferrin from human serum (Roche #10652202001)	150µg/ml
		Monothioglycerol (Sigma #M6145-25ML)	39nl/ml
		Protein-free hybridoma medium (Day 3 onwards) (Gibco #12040-077)	5%
KCM	Metanephric Mesenchyme	Minimum Essential Medium (SIGMA #M5650-500ML)	
		FBS (various, American origin)	10%
		Penicillin/Streptomycin (Gibco #15140-122)	100U/ml; 100µg/ml (1%)

2.2.2 Phase-separation pattern co-cultures

2.2.2.1 Heterotypic TREx-293 cells

Separate cultures of TREx-293^{Cdh1} and TREx-293^{Cdh3}/TREx-293$^{Cdh3\text{-}Wnt3a}$ cells were harvested via trypsinization and counted. TREx-293^{Cdh1} and TREx-293^{Cdh3}/TREx-293$^{Cdh3\text{-}Wnt3a}$ cells were mixed, resuspended in tetracycline-supplemented TCM (10μM), and plated according to the desired format and pattern outcome: For 2D cultures, 7.5-9.0x10^4 total cells/cm^2 were seeded in tetracycline-supplemented TCM. For 3D cultures, 1-20x10^3 cells were deposited per low-adhesion U-bottom 96-well. Even phase-separation was achieved by mixing equal numbers of TREx-293^{Cdh1} and TREx-293^{Cdh3} cells, whereas a 2:1 ratio was used for polka-style patterning (the less-represented cell type forming polka dot-islands within the more-represented type). Phase-separation was evaluated at least 24 hours after seeding, when cultures approached full confluence.

2.2.2.2 ESC-293 patterning (2D)

One day prior to mESC passaging, TREx-293^{Cdh3}/TREx-293$^{Cdh3\text{-}Wnt3a}$ culture medium was refreshed with tetracycline-supplemented TCM (10μM). Tetracycline-induced TREx-293^{Cdh3}-based cells and MEF-depleted mESCs were harvested and counted. Cells were mixed 7.5x10^4 each, resuspended in 1ml of tetracycline-supplemented mESM lacking LIF, and seeded in a 24-well plate. The time and day of seeding was considered 0 hour and day 0. Medium was refreshed on day 3 (1ml). Cultures at different days were used for different assays as described in the *Mesoderm Assays* methods section.

2.2.2.3 EB-293 patterning (3D)

TREx-293^{Cdh3}/TREx-293$^{Cdh3\text{-}Wnt3a}$ cultures were replenished with tetracycline-supplemented TCM. Embryoid Bodies (EBs) were formed by resuspending 75x10^3 MEF-depleted mESCs in 3ml freshly prepared EBM (without hybridoma medium), plating on a 6cm-diameter low adherence polystyrene petri dish (VWR #391-0866), and incubating on a rotator platform at 37ºC, 5% CO_2, 40 revolutions per minute (rpm). The time and day of seeding was considered 0 hour and day 0. On day 1, tetracycline-stimulated TREx-293^{Cdh3}/TREx-293$^{Cdh3\text{-}Wnt3a}$ cells were harvested and counted, and 4x10^4 cells were added to dedicated EB differentiation dishes. Tetracycline was also supplemented (10μM). For standalone controls, only tetracycline was added. Dishes were gently moved in figure-8 motions to mix the contents and returned to incubation. On day 3, EBM was replaced with freshly prepared EBM containing protein-free hybridoma medium and tetracycline. To aspirate medium without losing sample, the dish was moved in a circular manner to collect EBs in the middle, and the aspirator was swiftly moved along the edges/periphery of the dish. For details on the method, see Figure 32.

2.2.3 Mesoderm Assays

2.2.3.1 Time-lapse fluorescence microscopy (2D)

On day 3 co-cultures between TREx-293^{Cdh3}/TREx-293$^{Cdh3\text{-}Wnt3a}$ cells and *Tbrachyury::eGFP* mESCs, medium was refreshed with 1.5-2.0ml tetracycline-supplemented, LIF-free mESM. Plates were transferred to a Nikon Ti2-E Eclipse custom-equipped with a chamber and apparatus providing temperature and CO_2 regulation (37ºC, 5%). The 4x objective was used, focus was adjusted based on bright-field, and time lapse started at 72 hours of differentiation, capturing images at 30-minute intervals until the 120 hour of differentiation (97 time-stacks), for mCherry (excitation LED: 550nm at 50% intensity) and GFP (excitation LED: 470nm at 50% intensity) channels at exposure time 1000ms each. After time-lapse, day 5 cultures were fixed for immunostaining.

2.2.3.2 Immunostaining (2D)

Cultures at 96 or 120 hours of differentiation were fixed in 0.5ml fresh-thawed 4% PFA for 10 minutes, washed with 0.5ml PBS, and permeabilized with 0.5ml PBS-0.5% TritonX-100 (PBT) for 15 minutes. After washing, samples were blocked with 0.2ml PBS-10% donkey serum for 60 minutes. Blocking solution was replaced with 0.2ml PBS containing appropriate primary antibodies (Table 6) and incubated overnight at 4ºC. Following aspiration and two washes, samples were incubated in 0.2ml PBS containing 0.4μM DAPI and secondary antibodies (Table 6), and incubated at room temperature for 60 minutes or 4ºC overnight. Samples were finally washed twice and imaged in PBS. To limit detachment, fresh 4% PFA and PBS with calcium and magnesium were used.

2.2.3.3 Immunostaining (3D)

EBs at 96 hours of differentiation were collected in maximum 400μl solution and added to a 1.5ml Eppendorf tube containing 1ml PBS. Most EBs sediment in solution within 30-60”, after which the solution was gently aspirated and samples were kept on ice for all following steps. EBs were fixed in 0.6ml 4% PFA for 1 hour, gently mixing at 30 minutes. Following aspiration, EBs were washed with 0.9ml PBT for 30 minutes, three times, then blocked with 0.5ml PBT-10% donkey serum for 2 hours. EBs were stained in 0.4ml PBS containing appropriate antibodies (Table 6) at 4ºC overnight, on an Eppendorf tube rack placed on a rocking platform. Staining solution was aspirated and EBs washed in 0.9ml PBS for 30 minutes, three times on ice. The staining-washing process was repeated with secondary antibodies in PBS with 0.4μM DAPI.

2.2.3.4 EB Clearing & Mounting (3D)

Processing of EBs for 3D imaging was adapted from an embryonic aorta whole-mount imaging method (Yokomizo et al., 2012). EBs were dehydrated in 0.9ml 50% methanol for 10-15 minutes, then 0.9ml 100% methanol for 10-15 minutes, rocking at 4^{o}C. The FastWell (GraceBio-Labs #664113 FW20) chamber was prepared by peeling the adhesive from one side, carefully sealing it with a 25mm-wide, 0.15mm-thick round coverslip (VWR #631-1584), placing it coverslip-down on a low quality histology slide (simply serving as a base) and peeling the adhesive from the other side. Fresh BABB was prepared by mixing 0.5ml benzyl alcohol (Sigma #402834) with 1.0ml benzyl benzoate (Sigma #B6630) in glass scintillation vials using filter tips. A 50-50 BABB-methanol dilution was also prepared. Methanol was aspirated from dehydrated EBs, and the Eppendorf tube was mounted on a glass scintillation vial. EBs were cleared with 200µl 50% BABB for 1-2 minutes, gently discarding the solution afterwards, twice. Three more clearing washes with 200µl 100% BABB were performed. On the third step, EBs were transferred to the FastWell chamber in 190µl BABB and another coverslip was lowered with forceps to seal the chamber. In the case of excess BABB at the FastWell-coverslip junction, thin tissue was used to draw it out. Eight nail polish spots were applied around the top of the chamber, and a SuperFrost Ultra Plus histology slide (ThermoScientific #10417002) was placed on top. After one minute, the apparatus was flipped-over and the low quality histology slide carefully removed. EBs were imaged on a Leica TCS SP8 laser scanning confocal microscope using x40 lens and oil.

2.2.3.5 Flow cytometry

Two-dimensional cultures were harvested as for passaging using TrypLE Express (Gibco #12604-013), resuspended in 0.7ml flow buffer (PBS – 10% Heat-Inactivated FBS) and filtered through flow cytometry tube cap filters (Falcon/Corning #352235). EBs were collected in 0.5ml medium and washed in 3ml PBS added to a 14ml Falcon tube. After setting, supernatant was gently aspirated, 1ml TrypLE Express was added, and tubes were incubated in a 37^{o}C water bath. Tubes were manually shaken/rotated to assist with dissociation occurring within 8-10 minutes. Samples were mixed with 2ml flow buffer to dissociate, resuspended in 0.7ml flow buffer and filtered through flow cytometry tube cap filters. Hoechst viability dye was mixed in immediately prior to flow cytometry analysis.

2.2.4 Kidney & Metanephric Mesenchyme processing

At 72 hours of co-culture, transwell areas containing kidney/mesenchyme samples were cut with a fine syringe tip in a teardrop shape, dipped in PBS and fixed in methanol at -20^{o}C overnight. Samples were PBS washed (1ml) thrice, blocked with PBS comprising 0.2% Triton, 3% Serum and 10% DMSO for 1 hour, and stained with 0.2ml PBS containing 3% donkey serum and primary antibodies at 4^{o}C overnight (Table 6). Samples were washed and stained with secondary antibodies at 4^{o}C overnight. Following two PBS washes, samples were mounted on histology slides around which a frame was drawn with a liquid blocker pen. Two round coverslips were fixed at each side along the length of the slide using nail polish, stacked with another set, and after applying VectaSHIELD antifade mounting medium (Vectorlabs #H-1000-10) to the sample, were covered with a long rectangular coverslip. Samples were imaged on a Nikon A1R FLIM.

2.2.5 Image processing

Paired samples from a single experiment were imaged using the same settings. Images were processed on FiJi (https://fiji.sc). Generally, image processing for purposes of visual sharpening and quantitative analysis was done as long as i) staining specificity did not change, ii) specific staining was not lost (except for very weak live-cell fluorescence, where background and sample pixel values partially overlap), iii) distributions of positively and negatively stained areas in edited images were comparable to the originals and iv) stain intensity reductions and background subtractions (and thus data smoothening) were comparably performed for paired samples to the best of intention. In general, noise was subtracted either through the *Process->Subtract Background…* option (enabling *sliding paraboloid* and setting the *rolling ball radius* at 5pixels), or by raising the minimum value of depicted pixels if noise elimination was insufficient using the *Subtract Background* option. For simple 2D culture images, minimum depicted pixel values were raised until no background signal was observed (this was apparent in the GFP channel), and fluorescence grayscale was recorded through the *Analyze… Measure* option. For weak stains, the maximum was lowered as long as signal specificity was unaffected. The *Process->Noise->Despeckle* command was used if it improved image quality. In time-lapse GFP quantifications, squares (100x100μm) were drawn, placed at colony positions that were stationary over the time-lapse, saved to *ROI manager*, and the multi-measure option was used to measure GFP mean grayscale value over time stacks. For 3D imaging, Z-slices were stacked (metanephric mesenchyme, kidneys, Day 5 differentiations) or projected in 3D (EBs) through the *Image…Stacks* options.

Table 6. Antibody and staining details used for immunostaining

Antibody Target	Working Dilution	Supplier (Cat.Number; Lot)	Host (clonality)	Secondary
		Primaries		
Calbindin	1:200	Novus Biologicals (NBP2-50028)	Chicken (polyclonal)	Donkey-anti-chicken FITC
E-cadherin	1:200	Cell Signalling Technology (3195; 10)	Rabbit (monoclonal: 24E10)	Donkey-anti-rabbit 594
Eomes	1:400	Abcam (ab23345)	Rabbit (polyclonal)	Donkey-anti-rabbit 647
GFP	1:500	MBL (598; 076)	Rabbit (polyclonal)	Donkey-anti-rabbit 488
Jagged1	1:200	R&D Systems; (AF599)	Goat (polyclonal)	Donkey-anti-goat 647
mCherry	1:500	Novus Biologicals (NBP1-96752SS; 030219)	Mouse (monoclonal: 1C51)	Donkey-anti-mouse 594
N-cadherin	1:250	BD Biosciences (610920)	Mouse (monoclonal: clone 32)	Donkey-anti-mouse 488
T-brachyury	1:500	R&D Systems (AF2085; KQP0618071)	Goat (polyclonal)	Donkey-anti-goat 647
WT1 (rabbit)	1:200	Abcam (ab89901)	Monoclonal (CAN-R9(IHC)-56-2)	Donkey-anti-rabbit 594
		Secondaries		
Donkey anti-Chicken-FITC	1:200	Abcam (ab63507)		
Donkey anti-Goat-AlexaFluor647	1:200	ThermoFisher (A21447)		
Donkey anti-Mouse-AlexaFluor488	1:200	ThermoFisher (A21202)		
Donkey anti-Mouse-AlexaFluor594	1:200	ThermoFisher (A21203)		
Donkey anti-Rabbit-AlexaFluor488	1:200	ThermoFisher (A21206)		
Donkey anti-Rabbit-AlexaFluor594	1:200	ThermoFisher (A21207)		
Donkey anti-Rabbit-AlexaFluor647	1:200	ThermoFisher (A31573)		

3 RESULTS

3.1 Programming Pattern Formation

A wide array of adhesion-based patterns have been achieved in bacteria (Glass & Riedel-Kruse, 2018), whereas only homotypic cadherin-based phase-separation patterning has been engineered in mammalian cells (Cachat et al., 2016). To expand the mammalian self-organization toolbox, the opposite system could be engineered, whereby heterotypic adhesions drive the intermingling of cells and the potential formation of checkerboard or hyperuniform distributions. Inspiration for this system stems from the avian retina.

Avian retinas comprise five different photoreceptor cone types: four single cones individually dedicated to tetrachromatic colour perception (violet, blue, green, red) and one double-cone involved in luminance detection. These photoreceptor cones pattern the avian retina. Homotypic cones are never clustered or highly distant, that is, they are uniformly distributed with respect to their own type, establishing a form of patterning termed disordered hyperuniformity (Jiao et al., 2014; Kram et al., 2010). Although hyperuniform arrangements seem counter-intuitive to perceive as patterned (non-random), there are specific metrics to measure the orderly arrangement of single cell-points with respect to homotypic neighbours in a two-dimensional plane (Box 2). Using these metrics, image-derived cell positions can be interrogated with respect to order and disorder, and homotypic cone arrangements show significantly more regular arrangement compared to random coordinate simulations (Table 7) or heterotypic pairs (Kram et al., 2010). Different cone types have different spacing with respect to their nearest homotypic neighbour, probably scaling to their relative frequency in the retinal cone pool (Kram et al., 2010). However, the molecular basis underlying hyperuniformity in avian photoreceptors is unknown. To this end, synthetic biology bottom-up approaches could be used to (re)create conditions meeting hyperuniform distributions, providing insights into what molecular systems might impose hyperuniformity and/or expanding the synthetic self-organization mammalian toolbox.

A theoretical simulation model built on heterotypic cell adhesion can predict multicellular arrangements that meet hyperuniformity conditions (Davies, unpublished). The model starts from two distinct cell populations mixed in uneven ratio (one cell type sparse and the other in excess) and in random arrangements, and assumes that heterotypic cell connections are strongly favoured over homotypic. During cell

proliferation and adhesion-based neighbour exchange, the two populations intermingle, eliminating homotypic clusters. The final arrangement meets a condition of hyperuniformity, in that homotypic cells (of the sparse type) are never in direct contact and possess heterotypic neighbours. The model suggests that enforcing strong heterotypic adhesions between separate cognate cell lines might sufficiently drive formation of hyperuniform patterning.

Logically, the induction of preferential heterotypic connections between two cells should occur when one cell is expressing high levels of a cell surface receptor that recognizes and strongly binds to a ligand presented at high levels on the surface of another cell. Contrary to bacteria synthetic adhesions where mere surface presentation sufficiently drives intercellular adhesions (Glass & Riedel-Kruse, 2018), eukaryotic adhesion molecule functionality requires intracellular connection to the cytoskeleton. Integrins comprise some of the strongest heterophilic cell adhesion molecules that link the actin cytoskeleton to extracellular components, anchoring integrin-expressing cells to the ECM or heterotypic cells. This makes integrin proteins attractive candidates for enforcing heterotypic adhesions, and for investigating whether integrin-mediated heterotypic connections suffice to drive formation of hyperuniform distributions, in order to expand the mammalian self-organization synthetic toolbox.

Table 7. Hyperuniformity metric values examples (Kram et al., 2010).

Sample	Topological Order (P_6)	Topological Disorder (μ_2)	Regularity Index
Random distribution (100 simulations)	0.293±0.018	≈1.8±0.1	≈1.9
Perfectly uniform tiling model	1	0	N/A
Single Cones	0.454±0.019 to 0.494±0.031	0.634±0.060 to 0.734±0.046	≈7.5-7.8 Except violet ≈6.4
Double Cones	0.570±0.034	0.494±0.063	≈7.7
Epithelia	0.460±0.020	0.760±0.086	N/A

Box 2. Description of hyperuniformity metrics & related methods.

Topological Order: The fraction of Voronoi polygons that are hexagons (P_6), following conversion of cell centre positions into Voronoi chambers.

Topological Disorder: Variance of polygon side probability distribution relative to hexagons (μ_2), following conversion of cell centre positions into Voronoi chambers.

$$\mu_2 = \sum_{n=3}^{\infty} (n-6)^2 P_n$$

Regularity Index: Average nearest homotypic neighbour distance divided by its standard deviation.

Exclusion Zone: Circular region around a cell, within which no cells of the same type are present. When all cells of a two-dimensional field are taken into consideration (plotted through an autocorrelogram), the exlusion zone appears as an empty region around the autocorrelogram's origin point, indicating absence of points/homotypic cells. The radius of the exclusion zone is termed effective exclusion radius.

Voronoi tessellation: The two-dimensional cell field is transferred to a Cartesian system plotting field width and length. For each cone type, points (cell coordinates) are used as reference points for the tiling of Voronoi domains, the borders of which are drawn perpendicular to the midpoint between any two cells and within which any random point is nearest to the reference of that Voronoi domain compared to any other. Geometry of Voronoi domain polygons (number of sides) depends on the overall arrangement of surrounding points.

Autocorrelograms: When a two-dimensional cell sheet is considered as a binary Cartesian system, the position of all cells relative to any given cell (set as Cartesian origin 0,0) can be plotted as points. Repeating the process for all cells of the field and overlaying the results generates an autocorrelogram.

3.1.1 Integrin Biochemistry

Integrins represent a family of metazoan heterodimeric cell surface receptors that integrate processes of cell adhesion to signalling. Mammals possess 24 integrins, arising through differential heterodimerization of 18 α-subunits and 8 β-subunits (Figure 6). The structural, biochemical, and cellular nature of integrin biology is a rich topic (reviewed in (Kechagia et al., 2019)), and for the purposes of this manuscript, this section is restricted in providing an overview of integrin biochemistry, before considering which integrin-ligand axes would form suitable candidates for mediating strong heterotypic adhesions, based on respective biological contexts.

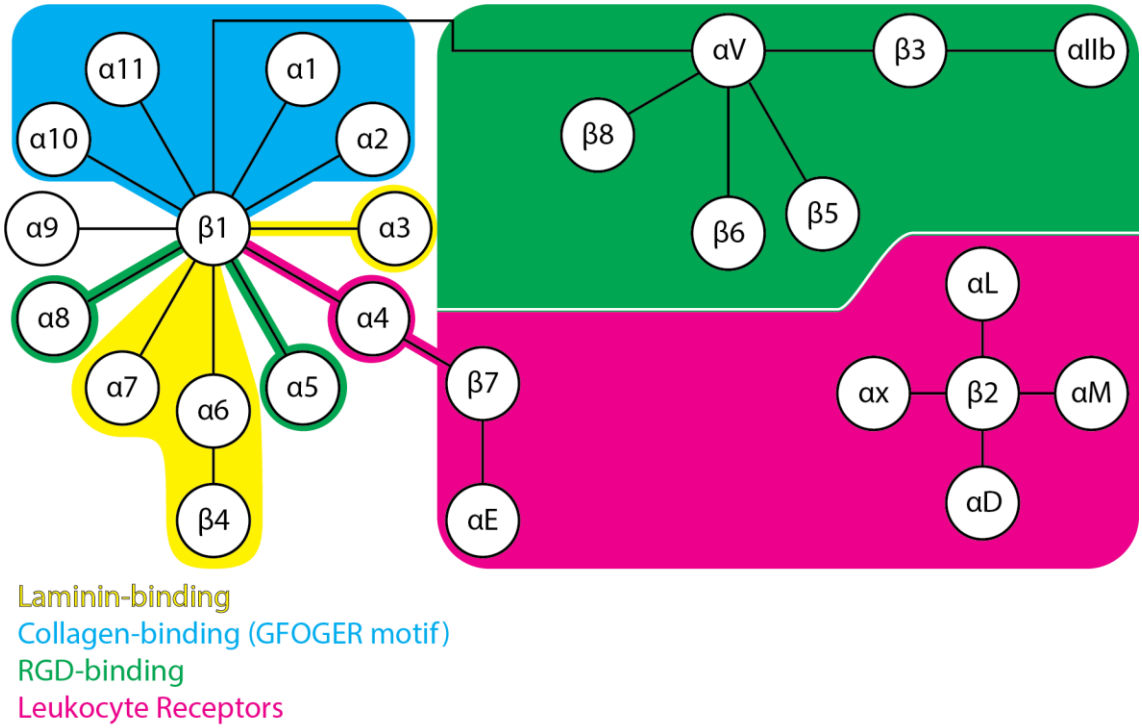

Figure 6. Overview of mammalian integrin receptor composition.
Adapted from (Arnaout, 2016; Campbell & Humphries, 2011).

Integrins take distinct conformations with different ligand-binding affinities. The bent state, produced when integrins fold relative to their longitudinal axis, brings the receptor headpiece close to the plasma membrane and hides ligand-binding epitopes, reducing affinity for ligands. In contrast, the extended conformation exposes ligand-binding epitopes to the extracellular space. Activation into the extended state occurs through conformational changes due to extracellular domain interactions with the extracellular milieu (outside-in activation), or biochemical modulation of intracellular subunit tails (inside-out activation). Mechanics of integrin activation and adhesion are best understood with respect to protein structure, summarized herein from consensus views of integrin structural biology (Arnaout, 2016; Campbell & Humphries, 2011).

Integrin subunits possess large N-terminal extracellular domains (ectodomains), a single transmembrane α-helix, and short C-terminal intracellular tails (Figure 7A). In α-subunits, ectodomains comprise a large β-blade propeller held on a thigh domain followed by two successive calf domains. These structures are rich in β-pleated sheets that confer rigidity, with two flexible linkers: one between the β-propeller and the thigh, and one between the thigh and the Calf-1 domain (termed the genu). These linkers act as hinges, allowing modulation of ligand-binding affinity by exposing/hiding ligand-binding epitopes. Additionally, 9/18 of α-subunits harbour a cation-regulated I-domain (also referred to as A-domain) between the second and third blade repeats of the β-propeller, involved in coordinating ligand-integrin interactions. In comparison, β-subunits have smaller ectodomains and slightly longer intracellular tails. All β-subunit ectodomains comprise an I-domain flanked by flexible hybrid regions and inserted within a plexin-semaphorin-integrin domain; this complex is superseded by a chain of four cysteine-rich EGF tandem repeats terminating on an integrin β-tail domain. Intramolecular association between hybrid domains, combined with disulphide bridge interlocking between the plexin-semaphorin-integrin domain and EGF repeats, allows the β-subunit I-domain to project distally and interact with the α-subunit (Figure 7B). This association between I-domains is critical in mechanics of integrin activation and ligand-binding. Intermolecular interaction between integrin subunits also occurs intracellularly, which is associated with integrin inactivation. Both intracellular and extracellular domains are amenable to biochemical regulation, allowing inside-out and outside-in integrin activation.

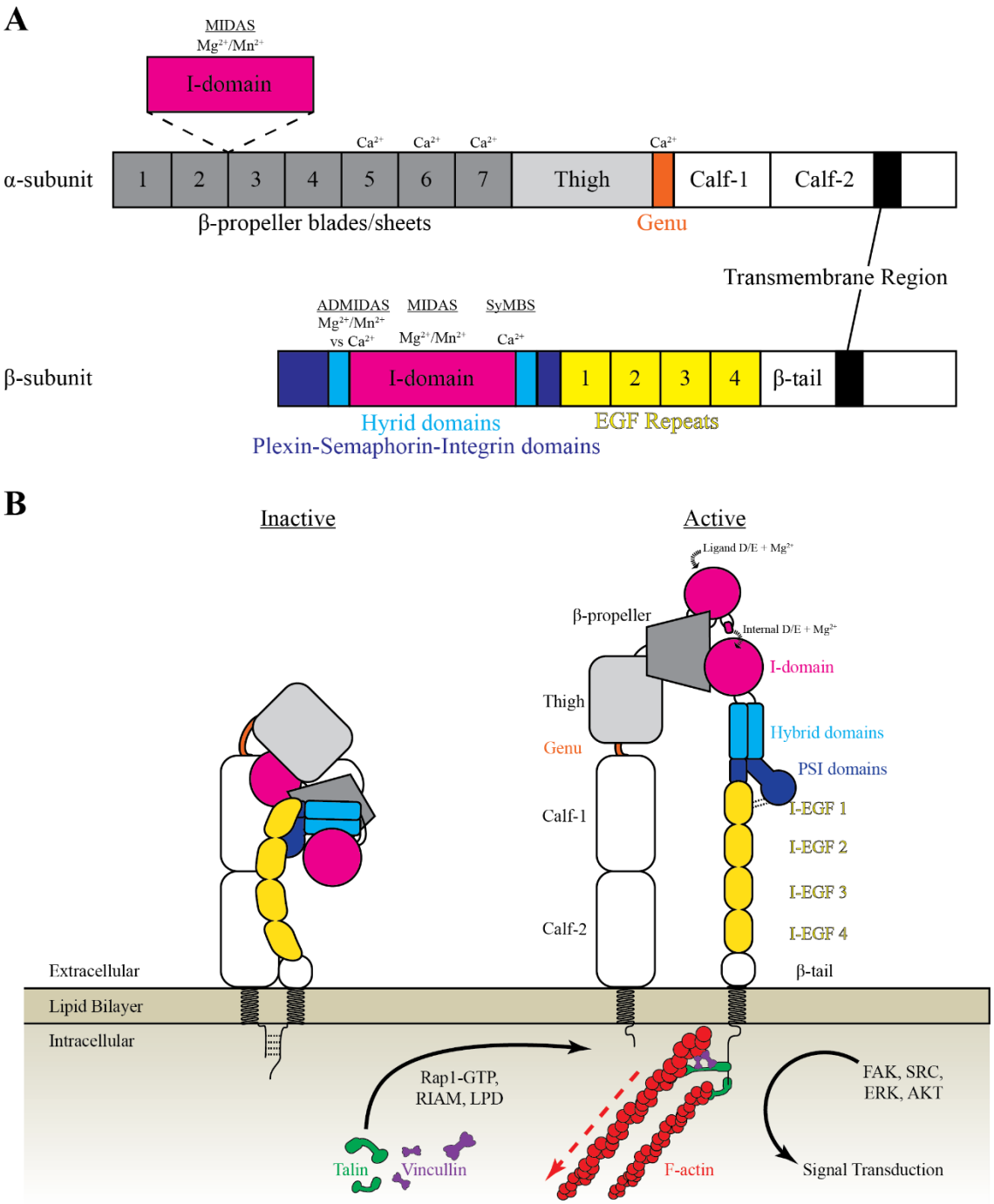

Figure 7. Structural composition of integrin receptors.

(A) Structural composition of α and β-subunits. Extracellular regions contain cation-regulated sites within I-domains and at α-subunit regions. Half of mammalian α-subunits contain an I-domain. All β-subunits contain an I-domain that associates with α-subunits extracellularly. **(B)** Integrin receptors adopt inactive/bent and active/extended conformations. Integrin activation is driven by extracellular Mg^{2+}/Mn^{2+} and physical tensile forces (outside-in), or by intracellular separation of α-β-subunit tails and phosphorylation events from signalling pathways (inside-out). Integrin activation leads to talin-mediated (green) connection to the actin cytoskeleton (red), and the activation of intracellular kinase cascades (FAK, SRC, ERK, AKT). Tensile forces (red dashed arrow) from integrin-ligand interactions propagate to talin unfolding, which allows vinculin (purple) to further cross-link talin to F-actin, reinforcing integrin activation. Adapted from (Arnaout, 2016; Campbell & Humphries, 2011; Kechagia et al., 2019).

Regulation of integrin conformation is controlled by occupancy of cation-binding sites in different protein regions (reviewed in (Campbell & Humphries, 2011)). Firstly, integrin activation is blocked by high Ca^{2+} levels, but intracellular Ca^{2+} is required for proper protein folding and assembly of α-β subunits in the ER prior to export as complete receptors (Tiwari et al., 2011). Cation-regulation of integrin conformation occurs extracellularly, primarily through I-domains that contain three cation binding sites (Box 3): the metal ion-dependent adhesion site (MIDAS), an adjacent site to MIDAS (ADMIDAS), and a synergistic metal binding site (SyMBS). Occupancy of MIDAS by Mg^{2+}/Mn^{2+} promotes integrin activation, marked by a 10Å-downward movement of the α7-helix and an upward movement of the α1-helix in I-domains. The ADMIDAS can be either occupied by Mn^{2+} which promotes integrin activation, or by Ca^{2+} which inhibits integrin activation. The SyMBS, when occupied by Ca^{2+} at micromolar concentrations, synergizes with MIDAS to augment ligand-binding affinity (J. F. Chen et al., 2003; J. O. Lee et al., 1995; Qu & Leahy, 1996). These three regions are present in β-subunit I-domains, whereas α-subunit I-domains only harbour MIDAS. Lastly, the genu is also Ca^{2+}-bound, but Ca^{2+} occupancy at the genu is found in both low and high-affinity integrins (Campbell & Humphries, 2011). Consequently, while the balance between Mg^{2+}/Mn^{2+} and Ca^{2+} controls the equilibrium between high and low-affinity integrins, micromolar Ca^{2+} levels facilitate ligand-binding and are required for biogenesis of complete receptors.

Cation regulation is interrelated to ligand-binding mechanics. Divalent Mg^{2+}/Mn^{2+} cations coordinate intermolecular interactions (catch-bonds) between MIDAS and carboxylate groups from negatively charged residues (Aspartate/Glutamate), bridging ligand-binding interactions between MIDAS and ligand-derived D/E residues, and between α- and β-subunit I-domains where the donor residue is intrinsic to the integrin (J. O. Lee et al., 1995; Shimaoka et al., 2003). The latter association occurs due to aforementioned downward movement of α7-helix and upward movement of α1-helix which, as occurring at both α- and β-subunit I-domains, closes the intervening three-dimensional space and allows the formation of intermolecular links that stabilize active integrin conformation and mechanical resistance (W. Chen et al., 2010; Rosetti et al., 2015). Securing this interaction greatly increases ligand-binding affinity, and is known as the “open-extended state” (Sen et al., 2018). In parallel to the ligand donating an acidic residue to MIDAS, a basic residue enters the α-subunit’s β-propeller. Accordingly, many integrin ligands bear the consensus amphoteric tripeptide RGD that is bound by integrins lacking α-subunit I-domains (with a few exceptions such as α4β1 recognizing the acidic motif LDV instead), whereas integrins with α-subunit I-domains bind their ligands at α-subunits (β-subunits there provide regulatory roles)(Campbell & Humphries, 2011).

Integrin-ligand binding exerts tensile forces that are propagated into the intracellular integrin domains, eliciting conformational changes that underpin firing of signalling cascades and adhesion reinforcement known as outside-in integrin activation.

Box 3. Description of structural domains relevant to integrins.

β-propellers: Topological protein nanodomains arising through intramolecular interactions among β-pleated sheets. Four-to-eight β-pleated sheets arrange radially, converging at the base and leaving a central empty space to form a β-propeller (the shape of which resembles a funnel). Each pleated sheet comprises ~60 amino-acids.

I-domain: Consists of a five β-sheet core surrounded by seven α-helices, and bears homology to von Willebrand Factor A. Contains cation-binding sites implicated in integrin activation and ligand-binding: MIDAS, ADMIDAS and SyMBS. I-domains are present in all β-subunits and 9/18 α-subunits. Size is ~200 amino-acids.

MIDAS: Metal ion-dependent adhesion site, formed by distant residues coalescing upon 3D protein folding (DXSXS…T…D). Promotes integrin activation when occupied by Mg^{2+}/Mn^{2+}.

ADMIDAS: Adjacent domain to MIDAS. Promotes integrin activation when bound by Mn^{2+}, or integrin inhibition when bound by Ca^{2+}.

SyMBS/LIMBS: Synergistic metal binding site. Occupied by Ca^{2+} at low concentrations, facilitating ligand-binding.

Intracellular subunit regions regulate integrin ligand-binding, signalling and adhesion. Many signalling events triggering inside-out integrin activation converge to talin, which directly links integrins (at NPx-Y/F motifs) to the actin cytoskeleton (Tadokoro et al., 2003). Following Rap1 Ras-GTPase activation, adapter/scaffold proteins (e.g. RIAM, lamellipodin) and talin are recruited to Rap1, driving plasma membrane localization and subsequent activity of talin (H. S. Lee et al., 2009). The ability of talin to induce integrin-dependent cell adherence and spreading requires co-activity of kindlins, which promote membrane protrusions by abundantly associating with Arp2/3 complexes in the first 5 minutes of cell attachment, followed by milder kindlin-Arp2/3 association, talin-kindlin co-localization, and recruitment/activation of FAK, Rac1 and paxillin (Böttcher et al., 2017). Integrin-ligand tensile forces propagates to talin unfolding, exposing epitopes recognized by vinculin which in turn cross-links talin to actin and reinforces nascent adhesions (Atherton et al., 2015; Humphries et al., 2007). These core

events, together with the recruitment of numerous proteins in an integrin and context-dependent manner, establish multi-protein hubs collectively termed as the adhesome (Horton et al., 2015). Most of the core events occur conversely and reciprocally: FAK also binds and recruits talin to adhesion sites (Lawson et al., 2012), constitutively active vinculin enhances integrin adhesions (Atherton et al., 2015; Humphries et al., 2007), and actin is thought to provide opposing tension that promotes adhesion reinforcement (Comrie et al., 2015; Nordenfelt et al., 2016). This reflects the multiple pathways and regulatory feedback loops promoting adhesion formation and maturation. Indeed, inside-out activation is also possible via α-subunits, as shown in the context of heat-shock proteins (Hsp90) activating integrins through α-subunit tails (α4)(Lin et al., 2019). It should be emphasized that extracellular and intracellular integrin-related events are bidirectional: ligand-binding induces the formation of intracellular integrin complexes (outside-in), and signalling events that initiate recruitment of intracellular partners to integrin tails promote integrin activation (inside-out).

Adhesion-based protein recruitment forms intracellular protein hubs that affect gene expression and cell behaviour. In terms of signalling, phosphorylation hubs involving paxillin, FAK and Src kinases initiate cascades that positively regulate cell proliferation and locomotion (Horton et al., 2016). Some mechanosensitive transcription factors are also activated through adhesion-dependent cytoskeletal remodelling; for example F-actin sequesters the inhibitory SWI/SNF complex to allow YAP/TAZ nuclear activity (Chang et al., 2018). These events allow integrins to translate extracellular biophysical forces into intracellular signalling events (mechanotransduction). In terms of adhesion, integrin-ligand pulling tension reinforce adhesions through aforementioned Mg^{2+}/Mn^{2+}-mediated α-β-subunit I-domain interactions, intracellular talin unfolding, vinculin recruitment, and kinase-initiated events. This occurs through a “catch-slip bond” model, whereby absence of mechanical force leads to low adhesiveness, excessive force breaks adhesive bonds, while intermediate forces (10-30pN) allows adhesive tension that interlocks and stabilizes adhesions (W. Chen et al., 2010; Rosetti et al., 2015; Strohmeyer et al., 2017). If early-formed nascent adhesions survive disassembly, they mature into large clustered adhesion complexes termed focal adhesions, marked by widespread membrane protrusions and cell spreading (Kalappurakkal et al., 2019). Active actin flow is required for organization and clustering of adhesive complexes (Comrie et al., 2015), which drops as stable adhesions are formed and actin polymerization increases (Nordenfelt et al., 2016). Focal adhesions influence many aspects of cell behaviour by amplifying growth factor-related signalling, facilitating anchorage-dependent cell proliferation, and driving cell locomotion/crawling towards regions of high ligand densities and/or stiffness (reviewed by (Kechagia et al., 2019)).

In summary, integrins are large heterodimeric receptors that adopt closed/open conformations that regulate ligand-binding. The equilibrium between these states is controlled outside-in, via extracellular cation balances and mechanical forces, and inside-out, through signal-dependent recruitment of kinases and cytoskeletal adapters to intracellular tails. Integrins form mature clustered focal adhesions that act as cell-autonomous mechanosensors, mediating cell adhesion, signalling, and migration. These biochemical properties (cation co-ordinated binding of heterotypic molecules, mechanical reinforcement of adhesions, clustering of actin-linked adhesive complexes) makes integrins suitable candidates for the purposes of this thesis. To test the hypothesis that preferential heterotypic intercellular adhesions can drive the formation of hyperuniform patterns, distinct cell types could be engineered to express either an integrin receptor or the cognate ligand. In this system, strong integrin-ligand heterophilic binding should promote heterotypic adhesions, maximum cell intermingling, and the emergence of hyperuniform arrangements. In choosing which integrin-ligand partners will be used to engineer heterotypic adhesions, the next section focuses on the context of leukocytes, where integrins and ligands mediate strong adhesions between different cell types as part of natural physiological processes.

3.1.2 Ligand-integrin pairs driving heterotypic adhesions

The majority of integrins anchor cells to non-cellular ligands such as collagen, laminin or RGD-containing ECM components (e.g. fibronectin), whereas strong intercellular adhesions are mostly mediated by leukocyte integrins (Figure 6). During inflammation, leukocytes attach to the inflamed endothelium through firm adhesions that withstand the circulation's flow current, allowing the execution of the inflammatory response and the clearing of infections. Pro-inflammatory stimuli including antigens (bacterial lipopolysaccharides) and cytokines (TNF-α, IL-1, IFNγ) stimulate endothelia to express cell adhesion molecules recognized by leukocytes. One of these molecules is ICAM-1, a high-affinity ligand for integrins αLβ2, expressed ubiquitously in leukocytes, and αMβ2 predominantly found on neutrophils and monocytes (Diamond et al., 1990; Dustin & Springer, 1988; Smith et al., 1989). These leukocytic integrins stay inactive due to the blood plasma cation balance, where concentration of Ca^{2+} (1.96-2.1mM) exceeds Mg^{2+} (0.46-0.76mM) (Ising et al., 1995; Ordak et al., 2017; Zehtabchi et al., 2004). At sites of inflammation, leukocyte integrins are activated inside-out, through inflamed endothelia-derived chemokines and cytokines, and outside-in, through higher Mg^{2+} concentrations and presumably tensile forces from transient ICAM-1-αLβ2/αMβ2 interactions (W. Chen et al., 2010; Rosetti et al., 2015). These steps secure integrin activation and ligand-binding, establishing firm heterotypic adhesions that arrest slow-rolling leukocytes to inflamed endothelia. Leukocytes have a complex and context-specific integrin interactome (Table 8), but the contribution of αLβ2 (CD11a/CD18; LFA-1) and αMβ2 (CD11b/CD18; MAC-1) in strong leukocyte-endothelial adhesions is well-documented.

Biochemical studies demonstrate the adhesion capacity of LFA-1 and MAC-1 to ICAM-1. Lymphocytes and lymphoblastoid lines adhere to ICAM-1 coated surfaces and TNF-α-stimulated HUVECs, and this adherence is largely abrogated with ICAM-1 or LFA-1 blocking antibodies (Dustin & Springer, 1988). Similarly, neutrophil adherence to purified ICAM-1 and LPS-stimulated HUVECs largely depends on ICAM-1-LFA-1 interactions (Smith et al., 1989). When stimulated HUVECs are seeded on purified MAC-1, adherence is blocked completely using anti-MAC-1, but partially using anti-ICAM-1, suggesting that MAC-1 also binds ICAM-1 among other ligands (Diamond et al., 1990). Amino-acid substitution experiments reveal that LFA-1 and MAC-1 bind ICAM-1 at different sites: LFA-1 binds ICAM-1 at the first immunoglobulin-like domain (critical residues E34 and Q73), whereas MAC-1 interacts with the third immunoglobulin-like domain (critical residues D229QR and E254DE) (Diamond et al., 1991). Notice that most of these residues are acidic and likely implicated in Mg^{2+} coordination with integrin MIDAS (Shimaoka et al., 2003). Interestingly, an N269QSQE/IQAEQ mutation that abrogates ICAM-1 glycosylation enhances adhesion to MAC-1, but not LFA-1, by 4.4-

fold (Diamond et al., 1991). Whether LFA-1 and MAC-1 function in an additive or independent/redundant manner in leukocyte adhesions is unclear; chemokine-stimulated neutrophils have been reported to show enhanced adherence to ICAM-1 due to additive MAC-1 contribution (Diamond et al., 1990; Smith et al., 1989), while others argue that neutrophil adhesions mediated by ICAM-1-LFA-1 are unaffected by MAC-1 blocking (Li et al., 2018). This discrepancy might funnel down to the ligands used, differentially regulating LFA-1/MAC-1 integrin activation through distinct signalling axes (Heit et al., 2005). In COS cells transfected with LFA-1 or MAC-1 chains, each receptor promotes adhesion to purified ICAM-1, with LFA-1 demonstrating higher avidity and adhesion strength compared to MAC-1 (Diamond et al., 1990). A recent in vitro biomechanics study compared binding strength of multiple ligands to LFA-1 and MAC-1 using atomic force microscopy to measure bond strengths via rupture forces (Li et al., 2018). The study corroborated that ICAM-1 forms stronger bonds with LFA-1 compared to MAC-1, and further showed that the strongest axes interactions, which are also implicated in neutrophil adhesion, occur between LFA-1-ICAM-1 and MAC-1-JAM-3 (Li et al., 2018). Hence, firm heterotypic adhesions are mediated through interactions between the ligand ICAM-1 and its integrin receptors LFA-1 and MAC-1.

The importance of β2 integrins in leukocyte adhesive strength is highlighted by the pathophysiology of Leukocyte Adhesion Deficiency (LAD), an autosomal recessive disease whereby patients show persistent neutrophilia and sporadic, unresolved bacterial and fungal infections. LAD-I is rooted in β2 hypomorphic mutations that hamper integrin heterodimerization, whereby integrin under-expression quantitatively correlates with disease severity (Springer et al., 1984). LAD-II occurs due to defective protein fucosylation, which causes pleiotropic defects in leukocyte slow-rolling and cognitive development (Helmus et al., 2006). LAD-III is caused by kinldin-3 loss-of-function mutations that impair leukocytic β2 and platelet β3 ligand-binding activity, leading to LAD-I-type symptoms combined with coagulopathy and bleeding predisposition (Moser et al., 2009; Svensson et al., 2009). CD18 knock-out mice are the standard LAD-I genetic model, as they demonstrate absence of neutrophil adherence and recruitment to endothelia, chronic neutrophilia, and ulcerative dermatitis (Scharffetter-Kochanek et al., 1998). Deletion of individual CD11 subunits, while producing various phenotypes ranging from neutrophilia and phagocytosis defects to impaired T-cell development and cytotoxic responses, does not mimic LAD traits, suggesting redundancy and/or compensation among β2-containing integrins (beyond the scope of this thesis, for details see (Arnaout, 2016)). The link between hindered β2 activity and LAD severity highlights these integrins as the key players in critically strong leukocyte-endothelia heterotypic adhesions.

Table 8. Heterophilic leukocyte integrins and their ligands

Leukocyte Integrin	Lineage Expression	Alias	Ligands	
			Main	Other
αLβ2	Leukocytes	LFA-1; CD11a/CD18	ICAM-1	ICAM-2, ICAM-3, ICAM-4, ICAM-5, JAM-1, ESM-1, telencephalin
αMβ2	Monocytes Neutrophils	MAC-1; CR3; CD11b/CD18	ICAM-1 JAM-3	ICAM-2, ICAM-3 ICAM-4, RAGE, fibrinogen, fibronectin
αxβ2	Dendritic Cells Alveolar macrophages	p150,95; CR4; CD11c/CD18	N/A	ICAM-1, ICAM-4, iC3b, VCAM-1
αDβ2	Monocytes Neutrophils Eosinophils	CD11d/CD18	N/A	ICAM-3, VCAM-1
αEβ7	Intraepithelial T-cells Mucosal mast cells	-	E-Cadherin	N/A
α4β7	Mucosal T-cells	LPAM-1	MAdCAM-1	Fibronectin, VCAM-1
α4β1	Monocytes Neutrophils Eosinophils Lymphocytes	VLA-4	VCAM-1	Fibronectin
αVβ3	Macrophages Platelets	-	Vitronectin	Fibronectin

3.1.3 Strategy to program hyperuniform pattern formation

Given the role of leukocyte integrins LFA-1/MAC-1 in driving strong heterophilic adhesions to endothelial ICAM-1, I hypothesized that cells overexpressing ICAM-1, when mixed with cells overexpressing LFA-1 or MAC-1, would arrange in non-random distributions that mimic conditions of hyperuniformity. To achieve this, I sought to create three different transgenic lines, each overexpressing one of ICAM-1/MAC-1/LFA-1 cell adhesion molecules coupled to a dedicated fluorescent mCherry/turboGFP/H2B-TagBFP cell-identity reporter. Both integrins (LFA-1, MAC-1) were chosen to independently test the efficacy of each receptor in forming heterotypic adhesions with ICAM-1, and in case either showed unexpected adhesion properties against ICAM-1 expressed in HEK-293. HEK-293 cells were chosen as a host, as they are a non-leukocytic cell line that should express none of these cell adhesion molecules, and which demonstrates low basal adhesion properties. Hence, the relative effect of the adhesion introduced would be magnified compared to endogenous basal adhesion.

To allow for conditional, controlled transgene expression and subsequently inducible pattern formation as illustrated previously (Cachat et al., 2016), the TetR/TetO system was chosen, which functionally resembles the bacterial lac operon. When a transcriptional promoter is succeeded by copies of the tetracycline operator motif (TetO), the TetO site allows the binding of the tetracycline transcriptional repressor (TetR), which impedes RNA polymerase recruitment and transcription via steric hindrance. Tetracycline binds to TetR, preventing binding to TetO and allowing transcription initiation. Transgenic HEK-293 cells stably expressing TetR (TREx-293) therefore allow for transgene transcription regulation using the TetR/TetO system, whereby tetracycline or doxycycline induces transgene expression. I thus sought to 1) assemble ICAM-1 with mCherry, MAC-1 with tGFP, and LFA-1 with H2B-BFP, 2) put each module under the control of the *CMV/2xTetO* promoter, 3) incorporate a drug-selection cassette with independent constitutive expression and 4) stably integrate each module into euchromatic regions of the TREx-293 human genome to permit transgene expression (eventually through CRISPR genome editing, see sections 3.1.4-3.1.7).

The following sections focus on engineering TREx-293 cells to adhere heterotypically, by expressing the integrin receptor LFA-1, the integrin receptor MAC-1, or the cognate ligand ICAM-1 in a drug-inducible manner (section 3.1). These transgenic cell systems are subsequently characterized and assayed for expression and functionality of introduced cell adhesion molecules, before evaluating pattern formation (section 3.2). This will allow to test the hypothesis that heterotypic cell adhesions can drive hyperuniform distributions, thereby expanding the toolkit for programming pattern formation and self-organization in mammalian cells using synthetic biology.

Hypothesis I

Heterotypic cell adhesions, through heterophilic binding between ICAM-1 and either LFA-1 or MAC-1, can drive hyperuniform cell distributions in HEK-293-based cells.

3.1.4 Molecular cloning of integrin receptor & ligand cDNA

The hypothesis formed states that when heterotypic HEK-293-based cells, one type expressing the integrin receptor and the other type expressing the cognate ligand, can arrange in hyperuniform distributions by means of integrin-ligand heterophilic interactions. To address the hypothesis, I sought to build genetic constructs that, when integrated into the genome of TREx-293 cells, drive overexpression of either integrin receptor or ligand cDNA and dedicated fluorescent reporters in a tetracycline drug-inducible manner. Given that integrins are heterodimeric receptors (LFA-1: CD11a+CD18; MAC-1:CD11b+CD18) while ligands derive from single peptides (ICAM-1: CD54), the initial step was to individually clone the genes encoding single peptides.

First, integrin-constituent cDNAs (*CD11a*, *CD11b*, *CD18*) were cloned from human peripheral blood mononuclear cells that physiologically express LFA-1 and MAC-1, into separate carrier plasmid vectors (Figure 8A). The initial strategy was to clone cDNA via Gateway technology, but PCR-amplification with recombinase-compatible adapters was only successful for *CD18* (Figure 8B, right panel); *CD11a* and *CD11b* were thus amplified with standard primers (Figure 8B) and cloned via T/A ligation (Figure 9A). Colony PCR was performed with vector-annealing primers flanking the insert site, so that the PCR product reflected the insert in size (Figure 9A). PCRs yielded bands of similar size to expected inserts (Figure 9B, compare with Figure 8B), suggesting the presence of desired cDNA in most bacterial colonies (90% for *pGEMs*; 66% for *pENTR*). PCR-screened colonies were further digested with restriction enzymes cutting once in the vector and once in expected gene inserts. Fragment products from these test-digestions (Figure 9C), with the exception of a few colonies (*pGEM-hCD11a*: #2; *pENTR-hCD18*: #1; #6), are in accordance with theoretical maps of desired recombinant plasmids (Figure 9A), demonstrating successful cloning of integrin-constituent peptide cDNA.

To clone *ICAM-1*, the 1.6kb coding region was acquired as two synthetic DNA fragments (gBlocks™, IDT) designed for direct Gibson assembly into a vacant *pTREx-IRES-mCherry* vector (Figure 10A). The vector was acquired through enzymatic digestion of *pTREx-myrCasp8-ERT2-IRES-mCherry* (Figure 10B) and assembled with ICAM-1-encoding gBlocks™. Colony-derived plasmids were screened using an enzyme that cuts once within the *ICAM-1* coding sequence and once in the vector, yielding two fragments in desired recombinants. Three-out-of-five digested colonies (#1; #3; #4) yielded two fragments with similar sizes to that of expected constructs, (Figure 10C, compare to Figure 10A), suggesting the successful construction of *pTREx-hICAM-1-IRES-mCherry*. Notably, the extracted vector was 2.0-2.5kb larger than expected (Figure 10B), which reflected in the recombinant constructs (Figure 10C). The matter of unreliable vectors is further addressed in later sections (sections 3.1.5-3.1.6).

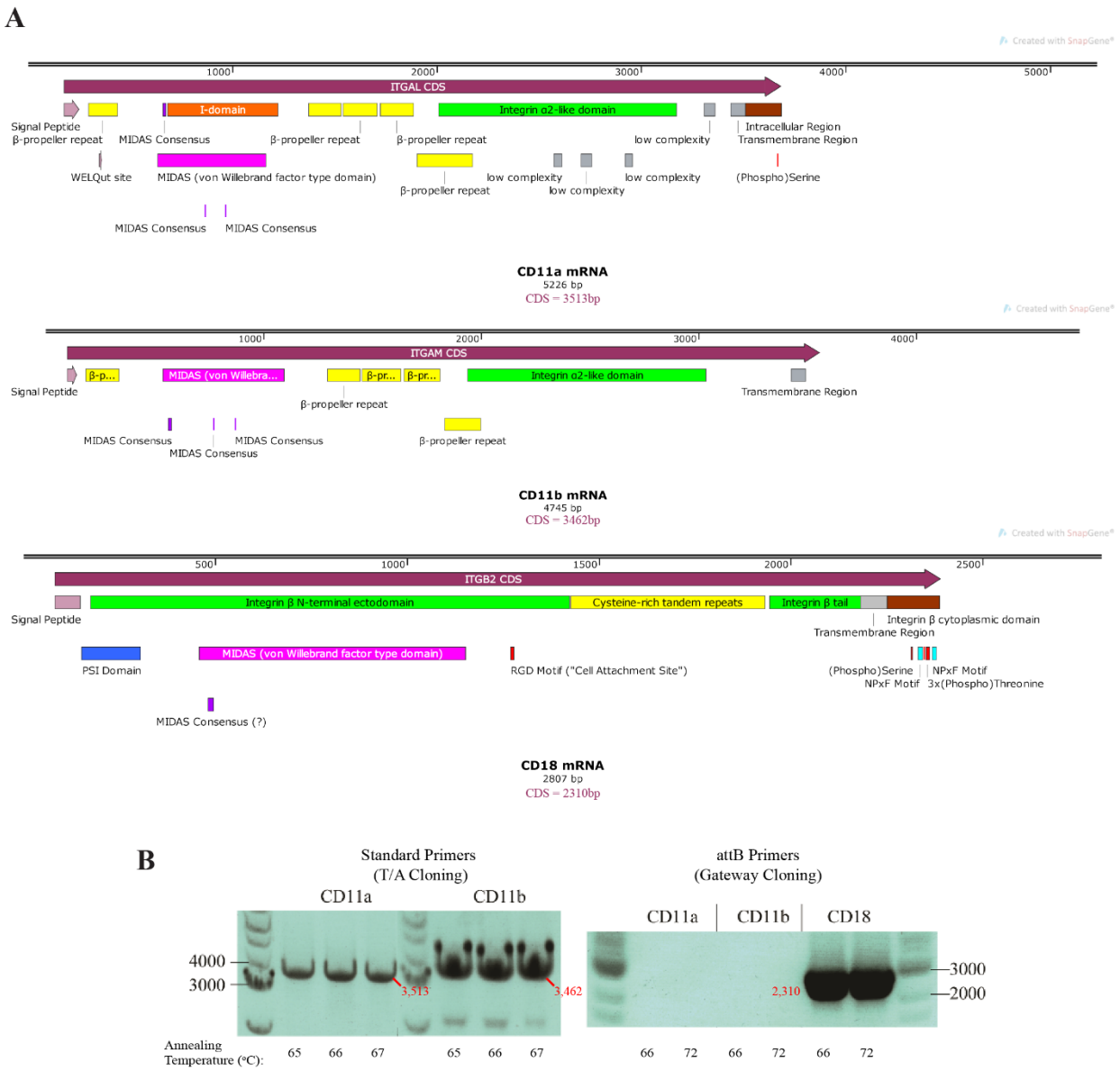

Figure 8. Information regarding cloning of integrin-subunit cDNA in carrier vectors.

(A) Annotated map of *CD11a* (top), *CD11b* (middle) and *CD18* (bottom) longest mRNA transcripts for coding sequence (CDS) and corresponding protein domains. Protein domain information was extracted from NCBI transcript information or predicted through Simple Modular Architecture Research Tool (SMART). **(B)** PCR-amplification results of *CD11a*, *CD11b* and *CD18* cDNA from primary peripheral blood mononuclear cells. Left panel: Amplification of *CD11a* and *CD11b* with standard primers for T/A ligation cloning into *pGEM-T* Easy. Right panel: Amplification of *CD18* with attB-flanked primers for Gateway cloning into *pDONR221*.

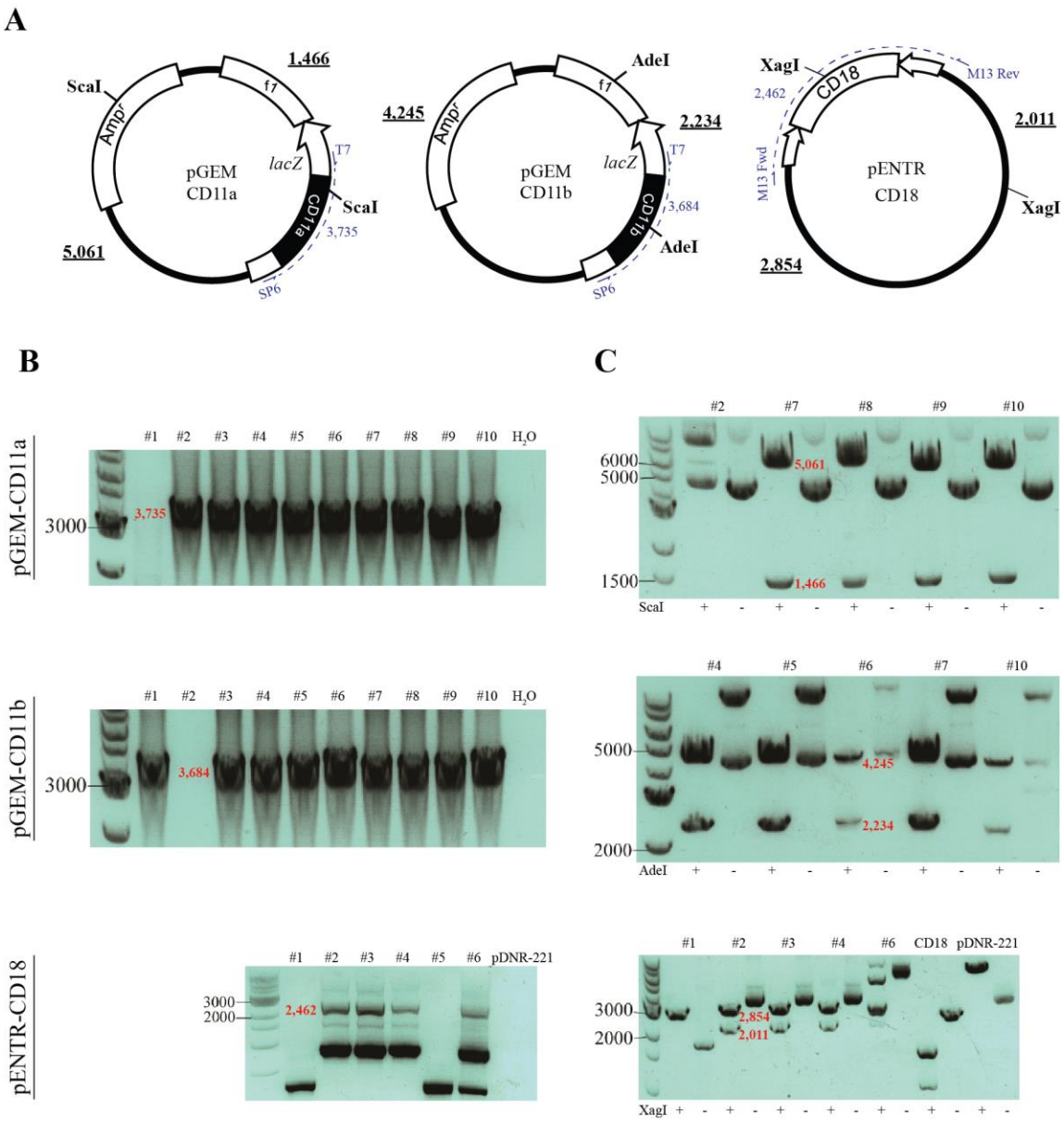

Figure 9 Cloning of integrin subunit-encoding cDNA.

(A) Plasmid maps of desired integrin-carrier constructs, showing primers and amplicons for diagnostic PCRs (purple), and restriction sites and fragment sizes for diagnostic digestions. **(B)** PCR detection of insert size from colony-derived bacterial plasmids. Top: *pGEM-hCD11a*; middle: *pGEM-hCD11b*; bottom: *pENTR-hCD18*. **(C)** Diagnostic digestions of colony-derived bacterial plasmids with corresponding restriction enzymes as shown in (A). Top: *pGEM-hCD11a*; middle: *pGEM-hCD11b*; bottom: *pENTR-hCD18*.

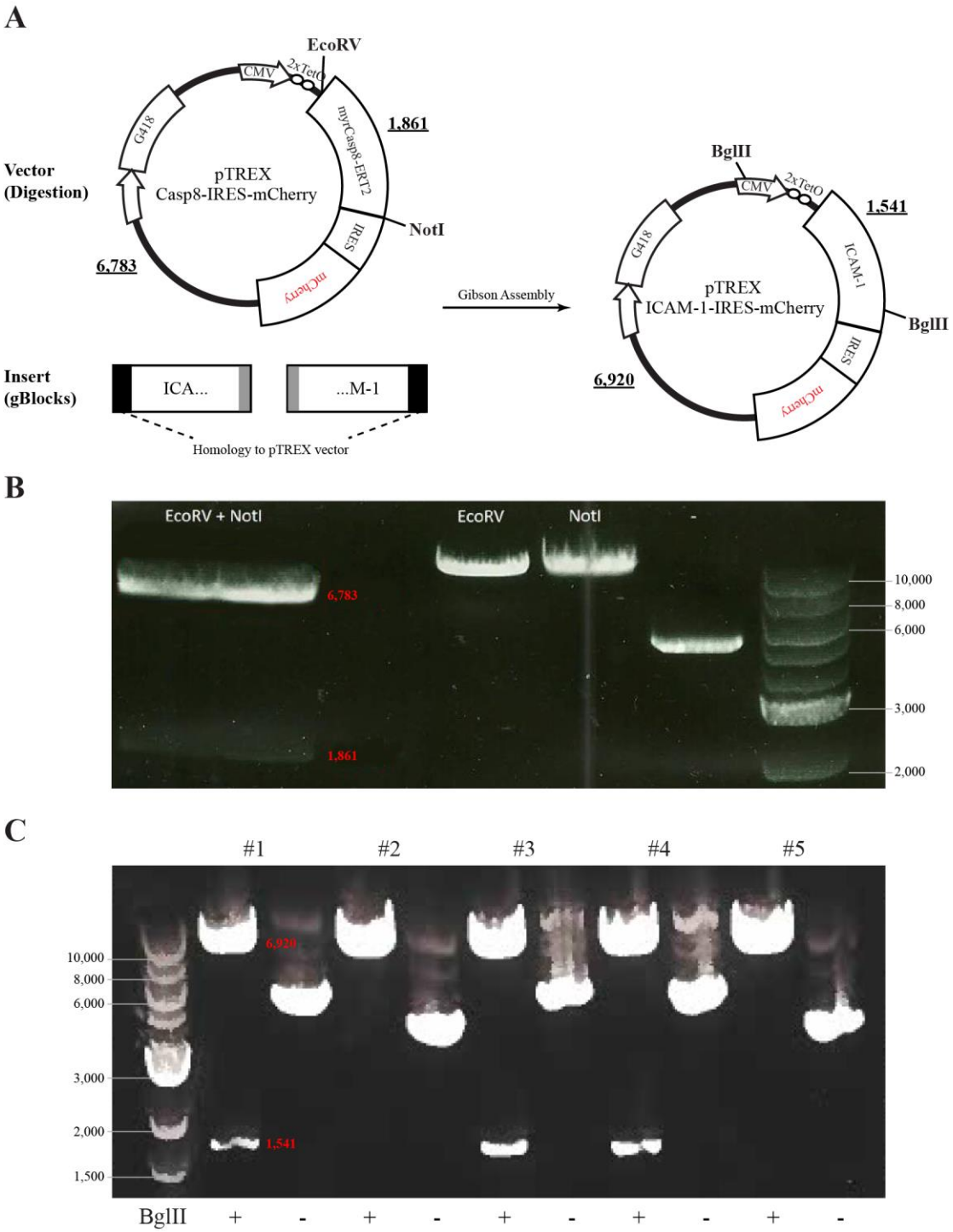

Figure 10. Cloning of synthetic *ICAM-1* cDNA into *pTREx* vector.

(A) Strategy for cloning synthetic ICAM-1-encoding gBlocks™ into *pTREX* vector purified after digestion of pre-existing construct with indicated restriction enzymes. ICAM-1 gBlocks™ are cloned via Gibson assembly through included homology regions shared between the gBlocks™ (gray) and with the vector (black). Map of the desired construct, appropriate restriction sites and expected fragment sizes for diagnostic digestion is also shown. **(B)** Acquisition of *pTREX* vector shown through enzymatic digestion of *pTREX-Casp8-IRES-mCherry*. The top-left double-digested fragment/band was excised and purified for assembly with gBlocks™. **(C)** Diagnostic digestion of colony-derived plasmids purified from assembly transformants as shown in (A).

3.1.5 Co-assembly of ICAM-1/MAC-1/LFA-1 mammalian expression cassettes

Next, integrin/ligand cDNA and fluorescent reporters were designed to be assembled in appropriate combinations, so that *ICAM-1* would be co-expressed with *mCherry*, while either LFA-1 (*CD11a*/*CD18*) or MAC-1 (*CD11b*/*CD18*) would be co-expressed with *turboGFP* at equimolar ratios and under the control of a tetracycline-regulated promoter. Different fluorescent proteins would report for transgene expression and discern positions of distinct cell types in co-culture experiments; equimolar expression would allow brightness in fluorescence based on high transgene expression. Equimolar gene expression from a single cistron is typically achieved via the viral 2A peptide that undergoes co-translational cleavage asymmetrically, leaving one proline in the downstream peptide and 17-24 amino-acids upstream (depending on the 2A variant (Daniels et al., 2014; Wang et al., 2015)).

The asymmetry in 2A cleavage entails the risk that the upstream 17-24 amino-acids, when left on the C-terminus of the upstream peptide, might interfere with protein function. This is important in integrins, in which intracellular C-terminal regions are involved in integrin activation and adhesion reinforcement through the recruitment of actin-linking adapters and kinase enzymes (see section 3.1.1). To minimize potentially detrimental amino-acid additions to transgenes of interest, expression cassettes were designed as *CMV/2xTetO::Reporter-2A-GeneOfInterest*, so that integrin/ligands inherit one proline at the N-terminus (eventually removed from the mature protein following N-terminal signal peptide recognition and cleavage), rather than 17-24 amino-acids at the C-terminus. *ICAM-1*, PCR-amplified from *pTREx-hICAM-1-IRES-mCherry*, was Gibson-assembled with a *pTREx-mCherry-2A* vector backbone, PCR-amplified from *pTREx-mCherry-2A-mCdh3*. For the heterodimeric LFA-1/MAC-1, *CD18* was joined with either *CD11a* or *CD11b* via the optimized foot-and-mouth disease virus GSG-P2A peptide (Wang et al., 2015): the last 48bp of GSG-P2A were contained in the 5-prime tail of the *CD18* forward primer, while the first 48bp of GSG-P2A were contained, in reverse complement, in the 5-prime tail of the *CD11a*/*CD11b* reverse primers. This generates a 30bp homology between the end of *CD11a*/*CD11b* and the beginning of *CD18* fragments that, upon Gibson assembly, joins the fragments together while recreating the 66bp/22amino-acid GSG-P2A sequence. These modules were assembled into *pTREX-tGFP-2A* bearing homology to either LFA-1 or MAC-1, PCR-amplified from *pTREx-tGFP-2A-mCdh1*. The *pTREx-mCherry-2A-mCdh3* and *pTREx-tGFP-2A-mCdh1* constructs, from which *pTREx* backbone vectors were amplified, had been pre-established in the Davies lab from past projects.

Recombinant constructs (Figure 11A) were tested using PCR and/or restriction digestions. Firstly, PCR was employed to screen for co-assembly among *pTREx*, *CD11a*/*CD11b*, and *CD18*, by targeting fragment-spanning amplicons (Figure 11B). This was omitted for *pTREx-mCherry-2A-hICAM-1* due to the simplicity of the two-fragment assembly. Co-assembly of all three amplicons was observed for four *pTREx-tGFP-2A-hLFA-1* colonies (#1; #2; #3; #6) and two *pTREx-tGFP-2A-hMAC-1* colonies (#2, #3). Further test-digestions were performed using enzymes that cut within individual insert coding sequences, yielding an expected number of fragments identifiable by size for desired recombinants (Figure 11A). Results from digestions were mixed (Figure 11C): across the three different *pTREx* constructs, digestions yielded the expected number of bands. Regarding size, bands corresponding to fragments between inserts and/or the *CMV/2xTetO* were identified at expected locations, whereas bands related to the vector were of unexpectedly smaller sizes. This is evident in all *pTREx-mCherry-2A-hICAM-1*, two *pTREx-tGFP-2A-hMAC-1* colonies (#2, #3), and five *pTREx-tGFP-2A-hLFA-1* colonies (#1; #2; #3; #4; #6) (Figure 11C). These results demonstrate the apparent construction of cassettes to drive tetracycline-inducible, equimolar co-expression among i) *CD11a*, *CD18* and *tGFP*; ii) *CD11b*, *CD18* and *tGFP*, iii) or *ICAM-1* with *mCherry*, but suggest that the *pTREx* vector is incomplete due to the smaller DNA fragment sizes relating to *pTREx* regions.

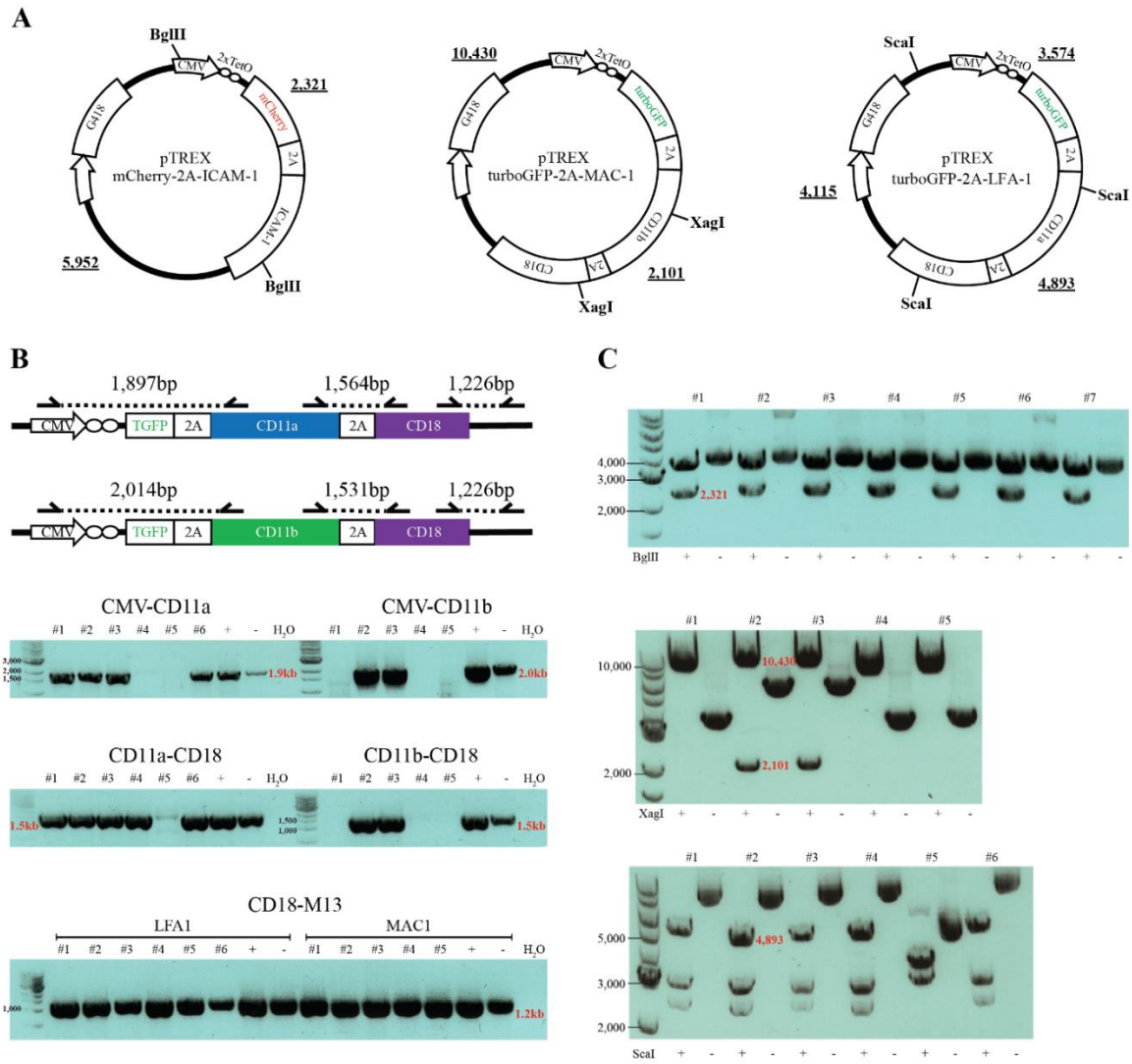

Figure 11. Assembly of tetracycline-inducible mammalian expression cassettes driving integrin receptor/ligand expression.

(A) Plasmid maps showing construct architecture, relevant restriction sites and expected fragment sizes after restriction of desired recombinants. **(B)** PCR screening strategy to evaluate *pTREx-tGFP-hMAC-1* and *pTREx-tGFP-hLFA-1* construct assembly through detection of fragment-spanning amplicons in transformant-purified plasmids. Each gel image is labelled by the two primer-binding sites, demarcating fragments between which the assembly is assayed. +: Aliquot of the Gibson assembly reaction mixture; -: Unassembled mixed fragments. **(C)** Diagnostic digestions of colony-derived plasmids for pTREx-mCherry-2A-hICAM1 (top), pTREx-tGFP-2A-hMAC1 (middle), and pTREx-tGFP-2A-hLFA1 (bottom) as shown in (A).

To assign dedicated reporters for each transgene, *pTREx-tGFP-2A-hLFA-1* was modified by replacing *tGFP* with *H2B-TagBFP*. Because no enzyme option was available to excise *tGFP* without compromising the LFA-1 reading frame, modifications were applied to the original Gibson assembly strategy (Figure 12A): Firstly, one primer was changed in the amplification of *pTREx* to exclude *tGFP*. Secondly, *H2B-TagBFP* was PCR-amplified from *pENTR-H2B-TagBFP* in two-steps: the first PCR generated a portion of the 2A peptide on the 3'-end, and homology to *pTREx* on the 5'-end; the second PCR reconstituted the full 2A peptide on the 3' end and extended homology to CD11a. This allowed the use of *CD11a* and *CD18* fragments as before, completing the assembly. When screening colonies for desired plasmids via diagnostic PCR (Figure 12B) and restriction digestions (Figure 12C), one colony (#14) yielded the expected PCR amplicon, but inconclusive restriction patterns. Notably, the HindIII-digestion cuts within *TagBFP*, *pTREx* (shortly after the transgene insertion site), and the G418 mammalian drug-selection cassette, yielding three fragments in desired recombinants (Figure 12A). Colony 14 produced two fragments (Figure 12C): one corresponding to the 6kb fragment that marks the transgenic region between *TagBFP* and the *pTREx* region shortly after the insertion site, and one unexpected band. That colony-derived plasmid was sequenced, validating that the *H2B-TagBFP-hLFA-1* cassette was successfully reconstructed in that plasmid. Combined with the above section, these results while showing successful modified assembly of *pTREx-H2B-TagBFP-hLFA-1*, corroborate that the vector is incomplete and further suggest that the G418 resistance cassette is absent/compromised.

The issue of the incomplete *pTREx* emerged in cell transfection experiments. TREx-293 cells successfully transfected with the *pTREx* constructs (evident from fluorescence after addition of tetracycline) did not survive G418 selection (data not shown). This finding consolidates the conclusion that the vectors used were missing a portion linked to G418 resistance marker expression, but the transgenic cassettes were intact. Relying on these established *pTREx* constructs as templates for fully-assembled integrin receptor/ligand expression cassettes, I decided to construct well-defined, CRISPR-compatible knock-in plasmids de novo. This approach would allow to precisely define the components contained within the plasmids, increase transgene integration efficiency by means of homologous recombination (utilized in CRISPR technology), and reduce clone-to-clone variation in transgene expression by facilitating transgene insertion in defined genomic loci (by virtue of homology arms entailed in the constructs).

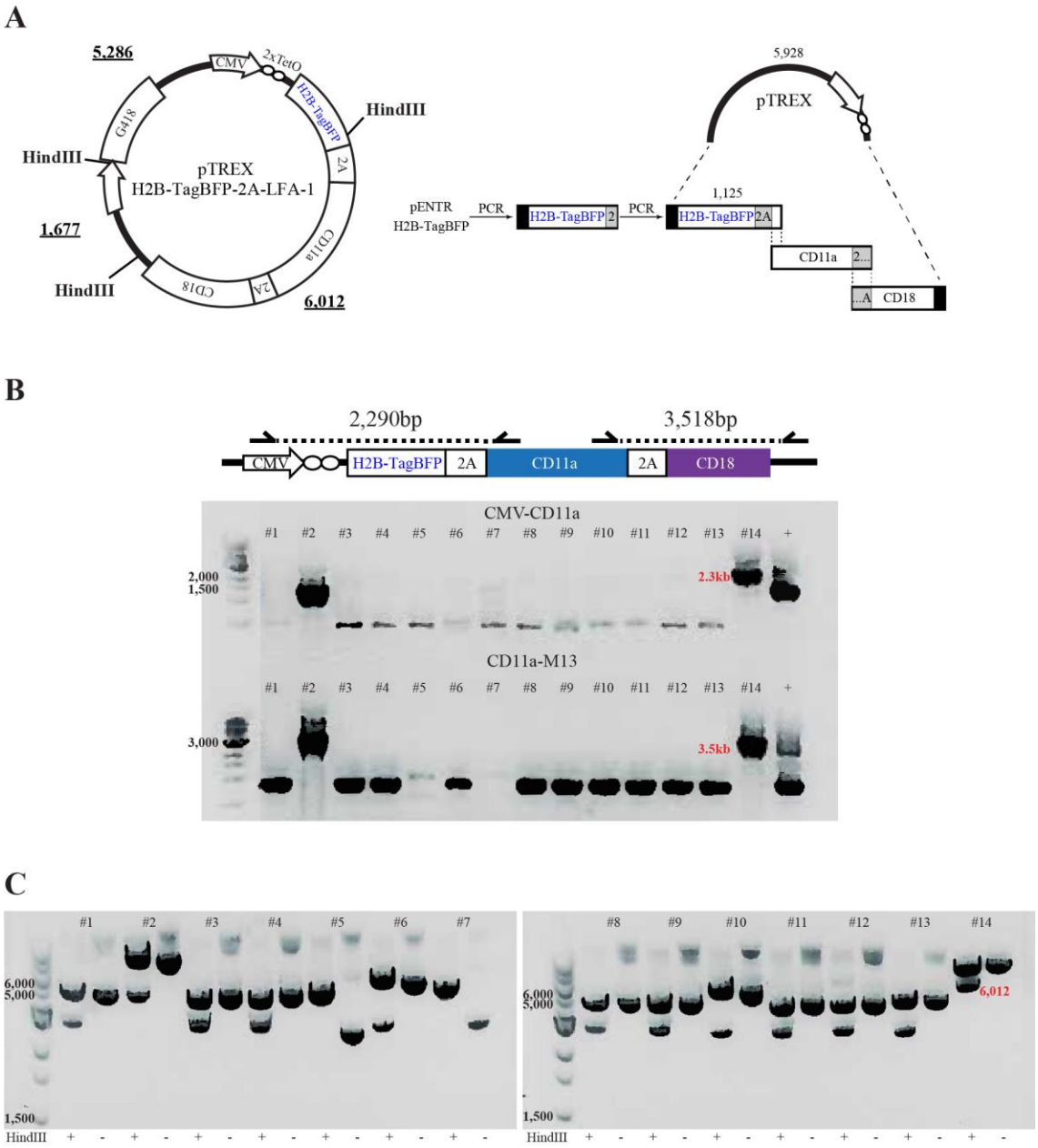

Figure 12. Modification of LFA-1 expression cassette to report transgene expression through H2B-TagBFP.

(A) Plasmid map showing construct architecture, relevant restriction sites and expected fragment sizes after restriction of desired recombinants. Overview of modification of assembly strategy used in Figure 3: H2B-TagBFP is PCR-amplified from a pENTR carrier in two PCR rounds: the first adds homology to pTREx (5'-end) and a portion of GSG-P2A (3'-end) to the reporter, and the second completes the 2A coding sequence and adds homology to the beginning of CD11a (3'-end). **(B)** Schematic representation of PCR screening for incorporation of LFA-1 and H2B-TagBFP by amplicon size in colony-derived plasmids. Gel images are labelled by the two fragments between which the assembly is assayed. +: Aliquot of the Gibson assembly reaction mixture. **(C)** Diagnostic digestions of colony-derived plasmids with HindIII cutting twice in the vector and once in H2B-TagBFP as shown in (A).

3.1.6 Construction of *ROSA26* transgene knock-in CRISPR systems

To increase genome editing efficiency and to tackle the absence of G418 resistance marker, I sought to employ CRISPR genome editing to knock-in the assembled expression cassettes in a “genomic safe harbour” locus of TREx-293. Genomic safe harbours are defined as loci ubiquitously rich in euchromatin, promoting stable transgene expression, and whose disruption shows no adverse phenotypic defects in host cells (Sadelain et al., 2012). The *AAVS1* locus has been conventionally used as a safe harbour for human genome editing, but the human *ROSA26* locus is less gene-rich than *AAVS1* (Sadelain et al., 2012). Thus, engineering-based disruption of *ROSA26* should cause fewer adverse effects in target cells compared to *AAVS1*. I thus sought to establish a CRISPR-based strategy to knock the pre-assembled expression cassettes into *ROSA26,* using a *pSpCas9-2A-eGFP-gRNA* complex to cleave the locus while another plasmid (*pHDR*) facilitates homology directed repair-mediated transgene insertion (Ran et al., 2013).

Firstly, *ROSA26* was bioinformatically identified as done previously by others (Irion et al., 2007). A 100bp portion/query from that study was mapped to the human genome using BLAST, identifying a single match of 100% identity on chromosome 3 (Figure 13A). A 6kb isolated fragment (extract) containing the query and transcription initiation sites of proximate genes (*SETD5*; *THUMPD3*) was used as a template for further work (Figure 13B). The CRISPR genome-editing strategy was based on that extract, annotating relevant components (Figure 13C). Regarding gRNA target-region selection, I built upon a pre-established method used to generate transgenic knock-in mice via *Rosa26* CRISPR genome-editing (Chu et al., 2016). The gRNA-targeting region from that study (Figure 13D, left panel) was mapped to the *Rosa26* locus region originally cloned by the Soriano lab (Friedrich & Soriano, 1991; Soriano, 1999), and the homologous cut-site in the human extract was subsequently identified (Figure 13D, right panel). The presence of the Cas9-PAM site and an XbaI restriction site homologue, that characteristically separates *Rosa26* homology arms but is mutated in the human genome, consolidate that the gRNA site annotated in the human locus is homologous to the murine counterpart (Figure 13C-D). Homology arms were designed to be 1,171bp (5’arm) and 2,727bp (3’arm), sufficient for homologous recombination (>800bp) and similar to the aforementioned original *Rosa26* targeting construct (1,087bp and 4,341bp respectively). This bioinformatic identification and CRISPR annotation of the human *ROSA26* locus based on previous studies provided a template for downstream plasmid construction.

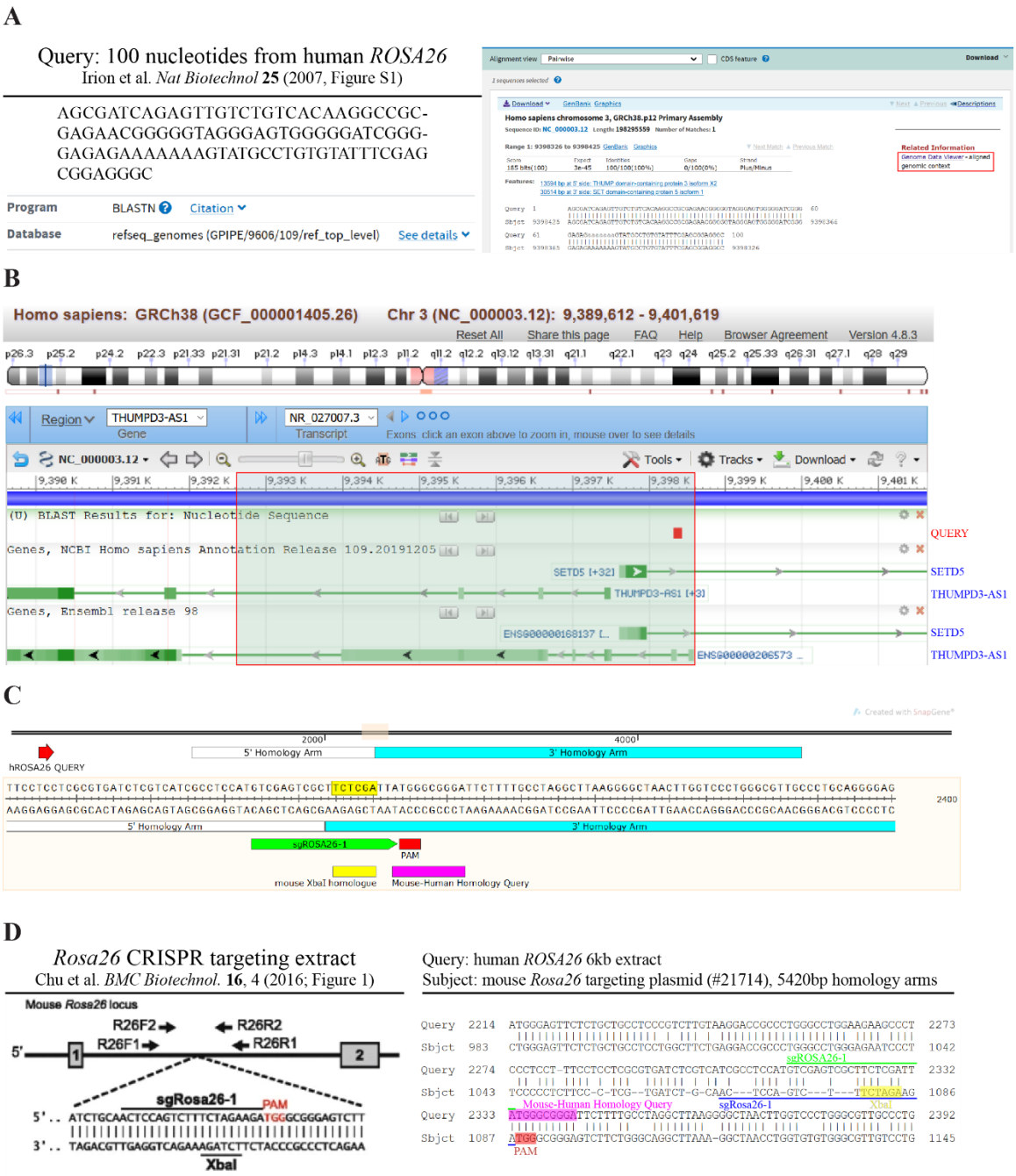

Figure 13. Bioinformatic analysis of *ROSA26* for CRISPR genome editing.

(A) BLASTN using a 100bp query of ROSA26 against the human genome (left) yields a single hit of 100% identity on chromosome 3 (right). The locus was visualized via the genome data viewer tool (red rectangle). **(B)** Genome view showing the 100bp query (red block) and transcript regions of nearby genes SETD5 and THUMPD3-AS1. Sequence NC_000003.12[9392601…9398600] was downloaded as template for annotation (green rectangle, red frame). **(C)** CRISPR design-annotation of ROSA26 extract from (B). Top panel shows the query and homology arms (1.2kb; 2.7kb) for CRISPR knock-in. Bottom panel (beige) shows magnification between homology arms, depicting gRNA-targeting region (green), adjacent Cas9-PAM site (red), the Rosa26 XbaI site homologue (yellow), and an identical 10bp sequence between murine and human loci (purple). **(D)** Rationale for gRNA choice. Left: extract from CRISPR gRNA-targeting in mouse *Rosa26* from cited study. Right: BLAST between *ROSA26* 6kb extract shown in (C) and the original plasmid clone of murine *Rosa26*, showing the sgRosa26-1 gRNA target (blue), the homologous sgROSA26-1 target (green) and associated annotations shown in (C).

To target *ROSA26* using CRISPR-Cas9 technology, a plasmid-based approach was followed, whereby separate mammalian promoters drive *Cas9-2A-eGFP* and gRNA expression from a single plasmid transfected into mammalian cells (Figure 14A). The *ROSA26*-targeting gRNA was cloned into a *pSpCas9-2A-eGFP* as described elsewhere (Ran et al., 2013), and successful insertion of the gRNA-coding sequence was confirmed via Sanger sequencing, establishing the *pSpCas9-2A-eGFP-gRNA* construct (Figure 14B).

A

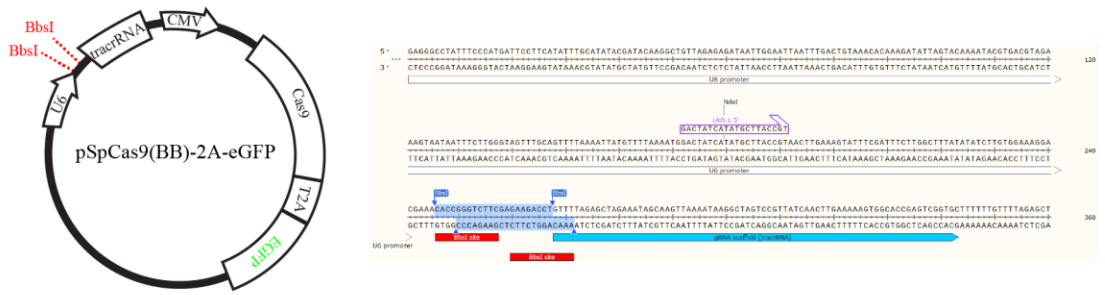

B

mouse sgRosa26-1: ACTCCAGTCTTTCTAGAAGA
human sgROSA26-1: GTCGAGTCGCTTCTCGATTA

Designed BbsI-compatible duplex: 5'-CACC - GTCGAGTCGCTTCTCGATTA-3'
3'-CAGCTCAGCGAAGAGCTAAT - CAAA-5'

Figure 14. Cloning of ROSA26-targeting gRNA in *pSpCas9-2A-eGFP* via Golden Gate assembly.

(A) Left: Map of the pSpCas9 vector driving CMV promoter-based expression of Cas9-2A-eGFP and U6 promoter-based expression of gRNA. The U6 module contains the tracrRNA backbone Cas9 association with Cas9, and the desired 20bp gRNA is cloned within the BbsI spacer (red). Right: Magnification of U6-spacer-tracrRNA module shown in left. The spacer (blue) is BbsI-excised and replaced with the gRNA-encoding duplex containing base-complementary 5' overhangs. Constructs are screened for presence of the gRNA via Sanger sequencing using the LKO1.5 primer (purple). **(B)** Cloning results of sgROSA26-1 in pSpCas9-2A-eGFP. Top: Sequence of murine sgRosa26-1 and human sgROSA26-1 as shown in Figure 5D, and the duplex carrying appropriate overhangs. Bottom: Sanger sequencing result with LKO1.5 primer showing the presence of sgROSA26-1 (yellow) within the construct.

Construction of CRISPR knock-in templates for *ROSA26* was based on Gibson assembly, generating *pHDR*s by fusing five PCR-amplified fragments: a plasmid backbone for amplification and selection in bacteria, two *ROSA26* homology arms, a puromycin resistance cassette for selection of transgenic mammalian cells, and one integrin receptor/ligand expression cassette. Homology arms were PCR-amplified from TREx-293 DNA, the puromycin cassette from a pre-established *pHDR-hGATA2-Venus* (Kauts et al., 2018), each of three transgenic expression cassettes from the aforementioned pTREx constructs, and the essential plasmid backbone from *pUC19* (Figure 15). Colony-derived plasmids were screened using restriction enzymes on the basis of cutting within at least two assembled fragments (Figure 16B, left panel): For *pHDR-mCherry-2A-hICAM-1* sites lay within the *ICAM-1* expression cassette and the *ROSA26* 5'-homology arm; for *pHDR-tGFP-2A-hMAC-1* sites lay within the MAC-1 expression cassette, the *ROSA26* 5'-homology arm and the puromycin resistance cassette; for *pHDR-H2B-TagBFP-hLFA-1* sites lay within the LFA-1 expression cassette, the puromycin resistance cassette, and the *ROSA26* 3'-homology arm. Therefore, identity validation of all fragments spans over the digestions of the three different constructs. Band patterns expected from positive/correct constructs appeared in all five *pHDR-mCherry-2A-hICAM-1* colonies (Figure 16B, top); two-out-of-five *pHDR-tGFP-2A-hMAC-1* colonies (Figure 16B, middle; #7, #4), and three-out-of-five *pHDR-H2B-TagBFP-hLFA-1* colonies (Figure 16B, bottom; #6, #7, #10). We ensured that transgene expression cassette open reading frames were intact through Sanger sequencing on the final construct sample used for mammalian cell transfections.

Overall, these results demonstrate the successful design and construction of new plasmids for CRISPR-mediated insertion of drug-inducible integrin receptor/ligand expression cassettes into the *ROSA26* locus of human TREx cell systems.

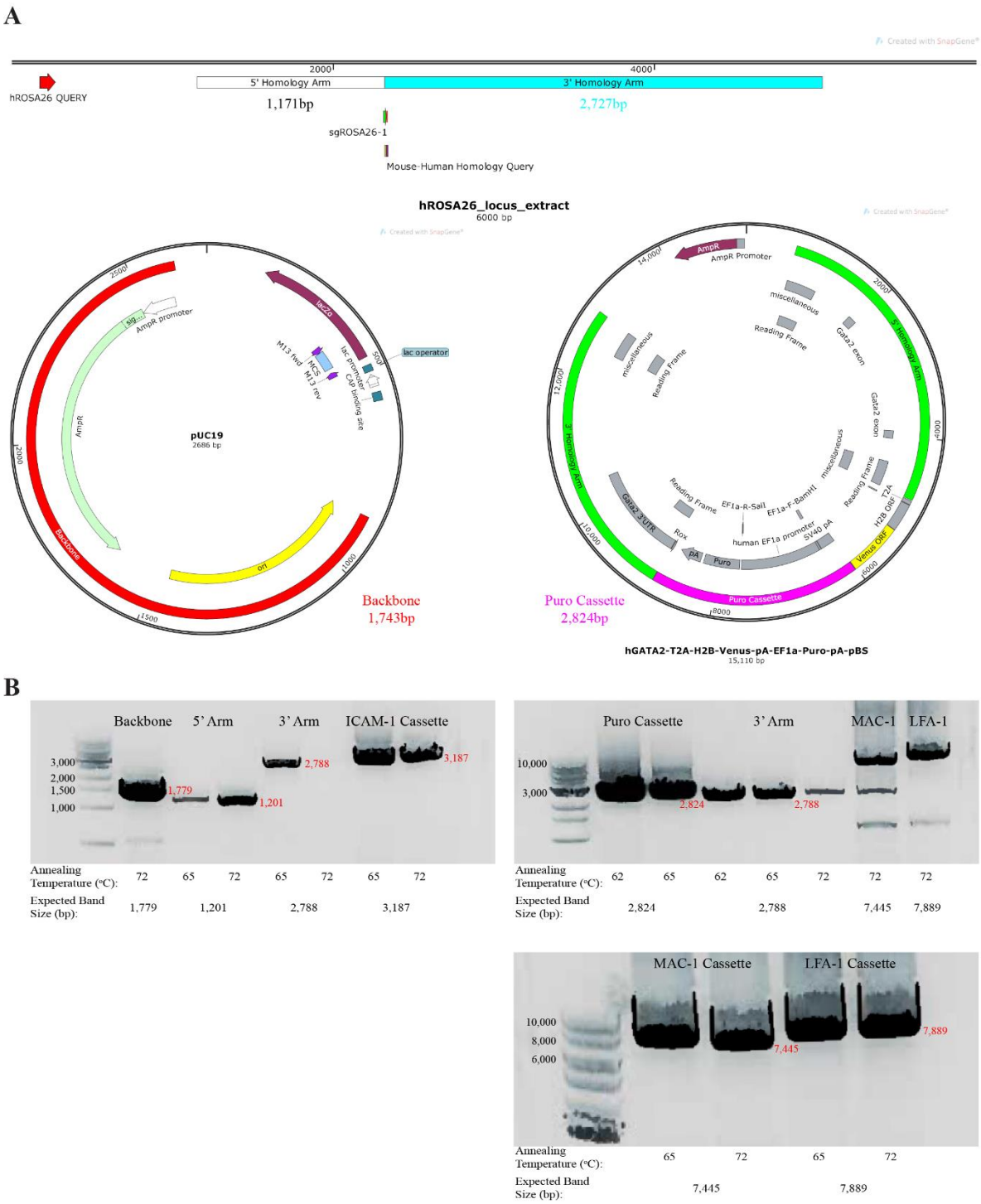

Figure 15. Information regarding *pHDR* CRISPR construct assembly.

(A) Annotated maps of templates from which fragments were generated to assemble pHDRs. Top: ROSA26 extract showing site and size of homology arms; the 100bp query from shown in Figure 5A is depicted as reference. Template for these arms was TREx-293 gDNA. Bottom left: pUC19 template from which the essential plasmid backbone (red) was generated. Bottom right: phGATA2-Venus template from which the puromycin resistance cassette (purple) was generated. **(B)** PCR-amplification results of assembly fragments from templates as shown in (A) and transgene expression cassettes from pTREx constructs shown in Figure 11 and Figure 12.

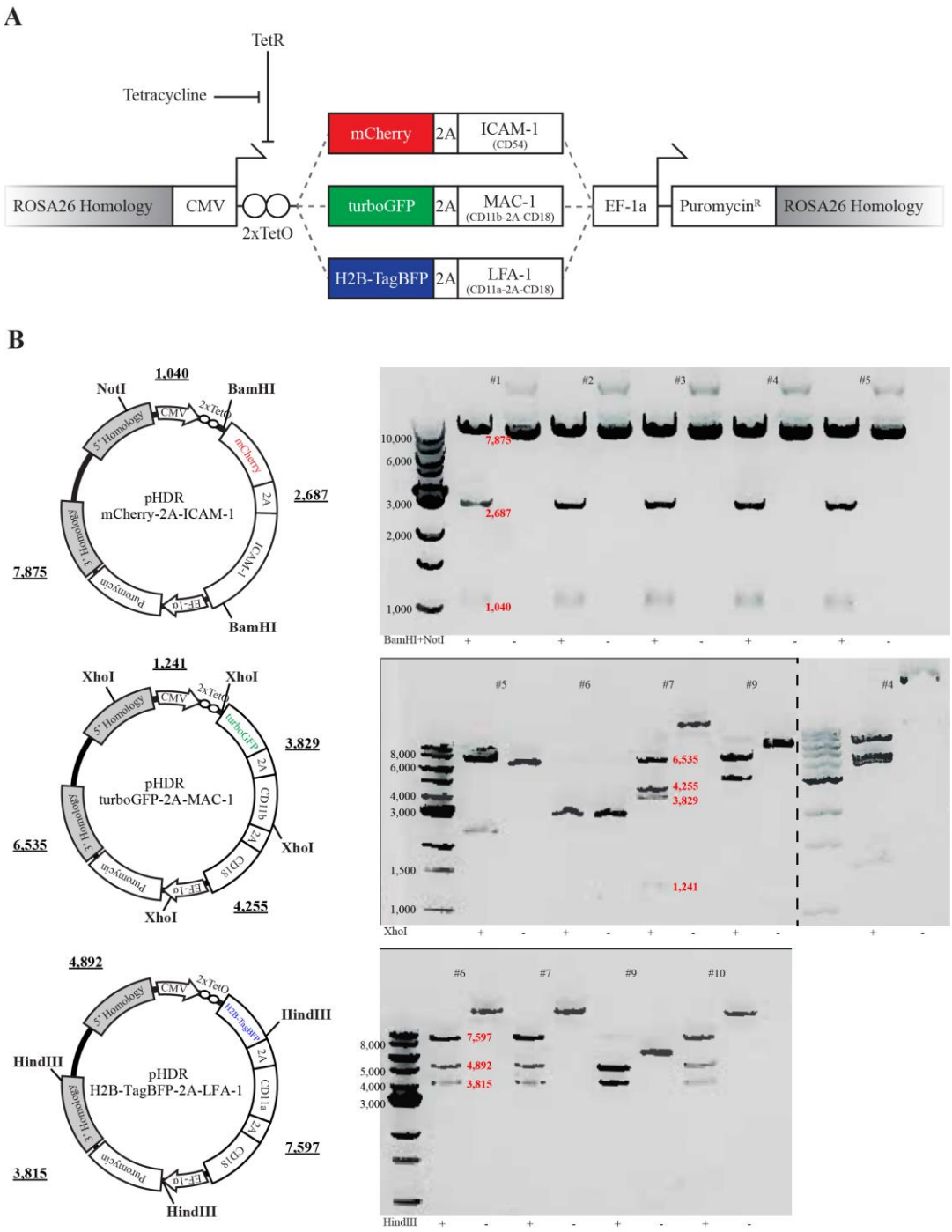

Figure 16. Generation of *pHDRs* for insertion of transgenes in the *ROSA26* locus.

(A) Schematic representation of CRISPR strategy for transgene knock-in at ROSA26. Constructs harbor ROSA26 homology arms containing either mCherry-2A-ICAM-1; tGFP-2A-CD11b-2A-CD18; or H2B-TagBFP-2A-CD11a-2A-CD18 under the control of a CMV/2xTetO promoter. In TREx cell systems stably expressing TetR, TetR represses transgene transcription via steric hindrance by binding TetO elements downstream the CMV promoter. Tetracycline binds and sequesters TetR, allowing transcription to resume. An independent puromycin resistance marker is constitutively expressed through an EF-1α promoter to select transgenic cells. **(B)** Plasmid maps showing construct architecture, relevant restriction sites and expected fragment sizes after restriction of desired recombinants (left) and corresponding diagnostic digestion results (right) of pHDR constructs for ICAM-1 (top), MAC-1 (middle), and LFA-1 (bottom) cell adhesion molecules.

3.1.7 Genome editing of TREx-293 cells using CRISPR vectors

To establish transgenic TREx-293 lines, wild-type cells were co-transfected with *pHDR* and *pSpCas9-2A-eGFP-gRNA*, or *pSpCas9-2A-eGFP-gRNA* only, and subjected to puromycin selection (Figure 17A). By the 8th day of selection, no viable/attached cells were detected in the *pSpCas9-2A-eGFP-gRNA*-only transfected control, whereas viable cell colonies could be seen in samples co-transfected with *pHDR* and *pSpCas9-2A-eGFP-gRNA* (not shown). Tetracycline was thus added to the medium of cells co-transfected with *pSpCas9-2A-eGFP-gRNA* and *pHDR* to induce transgene expression. Surviving colonies emitting expected fluorescence could be detected in *pHDR/pSpCas9-2A-eGFP-gRNA* co-transfected wells (Figure 17B). Given some colonies consisted of both fluorescent/transgenic and non-fluorescent/parental cells, raising the possibility of random integration of the puromycin cassette or persistence of the marker after transient expression, populations co-expressing fluorescent reporters and expected surface markers were purified via FACS (Figure 17C). Transgenic populations were stained using respective fluorophore-conjugated antibodies (listed in Materials and Methods, Table 4). This is contrary to wild-type TREx-293 that express none of the surface markers (Figure 17C, bottom panel). This is an important observation, as it demonstrates that wild-type TREx-293 do not endogenously express any of the cell adhesion molecules introduced via CRISPR, while transgene expression leads to successful localization of cell adhesion molecules to the plasma membrane. These genome-edited populations demonstrating puromycin resistance and expression of fluorescence and desirable surface markers, were expanded and used for further work.

It should be noted that transgenic populations, particularly TREx-293$^{MAC\text{-}1}$, demonstrate morphological changes: MAC-1/GFP^{+} cells appear flattened with increased surface area compared to non-fluorescent cells (Figure 17B). These morphological characteristics will be further analysed in the next chapter, and already elude to the biological functionality of engineered modules in changing adhesion properties of host cells. It is also crucial to note that hereafter, colony-derived populations are abbreviated as *clones* for succinctness, but true clonality is improbable and elusive due to TREx-293 cells not surviving single-cell sorting.

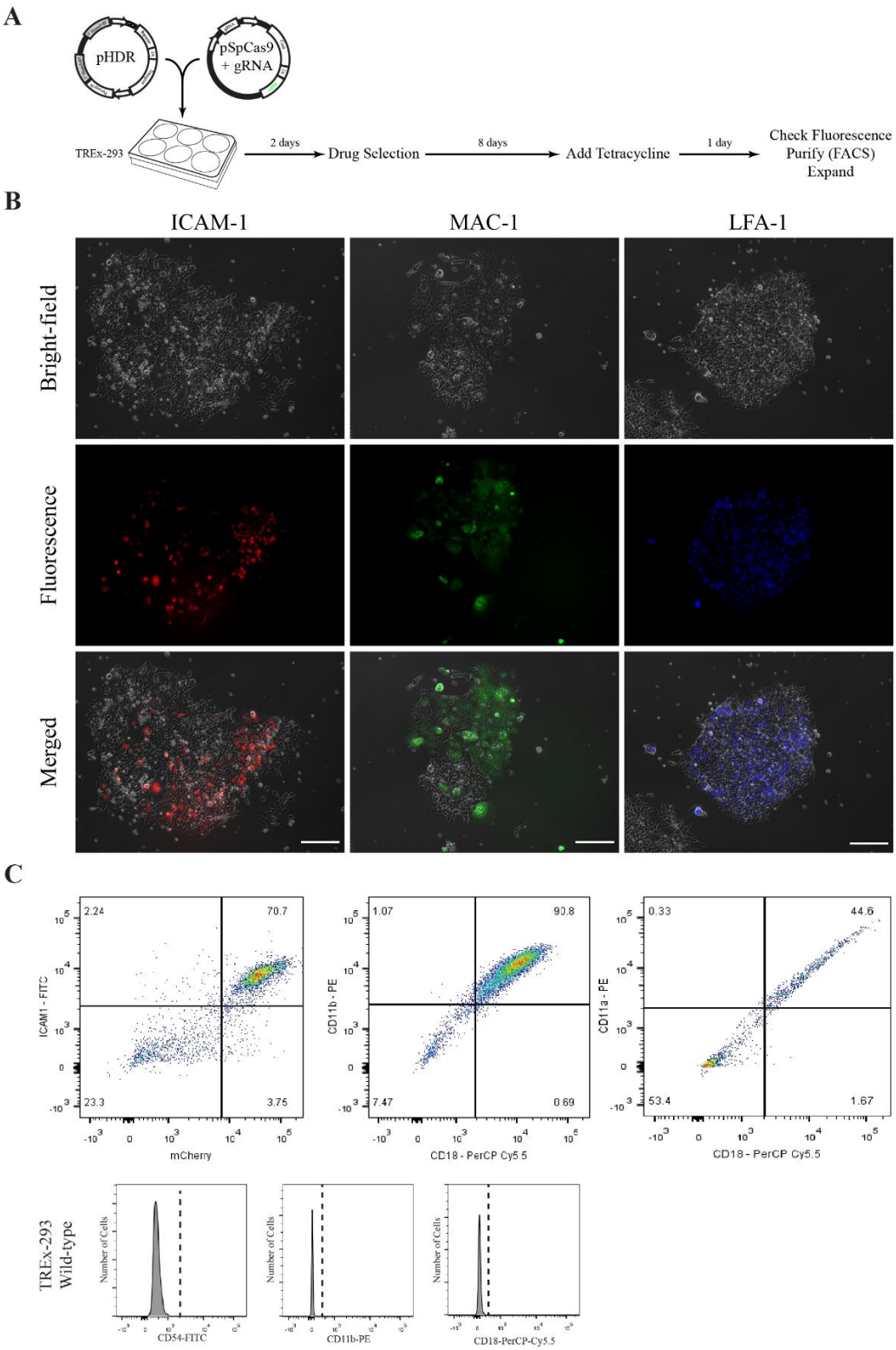

Figure 17. CRISPR genome editing of TREx-293 using CRISPR vector strategy.

(A) Workflow for transfection, selection and purification of transgenic populations. **(B)** Fluorescence microscopy of transfected populations at respective channels following 8 days of puromycin selection and 24 hours of tetracycline induction (10μg/ml). Scale bar: 200μm. **(C)** FACS dot plots of populations shown in (B) after live cell staining with antibodies against CD54 (ICAM-1, left); CD11b and CD18 (MAC-1, middle); CD11a and CD18 (LFA-1, right). For MAC-1 and LFA-1, panels shown are gated from GFP+ and BFP+ populations respectively. Bottom panels: wild-type TREx-293 with no detectably clear signal in any channel.

To isolate and detect populations expressing high transgene levels, TREx-293 colonies from low-density cultures were manually picked using a P200 pipette under a microscope, expanded and screened for transgene expression after a 24-hour exposure to tetracycline. SYBR Green-based qRT-PCR was performed using exon-spanning primers for *CD54* (TREx-293^{ICAM-1}), *CD11b* (TREx-293^{MAC-1}) and *CD11a* (TREx-293^{LFA-1}). Reaction quality control was evaluated through melting curve analyses, and all transgenic samples showed single melting peaks (not shown). Wild-type TREx-293 showed some background fluorescence for CD54 at the same melting temperature as TREx-293^{ICAM-1}, while non-template controls showed no detectable signal. This suggests that either CD54 primers amplify a non-specific region with similar amplicon size, or that TREx-293 endogenously express extremely low levels of CD54 mRNA and protein (see Figure 17C). In CD11a and CD11b reactions, multiple low-amplitude peaks suggesting non-specific amplification were detected in wild-type controls, but never in transgenic samples. To correct for this background, results from transgenic samples were normalized to wild-type TREx-293 using the ΔΔCt method (Schmittgen & Livak, 2008).

Expression of dedicated cell adhesion molecules across clones in all TREx-293$^{ICAM-1/MAC-1/LFA-1}$, albeit high compared to wild-type background, showed considerable variability (Figure 18A-C), potentially due to either transgene knock-in into both *ROSA26* alleles or random integrations throughout the genome. Strong heterophilic adhesions might occur between cognate clones showing either the highest transgene expression levels, or matching expression levels. Under this assumption, the following clones were selected for further work: TREx-293^{ICAM-1} clones 2, 7 and 9 (Figure 18A), TREx-293^{MAC-1} clones 3, 9 and 17 (Figure 18B), and TREx-293^{LFA-1} clones 1, 5 and 7 (Figure 18C). PCR-genotyping confirmed the presence of DNA segments predicted in correctly edited *ROSA26* transgenic cells (Figure 18D). However, additional random insertions cannot be ruled out without Southern Blot analyses, which could be present in TREx-293^{LFA-1} (Figure 18D, compare TREx-293^{LFA-1} clones 1 and 7 to TREx-293^{ICAM-1}), and which might explain the heterogeneity in transgene expression across clones of the same line (e.g. TREx-293^{ICAM-1} clone 9 vs clones 2 and 7). These transgenic clones were used as platforms for all analytical work presented in the next chapter.

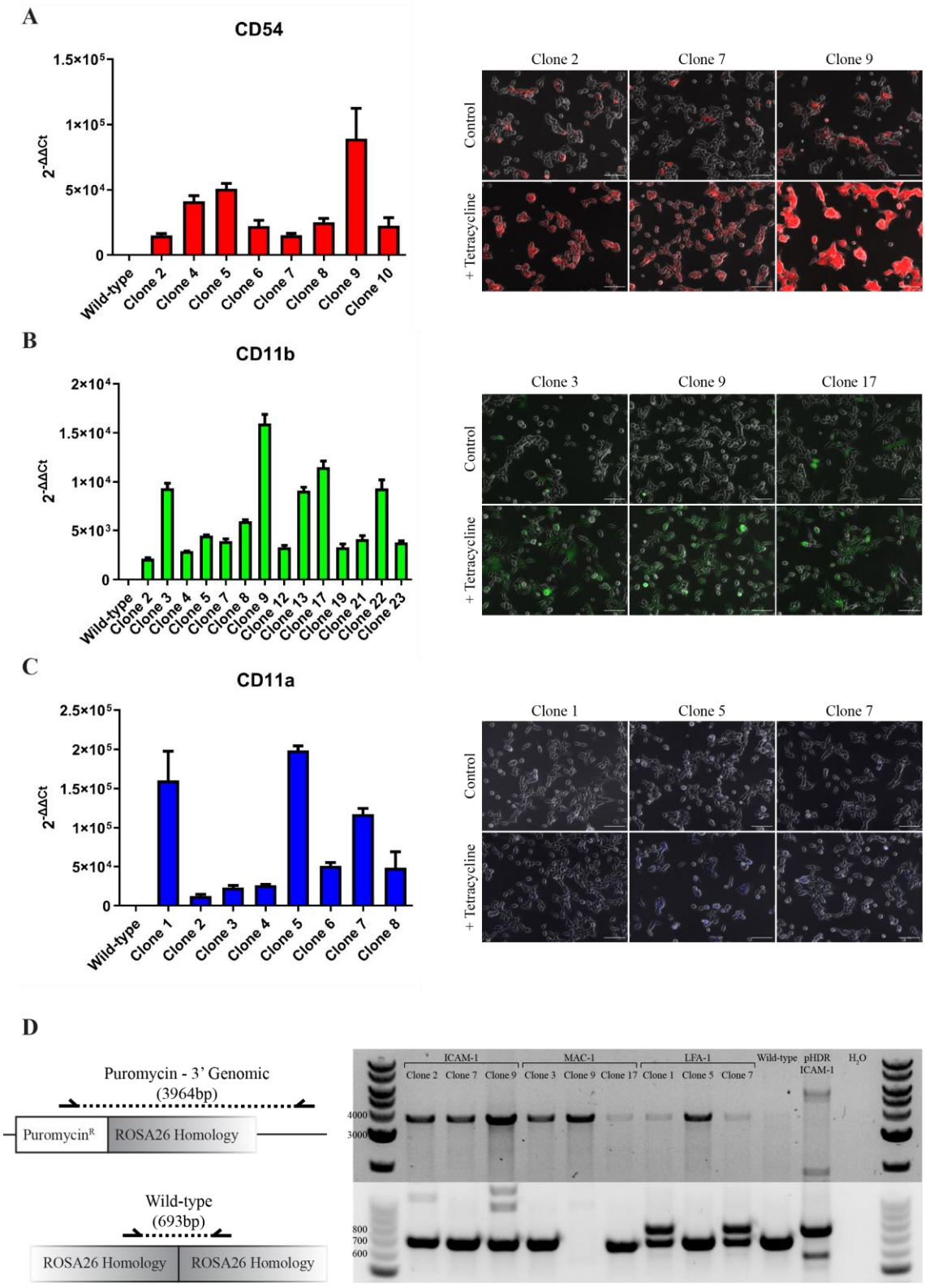

Figure 18. Transgenic TREx-293 screening for transgene expression and *ROSA26* integration.

(A-C) qRT-PCR of colony-picked expanded populations after 24h culture in 10μg/ml tetracycline (left) and fluorescence microscopy of selected clones in tetracycline-free and tetracycline-supplemented 24h cultures (right), for TREx-293^{ICAM-1} **(A)**, TREx-293^{MAC-1} **(B)** and TREx-293^{LFA-1} **(C)**. Scale bar: 100μm. **(D)** DNA genotype for transgene integration into ROSA26 (top panel) and for the wild-type ROSA26 allele (bottom panel) in selected clones.

3.2 Testing pattern formation

3.2.1 Characterization of the *ROSA26* transgenic system

I sought to characterize transgene behaviour in the established transgenic TREx-293 systems. Firstly, I wanted to test transgene inducibility in terms of input sensitivity as a dose-response, i.e. how much tetracycline is required to activate transgenes and at what level is saturation reached. To achieve this, TREx-293^{ICAM-1} fluorescence was quantified after 24-hour exposure to a range of tetracycline concentrations; the 24-hour mark was chosen arbitrarily to allow accumulation of transgene-derived peptides. The TREx-293^{ICAM-1} line was used to represent all transgenic populations for three reasons: mCherry brightness allows detection of low expression levels hence sensitivity in measurements; mCherry excitation/emission spectra are well-aligned with lasers/detectors in the plate reader; and tetracycline-stimulated TREx-293^{MAC-1} flatten out and increase their surface area, effectively diluting GFP in 2D space, making the GFP-producing line less suitable for detection of fluorescence. Across three different TREx-293^{ICAM-1} clones (Figure 19A), the effective concentration of tetracycline needed to activate 50% of maximal fluorescence (EC_{50}) at 24 hours-post-exposure was calculated at 64.4nM (SE=9.2). Detectable increase in fluorescence can be recorded with as little as 10nM, with maximal activation occurring at 1μM (Figure 19A). Hence the TetR/TetO system in the context of TREx-293, is inducible with nanomolar efficacy and reaches activation plateau past micromolar levels.

To validate protein trafficking to the cell surface in sufficient levels, live-cell flow-cytometry was performed. Live non-permeabilized TREx-293 were stained with antibodies that recognize extracellular regions of CD11a/CD11b/CD18/CD54, and transgenic populations were compared to reference cells physiologically expressing genes encoding these peptides. Human umbilical vein endothelial cells (HUVECs) have been routinely used for *ICAM-1* studies, expression of which is induced under pro-inflammatory stimuli. Therefore, expression profiles of tetracycline-stimulated TREx-293^{ICAM-1} were compared against TNF-α-stimulated HUVECs (mixed-donor pool, to capture biological variation in CD54 levels) in terms of anti-CD54-FITC fluorescence. Mixed-donor HUVECs showed widespread levels of ICAM-1 intensity whereas activated TREx-293^{ICAM-1} accumulated at the high-most end of the tail (Figure 19B). Non-stimulated TREx-293^{ICAM-1} showed undetectable or very low *ICAM-1* expression, suggesting leakiness of the TetR/TetO system or low tetracycline levels in the foetal calf serum present in the medium. Notably, tetracycline derivatives are used as prophylactic feed additives to support health and growth in farmed cattle, especially in the US wherefrom the serum used for TREx-293 cultures originated (Miller et al., 2018).

Leakiness was also evident under fluorescence microscopy (Figure 19A), but flow-cytometry provides a more comprehensive analysis due to higher sensitivity allowing detection of low transgene levels undetectable via microscopy. Hence, TREx-293^{ICAM-1} accumulate very high levels of transgenic ICAM-1 on the plasma membrane upon maximal transgene induction relative to mixed-donor HUVECs, while showing low-leaky expression in tetracycline-free conditions.

Similarly, TREx-293^{MAC-1} and TREx-293^{LFA-1} were compared against peripheral blood mononuclear cells (PBMCs) that include populations physiologically expressing MAC-1 and LFA-1. Averaging from experimental means of three TREx-293^{MAC-1} clones, 93.5% (SE=2.9) of live cells emitted GFP fluorescence (not shown), within which compartment 99.0% (SE=0.1) co-expressed *CD11b* and *CD18* (Figure 19C). To bring TREx-293^{MAC-1} events in-scale within cytometry panels (Figure 19D), photomultiplier voltages used in PBMCs analyses had to be reduced (CD11-PE: 390 to 270mV; CD18-PerCP/Cy5.5: 600 to 560mV), suggesting high *CD11b*/*CD18* expression in TREx-293^{MAC-1} compared to PBMCs. Similarly, 90.5% (SE=1.9) of TREx-293^{LFA-1} cells co-expressed *CD11a* and *CD18* (Figure 19E) and voltages were likewise reduced compared to PBMC templates (Figure 19F). However, CD11a/CD18 levels showed larger dispersal, and no endogenous BFP fluorescence was detected (Figure 19E). In both TREx-293^{MAC-1} and TREx-293^{LFA-1}, CD11+/CD18+ populations appeared high in the double positive gate compared to PBMCs, even with reduced voltages (Figure 19D, F), suggesting high integrin levels on the cell surface.

Collectively, these experiments demonstrate that the established TetR/TetO transgenic systems, while suffering from leaky expression, demonstrate tetracycline inducibility with nanomolar efficacy (EC_{50}=64.4 ± 9.2nM) through which high levels of transgenic cell adhesion molecules are expressed and localize to the plasma membrane.

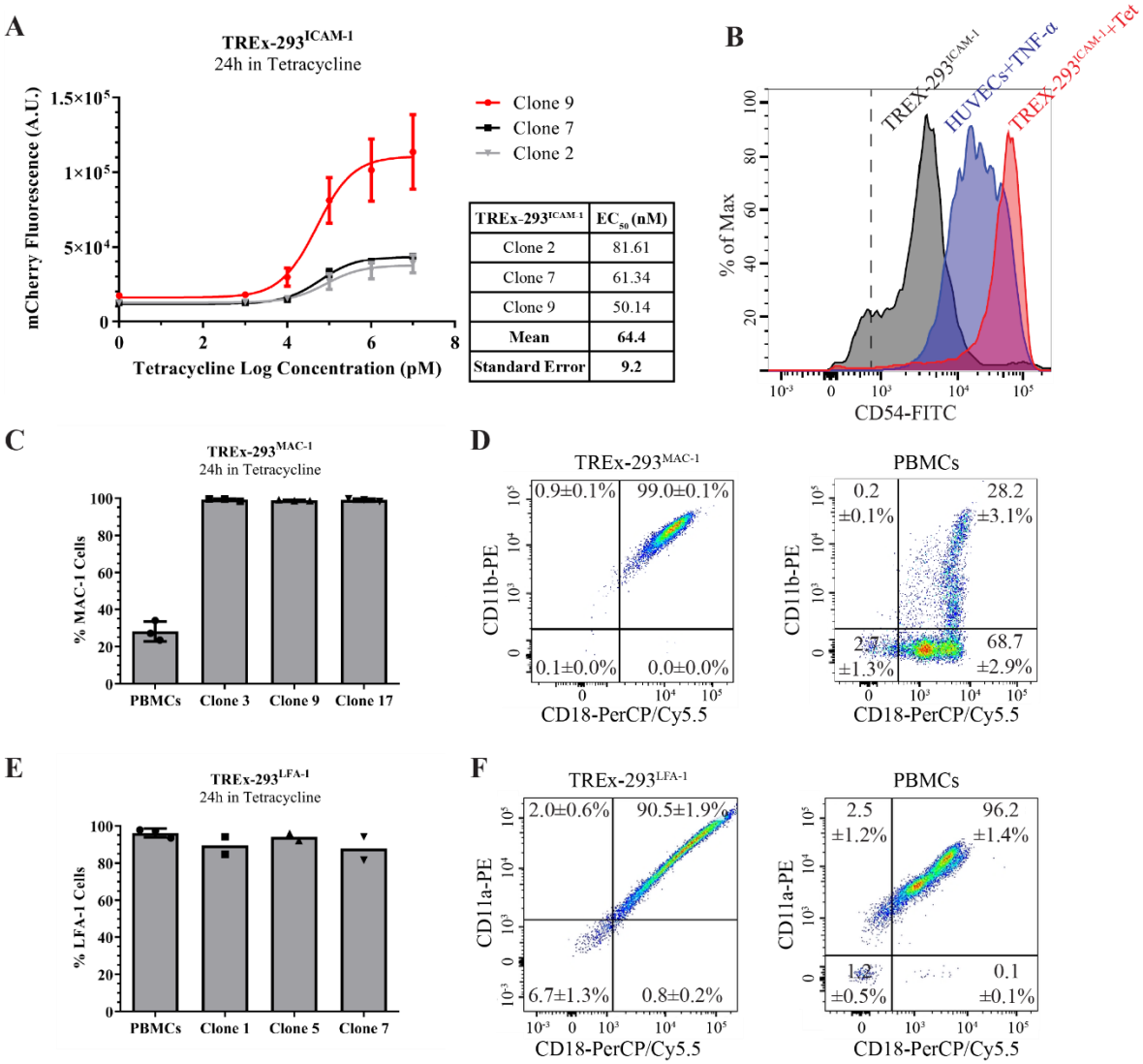

Figure 19. Transgene characterization in input sensitivity and output levels.

(A) Fluorescence readings of TREx-293^{ICAM-1} cells 24 hours after stimulation with 1nM-10μM tetracycline (N=4 independent experiments involving technical triplicates). The effective concentration of tetracycline to activate 50% of maximal fluorescence (EC_{50}) per clone is shown. **(B)** Flow cytometry comparisons of tetracycline-stimulated (10μM) TREx-293^{ICAM-1} and TNF-α-stimulated (150ng/ml) HUVECs (mixed-donor pool) for ICAM-1 expression levels. **(C)** Percentages of cells co-expressing CD11b and CD18 for tetracycline-stimulated TREx-293^{MAC-1} (gated within the GFP+ compartment) and PBMCs (N=3 independent experiments). Columns show means and error bars standard deviations. **(D)** Example flow cytometry panels for results shown in (C). Values show average of experimental means from all clones ± standard error. **(E)** Results of flow cytometry experiments as in (C), showing percentages of cells co-expressing CD11a and CD18 for TREx-293^{LFA-1} (gated in single live cells) and PBMCs (N=2-3 independent experiments). **(F)** Example flow cytometry panels for results shown in (E). Values show average of experimental means from all clones ± standard error. All tetracycline stimulations for flow: 10μM.

3.2.2 Adhesion properties of transgenic TREx-293 cells

To determine whether transgenic adhesion molecules were functionally adhesive, adhesion properties between transgenic TREx-293 cells and their respective binding partners were assayed (Figure 20A). Firstly, the propensity of PBMCs to adhere to TREx-293^{ICAM-1} relative to TREx-293 was tested through two assays: in the monolayer-based assay, PBMCs labelled with a green fluorescence dye were co-cultured on TREx-293/TREx-293^{ICAM-1} monolayers and green fluorescence was measured as a proxy for adherent cells. Across three independent experiments (Figure 20B), TREx-293^{ICAM-1} monolayers showed an average 1.93-fold increase (SE=0.27) in PBMC-derived fluorescence compared TREx-293 monolayers. Because fluorescence readout is arbitrary and basal values varied between experiments, results can be analysed either through unpaired t-tests within individual experiments, or one ratio-paired t-test from collective/pooled values; results were significant in both cases (Figure 21). This is corroborated in the suspension-based assay, in which dye-labelled PBMCs were mixed with TREx-293/TREx-293^{ICAM-1} cells in suspension, and multicellular aggregate size and composition was evaluated. Data from this assay are skewed with few large aggregates throwing-off the mean; medians and interquartile ranges (IQR) are therefore presented. In size (Figure 20C), PBMC-TREx-293^{ICAM-1} aggregates (median=42; IQR=57) were 3.8-fold larger than PBMC-TREx-293 (median=11; IQR=11), with high significance ($P<0.0001$, Mann-Whitney test). The proportion of PBMCs (Figure 20D) relative to TREx-293^{ICAM-1} (median=1.16; IQR=0.89) showed a significant ($P<0.0001$, Mann-Whitney test) 1.93-fold increase compared to TREx-293 (median=0.6; IQR=0.81), similar to the monolayer-based assay. These results suggest that integrin-expressing PBMCs adhere to TREx-293^{ICAM-1} cells nearly two-times more readily as to TREx-293, forming PBMC-decorated TREx-293 clusters (Figure 20E).

To assay the adhesion of transgenic integrins, TREx-293/TREx-293^{MAC-1}/TREx-293^{LFA-1} or PBMCs were seeded on ICAM-1-coated plates as described elsewhere (Strazza et al., 2014). The parental TREx-293 control, although lacking endogenous expression of MAC-1/LFA-1-constituent peptides (Figure 17C), unexpectedly adhered to ICAM-1 (Figure 20F). In addition, TREx-293^{MAC-1} showed enhanced adhesion to uncoated surfaces in which bovine serum albumin was used as a blocking agent (Figure 20F-G). However, a marginal increase in TREx-293^{LFA-1} adherence to ICAM-1-coated surfaces was observed (Figure 20F; $P<0.05$, two-way ANOVA). Altogether, the transgenic integrins expressed in HEK-293-based cells are functionally adherent, with TREx-293^{LFA-1} demonstrating slightly improved adhesion to immobilized ICAM-1 compared to TREx-293^{MAC-1}, the latter showing stronger adherence to conventional, uncoated tissue culture surfaces. Lastly, TREx-293 appear to adhere to ICAM-1 via a

MAC-1/LFA-1-independent receptor. This unexpected non-orthogonality of ICAM-1 with TREx-293 cell physiology might enhance homotypic adhesions in TREx-293^{ICAM-1}, which could interfere with desired heterotypic adhesions implicated in hyperuniform patterning.

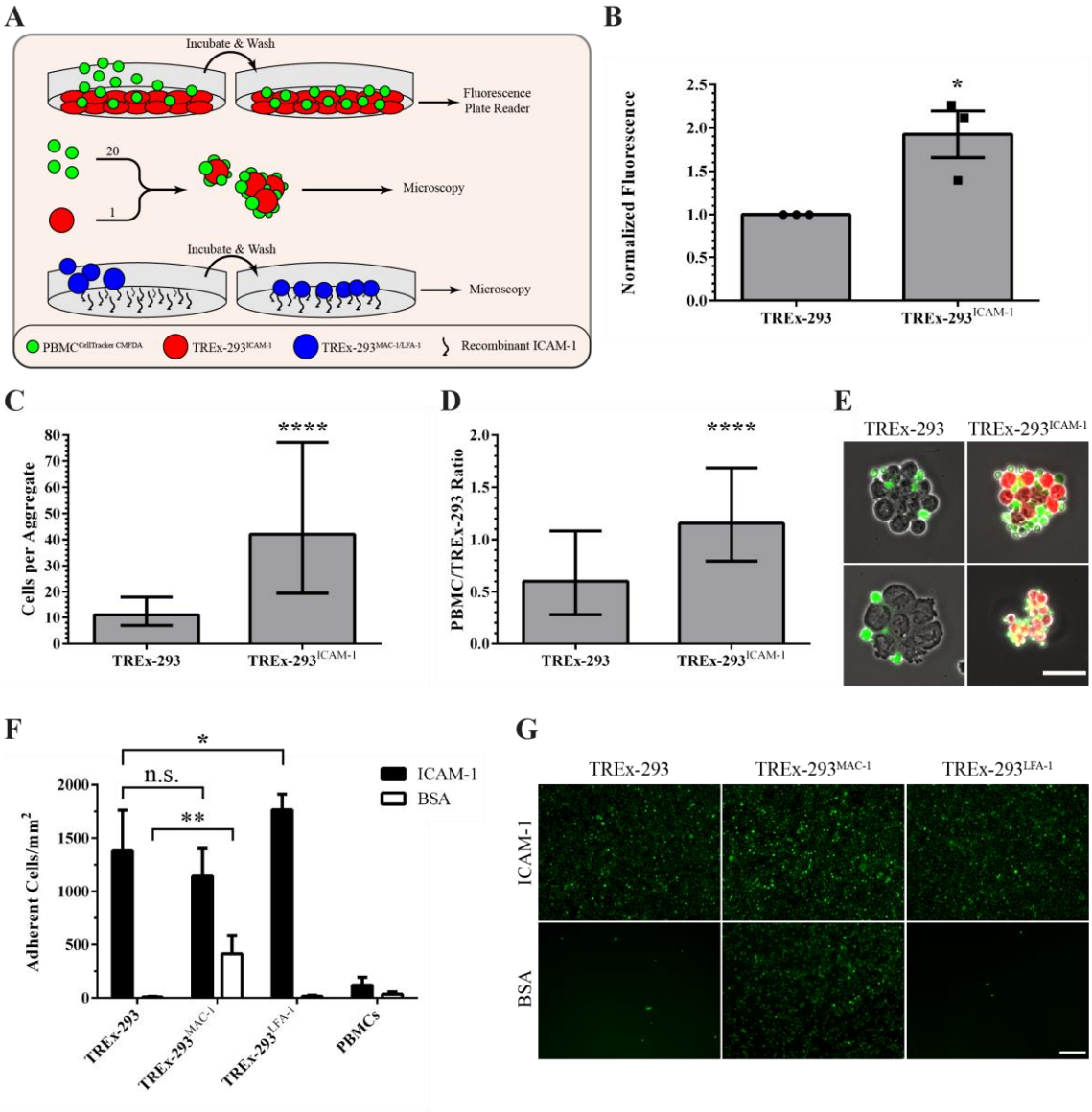

Figure 20. Adhesion Assays for transgenic TREx-293.

(A) Overview of adhesion assays for TREx-293^{ICAM-1} (monolayer assay: top; suspension assay: middle) and TREx-293$^{MAC-1/LFA-1}$ (immobilized ICAM-1: bottom). **(B)** Normalized PBMC-derived fluorescence from monolayer assay. Column shows mean of three independent experimental means (data points), each acquired from quadruplicates with the TREx-293^{ICAM-1} mean normalized to the TREx-293 mean pair-wise. Error bars show standard error. Statistic: see Figure 21. **(C-E)** Suspension-based assay results showing aggregate size **(C)** and ratio between PBMC:TREx-293 cells per aggregate **(D)**. Columns show median and error bars interquartile ranges (90-95 aggregates, three independent experiments). Statistic: Mann-Whitney test. **(E)** Example images of aggregates. Scale bar: 50µm. **(F)** Number of adherent cells per mm^2 for wild-type/transgenic TREx-293s and PBMCs seeded on ICAM-1-coated or uncoated culture surfaces. Columns show means from two independent experiments each capturing triplicate measurements in two different clones. Error bars show 95% confidence intervals. Statistic: two-way ANOVA with Sidak's multiple comparisons. **(G)** Example images from immobilized ICAM-1 adhesion assay shown in (F). Scale bar: 200µm. *, P<0.05; **, P<0.005; ****, P<0.0001.

A

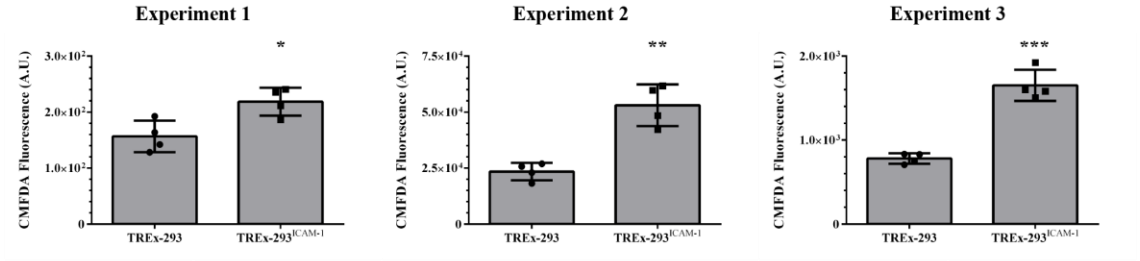

B

Experiment	TREx-293	TREx-293^{ICAM-1}	Unpaired t-test P value
Experiment 1	128.0465	186.5215	0.0164
	163.7585	240.6695	
	142.0505	211.4025	
	192.5875	235.5635	
Experiment 2	18127.39	42180.44	0.0011
	25716.71	61740.80	
	22942.67	59708.16	
	26909.73	48489.46	
Experiment 3	831.0470	1582.3140	0.0001
	707.4610	1598.5840	
	748.5510	1922.8960	
	833.4480	1503.4010	

Ratio paired t-test: **** P<0.0001

C

Experiment	TREx-293	TREx-293^{ICAM-1}	Fold-change
Experiment 1	156.6	218.5	1.4
Experiment 2	23424.0	53030.0	2.3
Experiment 3	780.1	1652.0	2.1

Figure 21. Details for monolayer adhesion assay results shown in Figure 20B.

(A) Breakdown of experimental means plotted in Figure 11B, showing results in each of three independent experiments. Columns show means and standard deviations from quadruplicate values. **(B)** Overview of values and statistics from monolayer adhesion experiments shown in (A). Basal arbitrary fluorescence values drastically differ from experiment to experiment. Results can thus be analysed either as one t-test per experiment or as a collective ratio paired t-test, all demonstrating significance. **(C)** Experimental mean values from (B) showing TREx-293^{ICAM-1}/TREx-293 fold-change. *, P<0.05; **, P<0.005; ***, P<0.001; ****, P<0.0001.

3.2.3 Adhesion transgenes impart cell morphological changes

Given the unexpected adhesion properties of TREx-293, cell morphological characteristics were further interrogated in tetracycline-supplemented cultures. Qualitative observations suggested that tetracycline-stimulated TREx-293^{MAC-1} cells showed a more flattened-out morphology compared to other lines (Figure 17B, Figure 20G). To roughly determine contact areas between different cells and culture surfaces, individual cell peripheries were measured in 24-hour cultures of wild-type and transgenic TREx-293 under tetracycline-free/supplemented conditions. Results from one experiment including multiple clones revealed a 2.2-fold increase ($P<0.05$, one-way ANOVA) in the adherence contact area of TREx-293^{MAC-1} compared to wild-type equivalents under tetracycline supplementation (Figure 22A). Some clone-to-clone variation was evident (Figure 22B), potentially due to variations such as multiple transgene integrations, mutations, or epigenetic alterations. This was validated through additional experiments in which tetracycline-stimulated TREx-293^{MAC-1} showed a significant 2.7-fold contact area increase ($P<0.05$, unpaired one-tail t-test) compared to tetracycline-stimulated wild-type TREx-293, areas of which were comparable to those of tetracycline-free TREx-293^{MAC-1} (Figure 22C). The average adherence contact area per TREx-293^{MAC-1} clone is shown (Figure 22D). Upon close inspection of tetracycline-stimulated TREx-293^{MAC-1} cultures, extensive cell spreading and fan-like membrane structures could be seen in low-density areas, potentially reflecting lamellipodia formation (Figure 22E). Staining TREx-293^{MAC-1} for markers of focal adhesions and lamellipodia, and imaging cells using high-resolution confocal sectioning microscopy, is required to validate this. These observations reveal that transgene activation in TREx-293^{MAC-1} imparts cell morphological changes characterized by extensive cell spreading, which translates to increased contact area between cells and surfaces, and the potential formation of lamellipodia.

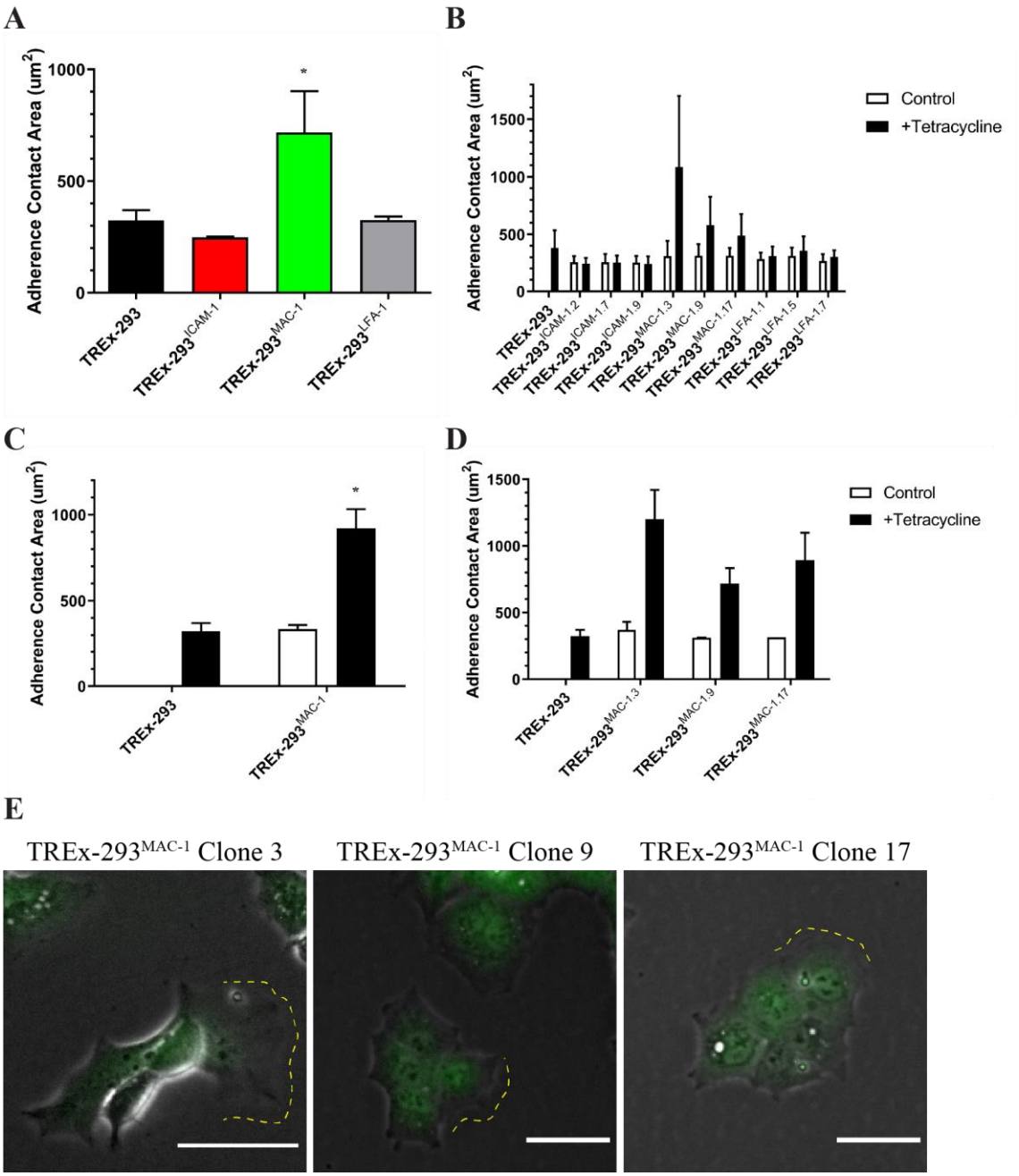

Figure 22. TREx-293^{MAC-1} show increased spreading in adherent cultures.

(A) Contact areas between cells and surfaces, for wild-type/transgenic TREx-293 cells from tetracycline-supplemented cultures (10μM, 24h). Columns show mean of three means, each acquired from a different clone (25-30 cells/clone, one experiment). Error bars show standard error. Statistic: One-way ANOVA with Dunnett's multiple comparisons test. *, P<0.05. **(B)** Breakdown of results shown in (A), depicting contact area means and standard deviations per clone (one experiment). X-axis labels name the cell line followed by clone number. **(C)** Average adherence contact areas of wild-type and TREx-293^{MAC-1} in tetracycline-free/supplemented 24h cultures, from minimum three independent experimental means (25 cells/mean); TREx-293^{MAC-1} summarizes three clones. Error bars show standard error. Statistic: unpaired t-test. *, P<0.05. **(D)** Breakdown of summarized results shown in (C), depicting measurements per clone from minimum three independent experiments (+Tetracycline), or two independent experiments (Control). **(E)** Magnified images of tetracycline-stimulated TREx-293^{MAC-1} clones showing flattened morphology, increased surface area, and potential lamellipodia formation (yellow lines). Scale bar: 50μm.

It was also noticed that the contact surface area of tetracycline-stimulated TREx-293^{ICAM-1} consistently lay at the lower end of wild-type area (Figure 22A). In these contemporary adherence cultures, sporadic three-dimensional clusters showing cyst/colony-like growth could be spotted in tetracycline-supplemented TREx-293^{ICAM-1} samples (Figure 23). This was pronounced for clone 9, which showed extremely high transgene expression (Figure 18A, Figure 19A), and which might correlate to the endogenous ability of TREx-293 cells to adhere to ICAM-1 (Figure 20F). Consequently, transgene activation in TREx-293^{ICAM-1} promotes cyst-like 3D growth in conventional 2D cultures, coupled to restricted contact area, suggesting a change of cell adhesion properties.

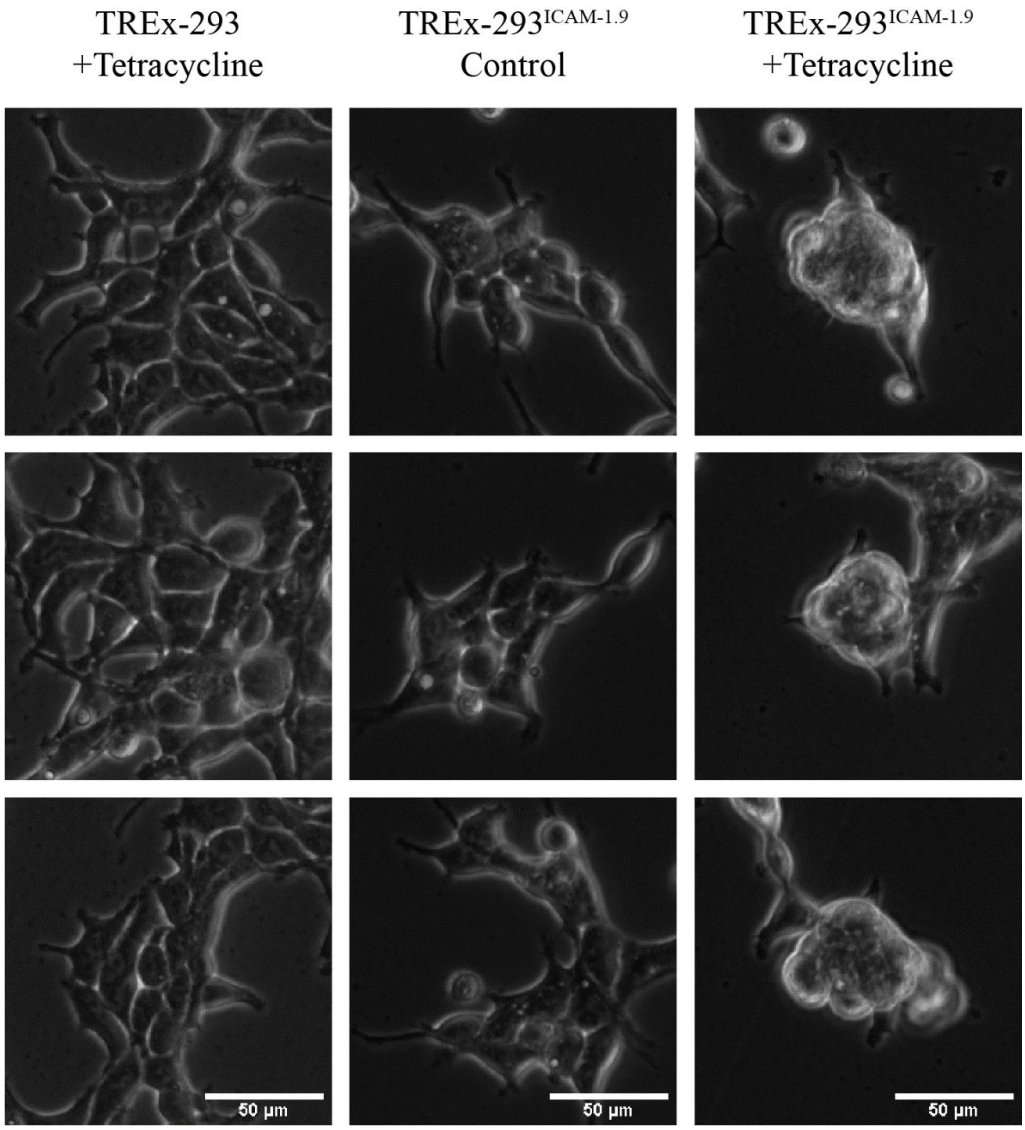

Figure 23. Tetracycline-activated TREx-293^{ICAM-1} demonstrate cyst-like 3D growth.

Example inlets from conventional 24-hour cell-cultures with/without tetracycline, imaged under phase-contrast. Left column: TREx-293 clone 9 with tetracycline supplementation; Middle column: TREx-293^{ICAM-1} without tetracycline supplementation; Right column: TREx-293^{ICAM-1} clone 9 with tetracycline supplementation. Scale bar: 50µm.

Finally, tetracycline-induced transgenic lines were compared in their ability to form spheroids in cell-repellent U-bottom 96-wells. Whereas TREx-293^{ICAM-1} and TREx-293^{LFA-1} aggregate into spheroids, TREx-293^{MAC-1} adhere to cell-repellent surfaces and grow as monolayers (Figure 24A). Spheroid quality was quantitated, assessed and compared among different lines (Figure 24B), based on an ordinal 5-degree ranking system, where '1' describes monolayers and '5' describes compact spheroids (Figure 24C). Hence, by rating the quality of resulting spheroids/aggregates, this ranking system describes the capacity of cells to aggregate into spheroids under 3D culture conditions. The propensity of TREx-293^{MAC-1} in forming 3D aggregates is significantly hindered compared to either TREx-293^{ICAM-1} or TREx-293^{LFA-1} ($P<0.001$, Kruskal-Wallis followed by Dunn's multiple comparisons tests), while no differences are found between TREx-293^{ICAM-1} and TREx-293^{LFA-1} (Figure 24B). These analyses further demonstrate how tetracycline-induced TREx-293^{MAC-1} adhere strongly to culture surfaces, even adhering on low-adhesion formats used for 3D cultures, limiting the capacity of TREx-293^{MAC-1} to form spheroids.

Collectively, these experiments validate the functionality of the transgenes and expressed molecules in TREx-293. Integrin-expressing PBMCs adhere to TREx-293^{ICAM-1} with nearly double the affinity compared to wild-type equivalents. TREx-293^{LFA-1} are marginally more adhesive to immobilized ICAM-1 than wild-types. TREx-293^{MAC-1} adhere strongly to adherent and repellent surfaces, showing flattened morphology and increased cell surface area, possible lamellipodia formation, and preferential 2D growth in 3D conditions. Conversely, TREx-293^{ICAM-1} demonstrate clustered cyst-like 3D growth in adherent 2D culture conditions. This reflects changes TREx-293^{ICAM-1} cell adhesion properties, which might correlate to the unexpected finding that wild-type TREx-293 adhere to ICAM-1, albeit lacking endogenous LFA-1 and MAC-1 expression. These findings suggest that ICAM-1 and MAC-1, when expressed in TREx-293 cells, possess an endogenous capacity to bind uncharacterized ligand/receptors, which might interfere with orthogonal heterotypic adhesions required for hyperuniform pattern formation. Nonetheless, given the establishment of these novel lines and to definitively answer whether hyperuniformity can emerge in this specific context, it is worth testing for pattern formation in co-cultures between TREx-293^{ICAM-1} and TREX-293^{MAC-1} or TREx-293^{LFA-1}.

A

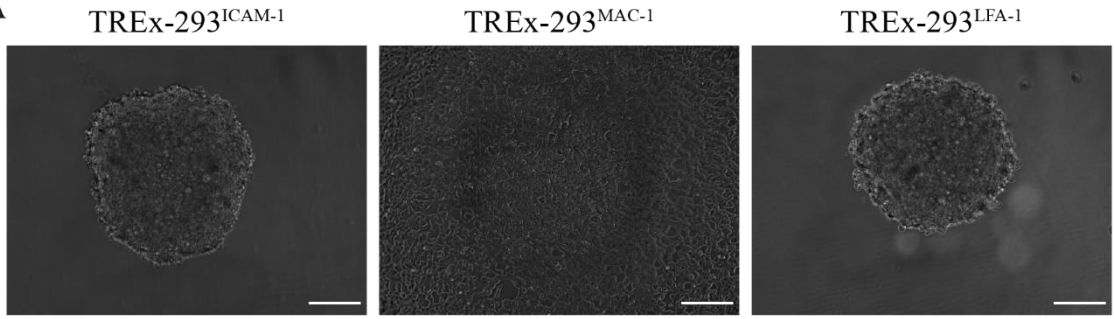

B

3D Rank	Experiment 1					Experiment 2					Median of Ranks (95% C.I.)	Multiple Comparisons Significance
	1	2	3	4	5	1	2	3	4	5		
TREx-293ICAM-1	-	-	1/5	4/5	-	-	-	-	-	4/4	4.0 (4.0, 5.0)	ICAM vs LFA: *n.s.*
TREx-293MAC-1	-	4/5	1/5	-	-	3/5	-	2/5	-	-	2.0 (1.0, 3.0)	MAC vs LFA: ***
TREx-293LFA-1	-	-	1/5	4/5	-	-	-	-	-	5/5	4.5 (4.0, 5.0)	MAC vs ICAM: ***

C

3D Rank	**1**	**2**	**3**	**4**	**5**
Description	Monolayer	Mixture of interspersed cells and clusters showing 3D growth	Attached layers with 3D growth	Loose spheroid; floating aggregate	Compact spheroid; dark areas within aggregate
Example	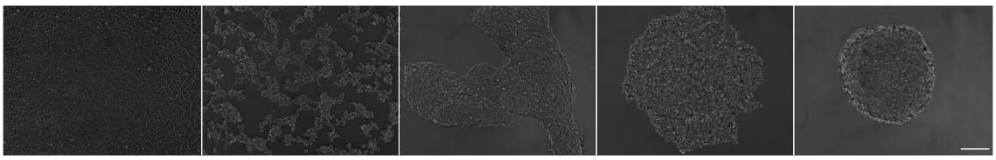				

Figure 24. Spheroid formation capacity of transgenic TREx-293 lines.

(A) Spheroid formation from tetracycline-induced transgenic TREx-293 after 24h culture in low-adhesion 96-well plates. Scale bar: 200µm. **(B)** Summary of 3D-aggregation scores from transgenic TREx-293 cultured as in (A). Statistic: Kruskal-Wallis with Dunn's multiple comparisons test. ***, P<0.001. **(C)** Ordinal 3D ranking system used to describe the spheroid-formation capacity of different samples in (B). For each 3D rank score, the corresponding characterization/description is given, and a phase-contrast example image from a 24-hour culture in low-adhesion/cell-repellent 96-wells, are shown. Scale bar: 200µm.

3.2.4 Evaluation of Hyperuniform Pattern Formation

To evaluate whether hyperuniform distributions emerge in mixed cultures between TREx-293^{ICAM-1} and integrin-expressing TREx-293 cells, different cell types were stimulated with tetracycline for 24 hours and harvested using accutase. TREx-293^{ICAM-1} cells were mixed with either wild-type, MAC-1-expressing, or LFA-1-expressing TREx-293 cells in Ca^{2+}-free culture media supplemented with tetracycline (10μM), high Mg^{2+} (10mM), and low Ca^{2+} (0.5μM) concentrations, in order to favour transgene expression and integrin-ligand binding activity. Heterotypic lines were mixed at unequal ratios (1:6), so that the less-represented cell type (TREx-293^{ICAM-1}) could intermingle with the more-represented counterpart and maximize uniform arrangement. Cells were seeded at near-confluence, and after 24 hours, cell positions were recorded via fluorescence microscopy (Figure 25A). Images were pre-processed so that distributions of the less-represented cell type (TREx-293^{ICAM-1}) were converted to Cartesian coordinates (Figure 25B), which were used to determine whether TREx-293^{ICAM-1} arranged in hyperuniform distributions.

The assessment of uniform distributions can be demonstrated through various metrics (see also Box 2 in the beginning of section 3.1). Hyperuniform distributions are characterized by the absence of homotypic neighbours for any given cell, and minimal variance in the distance among homotypic cells (Jiao et al., 2014; Kram et al., 2010). With regards to the former property, the coordinates of cells of interest (TREx-293^{ICAM-1}) can be expressed relative to any given homotypic cell and repeated for all cells of the field. Results can be visualized as an autocorrelogram or quantitatively expressed as an effective radius, which describes the zone around a cell within which no cells of the same type are found. In this experimental system, and given the diameter of TREx-293 cells (10-15μm), preferential heterotypic neighbours should lead to an effective radius of two cell diameters (20-30μm) for TREx-293^{ICAM-1}, as heterotypic adhesions should lead to TREx-293^{ICAM-1} cells being surrounded by a single TREx-293^{MAC-1}/TREx-293^{LFA-1} layer. Secondly, TREx-293^{ICAM-1} cell positions within the Cartesian field (Figure 25B) can be used to draw Voronoi diagrams, and the distribution of resulting Voronoi polygons can be used to estimate topological order and disorder. The frequency of hexagons (P_6) is considered a metric for topological order (in simulations, a perfectly uniform lattice has P_6=1), whereas the variance of the polygon distribution (μ_2) indicates deviation from hexagonal order and is thus a metric of topological disorder. Lastly, the average distance for the nearest homotypic neighbour for all TREx-293^{ICAM-1} cells of the field can be expressed relative to its standard deviation, assessing the uniformity in cell arrangement though the Regularity Index. These metrics are explicitly detailed in studies of retinal cell arrangement (Kram et al., 2010), and were used to interrogate uniformity of TREx-293^{ICAM-1} cells when co-cultured with different lines (Figure 25).

Across all mixed co-cultures (TREx-293, TREx-293^{MAC-1}, TREx-293^{LFA-1}), TREx-293^{ICAM-1} effective radii were indicative of one cell diameter (plot not shown). TREx-293^{ICAM-1} effective radii were comparable in co-cultures with TREx-293 (μ=9.7μm, σ=0.6μm, n=9) or TREx-293^{LFA-1} (μ=9.8μm, σ=1.0μm, n=9), but slightly larger in TREx-293^{MAC-1} co-cultures (μ=12.6, σ=4.2μm, n=29). This discrepancy likely reflects the larger surface area of TREx-293^{MAC-1} (Figure 22), which might alter the average distance and spacing among TREx-293^{ICAM-1} cells. Topological order (P_6) was comparable across TREx-293 (μ=0.186, σ=0.0206), TREx-293^{MAC-1} (μ=0.189, σ=0.0236), and TREx-293^{LFA-1} (μ=0.2, σ=0.0161). For comparison, these values are below the theoretical order of 100 simulated random distributions (μ=0.293, σ=0.018), and nowhere near the order of green cone photoreceptors (μ=0.454, σ=0.019, n=28) which represent the least ordered photoreceptor of avian retinas (Figure 25C)(Kram et al., 2010). Topological disorder (μ_2) for TREx-293 (μ=1.8, σ=0.0869) and TREx-293^{LFA-1} (μ=1.74, σ=0.116) was comparable to random distributions (μ=1.8, σ=0.1), whereas for TREx-293^{MAC-1} co-cultures, disorder was slightly lower (μ=1.63, σ=0.145) compared to the TREx-293 wild-type control ($P<0.01$, Kruskal-Wallis with Dunn's multiple comparisons test). This slight reduction of disorder might represent increased confluence and tighter packing that slightly affect overall cell arrangement and not specifically TREx-293^{ICAM-1} organization (P_6), as a result of the increased surface area covered by TREx-293^{MAC-1} (Figure 22A and C). Again, disorder was nowhere near the degree observed in green cone photoreceptors (μ=0.734, σ=0.046) (Figure 25D). This is confirmed when TREx-293^{ICAM-1} uniformity is assessed via the regularity index, which shows no difference across TREx-293 (μ=2.18, σ=0.337), TREx-293^{MAC-1} (μ=2.11, σ=0.261), and TREx-293^{LFA-1} (μ=2.14, σ=0.154) co-cultures. These values are closer to the regularity of random distributions (μ=1.9, σ N/A) than the regularity of violet cone photoreceptors (μ=6.4, σ=0.7, n=28), which represent the least frequent and regular photoreceptors in the avian retina (Figure 25E) (Kram et al., 2010). Therefore, other than a slight reduction of disorder (likely attributed to the increased surface area of TREx-293^{MAC-1} affecting overall cell packing), there are no differences in the topological metrics of TREx-293^{ICAM-1} when co-cultured with TREx-293, TREx-293^{MAC-1}, or TREx-293^{LFA-1}. TREx-293^{ICAM-1} distributions from these cultures are near random and show no comparability to results from hyperuniform distributions.

These analyses demonstrate that hyperuniform patterning does not emerge in TREx-293^{ICAM-1} cells co-cultured with TREx-293 expressing MAC-1 or LFA-1, contrary to what was expected in the hypothesis. The lack of hyperuniform pattern formation might be attributed to the non-orthogonality observed in this specific context (i.e. TREx-293 endogenously adhering to ICAM-1), rather than the general strategy employed to engineer the pattern (simulation of custom heterotypic adhesions predicts patterning).

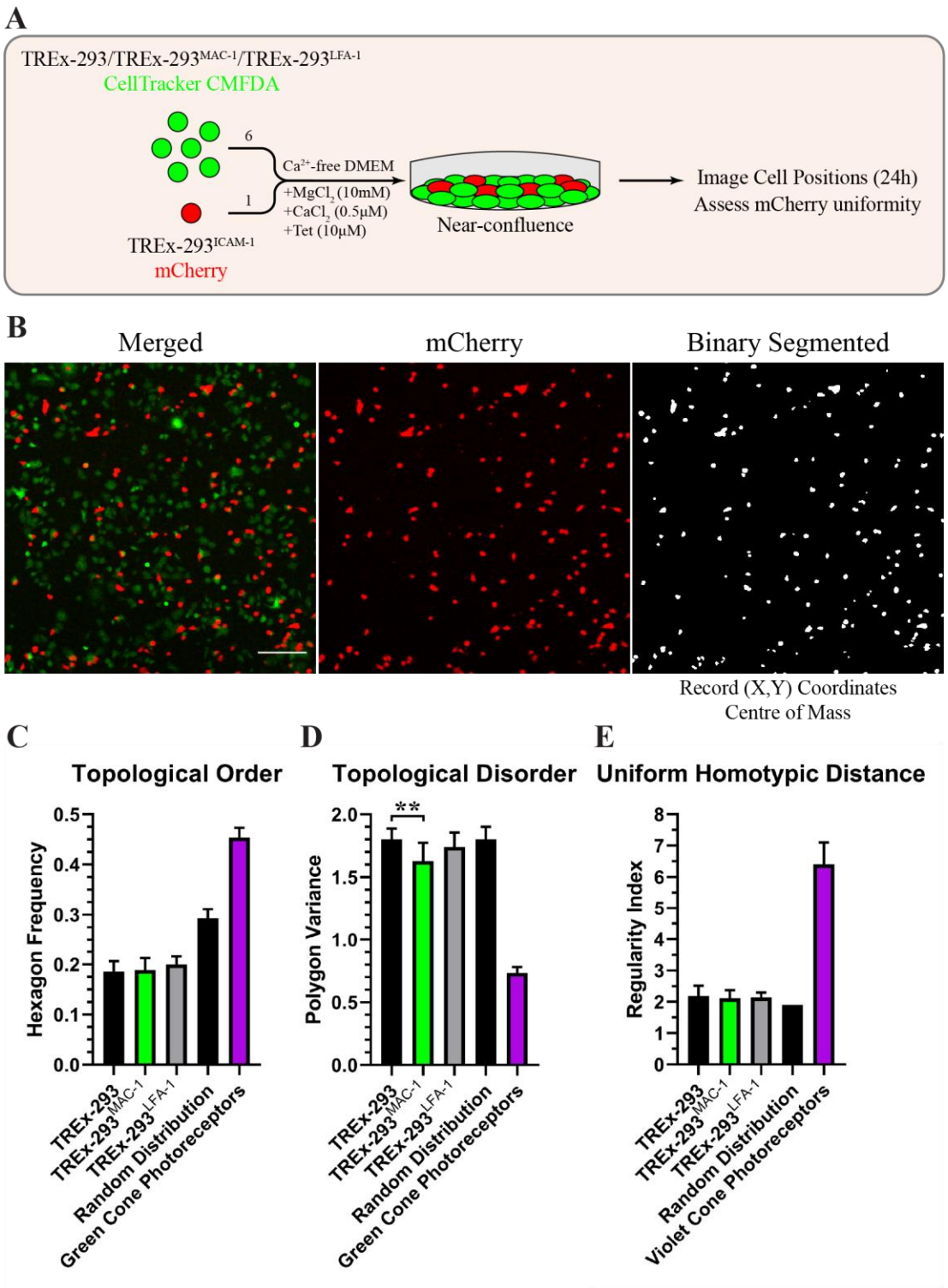

Figure 25. Evaluation of hyperuniform distributions in TREx-293 co-cultures.

(A) Overview of experimental setup. Tetracycline-stimulated TREx^{ICAM-1} are mixed with tetracycline-supplemented, CellTracker-labelled TREx-293/TREx-293^{MAC-1}/TREx-293^{LFA-1} in a 1:6 ratio. Cells are seeded at near confluence in the presence of tetracycline, high Mg^{2+}, and low Ca^{2+} to promote integrin expression and activity, and imaged after 24h. **(B)** Pre-processing uses the mCherry channel from co-cultures to acquire TREx-293^{ICAM-1} cell position coordinates. Scale bar: 200µm. **(C-E)** Hyperuniformity metrics of topological order **(C)**, topological disorder **(D)**, and uniform distances among TREx-293^{ICAM-1} cells **(D)** in mixed co-cultures. These metrics, and values for random distributions and cone photoreceptor control samples, are from (Kram et al., 2010). Statistic: Kruskal-Wallis test with Dunn's multiple comparisons. **, P<0.005.

3.2.5 Discussion

Synthetic biology has allowed the generation of genetic devices that impart self-organization or cell state segregation in naïve mammalian cell lines (Cachat et al., 2016; Matsuda et al., 2015; Morsut et al., 2016; Sekine et al., 2018; Toda et al., 2018). To expand the pattern formation toolbox, I explored whether heterotypic adhesions between distinct TREx-293 cell lines, engineered to express either an integrin receptor (MAC-1 or LFA-1) or the cognate ligand (ICAM-1), suffice to drive hyperuniform cell distributions akin to those observed in the avian retina (Jiao et al., 2014; Kram et al., 2010).

To address this hypothesis, human genes encoding individual peptides (*CD11a, CD11b, CD18, CD54*) were cloned from primary peripheral blood mononuclear cells (PBMCs) or synthetic DNA fragments (*CD54*), and assembled into tetracycline-inducible mammalian expression cassettes based on the TetR/TetO system. The primary hurdle during this DNA engineering step was the inconsistency regarding the size and composition of *pTREx* vector backbones that were acquired from pre-established constructs. To tackle this issue, novel plasmids were de novo generated in which transgene expression cassettes were joined with a puromycin resistance marker (Kauts et al., 2018), and together flanked with *ROSA26* homology arms. Together with a *pSpCas9-eGFP-gRNA* plasmid that cleaves the *ROSA26* locus, these constructs were used to insert transgenic modules into the *ROSA26* locus via CRISPR genome editing technology. The strategy employed led to the successful integration of transgene cassettes into the *ROSA26* locus, as revealed by PCR genotype. Transgenic TREx-293 clones generated through this approach demonstrate robust transgene expression and less clone-to-clone variation compared to a random integration-based transgenesis method. As such, the constructs generated in this thesis (section 3.1.6) might provide useful tools and a platform for CRISPR-based knock-in of desired genetic elements in the human *ROSA26* locus, for future genome engineering purposes.

Considering the nature of transgenic systems, this work has provided a characterization of transgene inducibility and expression strength, in the context of tetracycline driving CMV-based expression from the *ROSA26* locus through a TetR/TetO system. This work has shown that tetracycline induces transgene expression with nanomolar efficacy (EC_{50} roughly 50-100nM), reaching a plateau at micromolar amounts. At 24h post-induction, transgene expression reaches very high protein levels when transgenes are compared to reference cells physiologically expressing equivalent peptides based on flow cytometry. This work provides a characterization of the TetR/TetO system, at least for the parameters and in the context described, which can be generally useful for future work that builds on a similar genetic engineering blueprint (section 3.2.1).

Adhesion assays used to validate the functionality of transgenic cell adhesion molecules unearthed several unexpected findings. Although TREx-293 cells express neither of MAC-1 or LFA-1, they adhere to immobilized recombinant human ICAM-1. This could be explained if TREx-293 cells express a MAC-1/LFA-1-independent receptor for ICAM-1. Non-integrin ICAM-1 receptors have been described, such as CD44 that functions as a receptor for hyaluronan and ICAM-1 (Apaolaza et al., 2014; Uff et al., 1995), or MUC-1 that does not appear ubiquitously expressed in HEK-293 cells (Bernier et al., 2011; Shen et al., 2008). Additionally, TREx-293^{ICAM-1} cells and especially clones with high transgene expression (clone 9), show reduced cell surface area and demonstrate cluster/cyst-like growth under 2D adherence conditions when stimulated with tetracycline. It is plausible than an *ICAM-1* transgene dose-dependent effect enhances homotypic adhesion to the point of self-aggregation and 3D growth. It would therefore be interesting to investigate the molecular components underlying this adhesion, such as whether it occurs through ICAM-1 autonomous homotypic adhesion, ICAM-1-activated pathways triggering expression of ICAM-1 receptors, or LFA-1/MAC-1-independent receptors endogenously expressed in TREx-293 cells. Given the metabolic burden of transgenes to host cells, and the role of ICAM-1 in inflammation, eliminating alternatives (metabolic toxicity; pathway activation; pro-inflammatory state) through RNA-seq/Mass-spec is required to delineate this.

TREx-293^{MAC-1} cells show enhanced adhesion to conventional culture surfaces. This leads to extensive cell spreading and a flattened morphology, even adhering and forming monolayers in low-adhesion U-shaped wells that are used to form 3D aggregates and spheroids. Given the promiscuous ligand-repertoire of MAC-1 (Table 8 and references (Arnaout, 2016; Li et al., 2018)), TREx-293^{MAC-1} cells might strongly adhere to serum proteins that act as surface coatings in vitro (e.g. fibronectin, fibrinogen, or matrix proteins). Combined with the fact that TREx-293^{MAC-1} cells do not show enhanced adherence to ICAM-1 compared to wild-types, this means that in TREx-293^{MAC-1}-TREx-293^{ICAM-1} co-cultures, the plate/surface acts as a competitive inhibitor for MAC-1-ICAM-1 interactions. On that note, TREx-293^{LFA-1} cells showed a marginal (if not false-positive) increase in adherence to ICAM-1 and no overt morphological changes. Regardless, all TREx-293/TREx-293^{MAC-1}/TREx-293^{LFA-1} lines yielded similar results in co-culture experiments with TREx-293^{ICAM-1}, in which TREx-293^{ICAM-1} distributions were comparable and random. This suggests that the main issue is the unexpected adherence of TREx-293 cells to ICAM-1, which might translate into homotypic adhesion and aggregation in TREx-293^{ICAM-1} cells. This enhanced homotypic adhesion might increase the thermodynamic energy required to dismantle TREx-293^{ICAM-1} clusters during cell junction reorganization, making intermingling with TREx-293^{MAC-1}/TREx-293^{LFA-1} unfavourable.

Pattern formation capacity in co-cultures demonstrated that TREx-293^{ICAM-1} cells, when co-cultured with either TREx-293^{MAC-1} or TREx-293^{LFA-1} cells, did not adopt characteristics of hyperuniform distributions. Results from these co-cultures were comparable to those of wild-type TREx-293-TREx-293^{ICAM-1} co-cultures. The analysis of TREx-293^{ICAM-1} distributions was performed using the metrics employed originally to deduce hyperuniform distributions in the avian retina, and our results were compared to cone photoreceptors and simulated random distributions (Kram et al., 2010). Across all metric analyses and for all co-cultures reported herein, resulting values lay close to those from random distributions and never reached those reported for photoreceptors. The only oddity in these analyses was that topological order (P_6) in TREx-293^{ICAM-1} was always lower compared to theoretical random distributions. It is uncertain whether that is due to enhanced TREx-293^{ICAM-1} clustering compared to random distributions, or an artefact of simulated/theoretical randomness being more ordered compared to actual/empirical randomness. Regardless, this section conclusively answers Hypothesis I, showing that although LFA-1/MAC-1/ICAM-1 proteins are normally expressed and functional, they cannot drive hyperuniform cell distributions in HEK-293-based cells.

It should be noted that although these perplexing findings have nullified the original aim of the section, they are by no means useless. On the contrary, they open doors to other research areas. Firstly, given that ICAM-1 and MAC-1 induce morphological changes in TREx-293 cells, respective lines can be incorporated into the morphogenetic toolbox, which describes a set of genetic devices that impart morphogenetic changes in cells in vitro for purposes of synthetic morphology (Cachat et al., 2014). On that note, it would be interesting to subject TREx-293^{MAC-1} cells to migration assays and assess whether they demonstrate increased durotaxis or haptotaxis. Secondly, the unexpected finding of TREx-293 cell adherence to ICAM-1 through a MAC-1/LFA-1-independent endogenous receptor can be further investigated to discover novel ICAM-1 receptor(s), or mechanics through which ICAM-1 relates to cell adhesion. Thirdly, the transgenes established and assembled can be used as the basis for synthetic biology-inspired customizations. This follows the spirit of the SynNotch system, in which extracellular and intracellular Notch domains are replaced to trigger user-defined cell responses based on custom signal recognition (Morsut et al., 2016). Analogously, CD11a/CD11b ectodomains and ICAM-1 epitopes can be replaced so that desirable ligands (e.g. antigens) can be orthogonally bound by specified receptors (e.g. antigen-specific nanobodies), defining strong, custom heterophilic interactions while maintaining adhesion to the actin cytoskeleton. It would be interesting to explore whether this concept of “Synthegrins” can be materialized. However, none of the above are relevant to the scope of this thesis.

3.3 Coupling signal production to a self-organizing system

Engineering synthetic patterning systems provides the opportunity to model and control self-organization and morphogenesis. Multiple genetic devices driving pattern formation have been engineered in bacterial and mammalian cells, and although signalling events have been incorporated to control self-organization within those synthetic systems (covered in section 1.3.2), none of them have been engineered to provide signalling to natural biological systems. This latter modification could allow spatiotemporal control in the production of user-defined signals, such that signalling ligands emanating from self-organized multicellular structures could translate into new signalling response patterns in recipient cells. In embryonic development, polarized signal production from developmental organizers leads to the formation of morphogen gradients that pattern cell fate decisions in space. Being able to recreate or approximate such polarized, spatiotemporally controlled signal production could have interesting applications in contexts of improving self-organization in stem cell differentiations.

Theoretically, to achieve graduated signalling from synthetic patterning systems, there are certain factors and assumptions that need to be met. Firstly, the signalling ligand needs to be successfully produced and secreted in its biologically active form. For this, the cell host needs to endogenously express the molecular components involved in activity of the ligand, in matters of post-translational modifications, trafficking and secretion. Otherwise, these components will need to be introduced in the host together with the ligand. Secondly, the host should not endogenously express the ligand of choice, and preferably, no ligands of the same family. Thirdly, when the ligand of choice is introduced to a pattern formation system, it should not affect the system's ability to self-organize; i.e. the signalling ligand added during the "second-layer" engineering should be orthogonal and not cross-talk with any signalling axes regulating pattern formation in the "first-layer" of genetic engineering. Fourthly, in order to achieve localized and patterned signal emission, production and secretion of the ligand needs to be active only in topologically distinct domains of the pattern. This leads to the fifth assumption, which is that the diffusion rate of the signalling ligand should not exceed pattern periodicity. If this condition is not met, the ligand would freely diffuse beyond the spatial distribution and organization dictated by the patterning system. Lastly, the ligand needs to be involved in the regulation of biologically meaningful events, such as developmental and regenerative fate-decisions that are recapitulated during stem cell differentiation. The choice for expressing a signalling ligand from a self-organizing system thus depends on meeting these six criteria.

3.3.1 Wnt ligands show limited diffusion and regulate fate decisions

One family of molecules that fulfil these criteria are ligands of the Wnt/β-catenin pathway. The mechanics of the pathway have been extensively reviewed (MacDonald et al., 2009); in brief, the transcription factor β-catenin is constantly phosphorylated and tagged for degradation by the Axin multi-kinase complex (Axin/APC/GSK3/CK1). Wnt ligands bind to Frizzled and Lrp5/6 co-receptors, forming a synergistic complex that recruits the adaptor Dishevelled to Frizzled, and Axin and its kinases to Lrp5/6. It is thought that initiation of Wnt signalling promotes recruitment of Dishevelled to Frizzled, which in turn recruits the kinase-decorated Axin to Lrp5/6, phosphorylation of the latter at intracellular PPP(S/T)P motifs by GSK3 and CK1 leading to further Axin recruitment (Cong et al., 2004; Tamai et al., 2004; X. Zeng et al., 2008). These events preclude β-catenin phosphorylation-dependent degradation, allowing β-catenin to shuttle into the nucleus where it regulates gene expression through multiple binding-partners, such as TCF that bind to TCF/LEF DNA motifs (Figure 26). There are numerous proteins that regulate Wnt/β-catenin signalling at distinct levels, such as Lrp5/6 sequestration (inhibitors Dickkopf and SOST), Wnt sequestration (sFRPs and WIFs), intracellular Frizzled retention (Shisha), or reinforcement of Wnt/Frizzled/Lrp signalling (R-spondin). Wnt/Frizzled/Lrp complexes form clusters and can signal either from the cell surface, or from endocytosed vesicles (signalosomes), which likely possess distinct properties (reviewed in (MacDonald et al., 2009)).

Wnt ligands are relatively small glycoproteins (35-45kDa) that experience post-translational modifications which turn them highly lipophilic. Mouse Wnt3a biochemical purification requires addition of detergent (CHAPS or Triton X-114), as Wnt3a dissolves into the detergent phase. This hydrophobicity is caused by addition of palmitic acid at cysteine77, which is also imperative for the high activity (but not secretion) of Wnt3a in stabilizing β-catenin in as little as 10ng/ml or 0.3nM (Komekado et al., 2007; Willert et al., 2003). This cysteine palmitoylation is critical for association of Wnt3a with Frizzled/Lrp co-receptors (Cong et al., 2004). Another hydrophobic palmitoleic acid group is added at Serine209 by the endoplasmic reticulum-bound O-acyltransferase Porcupine, which is required for Wnt3a secretion (Takada et al., 2006). This latter acylation allows Wnt3a to bind its transporter, Wntless (also known as Evi or GPR177; (Bänziger et al., 2006; Bartscherer et al., 2006)), which mediates Wnt3a exocytosis via the secretory pathway (Coombs et al., 2010; Gao & Hannoush, 2014). Additionally, glycosylation of Asparagine87 and Asparagine298 both contribute to Wnt3a secretion and its ability to trigger Wnt/β-catenin signalling responses (Komekado et al., 2007). These lipophilic modifications presumably promote association of Wnt with biological membranes and extracellular matrix components, thereby restricting Wnt diffusion.

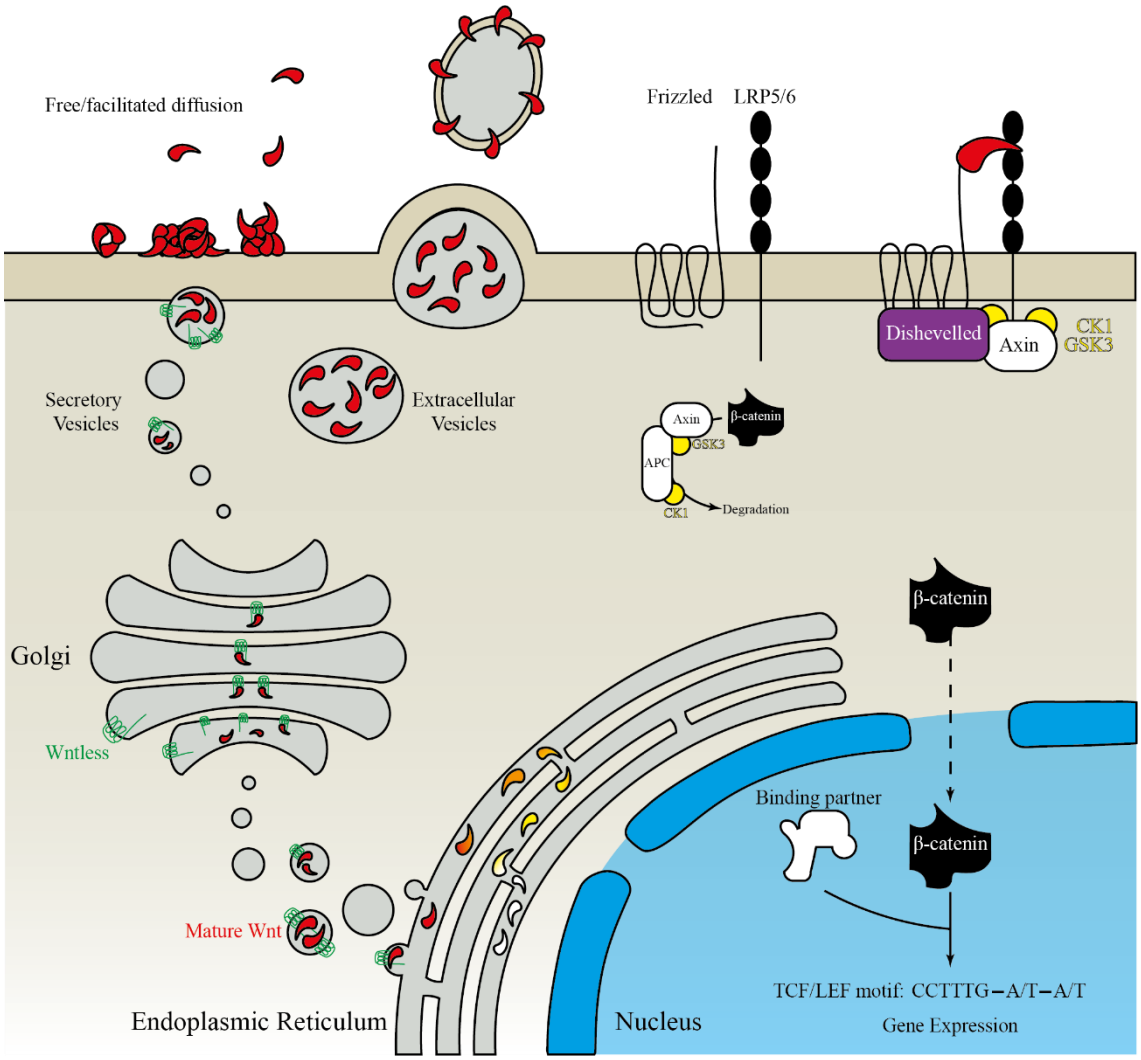

Figure 26. Overview of Wnt secretion and β-catenin activation.

Newly-translated immature Wnt (white teardrop) enters the endoplasmic reticulum, where it undergoes glycosylation (Asparagine87, Asparagine298) and acylation (palmitic acid at Cysteine77, palmitoleic acid at Serine209) modifications to yield mature, lipophilic, biologically active Wnt (red teardrop). Mature Wnt associates with its secretory chaperone Wntless/Evi/Gpr177 (green) and is transferred to the Golgi apparatus for secretion. Wnt is secreted through secretory vesicles, where it is largely retained near the plasma membrane and is largely present as multimers. Free diffusion is modulated through extracellular Wnt-binding partners (see text). Wnt can also be secreted as extracellular vesicles, including liposomes or CD63+ exosomes. Activation of the Wnt/β-catenin pathway occurs when Wnt forms a complex with the receptors Frizzled and LRP5/6, which recruit Dishevelled intracellularly and sequester the Axin complex. Because the Axin complex continuously phosphorylates β-catenin, tagging it for degradation, Axin sequestration through Wnt signalling allows β-catenin to enter the nucleus and drive gene expression changes along with various binding partners. Adapted from (MacDonald et al., 2009) and various references in text.

Analytical biochemistry and fluorescence correlation spectroscopy analyses have provided insights into the mechanics of Wnt diffusion (Takada et al., 2018). Wnt3a molecules aggregate into multimers and can be divided into two types: fast-migrating (19%, diffusing at 12.6±8.8μm^2/sec) and slow-migrating (81%, diffusing at 0.09±0.08μm^2/sec). Using analytical ultracentrifugation, the number of Wnt3a molecules per aggregate for different diffusion rates could be approximated, showing that slow-migrating aggregates consist of a diverse number of molecules per multimer. Importantly, Wnt3a molecules also aggregate in vivo, as demonstrated through fluorescence cross-correlation analyses of fluorescently tagged Wnt3a variants co-expressed in *Xenopus* embryos. Co-expression of sFRP2 reduces the frequency of multimers showing high Wnt3a numbers, while extending the area over which Wnt3a spreads (Takada et al., 2018). These findings suggest that Wnt3a has an autonomous propensity to self-aggregate once secreted, becoming confined to the production source, and that co-expression of Wnt-binding partners can modify Wnt diffusion in a ligand, context, and tissue-dependent manner. Given that multimers showing low numbers of Wnt3a molecules were unaddressed, the study highlights the fact that there are many Wnt-binding factors that remain unexplored.

Because Wnt ligands are usually found in contexts where binding partners increase their diffusion rates, in vivo examples of limited Wnt diffusion are scarce. In zebrafish, Wnt8 and Evi accumulate at filopodia initiation sites (Stanganello et al., 2015). Upon Cdc42-dependent actin polymerization, thin filopodia protrusions that average 17.0μm in length carry Wnt8/Evi puncta to extend Wnt distribution by a mode of 20μm. Inhibition of actin polymerization and filopodia formation, either through Cdc42 loss-of-function mutations or application of actin depolymerisation compounds, reduces activation of a TCF/Wnt reporter assay (Stanganello et al., 2015). While this suggests that filopodia promote the relay of otherwise non-diffusive Wnt8, it is difficult to exclude that the treatments mentioned do not interfere with processes implicated in Wnt diffusion, such as secretion. However, the study does show the filopodia relay Wnt ligands over a short radius of 1-3 cells. Accordingly, in intestinal organoid crypts where Paneth niche cells maintain ISCs via Wnt and Notch, the spread of Wnt ligands covers one to two cell widths (Farin et al., 2016). These contexts suggest that Wnt spread is limited and can be assisted through cell-autonomous events that influence actin remodelling and plasma membrane dynamics.

Extracellular Wnt-binding partners heavily modulate Wnt diffusion. In *Xenopus* gastrula-stage embryos, Wnt8 forms a long (>500μm) diffusion gradient throughout which Wnt8 protein docks to N-sulfo (but not N-acetyl) heparan sulfate proteoglycan nanoclusters. These clusters also recruit Lrp6 and can be seen both on plasma

membrane and intracellularly, suggesting that N-sulfo heparan sulfate proteoglycans act as cell-surface scaffolds for the assembly of Wnt signalling complexes and signalosomes (Mii et al., 2017). *Xenopus* Wnt ligand autonomous diffusion is restricted close to source cells, but extracellular soluble Frizzled-related proteins (sFRPs, such as Frzb and Cres) are highly diffusive and act as Wnt-binding partners, thus expanding Wnt diffusion (Mii & Taira, 2009). These sFRPs extend the diffusion of Wnt ligands while inhibiting Frizzled/Lrp-dependent Wnt/β-catenin signalling. It has been suggested that sFRPs preclude Wnts from associating with N-sulfo heparan sulfate proteoglycans and associated Frizzled/Lrp receptors, thus limiting the assembly and endocytosis of signalosomes (Mii et al., 2017). Some sFRP-Wnt pairs show biphasic relationships when expressed in different cells, whereby Wnt/β-catenin signalling is inhibited at high sFRP concentrations, but augmented at low sFRP concentrations (Mii & Taira, 2009). This concentration-dependent response might reflect transient interactions; high sFRP concentrations could demonstrate co-operative binding and ensure ligand retention, whereas low sFRP concentrations could allow transiently detached Wnt to interact with signalling complexes. There are other extracellular Wnt-binding proteins that might function analogous to sFRPs, such as the *Drosophila* lipocalin protein Swim (Mulligan et al., 2012), Wnt inhibitory factor 1 (Malinauskas et al., 2011), and the serum protein afamin (Takada et al., 2018). It is possible that Wnt diffusion is under dual control by heparan sulfate proteoglycans entrapping Wnt ligands (or relaying them over a very short range), free Wnt-binding expanders that facilitate long-scale diffusion, and composite interactions between the two.

In *Drosophila* wing imaginal discs, Wg (the *Drosophila* Wnt1 homologue) forms a narrow expression stripe along the dorsovental boundary. Wg is strongly expressed along the midline of the stripe at a width of 3-5 cells, and gradually diffuses laterally for about 10-20 cells at each side. Replacing wild-type Wg with a membrane-tethered version led to no overt defects in wing patterning, although protein localization was restricted (Alexandre et al., 2014). This finding could be explained from the fact that Wg has been shown to associate with lipophorin-containing liposomes, which promote Wg diffusion (Panáková et al., 2005). As such, membrane-tethered Wg might have successfully diffused through liposomes, compensating for limited free-protein diffusion in wing development. Wnt proteins have also been detected in CD63+ exosomes from fly, mouse and human cells, and these exosomes can faithfully activate β-catenin-dependent responses (Działo et al., 2019; Gross et al., 2012). These findings illustrate that long-distance diffusion can emerge through extracellular vesicles, which remains a largely undefined topic.

There appears to be a lack of consensus in the upper limit of Wnt diffusion. Wnt8 diffusion range in the *Xenopus* gastrula extends well beyond 500μm (Mii et al., 2017). In zebrafish embryos, polarized β-catenin responses appear to be cover a range between 300-350μm (Akieda et al., 2019). In mESC-derived aggregates, a Wnt-responsive element is activated over a range around 200μm (Takata et al., 2017). In *C. elegans*, the fluorescently tagged Wnt orthologue extends about 200-230μm from producer cells (Pani & Goldstein, 2018). These differences could reflect Wnt/β-catenin activation from previous developmental events, context-dependent regulation of Wnt diffusion, or/and evolutionary developmental adaptations in the modulation of Wnt diffusion. This potential modularity, together with the biochemically-defined limited autonomous diffusion rate, makes Wnt ligands suitable candidates for engineering within synthetic patterning systems.

Lastly, Wnt/β-catenin is pivotal in numerous developmental contexts, and stable supply of stable Wnt ligands is of particular interest to stem cell applications. Some of these include stem cell maintenance and self-renewal, as in mESCs (Berge et al., 2011) and ISCs (Farin et al., 2016; Sato et al., 2011), or differentiation in NPCs (Karner et al., 2011; Park et al., 2012). Throughout development, Wnts lie at the heart of diverse inductive processes, such as primitive streak formation during gastrulation (see section 1.2.2) and kidney nephrogenesis (see section 1.2.3). Due to their hydrophobic nature, the purification and storage of Wnts requires the use of detergent (Willert et al., 2003). When diluted into the culture medium, detergent levels are either too low to maintain Wnt activity over several hours, or remain high enough to destabilize biological membranes. This can be circumvented by the use of Wnt3a-conditioned serum-containing media, or coupling detergent-purified Wnt3a to in vitro-synthesized liposomes (80-85% efficiency) for serum-free formulations, which removes detergent and serum contaminants while maintaining long-term Wnt3a stability and biological activity (Tuÿsüz et al., 2017). Wnt3a liposomes efficiently promote mESC self-renewal, as well as formation and maintenance of intestinal and liver organoids (Tuÿsüz et al., 2017). In contrast, an adherence-based approach whereby WNT3A is covalently linked to aldehyde surfaces, while upregulating Wnt/β-catenin activation and related responses in stem cells (such as ESC self-renewal and osteogenic differentiation of mesenchymal stem cells), it does so heterogeneously and with limited magnitude, probably reflecting poor WNT3A stability (Lowndes et al., 2016). The importance of Wnt ligands in developmental contexts, their widespread applications in stem cell research, combined with the challenges of biochemical purification and stabilization, consolidate incentives to engineer Wnt ligand expression from cell-based, self-organizing systems.

3.3.2 Choice of Wnt ligand and patterning system

Given that Wnt ligands meet the criteria of low diffusion and meaningful biological impact, they form suitable candidates for expression from synthetic patterning systems. There are limited synthetic patterning systems established in mammalian cells, and most of them depend on signalling events for self-organization (see section 1.3.2). To completely eliminate any possibility of signal cross-talk, and to start from a basic and robust system, the phase-separation patterning system was chosen as the platform for Wnt introduction (Cachat et al., 2016). Phase-separation patterning occurs between two different (heterotypic) cell lines, each expressing different cadherins (*Cdh1*, *Cdh3*) in a tetracycline-inducible manner. As a consequence of cadherins mediating homophilic adhesions and different surface tensions, cells expressing the same cadherin self-aggregate; when the two cell lines are co-cultured, they segregate into patch-like phase-separation patterns. Because the patterning system depends on two distinct cell lines, Wnt ligand(s) can be distributed from one topological domain of the pattern by conveniently choosing which line the respective gene(s) will be engineered into. Importantly, pattern periodicity is easily controlled by changing the mixing ratios of the two lines prior to co-culture (Cachat et al., 2016). This system is based on HEK-293 cells, which have been routinely used for Wnt-overexpression due to their high transfection efficiency and absence of endogenous Wnt production as judged from conditioned media. However, the efficiency of HEK-293 in secretion and post-translational modifications of Wnt ligands has not been characterized. To minimize the risk of insufficient secretion, the mouse Wnt3a ligand was chosen as a candidate, as it is arguably the most characterized Wnt ligand in terms of biochemistry and biological effects, and due to its efficient secretion (MacDonald et al., 2009).

The following sections present a second round/layer of genetic engineering of TREx-293^{Cdh3}, through which production and secretion of functional Wnt3a is added to TREx-293^{Cdh3} cells. Given that TREx-293^{Cdh3} cells self-organize with TREx-293^{Cdh1} in phase-separation patterns, this simple modification has the capacity to allow the production of a developmentally important signalling ligand from an organized multicellular population. Considering the aforementioned low diffusion rate of Wnt ligands, the distribution of Wnt3a should be restricted close to TREx-293^{Cdh3} producer cells (TREx-293$^{Cdh3\text{-}Wnt3a}$). Hence, if TREx-293$^{Cdh3\text{-}Wnt3a}$ cells retain self-organization capacity with TREx-293^{Cdh1} cells, the patterned distribution of TREx-293^{Cdh3} cells should translate into an ordered distribution of signalling. This would convert the patterning system into a self-organizing signalling platform, allowing the spatially localized and organized activation of the Wnt/β-catenin pathway in recipient cells. By achieving this, it might be possible to control aspects of self-organization in stem cell fate decisions.

Hypothesis II

Wnt3a expression from HEK-293-based cells can exert spatially localized Wnt/β-catenin responses, when secreted in a phase-separation pattern.

3.3.3 Establishment of TREx-293$^{Cdh3\text{-}Wnt3a}$ clonal lines

Establishing a self-organized platform that emits signals with spatial control can be achieved through the modification of existing mammalian patterning systems. It has been reported that enforced expression of different cadherins in mammalian cells (*Cdh1; Cdh3*) drives formation of phase-separation patterns via differential adhesions (Cachat et al., 2016). To translate the arrangement of cell distributions into a pattern in signalling, one component of the phase-separation pattern was modified to constitutively express murine *Wnt3a* (Figure 27A), a developmentally important signal that exhibits limited diffusion. TREx-293^{Cdh3} cells were transfected with *pCMV::mCherry-2A-mWnt3a*, transgenic cells were hygromycin-selected, seeded at clonal density, and single-picked colonies individually expanded. These cells harbour aforementioned transgenes in unknown genomic locations by means of random integration, and this section describes the testing of TREx-293$^{Cdh3\text{-}Wnt3a}$ in terms of whether pattern formation is retained and whether transgene expression behaves as expected. The *pCMV::mCherry-2A-mWnt3a* construct was previously established by Elise Cachat in 2016.

Clonal lines were tested for emission of red fluorescence in the absence of tetracycline (deriving from *CMV::mCherry-mWnt3a*) and for pattern formation when co-cultured with TREx-293^{Cdh1} under tetracycline supplementation. From a screen panel of thirty TREx-293$^{Cdh3\text{-}Wnt3a}$ clones (not shown), three clones were chosen (#3, #7, #31) based on constitutive mCherry expression, mCherry brightness and the capacity to form phase-separation patterns (Figure 27B, top row). These characteristics indicate strong transgene expression that is fundamental for downstream work. While all three clones showed apparent patterning in 2D, clone 3 showed particularly tight and even phase-separation (Figure 27B, top row). This clone was subsequently co-cultured with TREx-293^{Cdh1} in 3D conditions, forming complete or incomplete phase-separation aggregates depending on amount of cell input (Figure 27B, bottom row), in agreement with previous reports (Cachat et al., 2016).

Finally, transgene behavior was characterized via qRT-PCR in tetracycline-free and tetracycline-supplemented 24h cultures. Expression of the *Cdh3* transgene, designed to be tetracycline-inducible, showed a 947-fold (SD=141) and 377-fold (SD=43.5) increase respectively in clones 3 and 31 cultured under tetracycline supplementation compared to tetracycline-free controls (Figure 27C). Curiously, *Wnt3a* showed an unexpected 2.7-fold increase (SD=0.4) when comparing tetracycline-supplemented to tetracycline-free conditions ($P<0.005$, unpaired two-tailed t-test) of clone 3 (Figure 27D), in disagreement with transgene architecture (Figure 27A) and the extent by which tetracycline activated the *CMV-TetR/TetO*-controlled *Cdh3* transgene (Figure 27C). This might reflect an unexpected effect of tetracycline in influencing

mammalian transcriptional activity, or transgene cross-talk, through which elevated *Cdh3* levels and Cdh3-dependent adhesion upregulate *Wnt3a* expression. Furthermore, tetracycline-inducible *Cdh3* expression in clone #3 was 2.5-fold higher compared to clone 31 ($P<0.005$, unpaired two-tailed t-test), and clone 3 qualitatively showed tighter and seemingly more ordered phase separation patterns compared to clone 31 (Figure 27B). This finding regarding differential transgene expression (possibly attributed to heterochromatic state of different integration sites) and the potential correlation to the degree of pattern formation, albeit an interesting point that will be discussed later, is per se irrelevant to the aims of this thesis. Having established self-organizing cells expressing a *mCherry-2A-mWnt3a* transgene, the next step was to demonstrate biological functionality of *Wnt3a*.

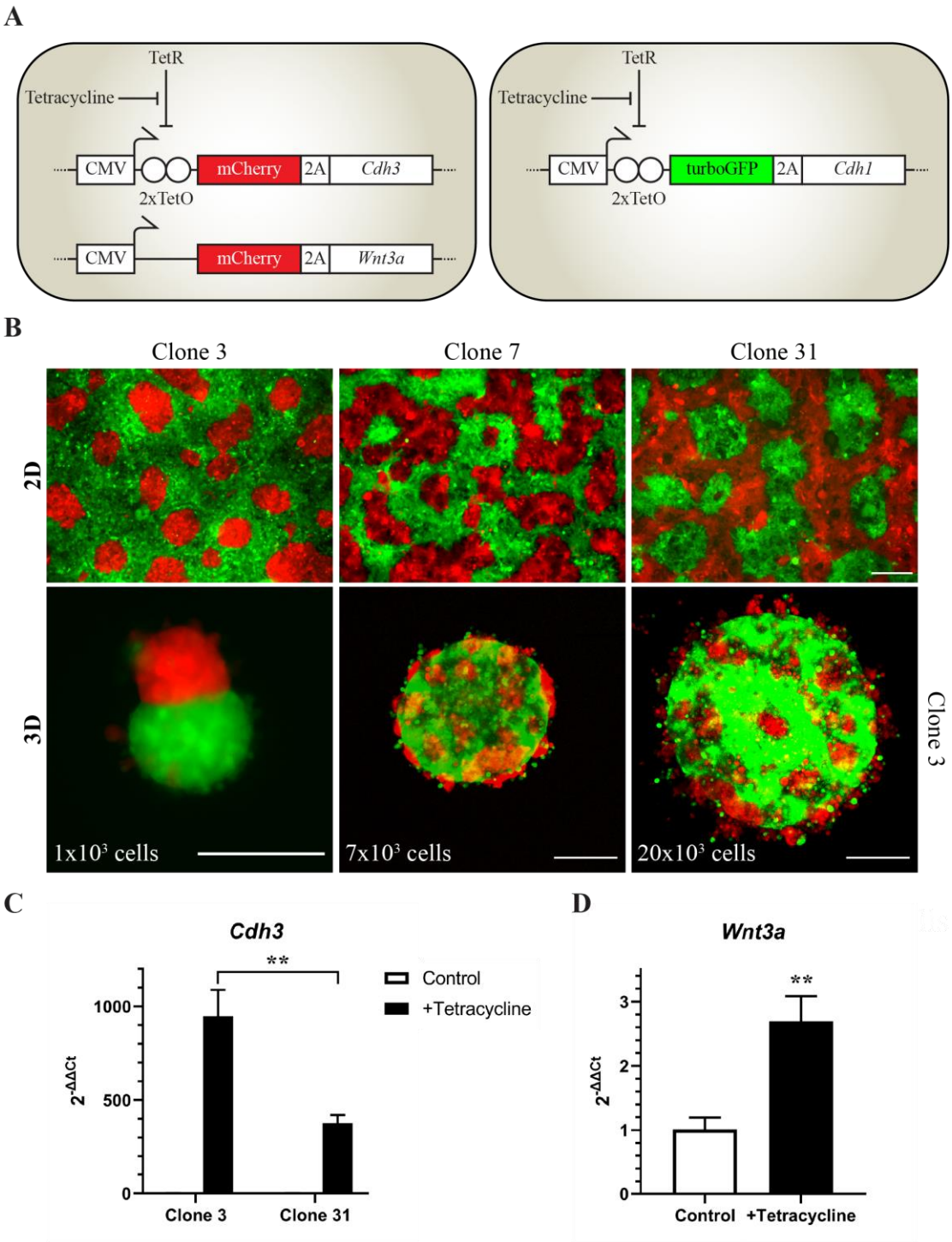

Figure 27. Characterization of self-organizing, signal-producing TREx-293$^{Cdh3\text{-}Wnt3a}$.

(A) Schematic overview of modified phase-separation patterning system. Rectangles represent the two TREx-293 lines, each expressing murine Cadherin-1 or Cadherin-3 and a dedicated fluorescent reporter in a tetracycline-inducible manner. The Cadherin-3 line was modified to constitutively overexpress *mCherry* and *Wnt3a*. **(B)** Pattern formation between TREx-293$^{Cdh3\text{-}Wnt3a}$ and TREx-293^{Cdh1} co-cultured under tetracycline supplementation for 24 hours. Top row shows adherent cultures of indicated TREx-293$^{Cdh3\text{-}Wnt3a}$ clones; bottom row shows three-dimensional cultures of clone 3 at indicated total cells seeded. Scale bars: 200µm. **(C-D)** Comparative transgene expression of TREx-293$^{Cdh3\text{-}Wnt3a}$ clones for *Cdh3* **(C)** and *Wnt3a* (clone 3 only) **(D)** in 24-hour cultures with/without tetracycline. Graphs show means and standard deviations of biological triplicates, each deriving from technical triplicates. Statistic: unpaired t-test. **, P<0.005.

3.3.4 Using TREx-293$^{Cdh3\text{-}Wnt3a}$ to activate Wnt/β-catenin signalling

To assay functional signalling from TREx-293$^{Cdh3\text{-}Wnt3a}$ senders to neighbouring receivers, Wnt/β-catenin-pathway reporter (TOPflash) HEK-293 lines were used on the premise that interactions between the two lines would activate the reporter. In TOPflash systems, expression of a reporter is tied to an upstream regulatory element containing multiple TCF consensus sites that are bound by β-catenin, thus reporting Wnt/β-catenin pathway activation. One such system based on HEK-293 cells had been previously established in the Davies lab (clone #1-13, made by Elise Cachat), in which a *TOPflash::mCherry* transgene reports β-catenin activity. A 24-hour treatment with the pharmacological compound CHIRON-99021, which abrogates β-catenin degradation by inhibiting the GSK3 protein of the β-catenin degradation complex, activated the reporter (Figure 28A). However, various dosages (10nM-10μM) of recombinant human WNT3A (rhWNT3A) failed to induce reporter activation based on fluorescence microscopy (Figure 28A). A fluorescence plate reader was used to improve detection sensitivity, and showed similar results (Figure 28B). Given that Wnt proteins exhibit low half-life and stability, a constant supply of Wnts was provided by co-culturing dissected embryonic murine spinal cord that physiologically produces Wnt ligands. Fluorescence measurements again did not detect any signal increase (Figure 28C).

To exclude the possibility that lack of detection was an artefact specific to the clone used, freshly transgenic cells were prepared by transfecting low-passage wild-type HEK-293 cells with *pTOPflash::H2B-BFP*, and selecting with G418. Again, fresh TOPflash reporters were activated with CHIRON-99021 but not rhWNT3A (Figure 28D). Finally, direct contact co-cultures between phase-separation patterns comprising TREx-293$^{Cdh3\text{-}Wnt3a}$ and TOPflash::BFP reporters was performed, yet no BFP expression could be seen proximal to TREx-293$^{Cdh3\text{-}Wnt3a}$ clusters (Figure 28E). These experiments demonstrate that HEK-293 cells are not reliable Wnt/β-catenin pathway reporters, and suggest they lack expression of key Wnt-pathway transducer(s) that acts upstream of GSK in the pathway cascade (e.g. LRP5/6).

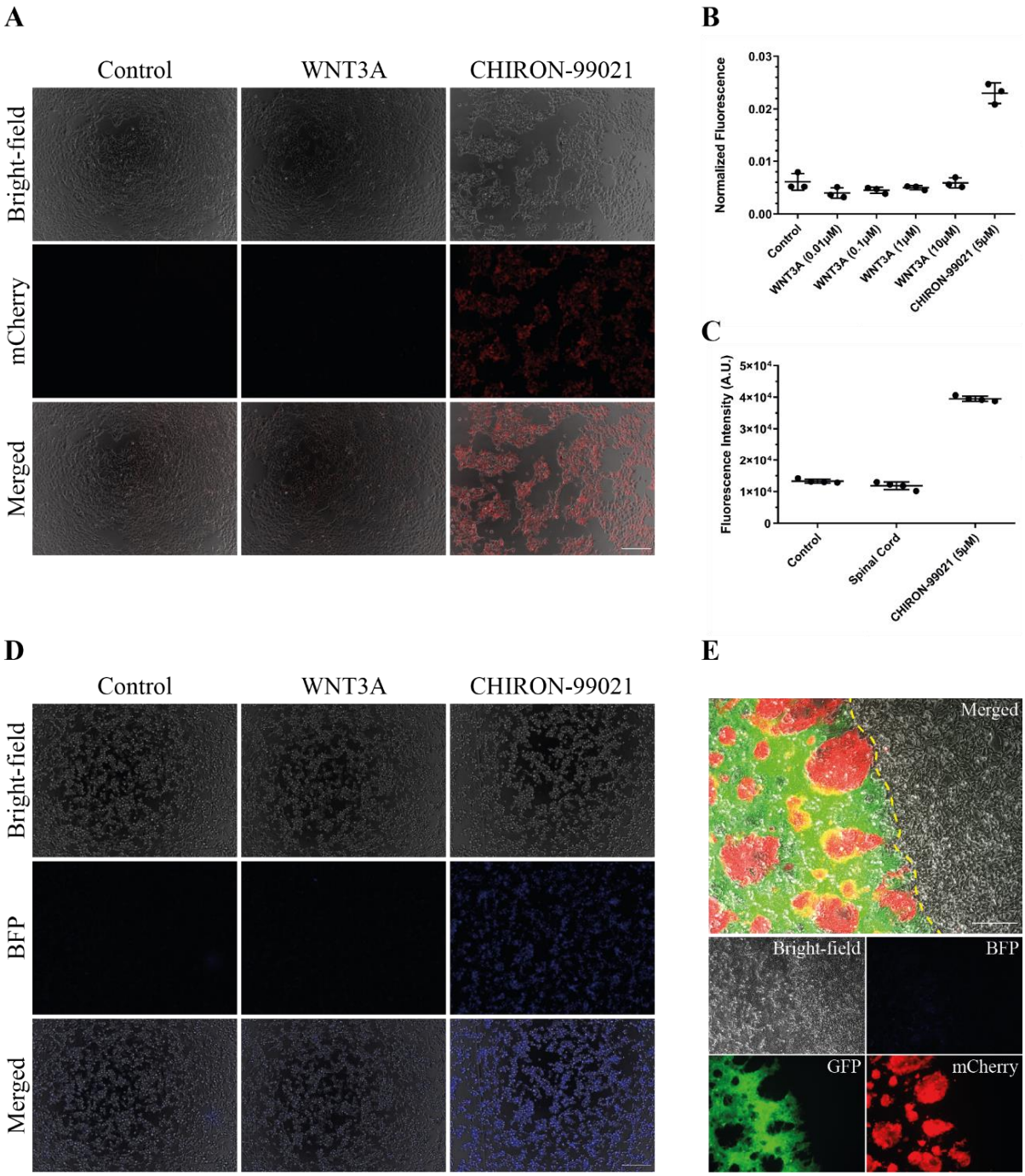

Figure 28. Using TREx-293 TOPFlash reporters to assay Wnt/β-catenin pathway activation.

(A) Fluorescence microscopy panels of pre-established TREx-293$^{TOPflash::mCherry}$ (clone 1-13) after 24h culture with human recombinant WNT3A (10μM) or CHIRON-99021 (5μM). **(B)** Quantification of mCherry fluorescence from cultures as in (A) using a fluorescence plate reader; mCherry fluorescence was normalized against CellTracker CMFDA fluorescence as a proxy for cell numbers. **(C)** Quantification as in (B) after TREx-293$^{TOPflash::mCherry}$ monocultures with/without CHIRON-99021, or co-culture with murine spinal cord. **(D)** Fluorescence microscopy panels of a newly-generated TREx-293$^{TOPflash::BFP}$ line, cultured as in (A). **(E)** Direct co-culture of TREx-293$^{TOPflash::BFP}$ and phase-separation patterns comprising TREx-293$^{Cdh3\text{-}Wnt3a}$ clone 3. Confluent phase-separation patterns were scratched and reporters were subsequently seeded and co-cultured for 24 hours. Scale bars: 200μm.

Due to the unreliability of HEK-293-based Wnt/β-catenin reporters, validated Wnt/β-catenin pathway reporting lines were sought, and *7xtcf/lef::eGFP* mouse embryonic stem cell (mESC)-based reporters were generously provided by Derk ten Berge (Erasmus MC, The Netherlands). These lines reliably report the Wnt/β-catenin pathway through eGFP fluorescence (ten Berge et al., 2008). Contrary to HEK-293, mESC reporters demonstrated expression of fluorescence in both CHIRON-99021 and WNT3A single treatment conditions (Figure 29A). Notably, this experiment also demonstrates the functionality of the recombinant WNT3A, as the same vial/sample used in the HEK-293-based reporter experiments (Figure 28A-B, D) was also used to activate mESC-based reporters (Figure 29A, C). To assay for the presence of biologically functional WNT3A in the culture medium of TREx-293$^{Cdh3\text{-}Wnt3a}$, mESC reporters were cultured in complete maintenance media, or 50% diluted with medium conditioned by TREx-293^{Cdh3}/TREx-293$^{Cdh3\text{-}Wnt3a}$. GFP fluorescence was detected in samples growing in medium conditioned by TREx-293$^{Cdh3\text{-}Wnt3a}$, but not TREx-293^{Cdh3} (Figure 29B). Though GFP emission was dim, quantification (Figure 29C) demonstrated that it was significant ($P<0.0001$, one-way ANOVA). This result was verified with additional experiments (Figure 29D), and GFP detection could be detected in cells exposed to as little as 10% TREx-293$^{Cdh3\text{-}Wnt3a}$-conditioned media (not shown). Taken together, these results demonstrate that TREx-293$^{Cdh3\text{-}Wnt3a}$, but not TREx-293^{Cdh3}, secrete Wnt ligands into the culture medium that functionally signal through the Wnt/β-catenin pathway.

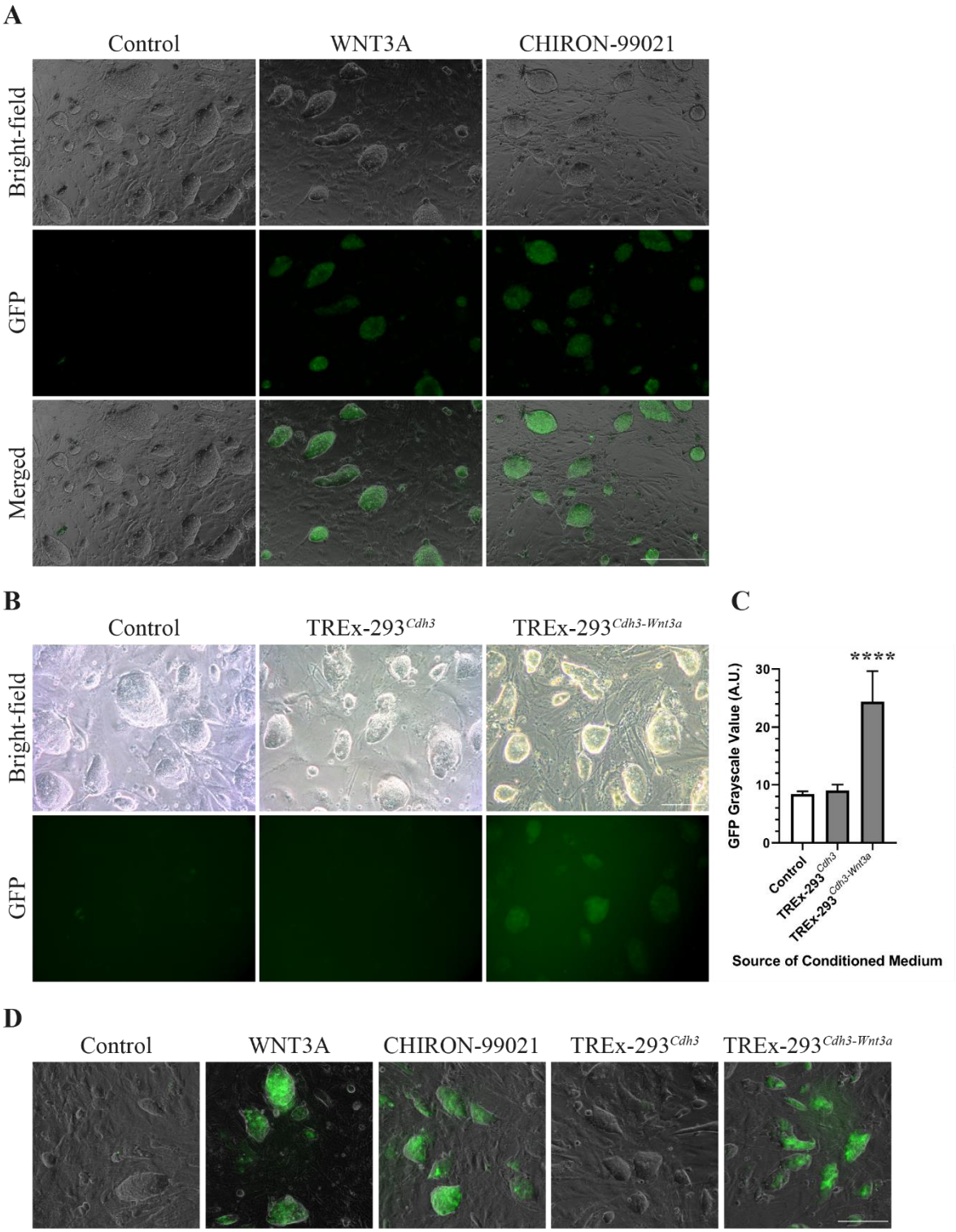

Figure 29. Using mouse ESC *7xtcf/lef::eGFP* reporters to assay Wnt/β-catenin pathway activation.

(A) Fluorescence microscopy panels of reporter mESCs on MEFs, after 24h culture with human recombinant WNT3A (10nM) or CHIRON-99021 (5μM). **(B)** Cultures as in (A) using 50% conditioned medium from TREx-293^{Cdh3} or TREx-293$^{Cdh3\text{-}Wnt3a}$. **(C)** Quantification of (B) showing mean grayscale value and standard deviation. Statistic: One-way ANOVA with Dunnett's multiple comparisons test. ****, P<0.0001. **(D)** Additional experiment entailing all conditions in 24-hour cultures. Scale bars: 200μm.

3.3.5 Self-organization and signalling events in mESCs-TREx-293$^{Cdh3\text{-}Wnt3a}$ co-cultures

This chapter has described the establishment of TREx-293^{Cdh3} systems that produce functional Wnt3A and self-organize in phase-separation patterns with TREx-293^{Cdh1}. Phase-separation patterning requires differential homotypic adhesion driven through expression of different cadherins; i.e. the two-component patterning system depends on one component expressing *Cdh3*, and the other *Cdh1.* While patterning occurs between TREx-293^{Cdh3} and TREx-293^{Cdh1}, it has not been yet determined whether any non-TREx-293 cell type expressing the equivalent cadherin can replace the TREx-293 counterpart, and still form phase-separation patterns when co-cultured with TREx-293 expressing the heterotypic cadherin. Mouse ESCs are well-documented to physiologically express *Cdh1*, making them an ideal candidate to investigate whether they can self-organize in phase-separation with TREx-293^{Cdh3} (Figure 30A).

Validation of endogenous *Cdh1* expression in two mESC lines was provided via immunostaining (Figure 30B). Wnt/β-catenin pathway-reporting ESCs were co-cultured with TREx-293^{Cdh3}/TREx-293$^{Cdh3\text{-}Wnt3a}$ and, after 48 hours, phase-separation cell distributions emerged (Figure 30C). Specifically, the bright-field channel revealed colonies and some patches of mESCs separated by TREx-293^{Cdh3}-occupied areas, while the mCherry channel showed TREx-293^{Cdh3} arranging in a sheet with interceding holes and patched-shaped void areas (Figure 30C). These are characteristic arrangements seen in traditional TREx-293-based phase-separation patterns (Figure 27B). GFP fluorescence was evident only in mESCs co-cultured with TREx-293$^{Cdh3\text{-}Wnt3a}$ (Figure 30C), corroborating aforementioned results that only TREx-293$^{Cdh3\text{-}Wnt3a}$ produce functional Wnt ligand. Critically, GFP fluorescence appeared considerably brighter compared to experiments with conditioned media (Figure 30C, compare to Figure 29B), whether due to continuous stable supply of Wnt3a or/and direct cell-cell contacts facilitating signalling.

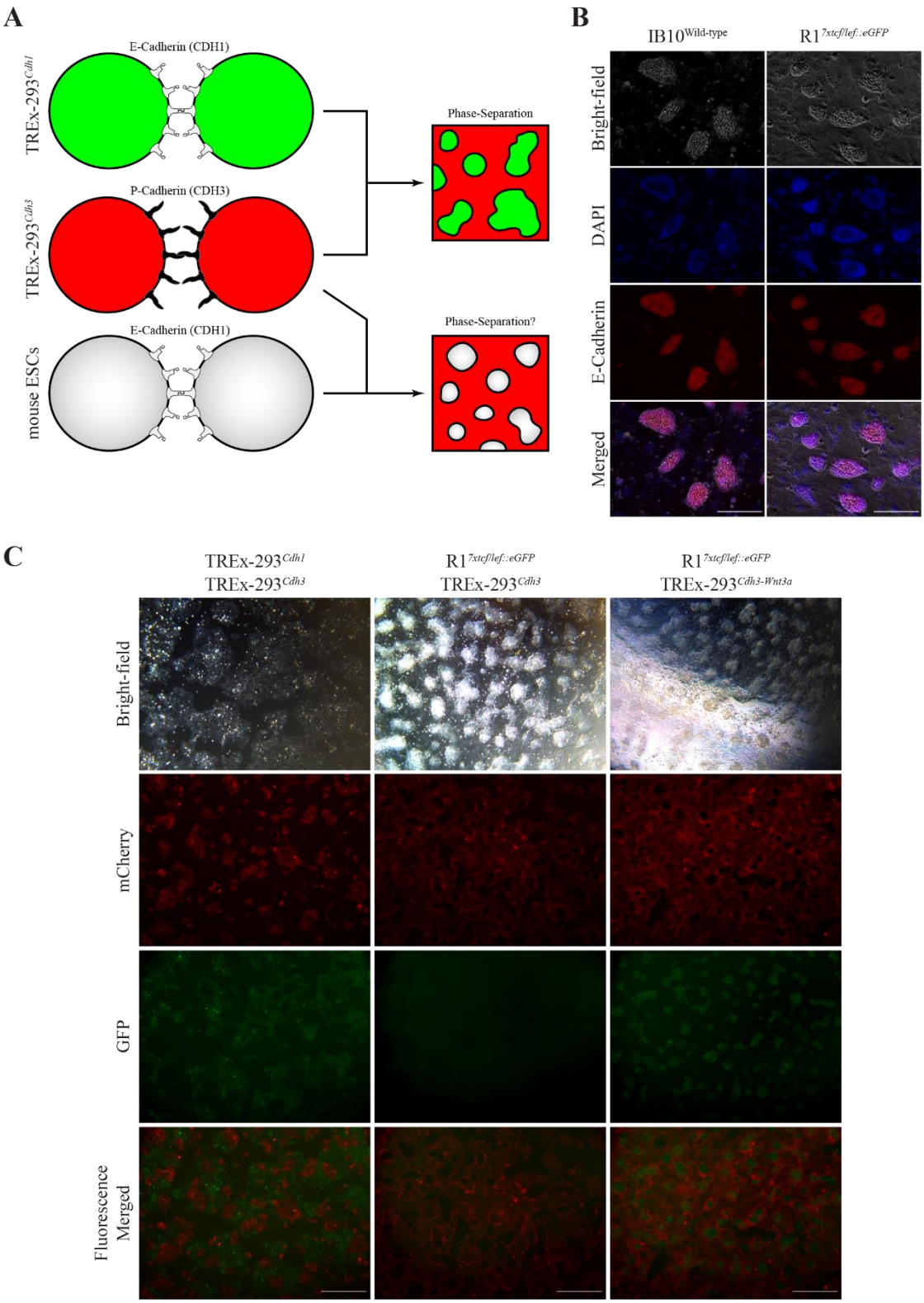

Figure 30. Phase-separation 2D patterning between mESCs and TREx-293*Cdh3*

(A) Schematic representation of experimental concept to replace TREx-293^{Cdh1} with mESCs in phase separation patterns. **(B)** CDH1 immunostaining in different mESC lines to verify natural/endogenous CDH1 expression. **(C)** Phase-separation patterns between mESCs and TREx-293^{Cdh3} or TREx-293$^{Cdh3\text{-}Wnt3a}$ after 48h of co-culture. Because mESCs report for Wnt/β-catenin pathway activation, GFP is evident only in co-cultures with TREx-293$^{Cdh3\text{-}Wnt3a}$. TREx-293^{Cdh3} cells form patch-like distributions with intervening gaps, typically seen in phase-separation patterns with TREx-293^{Cdh1}.

Phase-separation patterning emerges in both 2D and 3D conditions, and therefore mESCs should form phase-separation arrangements with TREx-293^{Cdh3} in 3D. To test this, mESCs were aggregated into embryoid bodies (EBs), tetracycline-induced TREx-293^{Cdh3} or TREx-293$^{Cdh3\text{-}Wnt3a}$ were added to the aggregate suspension one day later, and EBs were allowed to differentiate. On day 3 of differentiation, distinct TREx-293^{Cdh3} aggregates could be seen attached to larger EBs without heterotypic cell intermingling, akin to phase-separation (Figure 31). No endogenous Wnt/β-catenin signalling was evident in standalone EBs or EB-TREx-293^{Cdh3} co-aggregates on day 3, in terms of GFP detection through fluorescence microscopy. In EB-TREx-293$^{Cdh3\text{-}Wnt3a}$ co-aggregates, GFP fluorescence in the EB could be detected, with strong signal in areas close to TREx-293$^{Cdh3\text{-}Wnt3a}$ and gradually decreasing with increasing distance. On day 4, diffuse GFP could be detected in standalone EBs and less brightly in EB-TREx-293^{Cdh3} co-aggregates, compared to localized and gradual GFP intensity signals (Figure 31). Consequently, this method allows for self-organization between mESC-derived EBs and TREx-293^{Cdh3}-based cells, forming EB-293 phase-separation co-aggregates in which signalling pathways in EBs can be activated from TREx-293^{Cdh3} aggregates in a polarized manner.

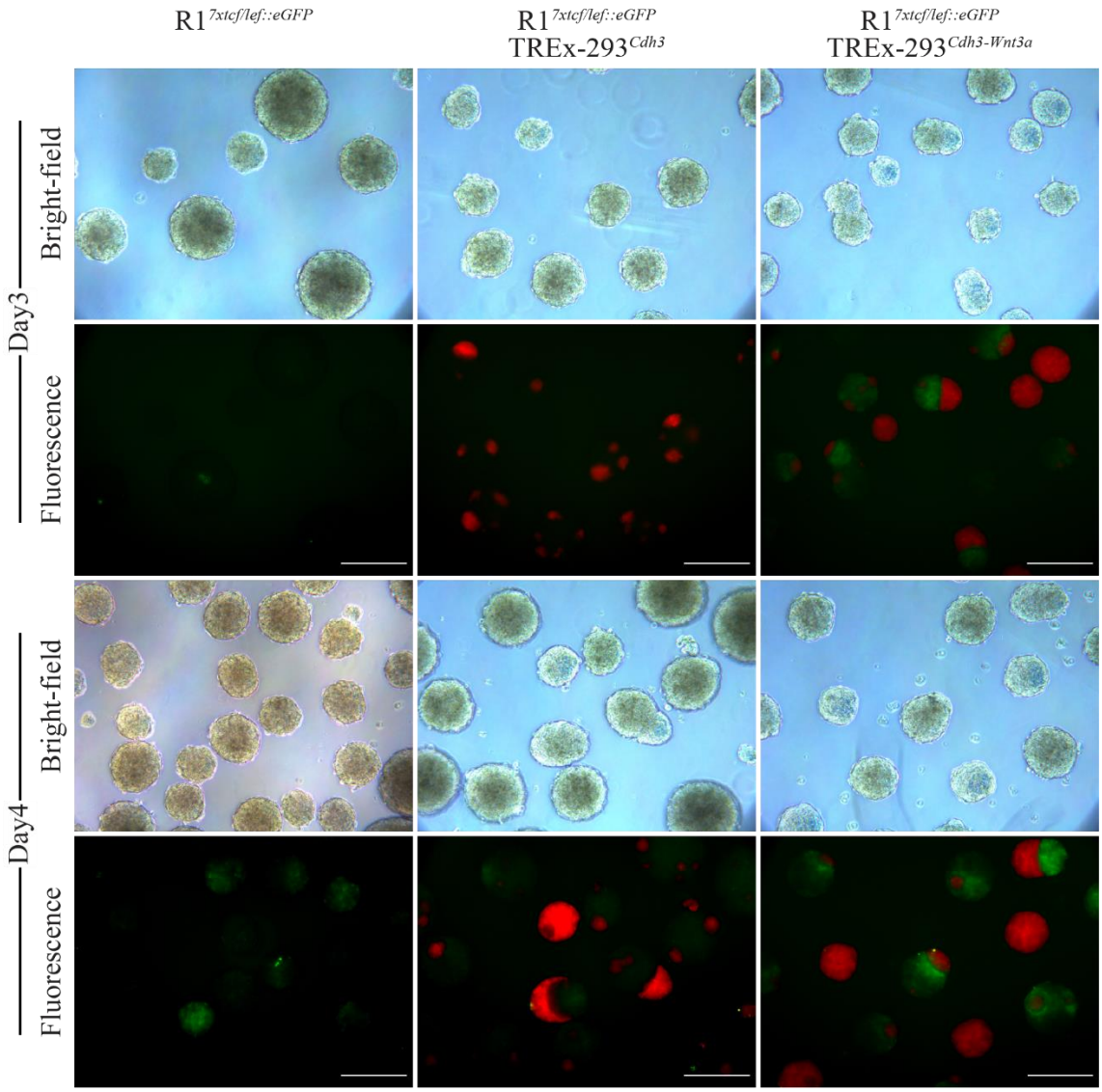

Figure 31. Phase-separation and polarized Wnt/β-catenin activity in EB-293 co-aggregates.

Phase-separation patterning between embryoid bodies and TREx-293^{Cdh3}/TREx-293$^{Cdh3\text{-}Wnt3a}$ at day 3 and day 4 of differentiation. The Wnt/β-catenin pathway is endogenously activated between day 3 and 4, and can be exogenously activated in polarized manner from TREx-293$^{Cdh3\text{-}Wnt3a}$. Scale bars: 200μm

Finally, the EB-293 3D phase-separation method (Figure 32A) was characterized in terms of co-aggregates generated. From a total of 304 aggregates screened at day 3 and day 4, 265 (87.2%) comprised EB-293 co-aggregates, while the other 39 (12.8%) were TREx-293^{Cdh3} or TREx-293$^{Cdh3\text{-}Wnt3a}$ (TREx-293^{Cdh3}-based) mono-aggregates. From the 265 EB-293 bodies, 253 (83.2% of total) comprised a single EB carrying multiple TREx-293^{Cdh3}-based aggregates, while 12 (4% of total) consisted of two EBs cross-linked by one TREx-293^{Cdh3}-based aggregate "belt" (Figure 32B). Most of the 253 single EBs possessed one (n=85) or two (n=88) TREx-293^{Cdh3}-based aggregates, with increasing number of TREx-293^{Cdh3}-based aggregates per EB diminishing in frequency steeply (Figure 32C). Only 1/253 single EBs had no TREx-293^{Cdh3}-based aggregates. Hence, while this dish-rotator method is highly efficient in generating EB-293 co-aggregates, there is considerable variation in the types of bodies produced. Further technical experimentation could allow co-aggregate standardization and the building of novel morphologies, such as the rarely observed cross-linked EBs.

These experiments demonstrate several findings important to the aims of this thesis. Firstly, mESCs can self-organize with TREx-293^{Cdh3} in phase-separation patterns, both in 2D and 3D. This represents a first layer of pattern formation. Signalling from TREx-293^{Cdh3} to mESCs can be functionally elicited, at least for Wnt3a. In 2D, this results in strong Wnt/β-catenin-activated colonies distributed among TREx-293$^{Cdh3\text{-}Wnt3a}$ layers in phase-separation patterns. In 3D, it results in exogenous signalling that can be applied prior to equivalent EB-autonomous, endogenous signalling events. Because exogenous signalling derives from a localized source of TREx-293$^{Cdh3\text{-}Wnt3a}$, the signalling response in the EB is polarized and gradual rather than diffuse. Specifically, the polarization in Wnt/β-catenin activity within the EB marks a form of symmetry breaking, while the gradual levels of Wnt/β-catenin pathway activation describe a form of pattern elaboration, given that β-catenin^{HIGH}, β-catenin$^{MEDIUM/LOW}$ and β-catenin^{OFF} cells emerge according to their distance to TREx-293$^{Cdh3\text{-}Wnt3a}$. This work allows for the further dissection of developmental cell fate-decisions that can be controlled within this self-organized, cell-based signalling platform, with the aim of improving the control and realism of EB patterning events.

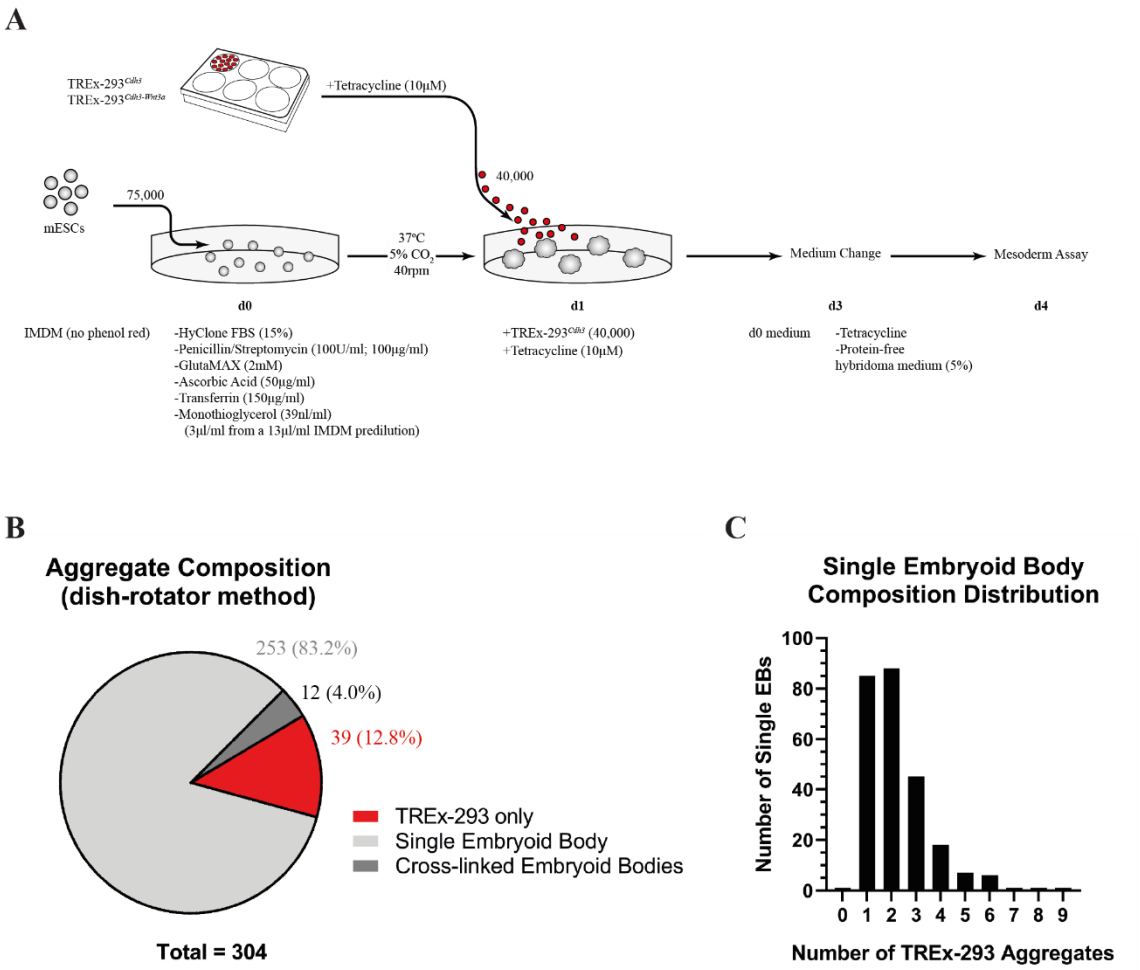

Figure 32. Overview of method for EB-293 co-aggregation in phase-separation, and characterization of output.

(A) Schematic outline of experimental method. On day 0, harvested and MEF-depleted mESCs are suspended in 3ml differentiation media, plated on a 6cm polystyrene petri dish, and grown overnight on a rotator platform. TREx-293^{Cdh3} and derivatives are replenished with tetracycline-supplemented media. On day 1, TREx-293^{Cdh3}-based cultures are harvested and 4x10^4 cells are added to EBs along with tetracycline. Following a medium change on day 3, EB-293 co-aggregates are ready to be assayed on day 4. **(B)** Pie-chart showing fractions of aggregate types emerging from method shown in (A). N=304 aggregates from days 3 and 4. **(C)** Histogram showing the number of single EBs from (B) that contain a certain number of TREx-293 aggregates (n=253).

3.4 Controlling stem cell fate decisions

The engineered TREx-293$^{Cdh3\text{-}Wnt3a}$ cell line described in the last section passes certain criteria. Firstly, biologically active Wnt3a was surprisingly produced and secreted from TREx-293 cells without the requirement of introducing post-translational modifiers (e.g. Porcupine) or chaperones (Wntless). TREx-293$^{Cdh3\text{-}Wnt3a}$ lines, but not parental TREx-293^{Cdh3} controls, could be used to activate the Wnt/β-catenin pathway in reporter *7xtcf/lef::eGFP* mESCs. The introduction of *Wnt3a* did not affect the ability of TREx-293$^{Cdh3\text{-}Wnt3a}$ to form phase-separation patterns with TREx-293^{Cdh1}. On the contrary, phase-separation was also possible with mESCs that naturally express *Cdh1*, representing pattern formation between TREx-293^{Cdh3}/TREx-293$^{Cdh3\text{-}Wnt3a}$ and mESCs. In these phase-separation co-cultures, Wnt3a produced from a localized TREx-293$^{Cdh3\text{-}Wnt3a}$ aggregate source was able to induce polarized and gradual β-catenin signalling responses in mESC-derived EBs in 3D culture conditions. The polarization in these EB responses marked symmetry breaking, whereas the graded responses marked pattern elaboration further to phase-separation pattern formation between TREx-293$^{Cdh3\text{-}Wnt3a}$ and mESCs. These characteristics suggest that TREx-293$^{Cdh3\text{-}Wnt3a}$ pass the criteria introduced in the beginning of section 3.3, and confirm hypothesis II, as Wnt3a produced from HEK-293-based cells could indeed exert spatially localized β-catenin responses, at least in mESC-derived EBs under 3D phase-separation co-culture conditions.

The final incentive for which Wnt3a was chosen as a candidate ligand, was that it plays pivotal roles in diverse developmental and stem cell contexts. Successful mESC responses in phase-separation with TREx-293$^{Cdh3\text{-}Wnt3a}$ described above were defined by β-catenin signalling activation. Realistically, and in conjunction to the role of Wnt3a in the context of development and ESC differentiation, these organized signalling responses should propagate into organized lineage differentiation responses. In development, the Wnt/β-catenin pathway and specifically Wnt3 ligands lie at the heart of mesoderm induction during gastrulation (Kelly et al., 2004; P. Liu et al., 1999; Morkel et al., 2003; Tortelote et al., 2013) (for details see section 1.2.2). Specifically, Wnt3a directly upregulates T-brachyury, a marker of nascent mesoderm, in the embryonic primitive streak (Yamaguchi, Takada, et al., 1999). This is also observed in mESC-derived EBs, where activation of the β-catenin pathway using Wnt3a upregulates expression of T-brachyury and other mesendodermal markers. Wnt/β-catenin active cells become positive for T-brachyury and undergo epithelial-to-mesenchymal transition (EMT) that is characteristic of mesendodermal commitment (ten Berge et al., 2008). Consequently, I set out to investigate whether pattern elaboration and symmetry breaking in Wnt3a/β-catenin signalling responses could propagate into pattern elaboration and symmetry breaking in ESC lineage output (mesoderm specification).

Hypothesis III

Organized and enhanced Wnt3a/β-catenin signalling responses, from mESC-TREx-293$^{Cdh3\text{-}Wnt3a}$ phase-separation patterned co-cultures, can exert changes in mESC mesoderm induction in terms of spatial organization or increased yield.

3.4.1 Augmenting and tracking mesoderm emergence in 2D differentiations

One of the most important cell fate-decisions during early ESC differentiation, is germ-layer specification that occurs during gastrulation. During gastrulation, pluripotent epiblast cells become specified to one of three germ layers: ectoderm, mesoderm or endoderm, each possessing restricted and unique developmental trajectories. The Wnt/β-catenin pathway is implicated in a gene regulatory network that promotes mesoderm specification and epithelial-to-mesenchymal transition (EMT).

To test whether mESCs in Wnt-inductive phase-separation show enhanced mesodermal induction, Wnt-reporting mESCs were differentiated in pattern with TREx-293^{Cdh3}/TREx-293$^{Cdh3\text{-}Wnt3a}$, in mESC maintenance medium lacking LIF, and fixed at day 4. Samples were immunostained for GFP (marking β-catenin activity), T-brachyury (nascent mesoderm marker), and DAPI (nuclei), and imaged using fluorescence microscopy under the same settings/configurations. Immunostaining revealed localized spots of intense T-brachyury signal within β-catenin-active/GFP+ colonies differentiated with TREx-293$^{Cdh3\text{-}Wnt3a}$. Dim GFP+ and T-brachyury signal could occasionally be detected in diffuse/mosaic distributions in TREx-293^{Cdh3}-co-cultured colonies, presumably due to mESC endogenous events (Figure 33A). To quantify stain intensities per colony, colony peripheries were demarcated using the freehand selection tool (FiJi) and grayscale values for GFP and T-brachyury channels within the drawn areas were measured and normalized against DAPI. The difference in T-brachyury signal intensity in colonies between the two conditions was significant ($P<0.05$, n=6 for TREx-293^{Cdh3}; n=10 for TREx-293$^{Cdh3\text{-}Wnt3a}$, Figure 33B), and holds in pooled comparisons from three independent experiments that showed an overall 2.2-fold change ($P<0.01$, n=27 for TREx-293^{Cdh3}; n=29 for TREx-293$^{Cdh3\text{-}Wnt3a}$, Figure 33C). The observation that not all mESC colonies differentiated in pattern with TREx-293$^{Cdh3\text{-}Wnt3a}$ showed T-brachyury clusters (Figure 33A), suggests either that different colonies are at other stages of differentiation, or that not all colonies undergo strong T-brachyury induction. Static fixation of samples for immunostaining limit our ability to reliably interrogate these possibilities.

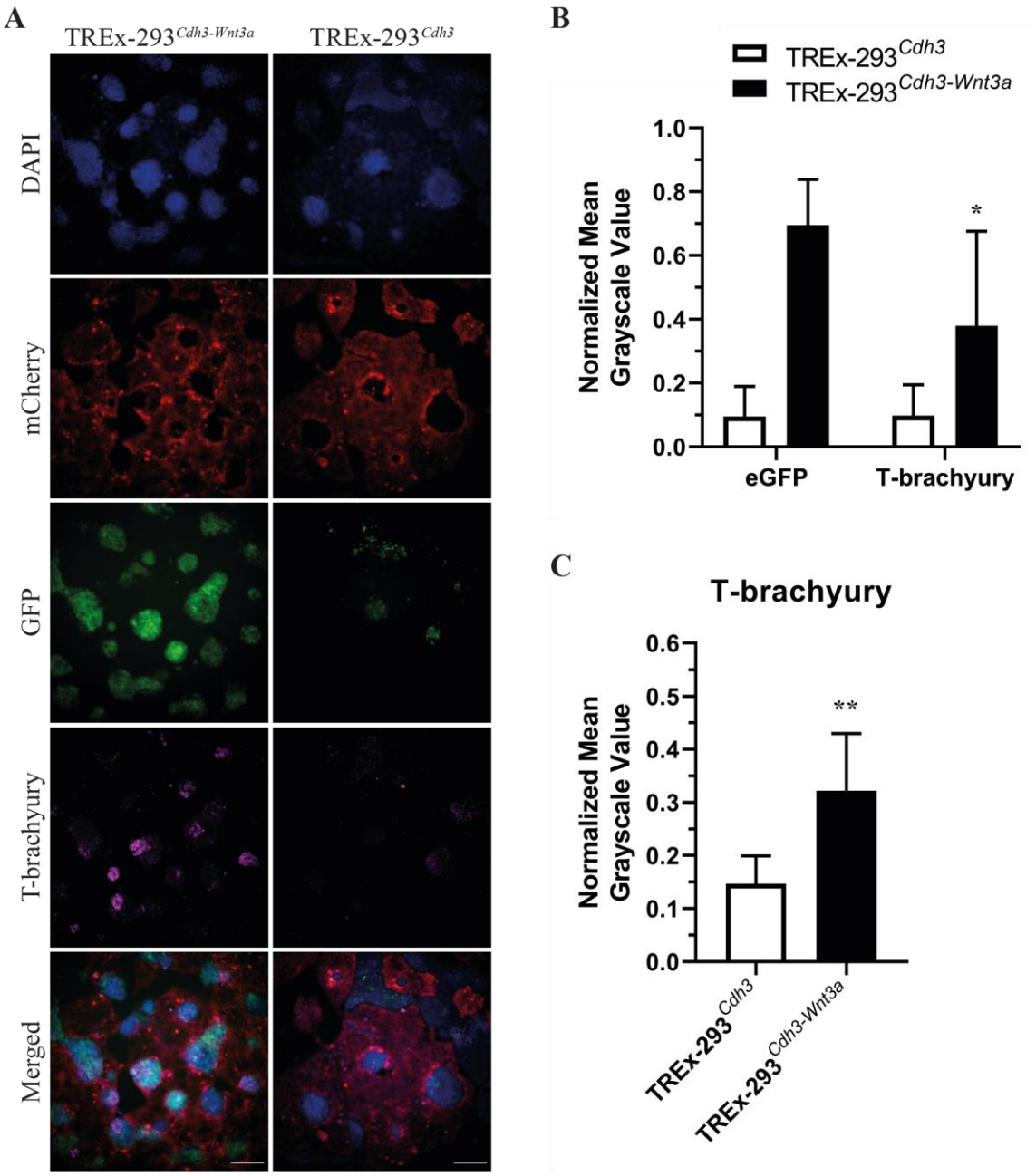

Figure 33. Immunofluorescence shows augmented T-brachyury induction in mESCs differentiated in 2D phase-separation with TREx-293$^{Cdh3\text{-}Wnt3a}$.

(A) Immunostaining for GFP and T-brachyury in phase-separation co-cultures using the *7xtcf/lef::eGFP* line fixed at 96h of differentiation. Red fluorescence derives from mCherry expressed in TREx-293^{Cdh3}/TREx-293$^{Cdh3\text{-}Wnt3a}$, fraction of which persists following PFA-based fixation. Scale bars: 200µm **(B)** Mean fluorescence and standard deviation from colonies shown in (A) normalized against DAPI (n=6 for TREx-293^{Cdh3}; n=10 for TREx-293$^{Cdh3\text{-}Wnt3a}$). Statistic: unpaired t-test. **(C)** Overall T-brachyury quantification from colonies across three independent experiments (n=27 for TREx-293^{Cdh3}; n=29 for TREx-293$^{Cdh3\text{-}Wnt3a}$). Statistic: unpaired t-test. *, P<0.05; **, P<0.005.

To better understand T-brachyury-specification dynamics within this system, a *T-brachyury::eGFP* mESC line was used, in which eGFP expression reports for T-brachyury and therefore early mesoderm (Fehling et al., 2003). *T-brachyury::eGFP* mESCs were differentiated in phase-separation under LIF withdrawal for 4 days, and following culture dissociation into single-cell suspension using TrypLE Express, GFP+/GFP- population compartments were assayed via flow cytometry. The gating strategy used allows for analysis of GFP+/GFP- compartments in single, live mESCs following elimination of mCherry-expressing TREx-293^{Cdh3}/TREx-293$^{Cdh3\text{-}Wnt3a}$, and assessment of mESC viability after TREx-293^{Cdh3}/TREx-293$^{Cdh3\text{-}Wnt3a}$ are initially excluded (Figure 34). Interestingly, mESC viability in phase-separation showed a significant 55% increase compared to standalone conditions (P=0.0001, one-way ANOVA, n=6 differentiations, 3 independent experiments), from 62.8% to 97.1% (Figure 35A-B). The T-brachyury/GFP positive and negative fractions in live cells are comparable among the standalone and the TREx-293^{Cdh3}/TREx-293$^{Cdh3\text{-}Wnt3a}$ phase-separation differentiation conditions (Figure 35C). However, the geometric mean GFP intensity in single mESCs co-cultured with TREx-293$^{Cdh3\text{-}Wnt3a}$ is 1.35-fold/1.45-fold higher (P<0.0001, one-way ANOVA) compared to TREx-293^{Cdh3} or standalone conditions respectively (Figure 35D). These analyses reveal that TREx-293-mESC phase-separation differentiations promote mESC survival, and stable Wnt3a provision from TREx-293$^{Cdh3\text{-}Wnt3a}$ exerts a qualitative effect in upregulating T-brachyury expression levels in single cells. The latter finding corroborates immunostaining results (Figure 33A-C) and additionally demonstrates that the T-brachyury intensity increase is due to elevated levels in single cells. However, the localized cluster-like distribution of T-brachyury within colonies in TREx-293$^{Cdh3\text{-}Wnt3a}$ co-cultures (Figure 33A) remains interesting from a pattern formation standpoint.

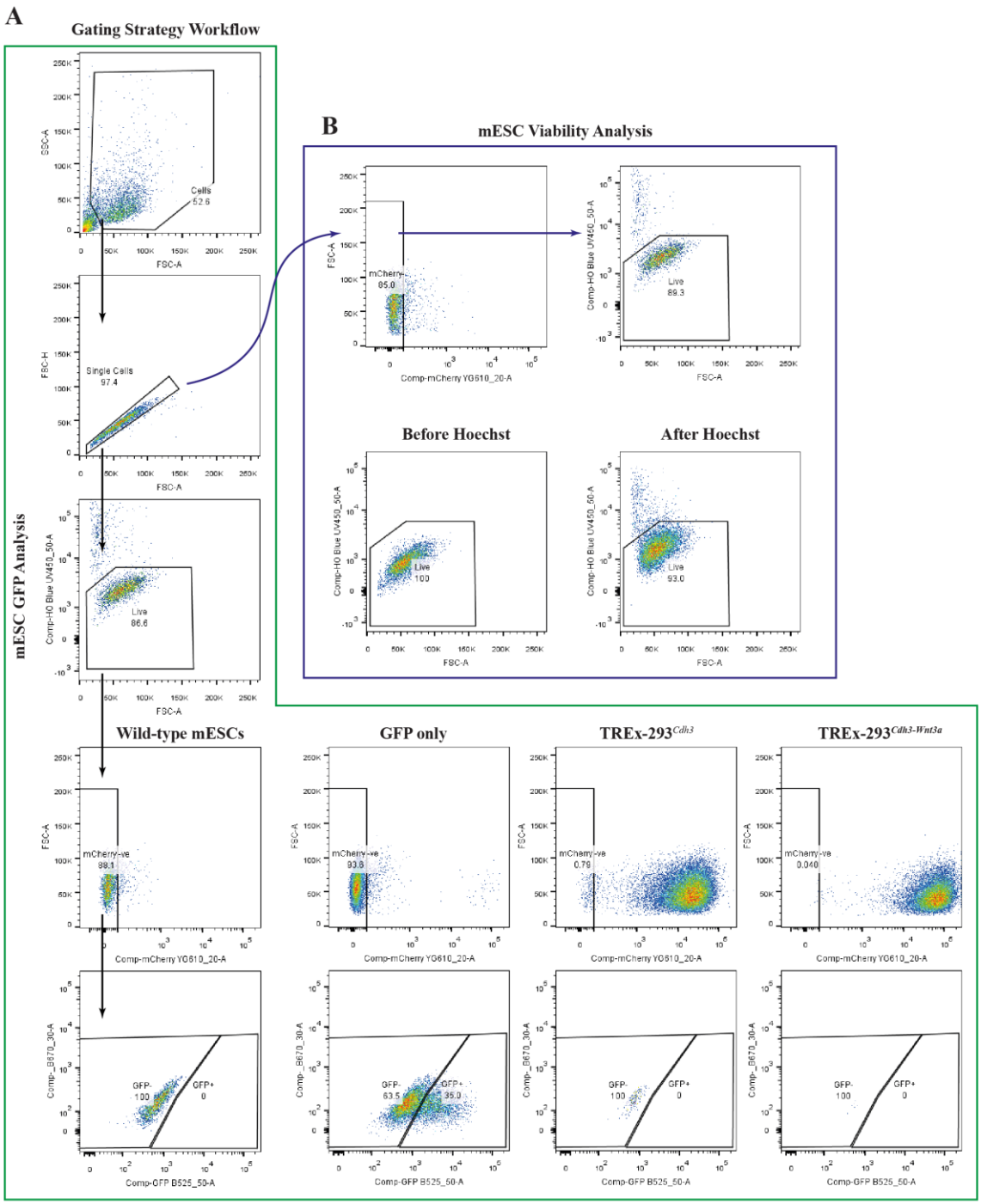

Figure 34. Flow cytometry gating strategy for *T-brachyury::eGFP* differentiations in phase-separation.

(A) Step-by-step course for analysis of GFP compartments in ESCs (black arrows, green rectangle), from top to bottom: Selecting cells among debris, choosing singlets through linear relationship between height and area, excluding cells with compromised membranes that stain positive for Hoechst, focusing on mESCs by excluding mCherry+ TREx-293^{Cdh3}/TREx-293$^{Cdh3\text{-}Wnt3a}$, and analysing GFP+/GFP- compartments. In the final bottom two rows, single-fluorescence gating controls are shown, from left to right: wild-type IB10 mESCs, *T-brachyury::eGFP* standalone, TREx-293^{Cdh3} only, TREx-293$^{Cdh3\text{-}Wnt3a}$ only. The mCherry exclusion gate is stringent to ensure purity in analysis of mESCs, **(B)** An alternative course (blue arrows, blue rectangle) assesses mESC viability, through exclusion of mCherry+ events prior to viability measurements. The same sample analysed before and after addition of Hoechst is shown, serving as a gating control.

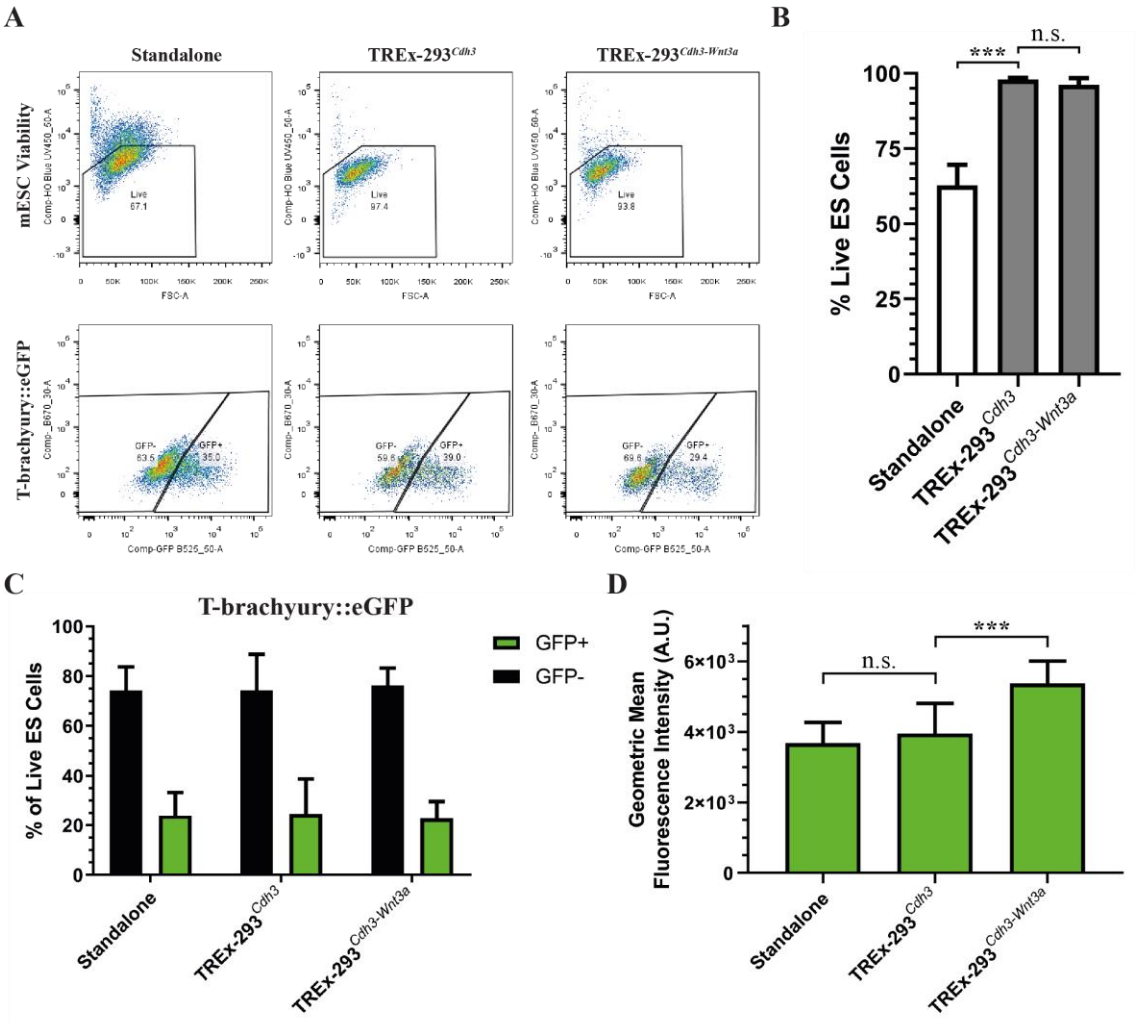

Figure 35. Flow cytometry analysis of *T-brachyury::eGFP* differentiations in 2D phase-separation on day 4.

(A) Example flow-cytometry panels assessing mESC viability (top row) and GFP compartments (bottom row) in *T-brachyury::eGFP* mESCs differentiated standalone (left), or in phase-separation with TREx-293^{Cdh3} (middle) or TREx-293$^{Cdh3\text{-}Wnt3a}$ (right) for 96 hours. **(B)** ESC viability at 96h of differentiation under LIF withdrawal conditions. Graph shows means and standard deviations (n=6 differentiations, 3 independent experiments). Statistic: One-way ANOVA with Tukey's multiple comparisons. **(C)** Flow cytometry-analysis of GFP compartments in live mESCs at 96h. Graph shows means and standard deviations (n=6 differentiations, 3 independent experiments). **(D)** Average GFP geometric mean fluorescence intensity and standard deviation from GFP+ populations shown in (C). Statistic: One-way ANOVA with Tukey's multiple comparisons. ***, P<0.001.

To interrogate the dynamics of T-brachyury expression (mesoderm specification), time-lapse fluorescence microscopy of live phase-separation and standalone cultures was performed between 72h and 120h of differentiation at 30-minute intervals. The increased eGFP intensity in TREx-293$^{Cdh3\text{-}Wnt3a}$ co-cultures (Figure 35D) allowed for visualization of T-brachyury emergence via fluorescence microscopy, which showed a wave of transient expression between 72h and 120h of differentiation (Figure 36A, top row). The distribution of eGFP in these samples is localized and clustered, reflecting T-brachyury immunostaining results (Figure 33A). In comparison, the majority of colonies in TREx-293^{Cdh3} co-cultures showed no detectable fluorescence, with few showing dim levels (Figure 36A, bottom row). Quantification of fluorescence in single colonies allowed the visualization and modelling of T-brachyury induction in these systems (Figure 36B). Fluorescence levels in mESCs differentiating standalone or in pattern with TREx-293^{Cdh3} were either undetectable, dim or exhibited high area-to-area variation over time, and thus median intensities barely rose above basal/noise levels. On the contrary, colony GFP levels in mESC-TREx-293$^{Cdh3\text{-}Wnt3a}$ co-cultures rose well above starting points, revealing the wave of T-brachyury expression that peaked on average at 98.7h of differentiation (95% confidence interval: {96.2, 101}, n=33, three independent experiments). In one experiment, that wave could be well-fitted into a Gaussian curve (Robust Sum of Squares=477.1) (Figure 36B, top left panel). The variance shown in these quantifications stem from biological and technical factors: colonies are not in complete synchrony and differentiate in slightly staggered rates, while the high exposure required to capture T-brachyury-eGFP events adds noise. As colony coordinates change during dynamic growth, this system can serve as a platform for the development of algorithms to execute automatic colony-tracking and robust fluorescence quantification. Regardless, this system has proved its efficacy to enhance T-brachyury induction events, which are associated with the emergence of nascent mesoderm, and monitor their course in real-time.

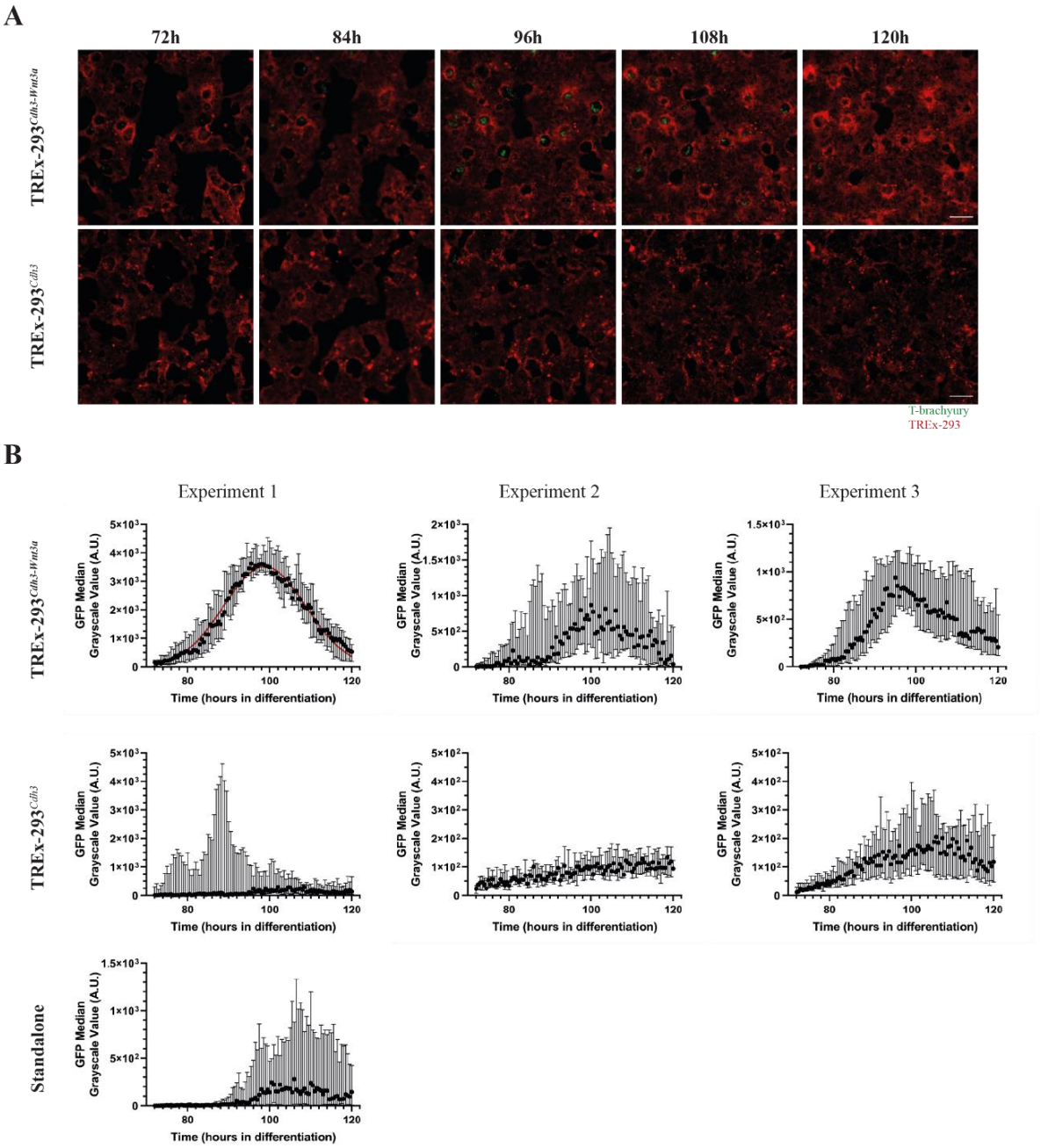

Figure 36. Time-lapse marks mesoderm specification in *T-brachyury::eGFP* differentiations in phase-separation.

(A) Example panels of *T-brachyury::eGFP* mESCs differentiating in phase-separation with TREx-293$^{Cdh3\text{-}Wnt3a}$ (top row) or TREx-293^{Cdh3} (bottom row) at different time points. Red/mCherry signal marks TREx-293, whereas green/GFP marks T-brachyury-positive mESC populations. **(B)** Quantification of GFP grayscale value between 72h and 120h of differentiation at 30-minute intervals. Plots show median and interquartile ranges, because few colonies in TREx-293^{Cdh3} co-cultures emit detectable levels of fluorescence that skew the mean and misrepresent overall readings. Colony values calculated from n=8 (experiment 1); n=11 (experiment 2); n=14 (experiment 3). For standalone differentiation, n=16 areas showing detectable GFP. Red line shows robust regression of Gaussian curve.

Finally, to demonstrate fulfilment of mesoderm emergence, day 5 differentiations were assayed for the presence of markers indicative of gastrulation-related developmental changes. Gastrulation and mesoderm emergence is characterized by EMT, which describes changes in expression of transcriptional regulators, cadherin profiles, and overall adhesion properties. Phase-separation patterned co-cultures were fixed on differentiation day 5 and immunostained for CDH2 and eomesodermin (EOMES), two critical factors implicated in EMT. In both TREx-293^{Cdh3} and TREx-293$^{Cdh3\text{-}Wnt3a}$ co-cultures, colonies expressing CDH2 and/or EOMES were apparent (Figure 37A). Importantly, EOMES staining appeared nuclear whereas CDH2 membrane-localized, further confirming staining specificity (Figure 37A-B). Interestingly, EOMES/CDH2 co-expression appeared predominantly at the edges of mouse colonies/patches, at the mouse-293 interphase, raising the possibility of emergent self-organization and pattern elaboration during mESC differentiation. This finding therefore demonstrates successful EMT and mesoderm emergence, and importantly highlights the dynamic nature of the phase-separation pattern which, as differentiations proceed, might elaborate or disintegrate.

Collectively, this line of experiments demonstrates that mESC differentiations in phase-separation with TREx-293^{Cdh3} benefit from increased viability, while differentiations with modified TREx-293$^{Cdh3\text{-}Wnt3a}$ show enhanced nascent mesoderm specification. This is not due to a quantitative increase in T-brachyury+ populations, but rather a qualitative increase of T-brachyury levels on a single-cell basis. In colonies of this TREx-293$^{Cdh3\text{-}Wnt3a}$ system, T-brachyury transiently emerges as localized clusters, following a Gaussian-like transient expression wave that peaks between 96-101h of differentiation. By day 5, mESC-derived populations undergo EMT and adopt a mesodermal profile, which might lead to changes in the composition of the phase-separation pattern. Overall, this self-organized system allows the real-time tracking of early developmental events, and is able to exert meaningful changes in stem cell fate decisions in an organized manner. These changes could potentially feed-back into the system’s self-organization properties.

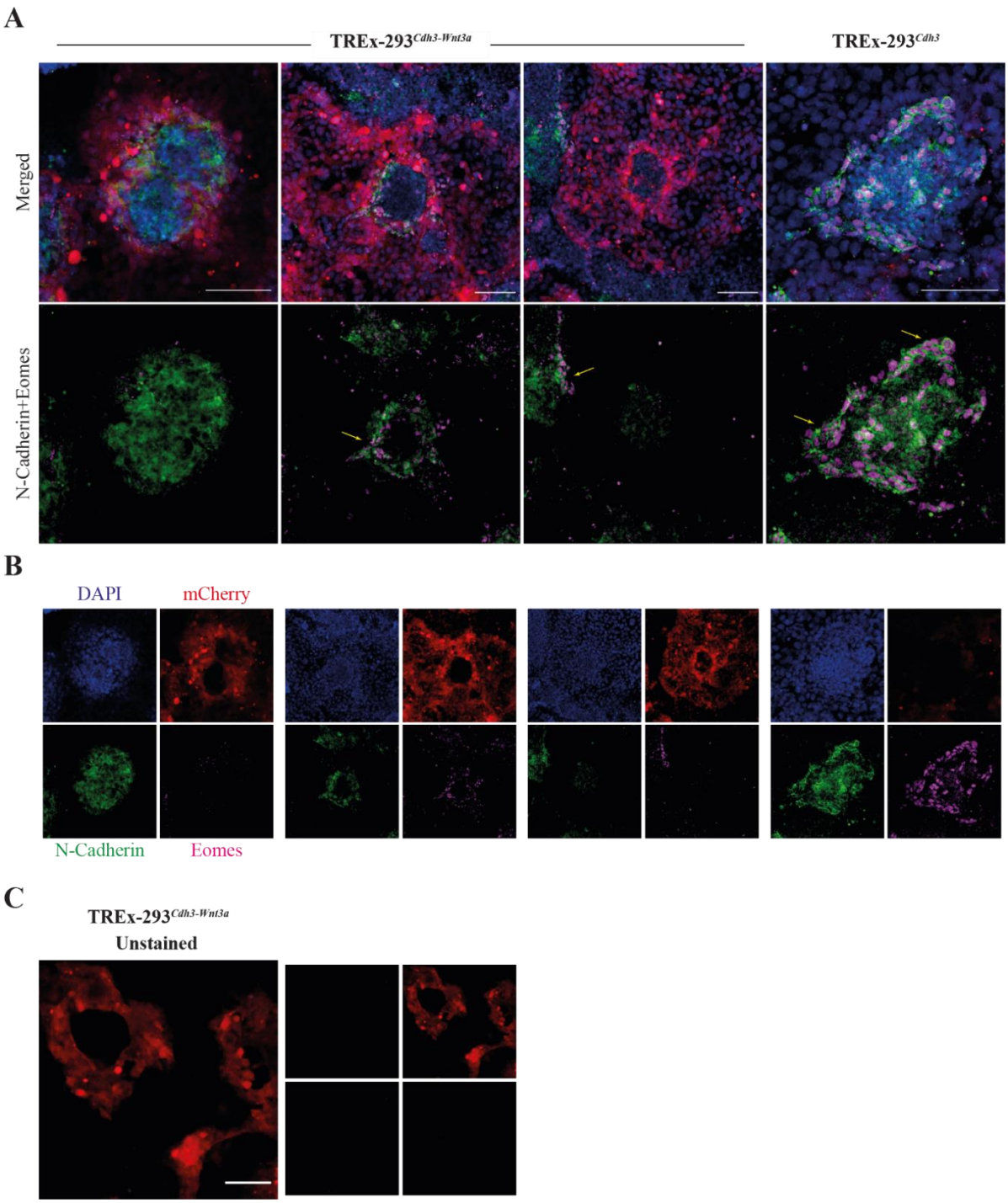

Figure 37. Definitive mesoderm emergence in phase-separation co-cultures on day 5.

(A) Immunostaining for Eomesodermin (magenta) and N-cadherin (green) in phase-separation mESCs differentiations fixed on day 5. All-merged and Eomes+N-cadherin panels are shown for clarity. **(B)** Single-channel panels of images shown in (A). Red mCherry fluorescence stems from TREx-293^{Cdh3}/TREx-293$^{Cdh3\text{-}Wnt3a}$. EOMES and CDH2 signals do not overlap with mCherry. **(C)** Unstained control showing only TREx-293-derived mCherry. Images are Z-stacks of selected Z-slices chosen based on imaging clarity. Scale bars: 100μm.

3.4.2 Specifying mesoderm organization in 3D embryoid bodies

Embryonic stem cell differentiation in 3D aggregates termed embryoid bodies (EBs) forms the basis for increasing self-organization and output complexity by approximating a development-like system. While these systems demonstrate endogenous signalling events that lead to complex interactions and lineage specifications, exogenous application of a polarized cell-based Wnt3a signalling via phase-separation patterning allowed for an organized graduated β-catenin response in EBs (Figure 31). Given the implication of Wnt/β-catenin signalling in mesodermal specification, *T-brachyury::eGFP* mESCs were differentiated as EBs in phase-separation with TREx-293^{Cdh3}, TREx-293$^{Cdh3\text{-}Wnt3a}$, or standalone. No detectable GFP signalling was detected under fluorescence microscopy on day 3 (not shown), mimicking the Wnt/β-catenin signalling timeline (Figure 31). At day 4, T-brachyury/GFP expression could be detected within EBs via fluorescence microscopy (Figure 38A). In standalone differentiations, GFP followed limited localization and diffuse distribution (Figure 38A, left). In EB-TREx-293^{Cdh3} co-aggregates, GFP assumed a similar distribution with no consistent relationship to TREx-293^{Cdh3}; GFP signal could be detected close to TREx-293^{Cdh3}, avoiding TREx-293^{Cdh3}, or ignoring TREx-293^{Cdh3} locales (Figure 38A, middle). However, T-brachyury/GFP populations emerged within EB areas juxtaposed to TREx-293$^{Cdh3\text{-}Wnt3a}$ (Figure 38A, right), suggesting mesodermal specification is controlled by TREx-293-derived Wnt3a in these systems. This reflects the signalling responses seen in *7xtcf/lef* EBs (Figure 31), albeit in a more restricted area and in dimmer intensity. However, GFP could be seen occasionally in areas beyond TREx-293-juxtaposed locales, suggesting that either mesoderm can also emerge through mESC-autonomous events, or that TREx-293$^{Cdh3\text{-}Wnt3a}$-specified mesoderm undergoes deep migrations within/along the EB.

To elucidate Wnt/β-catenin-dependent mesodermal specification in three-dimensional detail, *7xtcf/lef::eGFP* EB-TREx-293$^{Cdh3\text{-}Wnt3a}$ co-aggregates were fixed on day 4, stained, cleared and imaged using confocal microscopy. Z-stack reconstruction and 3D projection revealed co-aggregates (DAPI, blue) in which TREx-293$^{Cdh3\text{-}Wnt3a}$ (mCherry, red), Wnt/β-catenin activated cells (GFP, green) and specified nascent mesoderm (T-brachyury, magenta) were marked (Figure 38B-C). In single EBs bearing a single TREx-293$^{Cdh3\text{-}Wnt3a}$ aggregate (Figure 38B, left), Wnt/β-catenin activated mouse cells stained bright in direct juxtaposition to TREx-293$^{Cdh3\text{-}Wnt3a}$, with cells further away decreasing in intensity and eventually reaching non-activated zones (Figure 38B-C). This reflects a polarized EB response to the localized Wnt3a source from TREx-293$^{Cdh3\text{-}Wnt3a}$. Most T-brachyury+ cells were in direct juxtaposition to TREx-293$^{Cdh3\text{-}Wnt3a}$ over a large area/interphase, with few events appearing deeper within the EB. In rare events of two EBs cross-linked by one TREx-293$^{Cdh3\text{-}Wnt3a}$ aggregate belt, most T-brachyury cells

emerged next to either side of the TREx-293$^{Cdh3\text{-}Wnt3a}$ linker within each EB (Figure 38B, right). While these experiments do not provide answers on how T-brachyury+ cells distant from TREx-293$^{Cdh3\text{-}Wnt3a}$ appeared there, they illustrate that TREx-293$^{Cdh3\text{-}Wnt3a}$ apply a gradual wave of Wnt/β-catenin signalling to the EB, and further specify T-brachyury mesoderm in directly juxtaposed mES-derived cells where strong Wnt/β-catenin signalling is active. This adds a form of pattern elaboration to the EB.

To investigate whether different conditions quantitatively affect nascent mesoderm outputs, day 4 *T-brachyury::eGFP* EBs were dissociated and analysed via flow-cytometry (akin to Figure 34 and Figure 35). A one-way ANOVA on GFP+ population compartments across the three conditions revealed no statistically significant differences (Figure 39A). When the five independent experiments were examined individually, mESC-derived EBs co-differentiated with TREx-293^{Cdh3} consistently showed a reduction in GFP+ output compared to standalone controls (Figure 39B), which was validated through a Tukey's multiple comparisons test ($P<0.05$, $n=5$). The lack of strong significance detection from the initial ANOVA might be attributed to the high experiment-to-experiment variation in overall T-brachyury induction. Interestingly, that variation was less pronounced in mESC-TREx-293$^{Cdh3\text{-}Wnt3a}$ co-aggregates (error bars in Figure 39A). When standalone T-brachyury output was high, mESC-TREx-293$^{Cdh3\text{-}Wnt3a}$ co-aggregates showed reduced T-brachyury+ fractions, whereas in experiments showing inefficient T-brachyury induction, mESC-TREx-293$^{Cdh3\text{-}Wnt3a}$ co-aggregates had increased T-brachyury yields (Figure 39B). This suggests that TREx-293$^{Cdh3\text{-}Wnt3a}$ might normalize T-brachyury emergence in EBs. To test whether distributions of T-brachyury/GFP+ percentages were significantly different between mESC-TREx-293$^{Cdh3\text{-}Wnt3a}$ and standalone conditions, the non-parametric Kolmogorov-Smirnov test was employed. Differences between compared cumulative distributions were not significant ($P=0.08$; $D=0.8$); similar results were given when comparing variances using the parametric F-test ($P=0.16$). Normalized geometric mean fluorescence intensities of GFP+ populations were also comparable ($P>0.05$, one-way ANOVA) among conditions (Figure 39C-D); fluorescence measurements were pair-wise expressed relative to standalone controls as experiments were analysed on different cytometers. Together, these results suggest that T-brachyury specification was already augmented in 3D conditions, and that EB-TREx-293$^{Cdh3\text{-}Wnt3a}$ co-aggregates differed only in the localization, and not efficiency, of T-brachyury emergence. However, TREx-293^{Cdh3} tended to reduce T-brachyury yields, whereas TREx-293$^{Cdh3\text{-}Wnt3a}$ showed a trend to normalize them by reducing experimental variation, and follow-up studies might be able to answer whether these trends are significant.

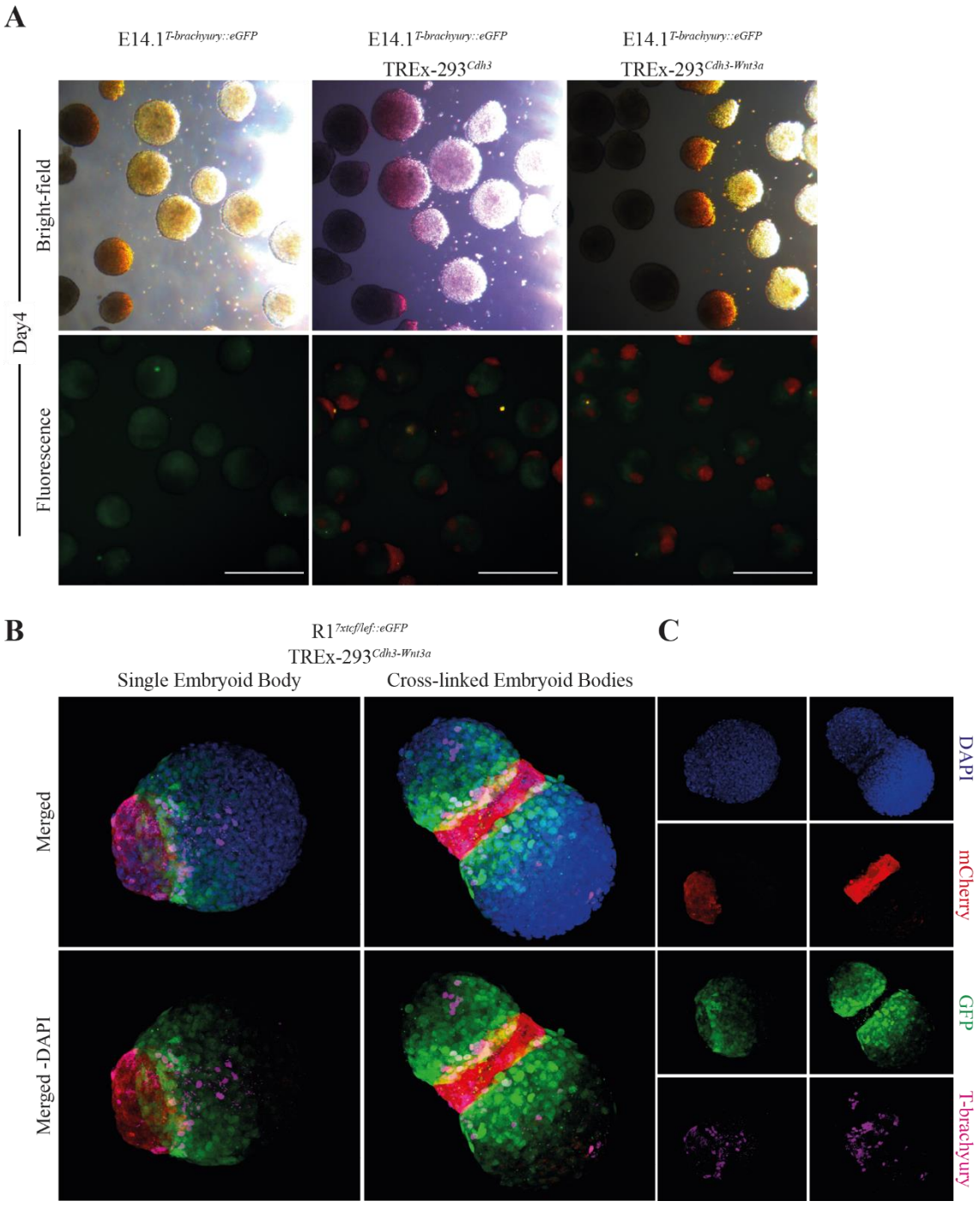

Figure 38. TREx-293$^{Cdh3\text{-}Wnt3a}$ spatially specify mesoderm induction and induce pattern elaboration in 3D embryoid body differentiations.

(A) Fluorescence microscopy of *T-brachyury::eGFP EBs* at day 4 of differentiation, marking T-brachyury expression. Scale bars: 200μm. **(B-C)** 3D-reconstructed projections of BABB-cleared *7xtcf/lef::eGFP* EBs co-cultured with TREx-293$^{Cdh3\text{-}Wnt3a}$ and fixed at day 4 of differentiation. **(B)** Shows full-colour and minus-DAPI merged panels of a single EB with a single TREx-293$^{Cdh3\text{-}Wnt3a}$ aggregate (left), or two EBs cross-linked by a TREx-293$^{Cdh3\text{-}Wnt3a}$ aggregate belt (right). **(C)** Shows single-stain channels of panels in (B). Staining panel: nuclei/DAPI (blue), TREx-293$^{Cdh3\text{-}Wnt3a}$/mCherry (red), Wnt/β-catenin pathway-activated mESCs/GFP (green), and nascent mesoderm/T-brachyury (magenta). Images were taken at magnification: x40; Zoom: 1.15.

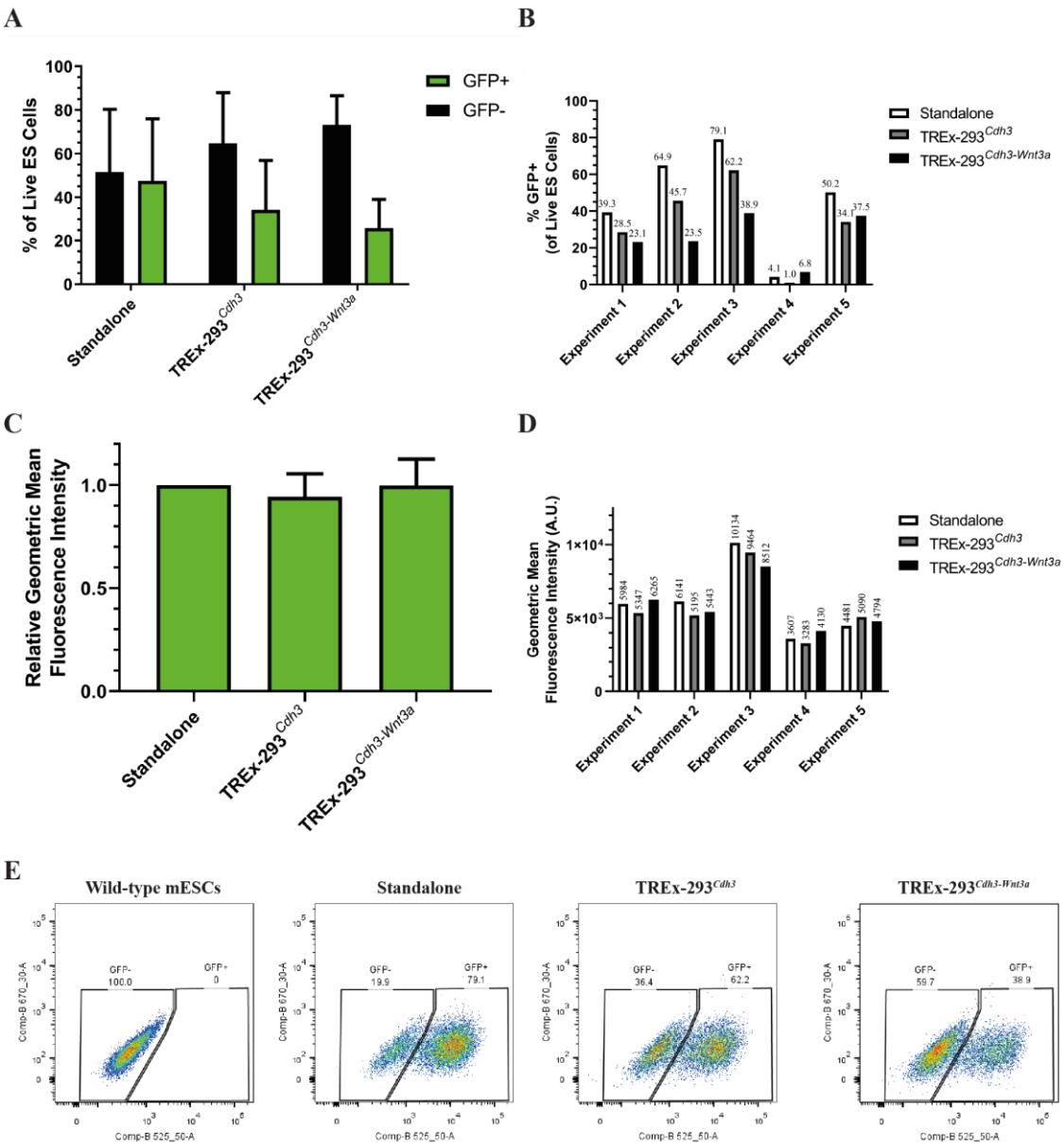

Figure 39. TREx-293$^{Cdh3\text{-}Wnt3a}$ do not affect T-brachyury percentage yields or level intensity during EBs differentiation.

(A) Flow-cytometry analysis of T-brachyury positive and negative populations from dissociated *T-brachyury::eGFP* EBs at day 4 of differentiation. Graph shows means and standard deviations from five independent experiments. **(B)** Case-by-case T-brachyury/GFP+ cells from day 4 EBs across five independent experiments shown in (A). **(C)** Geometric mean fluorescence intensity of T-brachyury/GFP+ populations. Fluorescence intensity measurements were normalized to standalone controls pair-wise, because experiments experiments 2, 4 and 5 were analysed on the same instrument/configuration, whereas experiments 1 and 3 were each analysed on different cytometers. **(D)** Case-by-case GFP geometric mean fluorescence intensities summarized in (C), paired to experiments shown in (B). **(E)** Example flow cytometry panels of day 4 *T-brachyury::eGFP* EBs at tested conditions, and day 4 EBs from wild-type IB10 blank controls (left-most panel).

3.4.3 Applying synthetic-signalling cells to higher systems

An important consideration that is especially important to synthetic biology, is modularity of engineered systems. Namely, cells engineered to express user-defined ligands should be applicable to numerous different contexts, and in more complex biological systems. To illustrate this point, focus was turned to the embryonic kidney development system, which develops from complex interactions among three populations: ureteric progenitors yielding the ureteric tree, nephrogenic progenitors that give rise to blood-filtering units termed nephrons, and stromal progenitors that form interstitial populations. These three progenitors coexist in complex communication networks, part of which is the provision of Wnt ligands from ureteric populations to nephrogenic progenitors, which triggers nephrogenesis (see section 1.2.3). This system thus provides a suitable opportunity to assess whether engineered TREx-293 systems could be applied to different biological frameworks.

Metanephric mesenchyme containing nephrogenic progenitors was dissected from the E11.5 mouse embryo by various members of the Davies lab (Julia Tarnick, Mona Elhendawi, Jamie Davies), taking care to prevent contamination from ureteric populations. Mesenchyme from 5-10 kidneys was centrifuged into an aggregate that was deposited at the air-liquid interphase of transwells seeded with TREx-293^{Cdh3}/TREx-293$^{Cdh3\text{-}Wnt3a}$. After three days of co-culture, aggregates were fixed, stained and imaged for the presence of nephrogenic progenitors (WT1, red), ureteric progenitors (Calbindin, grey), and nephrons (Jagged1, green)(Lindström et al., 2014). Metanephric mesenchyme aggregates grown on TREx-293^{Cdh3} did not exhibit nephrogenesis, except in the case of occasional contamination with a piece of ureteric bud, around which limited nephrons could be detected (Figure 40A, yellow arrow). Pronounced nephrogenesis was observed in TREx-293$^{Cdh3\text{-}Wnt3a}$ co-cultures (Figure 40A), which is statistically significant in comparison to TREx-293^{Cdh3} ($P<0.01$, unpaired t-test, $n=7$) following quantification (Figure 40B). By no means do these cultures reach the extent of nephrogenesis or self-organization exhibited in an intact kidney cultured ex vivo for the same amount of time (Figure 40A-B), but the consistency observed following experimental reproducibility (Figure 40C) highlights the achievement of a first step towards future work.

This experiment provides proof-of-concept that transgenic TREx-293 systems engineered to act as synthetic signalling centres can be applied to developmental contexts beyond early mESC differentiation.

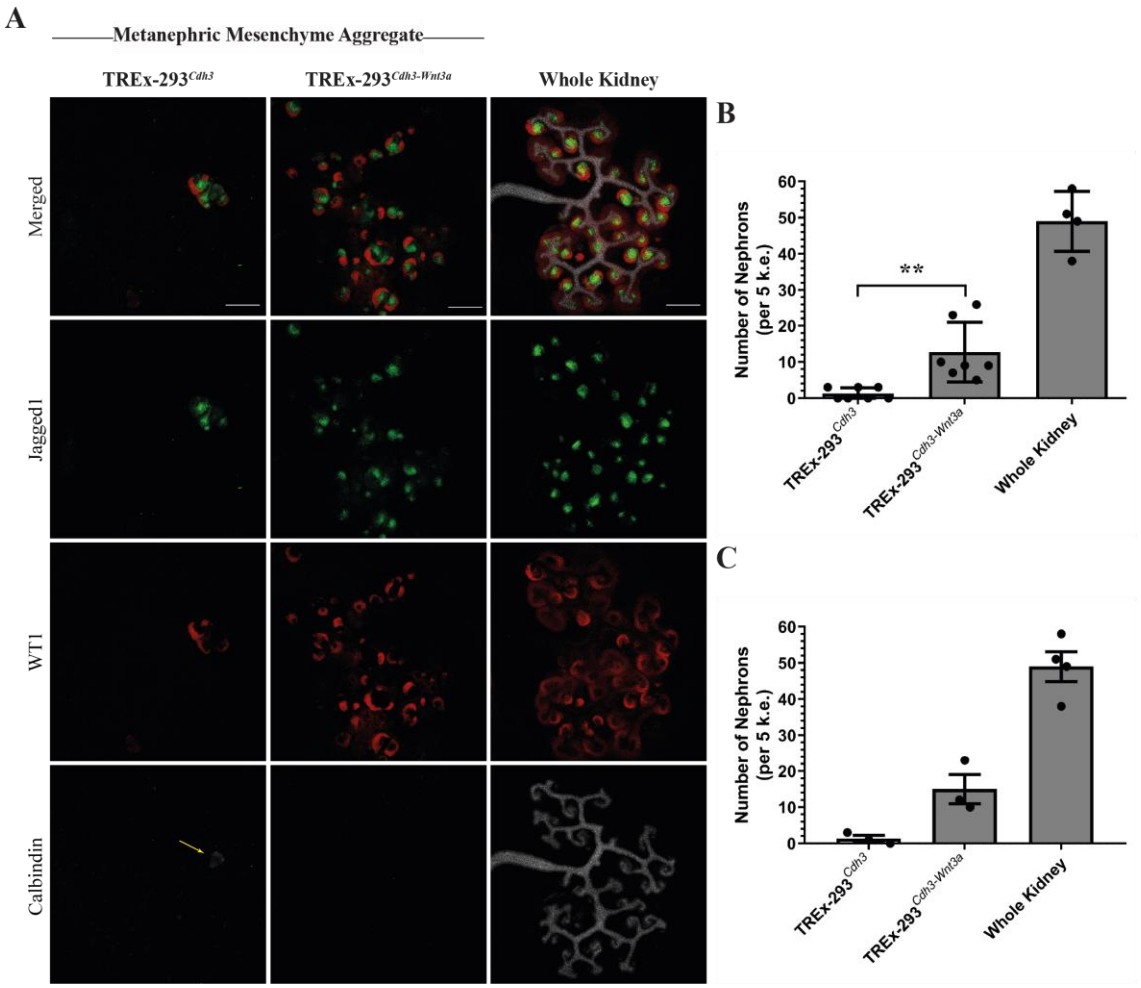

Figure 40. TREx-293$^{Cdh3\text{-}Wnt3a}$ facilitate nephrogenesis in mouse embryonic metanephric mesenchyme.

(A) Z-stack projection imaging of dissected mouse embryonic metanephric mesenchyme co-cultured directly on top of TREx-293^{Cdh3}/TREx-293$^{Cdh3\text{-}Wnt3a}$ at the air-liquid interphase of transwells for three days. Whole intact kidneys grown at the air-liquid interphase of transwells for three days are presented as staining/anatomical controls. Staining panel: Nephrons/Jagged1 (green), Nephrogenic progenitors/WT1 (red), Ureteric bud/Calbindin (grey). Yellow arrow shows ureteric bud contamination. Scale bars: 200μm. **(B)** Quantification of number of nephrons from explant cultures across three independent experiments. The number of nephrons is normalized against metanephric mesenchyme from 5 kidney equivalents (k.e.). Graph shows means and standard deviations. Statistic: unpaired t-test. **, P<0.005. **(C)** Experimental means and standard error for values shown in (B).

3.4.4 Discussion

Self-organization depends on intercellular signalling events to drive cell state segregation and pattern formation. Accordingly, many synthetic self-organizing mammalian systems rely on these principles (Matsuda et al., 2015; Morsut et al., 2016; Sekine et al., 2018; Toda et al., 2018), whereas others utilize cell-autonomous morphogenetic mechanisms such as differential adhesion (Cachat et al., 2016). However, these synthetic systems have not been utilized to control signalling events in natural systems. Addressing this gap would provide an opportunity to convert synthetic pattern formation systems into synthetic niches or organizers, thereby translating synthetic self-organization into biological self-organization.

The last two chapters describe the first steps towards this direction. By introducing Wnt3a expression in TREx-293^{Cdh3}, a developmentally important ligand is being constitutively produced and secreted in a cell-autonomous manner. Wnt3a ligand is biologically active and accumulates into the extracellular medium of these modified derivatives (TREx-293$^{Cdh3\text{-}Wnt3a}$), which can be used to successfully activate the Wnt/β-catenin pathway as judged through *7xtcf/lef::eGFP* reporter cells. A limitation of the present work is the absence of biochemical characterization in Wnt3a secretion. Specifically, post-translational modifications, namely glycosylation at Asparagine87 and Asparagine289, addition of palmitoleic acid at Serine 209, and addition of palmitic acid at Cystine77 were not evaluated (Komekado et al., 2007; Takada et al., 2006; Willert et al., 2003). More importantly, the method/form of Wnt3a secretion was not assessed either. It is unknown whether TREx-293$^{Cdh3\text{-}Wnt3a}$ conditioned media contain Wnt3a in free-diffusing monomers or oligomers, protein-bound complexes (sFRPs, WIFs, SWIM homologues, serum afamin), or in extracellular vesicles such as exosomes or liposomes (Działo et al., 2019; Gross et al., 2012; Malinauskas et al., 2011; Mii et al., 2017; Mii & Taira, 2009; Mulligan et al., 2012; Panáková et al., 2005; Takada et al., 2018). The delineation of these properties require the use of biochemical assays to investigate protein modifications (immunoblot, MassSpec) and vesicle-coupled secretion (medium fractionation and vesicle purification). Given purification and stabilization of biologically active Wnt3a offers considerable value to stem cell and organoid maintenance (Tuÿsüz et al., 2017), the established TREx-293$^{Cdh3\text{-}Wnt3a}$ line might provide an easy and stable supply of biologically active Wnt3a. For these reasons, the biochemical characterization of Wnt3a maturation and secretion from TREx-293$^{Cdh3\text{-}Wnt3a}$ becomes an important consideration.

Importantly TREx-293$^{Cdh3\text{-}Wnt3a}$ retain pattern formation capacity with Cdh1-expressing cells, such as TREx-293^{Cdh1} or mESCs. This allows self-organization between mESCs and TREx-293$^{Cdh3\text{-}Wnt3a}$ in 2D adherent conditions. Because pattern

topography depends on the initial ratio of cells mixed coupled to the growth rates of the two cells types, this system offers an easy, flexible, and user-friendly method of achieving two-dimensional mESC self-organization without the requirement of substrate micropatterning (Deglincerti et al., 2016; Manfrin et al., 2019; Warmflash et al., 2014). However, mESC colonies/shapes in the system presented herein show considerable heterogeneity, contrary to substrate micropatterning. In the future, it would be interesting to attempt to break symmetry in mESC-293 patterning systems, by coupling microfluidics-based flow to mESCs differentiating under phase-separation. Intricate experiments could be subsequently performed, such as using microfluidics to link one chamber containing differentiating mESCs (self-organized or not) to another chamber containing TREx-293 expressing user-defined signals. This has so far been performed using micropatterned colonies and biochemically purified ligands (Manfrin et al., 2019); the demonstration of cell-based organized signalling shown herein presents proof-of-concept that microfluidics-based symmetry breaking could occur using cell-based signal sources.

Importantly, the platform established herein allows self-organization and signalling in 3D conditions, which provides a significant advance compared to substrate micropatterning that is limited to 2D ESC colonies. There have been recent advances in 3D “micropatterning”, in which geometrically defined U-shaped microcavity arrays are produced and moulded with polyethylene glycol hydrogels. In these microfabricated arrays, careful consideration of seeding cell density allows for user-defined organoid homogeneity on a large scale (Brandenberg et al., 2020). Attempts to couple EB-293 phase-separation patterning to such standardized platforms, or conventional U-shaped 96-well plates to begin with, could reduce the heterogeneity of EB-293 co-aggregates and achieve highly-defined EB-293 bodies of desirable composition. This would pose an improvement to the highly heterogeneous output of EB-293 co-aggregates generated using the rotator-dish method. Initial cell ratios and seeding densities are likely to have a big impact in EB-293 composition output.

Phase-separation patterning between mESCs and TREx-293^{Cdh3} describes a first level of pattern formation. In 2D patterns, TREx-293$^{Cdh3\text{-}Wnt3a}$ activate the Wnt/β-catenin pathway homogeneously within mESC colonies, demonstrating that the state of mESC patterned colonies in these phase-separation systems can be changed by modifying TREx-293^{Cdh3} cells. In 3D patterns, mESC-derived EBs respond to localized Wnt3a production from TREx-293$^{Cdh3\text{-}Wnt3a}$ in a polarized and graduated manner. Activation of the Wnt/β-catenin pathway occurs asymmetrically within the EB, and polarized towards the TREx-293$^{Cdh3\text{-}Wnt3a}$ aggregate, demonstrating an event of symmetry breaking with regards to signal activation. Additionally, Wnt/β-catenin pathway

activation is strong in EB cells lying juxtaposed to TREx-293$^{Cdh3\text{-}Wnt3a}$, and weaker as the distance increases, representing pattern elaboration in β-catenin activation states.

Critically, organized signalling responses are propagated into meaningful lineage specification changes. In 2D phase-separation differentiations under LIF-withdrawal conditions, mESC viability is improved by 55% on average. Stable Wnt3a provision from TREx-293$^{Cdh3\text{-}Wnt3a}$ strongly upregulates T-brachyury expression at the single-cell level, as deduced from *T-brachyury::eGFP* reporter mESCs (Fehling et al., 2003). Interestingly, T-brachyury intensity appears as localized clusters within mESC colonies, suggesting further self-organization events that spatially pattern nascent mesoderm (T-brachyury) from non-mesodermal lineages within mESC colonies. It would be interesting to investigate how neuroectodermal (Sox2 or Otx2) and endodermal (FoxA2 or Sox17) markers are arranged with respect to nascent mesoderm (T-brachyury) in mESC colonies differentiated with TREx-293$^{Cdh3\text{-}Wnt3a}$ for 4 days. The increased intensity of T-brachyury in mESC colonies differentiated in phase-separation with TREx-293$^{Cdh3\text{-}Wnt3a}$ also permit the tracking and visualization of the transient T-brachyury wave, which peaked between 96-101h of differentiation (95% confidence intervals). This was not possible in mESC standalone or mESC-TREx-293^{Cdh3} control differentiations. Consequently, combining phase-separation patterning of TREx-293^{Cdh3}-mESCs, appropriate signalling ligand production from TREx-293^{Cdh3}, and relevant lineage reporters in mESCs, allow the real-time monitoring of lineage specification events during mESC differentiations, and with some spatial information.

When 2D phase-separation differentiations were extended to day 5, the presence of Eomes and Cdh2 indicated successful mesoderm induction and EMT. Interestingly, Eomes/Cdh2 co-expression appeared predominantly at the edges of mouse colonies/patches, raising the possibility of emergent self-organization and pattern elaboration. This could be explained in two ways: EMT occurs at the borders between TREx-293 and mESCs, or EMT occurs in cells within the colony and changes in adhesion properties lead their migration to the colony periphery. Given that EMT proceeds via change of cadherin profiles (loss of Cdh1, gain of Cdh2), it is possible that EMT-undergoing populations exit the Cdh1-positive milieu and form a new border population at the mouse-293 interphase. If this is true, it would not only represent a form of pattern elaboration, but also the demonstration that mESC-TREx-293^{Cdh3} systems are morphodynamic, meaning that morphogenetic changes occurring within differentiating mESCs feed-back and change the properties of the phase-separation pattern. Therefore, there is the possibility that, as mESCs differentiate, the mESC-TREx-293^{Cdh3} pattern undergoes elaboration or disintegration. Future experiments are required to explore these possibilities.

In 3D EB differentiations, polarized Wnt/β-catenin activation from TREx-293$^{Cdh3\text{-}Wnt3a}$ aggregates leads to asymmetry in T-brachyury specification. Specifically, the majority of T-brachyury+ cells emerge proximal/juxtaposed to the TREx-293$^{Cdh3\text{-}Wnt3a}$ cluster, representing symmetry breaking within the EB at the level of lineage specification. As in 2D differentiations, EB phase-separation differentiations do not produce any quantitative difference in T-brachyury+ output. It should be noted that not all T-brachyury+ cells emerge juxtaposed to TREx-293$^{Cdh3\text{-}Wnt3a}$, suggesting that TREx-293^{Cdh3}-based cells influence, but do not absolutely determine, differentiation events within the EB. Additionally, there is considerable experiment-to-experiment variation in T-brachyury+ output, potentially due to subtle differences in starting differentiation conditions, specifically the state of mESCs at the beginning of differentiation, which might amplify into large changes along EB differentiation. Some of these culture factors might be i) MEF age-dependent quality (i.e. irradiated MEFs being qualitatively different at 3 vs 6 days post-thawing), ii) average colony size and iii) colony density per well. It is currently unknown how specifically these factors affect the epigenetic state of mESCs, and their lineage propensity/bias following differentiation. However, TREx-293$^{Cdh3\text{-}Wnt3a}$ tend to normalize T-brachyury outputs in *Tbrachyury::eGFP* day 4 EBs. These results demonstrate the first steps taken towards controlling cell fate decisions during EB differentiation at the level of spatial organization, by engineering synthetic developmental organizers. The unique property of this system is that “synthetic organizer cells” retain self-organization with respect to the differentiation entity (EB), showing spatial segregation and minimal intermingling due to cadherin-based phase-separation. This represents a significant advance compared to previous synthetic biology-inspired attempts, in which signal-producing cells and differentiation samples did not retain any self-organization properties with respect to one another, which hinder the organization of differentiation responses (Cederquist et al., 2019; Sagy et al., 2019). The possibility of readily controlling EB-293 co-aggregate composition by modulating mESC:293 cell ratios and initial seeding density, combined with the conditional expression of user-defined signals, will lead to further progress in controlling self-organization in stem cell-derived EB and organoid differentiations.

Altogether, this line of work validates hypothesis II, showing that Wnt3a expression from HEK-293 based cells exerts organized Wnt/β-catenin responses in a phase-separation pattern, at least in 3D. These polarized Wnt3a/β-catenin signalling events influence the spatial localization of nascent mesoderm induction in patterned co-cultures, without affecting yields, thus also addressing hypothesis III.

4 FINAL DISCUSSION

Patterning underpins the emergence of complexity in an orderly fashion within the developing organism. Pattern formation is typically followed by growth and further pattern elaboration to increase organization of a dynamic multicellular field. While patterning can be symmetrical, it often exhibits a degree of asymmetry and acquires a sense of polarity through a process described as symmetry breaking. These themes, summarized as self-organization, operate recurrently at various scales throughout development, leading to formation of highly structured tissues and organs.

Self-organization is imperative for regenerative medicine. The derivation of physiological organoids from embryonic and adult stem cells is critical for modelling of multicellular processes (development, homeostasis, regeneration), accurate pharmacological screening, and eventually therapeutic transplantations. For these reasons, engineering self-organization in stem cell-derived organoids is important for both basic research and biomedical applications (reviewed in (Brassard & Lutolf, 2019)).

In their ability to model embryonic development, embryonic stem cells (ESCs) possess remarkable inherent self-organization capacities. When ESCs are micro-patterned as geometrically defined colonies and are allowed to differentiate, lineage markers emerge in radial concentric domains depending on the specific differentiation conditions (Britton et al., 2019; Etoc et al., 2016; Heemskerk et al., 2019; Tewary et al., 2017; Warmflash et al., 2014). Symmetry can be broken through the polarized delivery of growth factors using microfluidics (Manfrin et al., 2019). When ESCs are aggregated into three-dimensional spheroids termed embryoid bodies (EBs), they also demonstrate self-organization during differentiation. Akin to the developing embryo, the Wnt/β-catenin pathway is implicated in mesodermal specification and endothelial-to-mesenchymal transition (EMT) that is characteristic of gastrulation (ten Berge et al., 2008). By activating the Wnt/β-catenin pathway between 48-72h of differentiation, through exogenous provision of Wnt3a or CHIRON-99021, small EBs undergo symmetry breaking and develop into gastruloids that acquire characteristics of anteroposterior patterning and gastrulation events (Beccari et al., 2018; Turner et al., 2017; Van Den Brink et al., 2014). Three-dimensional gastruloids have also been established from human ESCs, providing a window to interrogate processes of gastrulation in vitro (Moris et al., 2020). Early attempts to control EB and organoid heterogeneity and organization have focussed on user-defined microfabrication of hydrogel-moulded cavities (Brandenberg et al., 2020).

An entirely different approach towards engineering self-organization is to program it using synthetic biology. Bottom-up engineering of genetic circuits that drive pattern formation has been used to produce self-organization in bacteria (Basu et al., 2005; Boehm et al., 2018; Glass & Riedel-Kruse, 2018; C. Liu et al., 2011) and mammalian cells (Cachat et al., 2016; Matsuda et al., 2015; Morsut et al., 2016; Sekine et al., 2018; Toda et al., 2018) in vitro. In these genetic modules, pattern formation was achieved either through cell-autonomous morphogenetic mechanisms (e.g. programmable adhesions), customized responses to positional information, or integration of the two. These devices test pattern formation in a direct manner (level-one), i.e. whether the genetic devices themselves can impart self-organization to the desirable hosts into which they were introduced. As such, they represent early steps of programming pattern formation using synthetic biology. More mature approaches, through which synthetic self-organizing systems can modulate pattern formation in natural non-engineered cells (level-two) are currently lacking.

Synthetic biology-inspired approaches to enhance self-organization in stem cell-derived systems have been described. These approaches rely on overexpression of transcription factors and emergent self-organization based on uncharacterized mechanisms (Guye et al., 2016), the use of signal-producing cell lines to skew EB differentiation (Sagy et al., 2019), or chimeric organoids formed through the fusion of wild-type and signal-producing pluripotent stem cells (Cederquist et al., 2019). However, these strategies suffer from differing degrees of high heterogeneity, poor efficiency, or lack of characterization, and in none of them are the signal-producing cells self-organized with respect to the differentiation entity of interest. Moreover, the modularity of these tools has not been proven, and this is a significant setback in consideration of standards for synthetic biology.

This thesis set out to provide proof-of-concept work to bridge synthetic pattern formation with biological stem cell self-organization. To pursue and illustrate this, a rational step-wise workflow was followed: The first aim was to program a new synthetic pattern formation system. The second aim was to couple signal production to specific topological domains of a self-organizing system. The third aim was to use these self-organizing, signal-producing systems as tools to control developmental and stem cell fate decisions. In essence, such systems should act as prototypic synthetic niches or synthetic organizers.

To expand the synthetic pattern formation toolbox, the first aim focused on generating a new pattern formation system. Inspired by hyperuniform distributions of cone photoreceptors in the avian retina (Jiao et al., 2014; Kram et al., 2010), it was hypothesized that heterotypic cell adhesions mediated by integrin-ligand heterophilic

adhesions would suffice to mimic elements of hyperuniformity. Dedicated integrins (LFA-1 or MAC-1) and cognate ligand (ICAM-1) were separately introduced in HEK-293 derivative cells (TREx-293) by knocking tetracycline-inducible transgenes into the *ROSA26* locus via CRISPR genome editing. Although transgenes were expressed in a tetracycline-inducible manner, accumulated on the cell surface at very high levels, and were biologically functional, they were not able to drive heterotypic intermingling and the formation of hyperuniform-type patterns. A few unexpected findings from this section deserve mentioning. Firstly, MAC-1 and ICAM-1 imparted morphological changes to TREx-293 cells: MAC-1 led to extensive cell spreading, flattened morphology, potential lamellipodia formation, and strong adherence for conventional and low-adherence culture surfaces. ICAM-1 led to reduced cell surface and cluster-like three-dimensional growth during adherent culture. As such, TREx-293^{ICAM-1} and TREx-293^{MAC-1} cells unexpectedly expand the morphogenetic toolkit for purposes of synthetic morphology (Cachat et al., 2014). Secondly, the unexpected adherence of TREx-293 to ICAM-1 via a MAC-1/LFA-1-independent receptor can be further explored to identify a novel ICAM-1 receptor. Thirdly, given that these integrin-ligand pairs failed to induce pattern formation, the original strategy for engineering hyperuniformity should be revisited, with focus on ensuring orthogonal, custom heterophilic interactions. This could be achieved by replacing ectodomains of mammalian receptors (integrins, or even better cadherins) with ligand/receptor epitopes characterized by defined interactions (e.g. antigen-nanobody). This bottom-up engineering should combine custom heterotypic interactions, as utilized in synthetic bacterial adhesins (Glass & Riedel-Kruse, 2018), with mammalian receptor engineering, as described in the construction of SynNotch (Morsut et al., 2016).

Given that the integrin-ligand heterophilic approach did not lead to pattern formation, the signalling ligand of choice was added to a pre-existing synthetic patterning system for the second aim of the thesis. The murine Wnt3a signalling ligand was chosen due to its lipophilic nature and associated limited diffusion range (Komekado et al., 2007; Takada et al., 2006, 2018; Willert et al., 2003), its involvement in developmental and stem cell contexts (Berge et al., 2011; P. Liu et al., 1999; ten Berge et al., 2008; Yamaguchi, Takada, et al., 1999), and the combination of challenges surrounding Wnt3a biochemical purification and benefits in organoid applications (Tuÿsüz et al., 2017). By introducing Wnt3a expression from TREx-293^{Cdh3}, which form phase-separation patterns with TREx-293^{Cdh1} (Cachat et al., 2016), the slowly diffusing Wnt3a ligand could be produced from topologically distinct compartments of a synthetic pattern formation system. It was also demonstrated that TREx-293^{Cdh3}-based cells could self-organize with mESCs that physiologically express Cdh1, suggesting modularity of the phase-separation patterning system on the grounds of distinct cells differentially expressing

Cdh1 or Cdh3. Importantly, TREx-293$^{Cdh3\text{-}Wnt3a}$ cells could activate β-catenin responses in mESCs: strongly and homogeneously in two-dimensional co-cultures, but polarized and in a gradient-like manner in EB-293 three-dimensional co-aggregates. In the EB-293 co-aggregates, β-catenin responses extended well beyond 1-3 cell layers, in contrast to narrow diffusion ranges observed in other previously examined conditions (Farin et al., 2016; Mii et al., 2017; Stanganello et al., 2015). These could be attributed to the expression of Wnt expanders from mESCs, TREx-293 cell-autonomous long-range secretion (Wnt expanders/extracellular vesicles), or other factors (serum proteins or transcytosis). Alternatively, the extension of β-catenin responses could be a function of high (CMV-based) Wnt3a expression and mESC:TREx-293$^{Cdh3\text{-}Wnt3a}$ cell ratios in EB-293 co-aggregates. The establishment of this synthetic system allows for delineation of these possibilities. Importantly, it represents the first “level-two” self-organization platform, whereby an engineered, synthetic pattern formation system can exert changes in pattern formation and elaboration to a non-engineered, natural, stem cell-based system.

To address the third aim of this thesis, the phase-separation Wnt-producing patterning system was used to control mESC differentiation decisions (nascent mesoderm induction via expression of the T-brachyury marker) in two and three-dimensional differentiation conditions. In 2D, this platform upregulated the expression of a *T-brachyury::eGFP* fluorescent reporter at the single-cell level. In differentiating colonies, T-brachyury emerged in localized clusters, implying further self-organization potentially occurring within mESC colonies. Due to the increased cellular fluorescent levels in combination with the clustered emergence, this platform permitted the real-time tracking of nascent mesoderm specification in stem cell differentiations. These cultures fulfilled mesoderm induction and epithelial-to-mesenchymal transition by day 5, showing expression of Eomes and Cdh2. Notably, these markers appeared predominantly at the interface between Cdh3-expressing TREx-293 and mESC-derived colonies, raising the possibility of pattern elaboration through a three-layer (Cdh3-Cdh2-Cdh1) phase-separation. This would illustrate the morphodynamic nature of this self-organizing system. In 3D, the polarized β-catenin signalling responses in EB-293 co-aggregates were able to break symmetry in the EB, through the majority of T-brachyury positive cells emerging proximal to the TREx-293$^{Cdh3\text{-}Wnt3a}$ cluster. Consequently, the fulfilment of this thesis aim provides proof-of-concept that synthetic self-organizing systems, when engineered to express appropriate ligands, can be used to control self-organization during stem cell differentiation.

Contrary to previous synthetic biology-inspired approaches (Cederquist et al., 2019; Guye et al., 2016; Sagy et al., 2019), the tools generated through this thesis are stable, can be systematically and extensively characterized, and retain self-organization

with the differentiating stem cells of interest (at least mESC on the basis of Cdh1 expression). In addition, modularity of this synthetic system was demonstrated through its ability to facilitate nephrogenesis from mouse embryo-derived metanephric mesenchyme, a tissue that contains nephrogenic progenitor cells that can develop into blood-filtering nephrons when stimulated by the Wnt/β-catenin pathway (Karner et al., 2011; Park et al., 2012). This demonstrates that TREx-293$^{Cdh3\text{-}Wnt3a}$ can be used as tools to control fate decisions in higher/maturing developmental systems. A further advancement and consolidation of this point would be to use TREx-293$^{Cdh3\text{-}Wnt3a}$ to enhance nephrogenesis from human induced pluripotent stem cell-derived kidney organoids (in progress).

This line of work represents early steps in the maturation of synthetic biology-based self-organizing systems. The majority (if not all) of synthetic pattern formation systems test whether genetic devices can implement pattern formation when introduced in host cells of interest (level-one). This thesis describes the first establishment of synthetic self-organizing cell systems that can exert control over self-organization (pattern formation, elaboration, symmetry breaking) in natural non-engineered systems (level-two). This relationship is linear/unidirectional, meaning that synthetic organized signal producer cells trigger hierarchical induction in differentiating stem cells. In the future, synthetic organized signal producer cells could be engineered to respond to signalling molecules produced from certain stem cell-derived lineages. The responses could provide feedback to the production of the initial signalling ligand, modulation of its diffusion range, production of a different signalling ligand, expression of a fluorescent reporter, or morphogenetic behaviours such as change of adhesion properties, migration or apoptosis (Cachat et al., 2014). In essence, synthetic cells would detect when differentiations reach a certain developmental point or output efficiency, and respond accordingly to report for emergence of desired lineages or automatically shape differentiation trajectories. In effect, engineering feedback loops between synthetic and natural cells would change induction events from hierarchical to emergent (level-three), allowing the construction of highly sophisticated synthetic organizers. Such cell-based devices would be able to recapitulate natural developmental interactions more realistically, as complex patterning and self-organization mechanisms rely on complex regulatory networks that demonstrate a high degree of interconnection of their constituent components/modules (see section 1.1-1.2). By demonstrating the efficacy of level-two systems, this thesis allows for advancement to level-three.

During development, events of fate induction, positional information, and axial patterning rely on localized groups of cells known as developmental organizers. Within the patterning field in which they operate, organizers secrete pathway agonists and

localize at one pole, whereas counter-organizers secrete pathway antagonists and localize to the opposite pole, setting opposing Wolpert-style gradients (see section 1.2.2). Based on synthetic biology approaches described herein, naïve cell lines can be converted to synthetic organizers or counter-organizers, by engineering expression of dedicated pathway agonists or antagonists respectively. Concerning gastrulation, TREx-293^{Cdh3} cells could be converted into organizers by introducing co-expression of *Wnt3a* and *Fgf8*, or counter-organizers by introducing co-expression of *Cer1* and *Lefty1*. Engineering such synthetic organizers/counter-organizers, and coupling them to opposing poles of differentiating EBs or gastruloids, might lead to unprecedented improvements in developmental self-organization in vitro. This thesis aims to provide proof-of-concept that this synthetic biology-based approach to engineer self-organization in stem cell-derived entities is feasible.

In 1978, Schofield proposed the idea of a dedicated anatomical site that enabled the maintenance and self-renewal of stem cells and inhibited their differentiation, in what he called “the stem cell niche” (Schofield, 1978). It is now widely accepted that stem cell behaviour and fate fecisions are highly dependent on their microenvironment and interactions occurring at distinct niches. Over the years, there has been increasing interest in studying, characterizing, isolating and recreating stem cell niches; the idea of engineering synthetic stem cell niches is not new. Synthetic biology provides an alternative bottom-up approach to engineer such synthetic niches. The work in this thesis illustrates that, by engineering expression of desirable factors in naïve cell lines, and by co-culturing such synthetic signal producers with stem cells in a patterned manner, stem cell decisions can be predictably controlled on the basis of inductive intractions. This work provides an alternative outlook to the construction of synthetic stem cell niches.

Through this thesis, I argue that synthetic biology can be used to improve self-organization in contemporary stem cell differentiation regimes by engineering synthetic niches or synthetic organizers. Naïve cell lines, initially programmed to undergo pattern formation, subsequently produce signalling ligands from discrete pattern domains. These synthetic cell-based systems activate signalling responses in an organized fashion, and control aspects of fate decisions, pattern elaboration, and symmetry breaking in stem cell differentiations. They can be considered as modular devices, applicable to different contexts. Prototypic synthetic niches/organizers generated through this line of work, in combination with proof-of-concept experiments, and in light of the points raised in the discussion, should provide the foundations for future work. The contribution of this thesis to the scientific community and general human knowledge is desired to be conceptual.

5 REFERENCES

Akieda, Y., Ogamino, S., Furuie, H., Ishitani, S., Akiyoshi, R., Nogami, J., Masuda, T., Shimizu, N., Ohkawa, Y., & Ishitani, T. (2019). Cell competition corrects noisy Wnt morphogen gradients to achieve robust patterning in the zebrafish embryo. *Nature Communications*, *10*(1). https://doi.org/10.1038/s41467-019-12609-4

Alexandre, C., Baena-Lopez, A., & Vincent, J. P. (2014). Patterning and growth control by membrane-tethered wingless. *Nature*, *505*(7482), 180–185. https://doi.org/10.1038/nature12879

Andersson, O., Bertolino, P., & Ibáñez, C. F. (2007). Distinct and cooperative roles of mammalian Vg1 homologs GDF1 and GDF3 during early embryonic development. *Developmental Biology*, *311*(2), 500–511. https://doi.org/10.1016/j.ydbio.2007.08.060

Andre, P., Song, H., Kim, W., Kispert, A., & Yang, Y. (2015). Wnt5a and Wnt11 regulate mammalian anterior-posterior axis elongation. *Development (Cambridge)*, *142*(8), 1516–1527. https://doi.org/10.1242/dev.119065

Apaolaza, P. S., Delgado, D., Pozo-Rodríguez, A. Del, Gascón, A. R., & Solinís, M. Á. (2014). A novel gene therapy vector based on hyaluronic acid and solid lipid nanoparticles for ocular diseases. *International Journal of Pharmaceutics*, *465*(1–2), 413–426. https://doi.org/10.1016/j.ijpharm.2014.02.038

Argelaguet, R., Clark, S. J., Mohammed, H., Stapel, L. C., Krueger, C., Kapourani, C. A., Imaz-Rosshandler, I., Lohoff, T., Xiang, Y., Hanna, C. W., Smallwood, S., Ibarra-Soria, X., Buettner, F., Sanguinetti, G., Xie, W., Krueger, F., Göttgens, B., Rugg-Gunn, P. J., Kelsey, G., … Reik, W. (2019). Multi-omics profiling of mouse gastrulation at single-cell resolution. *Nature*, *576*(7787), 487–491. https://doi.org/10.1038/s41586-019-1825-8

Arnaout, M. A. (2016). Biology and structure of leukocyte β2 integrins and their role in inflammation. *F1000Research*, *5*, 2433. https://doi.org/10.12688/f1000research.9415.1

Atherton, P., Stutchbury, B., Wang, D. Y., Jethwa, D., Tsang, R., Meiler-Rodriguez, E., Wang, P., Bate, N., Zent, R., Barsukov, I. L., Goult, B. T., Critchley, D. R., & Ballestrem, C. (2015). Vinculin controls talin engagement with the actomyosin machinery. *Nature Communications*, *6*. https://doi.org/10.1038/ncomms10038

Bänziger, C., Soldini, D., Schütt, C., Zipperlen, P., Hausmann, G., & Basler, K. (2006). Wntless, a Conserved Membrane Protein Dedicated to the Secretion of Wnt Proteins from Signaling Cells. *Cell*, *125*(3), 509–522. https://doi.org/10.1016/j.cell.2006.02.049

Bardot, E. S., & Hadjantonakis, A. K. (2020). Mouse gastrulation: Coordination of tissue patterning, specification and diversification of cell fate. *Mechanisms of Development*, *163*. https://doi.org/10.1016/j.mod.2020.103617

Bartscherer, K., Pelte, N., Ingelfinger, D., & Boutros, M. (2006). Secretion of Wnt ligands requires Evi, a conserved transmembrane protein. *Cell*, *125*(3), 523–533. https://doi.org/10.1016/j.cell.2006.04.009

Basson, M. A., Akbulut, S., Watson-Johnson, J., Simon, R., Carroll, T. J., Shakya, R., Gross, I., Martin, G. R., Lufkin, T., McMahon, A. P., Wilson, P. D., Costantini, F. D., Mason, I. J., & Licht, J. D. (2005). Sprouty1 is a critical regulator of GDNF/RET-

mediated kidney induction. *Developmental Cell*, *8*(2), 229–239. https://doi.org/10.1016/j.devcel.2004.12.004

Basu, S., Gerchman, Y., Collins, C. H., Arnold, F. H., & Weiss, R. (2005). A synthetic multicellular system for programmed pattern formation. *Nature*, *434*(7037), 1130–1134. https://doi.org/10.1038/nature03461

Beccari, L., Moris, N., Girgin, M., Turner, D. A., Baillie-Johnson, P., Cossy, A. C., Lutolf, M. P., Duboule, D., & Arias, A. M. (2018). Multi-axial self-organization properties of mouse embryonic stem cells into gastruloids. *Nature*, *562*(7726), 272–276. https://doi.org/10.1038/s41586-018-0578-0

Beck, S., Le Good, J. A., Guzman, M., Haim, N. Ben, Roy, K., Beermann, F., & Constam, D. B. (2002). Extraembryonic proteases regulate Nodal signalling during gastrulation. *Nature Cell Biology*, *4*(12), 981–985. https://doi.org/10.1038/ncb890

Becker, A. J., McCulloch, E. A., & Till, J. E. (1963). Cytological demonstration of the clonal nature of spleen colonies derived from transplanted mouse marrow cells. *Nature*, *197*(4866), 452–454. https://doi.org/10.1038/197452a0

Ben-Haim, N., Lu, C., Guzman-Ayala, M., Pescatore, L., Mesnard, D., Bischofberger, M., Naef, F., Robertson, E. J. J., & Constam, D. B. (2006). The Nodal Precursor Acting via Activin Receptors Induces Mesoderm by Maintaining a Source of Its Convertases and BMP4. *Developmental Cell*, *11*(3), 313–323. https://doi.org/10.1016/j.devcel.2006.07.005

Berge, D. Ten, Kurek, D., Blauwkamp, T., Koole, W., Maas, A., Eroglu, E., Siu, R. K., & Nusse, R. (2011). Embryonic stem cells require Wnt proteins to prevent differentiation to epiblast stem cells. *Nature Cell Biology*, *13*(9), 1070–1077. https://doi.org/10.1038/ncb2314

Bernier, A. J., Zhang, J., Lillehoj, E., Shaw, A. R. E., Gunasekara, N., & Hugh, J. C. (2011). Non-cysteine linked MUC1 cytoplasmic dimers are required for Src recruitment and ICAM-1 binding induced cell invasion. *Molecular Cancer*, *10*. https://doi.org/10.1186/1476-4598-10-93

Bier, E., & De Robertis, E. M. (2015). BMP gradients: A paradigm for morphogen-mediated developmental patterning. *Science*, *348*(6242), aaa5838–aaa5838. https://doi.org/10.1126/science.aaa5838

Boehm, C. R., Grant, P. K., & Haseloff, J. (2018). Programmed hierarchical patterning of bacterial populations. *Nature Communications*, *9*(1). https://doi.org/10.1038/s41467-018-03069-3

Böttcher, R. T., Veelders, M., Rombaut, P., Faix, J., Theodosiou, M., Stradal, T. E., Rottner, K., Zent, R., Herzog, F., & Fässler, R. (2017). Kindlin-2 recruits paxillin and Arp2/3 to promote membrane protrusions during initial cell spreading. *Journal of Cell Biology*, *216*(11), 3785–3798. https://doi.org/10.1083/jcb.201701176

Bradley, A., Evans, M., Kaufman, M. H., & Robertson, E. (1984). Formation of germ-line chimaeras from embryo-derived teratocarcinoma cell lines. *Nature*, *309*(5965), 255–256. https://doi.org/10.1038/309255a0

Brandenberg, N., Hoehnel, S., Kuttler, F., Homicsko, K., Ceroni, C., Ringel, T., Gjorevski, N., Schwank, G., Coukos, G., Turcatti, G., & Lutolf, M. P. (2020). High-throughput automated organoid culture via stem-cell aggregation in microcavity arrays. *Nature Biomedical Engineering*, 1–12. https://doi.org/10.1038/s41551-020-0565-2

Brassard, J. A., & Lutolf, M. P. (2019). Engineering Stem Cell Self-organization to Build Better Organoids. In *Cell Stem Cell* (Vol. 24, Issue 6, pp. 860–876). Cell Press. https://doi.org/10.1016/j.stem.2019.05.005

Brennan, J., Lu, C. C., Norris, D. P., Rodriguez, T. A., Beddington, R. S. P., & Robertson, E. J. (2001). Nodal signalling in the epiblast patterns the early mouse embryo.

Nature, *411*(6840), 965–969. https://doi.org/10.1038/35082103

Britton, G., Heemskerk, I., Hodge, R., Qutub, A. A., & Warmflash, A. (2019). A novel self-organizing embryonic stem cell system reveals signaling logic underlying the patterning of human ectoderm. *Development (Cambridge)*, *146*(20). https://doi.org/10.1242/dev.179093

Cachat, E., Liu, W., Hohenstein, P., & Davies, J. A. (2014). A library of mammalian effector modules for synthetic morphology. *Journal of Biological Engineering*, *8*(1), 26. https://doi.org/10.1186/1754-1611-8-26

Cachat, E., Liu, W., Martin, K. C., Yuan, X., Yin, H., Hohenstein, P., & Davies, J. A. (2016). 2- and 3-Dimensional Synthetic Large-Scale De Novo Patterning By Mammalian Cells Through Phase Separation. *Scientific Reports*, *6*, 20664. https://doi.org/10.1038/srep20664

Campbell, I. D., & Humphries, M. J. (2011). Integrin structure, activation, and interactions. *Cold Spring Harbor Perspectives in Biology*, *3*(3), 1–14. https://doi.org/10.1101/cshperspect.a004994

Cano, A., Pérez-Moreno, M. A., Rodrigo, I., Locascio, A., Blanco, M. J., Del Barrio, M. G., Portillo, F., & Nieto, M. A. (2000). The transcription factor Snail controls epithelial-mesenchymal transitions by repressing E-cadherin expression. *Nature Cell Biology*, *2*(2), 76–83. https://doi.org/10.1038/35000025

Carroll, T. J., Park, J. S., Hayashi, S., Majumdar, A., & McMahon, A. P. (2005). Wnt9b plays a central role in the regulation of mesenchymal to epithelial transitions underlying organogenesis of the mammalian urogenital system. *Developmental Cell*, *9*(2), 283–292. https://doi.org/10.1016/j.devcel.2005.05.016

Carver, E. A., Jiang, R., Lan, Y., Oram, K. F., & Gridley, T. (2001). The Mouse Snail Gene Encodes a Key Regulator of the Epithelial-Mesenchymal Transition. *Molecular and Cellular Biology*, *21*(23), 8184–8188. https://doi.org/10.1128/mcb.21.23.8184-8188.2001

Cederquist, G. Y., Asciolla, J. J., Tchieu, J., Walsh, R. M., Cornacchia, D., Resh, M. D., & Studer, L. (2019). Specification of positional identity in forebrain organoids. *Nature Biotechnology*, *37*(4), 436–444. https://doi.org/10.1038/s41587-019-0085-3

Chang, L., Azzolin, L., Di Biagio, D., Zanconato, F., Battilana, G., Lucon Xiccato, R., Aragona, M., Giulitti, S., Panciera, T., Gandin, A., Sigismondo, G., Krijgsveld, J., Fassan, M., Brusatin, G., Cordenonsi, M., & Piccolo, S. (2018). The SWI/SNF complex is a mechanoregulated inhibitor of YAP and TAZ. *Nature*, *563*(7730), 265–269. https://doi.org/10.1038/s41586-018-0658-1

Chazaud, C., Yamanaka, Y., Pawson, T., & Rossant, J. (2006). Early Lineage Segregation between Epiblast and Primitive Endoderm in Mouse Blastocysts through the Grb2-MAPK Pathway. *Developmental Cell*, *10*(5), 615–624. https://doi.org/10.1016/j.devcel.2006.02.020

Chen, C., Ware, S. M., Sato, A., Houston-Hawkins, D. E., Habas, R., Matzuk, M. M., Shen, M. M., & Brown, C. W. (2006). The Vg1-related protein Gdf3 acts in a Nodal signaling pathway in the pre-gastrulation mouse embryo. *Development*, *133*(2), 319–329. https://doi.org/10.1242/dev.02210

Chen, J. F., Salas, A., & Springer, T. A. (2003). Bistable regulation of integrin adhesiveness by a bipolar metal ion cluster. *Nature Structural Biology*, *10*(12), 995–1001. https://doi.org/10.1038/nsb1011

Chen, Q., Shi, J., Tao, Y., & Zernicka-Goetz, M. (2018). Tracing the origin of heterogeneity and symmetry breaking in the early mammalian embryo. *Nature Communications*, *9*(1), 1819. https://doi.org/10.1038/s41467-018-04155-2

Chen, W., Lou, J., & Zhu, C. (2010). Forcing switch from short- to intermediate- and long-

lived states of the αA domain generates LFA-1/ICAM-1 catch bonds. *Journal of Biological Chemistry*, *285*(46), 35967–35978. https://doi.org/10.1074/jbc.M110.155770

Cheng, H. T., Kim, M., Valerius, M. T., Surendran, K., Schuster-Gossler, K., Gossler, A., McMahon, A. P., & Kopan, R. (2007). Notch2, but not Notch1, is required for proximal fate acquisition in the mammalian nephron. *Development*, *134*(4), 801–811. https://doi.org/10.1242/dev.02773

Chi, X., Michos, O., Shakya, R., Riccio, P., Enomoto, H., Licht, J. D., Asai, N., Takahashi, M., Ohgami, N., Kato, M., Mendelsohn, C., & Costantini, F. (2009). Ret-Dependent Cell Rearrangements in the Wolffian Duct Epithelium Initiate Ureteric Bud Morphogenesis. *Developmental Cell*, *17*(2), 199–209. https://doi.org/10.1016/j.devcel.2009.07.013

Chu, V. T., Weber, T., Graf, R., Sommermann, T., Petsch, K., Sack, U., Volchkov, P., Rajewsky, K., & Kühn, R. (2016). Efficient generation of Rosa26 knock-in mice using CRISPR/Cas9 in C57BL/6 zygotes. *BMC Biotechnology*, *16*(1), 4. https://doi.org/10.1186/s12896-016-0234-4

Ciruna, B., & Rossant, J. (2001). FGF Signaling Regulates Mesoderm Cell Fate Specification and Morphogenetic Movement at the Primitive Streak. *Developmental Cell*, *1*(1), 37–49. https://doi.org/10.1016/S1534-5807(01)00017-X

Comrie, W. A., Babich, A., & Burkhardt, J. K. (2015). F-actin flow drives affinity maturation and spatial organization of LFA-1 at the immunological synapse. *Journal of Cell Biology*, *208*(4), 475–491. https://doi.org/10.1083/jcb.201406121

Cong, F., Schweizer, L., & Varmus, H. (2004). Wnt signals across the plasma membrane to activate the β-catenin pathway by forming oligomers containing its receptors, Frizzled and LRP. *Development*, *131*(20), 5103–5115. https://doi.org/10.1242/dev.01318

Conlon, F. L., Lyons, K. M., Takaesu, N., Barth, K. S., Kispert, A., Herrmann, B., & Robertson, E. J. (1994). A primary requirement for nodal in the formation and maintenance of the primitive streak in the mouse. *Development*, *120*(7), 1919–1928. https://doi.org/10.1016/0168-9525(94)90026-4

Coombs, G. S., Yu, J., Canning, C. A., Veltri, C. A., Covey, T. M., Cheong, J. K., Utomo, V., Banerjee, N., Zhang, Z. H., Jadulco, R. C., Concepcion, G. P., Bugni, T. S., Harper, M. K., Mihalek, I., Jones, C. M., Ireland, C. M., & Virshup, D. M. (2010). WLS-dependent secretion of WNT3A requires Ser209 acylation and vacuolar acidification. *Journal of Cell Science*, *123*(19), 3357–3367. https://doi.org/10.1242/jcs.072132

Corson, F., Couturier, L., Rouault, H., Mazouni, K., & Schweisguth, F. (2017). Self-organized Notch dynamics generate stereotyped sensory organ patterns in Drosophila. *Science*, *356*(6337). https://doi.org/10.1126/science.aai7407

Costantini, F., & Kopan, R. (2010). Patterning a complex organ: Branching morphogenesis and nephron segmentation in kidney development. In *Developmental Cell* (Vol. 18, Issue 5, pp. 698–712). Dev Cell. https://doi.org/10.1016/j.devcel.2010.04.008

Couturier, L., Mazouni, K., Corson, F., & Schweisguth, F. (2019). Regulation of Notch output dynamics via specific E(spl)-HLH factors during bristle patterning in Drosophila. *Nature Communications*, *10*(1), 1–13. https://doi.org/10.1038/s41467-019-11477-2

Daniels, R. W., Rossano, A. J., Macleod, G. T., & Ganetzky, B. (2014). Expression of Multiple Transgenes from a Single Construct Using Viral 2A Peptides in Drosophila. *PLoS ONE*, *9*(6), e100637. https://doi.org/10.1371/journal.pone.0100637

Das, A., Tanigawa, S., Karner, C. M., Xin, M., Lum, L., Chen, C., Olson, E. N., Perantoni, A. O., & Carroll, T. J. (2013). Stromal-epithelial crosstalk regulates kidney progenitor cell differentiation. *Nature Cell Biology*, *15*(9), 1035–1044. https://doi.org/10.1038/ncb2828

Davies, J. A., & Glykofrydis, F. (2020). Engineering pattern formation and morphogenesis. *Biochemical Society Transactions*. https://doi.org/10.1042/BST20200013

Deglincerti, A., Etoc, F., Guerra, M. C., Martyn, I., Metzger, J., Ruzo, A., Simunovic, M., Yoney, A., Brivanlou, A. H., Siggia, E., & Warmflash, A. (2016). Self-organization of human embryonic stem cells on micropatterns. *Nature Protocols*, *11*(11), 2223–2232. https://doi.org/10.1038/nprot.2016.131

Di-Gregorio, A., Sancho, M., Stuckey, D. W., Crompton, L. A., Godwin, J., Mishina, Y., & Rodriguez, T. A. (2007). BMP signalling inhibits premature neural differentiation in the mouse embryo. *Development*, *134*(18), 3359–3369. https://doi.org/10.1242/dev.005967

Diamond, M. S., Staunton, D. E., De Fougerolles, A. R., Stacker, S. A., Garcia-Aguilar, J., Hibbs, M. L., & Springer, T. A. (1990). ICAM-1 (CD54): A counter-receptor for Mac-1 (CD11b/CD18). *Journal of Cell Biology*, *111*(6 II), 3129–3139. https://doi.org/10.1083/jcb.111.6.3129

Diamond, M. S., Staunton, D. E., Marlin, S. D., & Springer, T. A. (1991). Binding of the integrin Mac-1 (CD11b/CD18) to the third immunoglobulin-like domain of ICAM-1 (CD54) and its regulation by glycosylation. *Cell*, *65*(6), 961–971. https://doi.org/10.1016/0092-8674(91)90548-D

Diaz-Cuadros, M., Wagner, D. E., Budjan, C., Hubaud, A., Tarazona, O. A., Donelly, S., Michaut, A., Al Tanoury, Z., Yoshioka-Kobayashi, K., Niino, Y., Kageyama, R., Miyawaki, A., Touboul, J., & Pourquié, O. (2020). In vitro characterization of the human segmentation clock. *Nature*, *580*(7801), 113–118. https://doi.org/10.1038/s41586-019-1885-9

Dunn, N. R., Vincent, S. D., Oxburgh, L., Robertson, E. J., & Bikoff, E. K. (2004). Combinatorial activities of Smad2 and Smad3 regulate mesoderm formation and patterning in the mouse embryo. *Development*, *131*(8), 1717–1728. https://doi.org/10.1242/dev.01072

Dustin, M. L., & Springer, T. A. (1988). Lymphocyte function-associated antigen-1 (LFA-1) interaction with intercellular adhesion molecule-1 (ICAM-1) is one of at least three mechanisms for lymphocyte adhesion to cultured endothelial cells. *Journal of Cell Biology*, *107*(1), 321–331. https://doi.org/10.1083/jcb.107.1.321

Działo, E., Rudnik, M., Koning, R. I., Czepiel, M., Tkacz, K., Baj-Krzyworzeka, M., Distler, O., Siedlar, M., Kania, G., & Błyszczuk, P. (2019). WNT3a and WNT5a transported by exosomes activate WNT signaling pathways in human cardiac fibroblasts. *International Journal of Molecular Sciences*, *20*(6). https://doi.org/10.3390/ijms20061436

Eiraku, M., Takata, N., Ishibashi, H., Kawada, M., Sakakura, E., Okuda, S., Sekiguchi, K., Adachi, T., & Sasai, Y. (2011). Self-organizing optic-cup morphogenesis in three-dimensional culture. *Nature*, *472*(7341), 51–58. https://doi.org/10.1038/nature09941

Etoc, F., Metzger, J., Ruzo, A., Kirst, C., Yoney, A., Ozair, M. Z., Brivanlou, A. H., & Siggia, E. D. (2016). A Balance between Secreted Inhibitors and Edge Sensing Controls Gastruloid Self-Organization. *Developmental Cell*, *39*(3), 302–315. https://doi.org/10.1016/j.devcel.2016.09.016

Evans, M. J., & Kaufman, M. H. (1981). Establishment in culture of pluripotential cells

from mouse embryos. *Nature*, *292*(5819), 154–156. https://doi.org/10.1038/292154a0

Farin, H. F., Jordens, I., Mosa, M. H., Basak, O., Korving, J., Tauriello, D. V. F., De Punder, K., Angers, S., Peters, P. J., Maurice, M. M., & Clevers, H. (2016). Visualization of a short-range Wnt gradient in the intestinal stem-cell niche. *Nature*, *530*(7590), 340–343. https://doi.org/10.1038/nature16937

Fehling, H. J., Lacaud, G., Kubo, A., Kennedy, M., Robertson, S., Keller, G., & Kouskoff, V. (2003). Tracking mesoderm induction and its specification to the hemangioblast during embryonic stem cell differentiation. *Development*, *130*(17), 4217–4227. https://doi.org/10.1242/dev.00589

Festuccia, N., Osorno, R., Halbritter, F., Karwacki-Neisius, V., Navarro, P., Colby, D., Wong, F., Yates, A., Tomlinson, S. R., & Chambers, I. (2012). Esrrb is a direct Nanog target gene that can substitute for Nanog function in pluripotent cells. *Cell Stem Cell*, *11*(4), 477–490. https://doi.org/10.1016/j.stem.2012.08.002

Fisher, C. E., Michael, L., Barnett, M. W., & Davies, J. A. (2001). Erk MAP kinase regulates branching morphogenesis in the developing mouse kidney. *Development*, *128*(21), 4329–4338.

Foty, R. A., & Steinberg, M. S. (2005). The differential adhesion hypothesis: A direct evaluation. *Developmental Biology*, *278*(1), 255–263. https://doi.org/10.1016/j.ydbio.2004.11.012

Friedrich, G., & Soriano, P. (1991). Promoter traps in embryonic stem cells: A genetic screen to identify and mutate developmental genes in mice. *Genes and Development*, *5*(9), 1513–1523. https://doi.org/10.1101/gad.5.9.1513

Funa, N. S., Schachter, K. A., Lerdrup, M., Ekberg, J., Hess, K., Dietrich, N., Honoré, C., Hansen, K., & Semb, H. (2015). β-Catenin Regulates Primitive Streak Induction through Collaborative Interactions with SMAD2/SMAD3 and OCT4. *Cell Stem Cell*, *16*(6), 639–652. https://doi.org/10.1016/j.stem.2015.03.008

Gagliardi, A., Mullin, N. P., Ying Tan, Z., Colby, D., Kousa, A. I., Halbritter, F., Weiss, J. T., Felker, A., Bezstarosti, K., Favaro, R., Demmers, J., Nicolis, S. K., Tomlinson, S. R., Poot, R. A., & Chambers, I. (2013). A direct physical interaction between Nanog and Sox2 regulates embryonic stem cell self-renewal. *EMBO Journal*, *32*(16), 2231–2247. https://doi.org/10.1038/emboj.2013.161

Gao, X., & Hannoush, R. N. (2014). Single-cell imaging of Wnt palmitoylation by the acyltransferase porcupine. *Nature Chemical Biology*, *10*(1), 61–68. https://doi.org/10.1038/nchembio.1392

Georgas, K., Rumballe, B., Valerius, M. T., Chiu, H. S., Thiagarajan, R. D., Lesieur, E., Aronow, B. J., Brunskill, E. W., Combes, A. N., Tang, D., Taylor, D., Grimmond, S. M., Potter, S. S., McMahon, A. P., & Little, M. H. (2009). Analysis of early nephron patterning reveals a role for distal RV proliferation in fusion to the ureteric tip via a cap mesenchyme-derived connecting segment. *Developmental Biology*, *332*(2), 273–286. https://doi.org/10.1016/j.ydbio.2009.05.578

Gierer, A., & Meinhardt, H. (1972). A theory of biological pattern formation. *Kybernetik*, *12*(1), 30–39. https://doi.org/10.1007/BF00289234

Glass, D. S., & Riedel-Kruse, I. H. (2018). A Synthetic Bacterial Cell-Cell Adhesion Toolbox for Programming Multicellular Morphologies and Patterns. *Cell*, *174*(3), 649-658.e16. https://doi.org/10.1016/j.cell.2018.06.041

Goolam, M., Scialdone, A., Graham, S. J. L., MacAulay, I. C., Jedrusik, A., Hupalowska, A., Voet, T., Marioni, J. C., & Zernicka-Goetz, M. (2016). Heterogeneity in Oct4 and Sox2 Targets Biases Cell Fate in 4-Cell Mouse Embryos. *Cell*, *165*(1), 61–74. https://doi.org/10.1016/j.cell.2016.01.047

Grimm, O., Coppey, M., & Wieschaus, E. (2010). Modelling the Bicoid gradient. In *Development* (Vol. 137, Issue 14, pp. 2253–2264). Company of Biologists. https://doi.org/10.1242/dev.032409

Gross, J. C., Chaudhary, V., Bartscherer, K., & Boutros, M. (2012). Active Wnt proteins are secreted on exosomes. *Nature Cell Biology*, *14*(10), 1036–1045. https://doi.org/10.1038/ncb2574

Guye, P., Ebrahimkhani, M. R., Kipniss, N., Velazquez, J. J., Schoenfeld, E., Kiani, S., Griffith, L. G., & Weiss, R. (2016). Genetically engineering self-organization of human pluripotent stem cells into a liver bud-like tissue using Gata6. *Nature Communications*, *7*. https://doi.org/10.1038/ncomms10243

Hartwig, S., Ho, J., Pandey, P., MacIsaac, K., Taglienti, M., Xiang, M., Alterovitz, G., Ramoni, M., Fraenkel, E., & Kreidberg, J. A. (2010). Genomic characterization of Wilms' tumor suppressor 1 targets in nephron progenitor cells during kidney development. *Development*, *137*(7), 1189–1203. https://doi.org/10.1242/dev.045732

Hatini, V., Huh, S. O., Herzlinger, D., Soares, V. C., & Lai, E. (1996). Essential role of stromal mesenchyme in kidney morphogenesis revealed by targeted disruption of Winged Helix transcription factor BF-2. *Genes and Development*, *10*(12), 1467–1478. https://doi.org/10.1101/gad.10.12.1467

Heemskerk, I., Burt, K., Miller, M., Chhabra, S., Guerra, M. C., Liu, L., & Warmflash, A. (2019). Rapid changes in morphogen concentration control self-organized patterning in human embryonic stem cells. *ELife*, *8*. https://doi.org/10.7554/eLife.40526

Heit, B., Colarusso, P., & Kubes, P. (2005). Fundamentally different roles for LFA-1, Mac-1 and α 4-integrin in neutrophil chemotaxis. *Journal of Cell Science*, *118*(22), 5205–5220. https://doi.org/10.1242/jcs.02632

Helmus, Y., Denecke, J., Yakubenia, S., Robinson, P., Lühn, K., Watson, D. L., McGrogan, P. J., Vestweber, D., Marquardt, T., & Wild, M. K. (2006). Leukocyte adhesion deficiency II patients with a dual defect of the GDP-fucose transporter. *Blood*, *107*(10), 3959–3966. https://doi.org/10.1182/blood-2005-08-3334

Horton, E. R., Byron, A., Askari, J. A., Ng, D. H. J., Millon-Frémillon, A., Robertson, J., Koper, E. J., Paul, N. R., Warwood, S., Knight, D., Humphries, J. D., & Humphries, M. J. (2015). Definition of a consensus integrin adhesome and its dynamics during adhesion complex assembly and disassembly. *Nature Cell Biology*, *17*(12), 1577–1587. https://doi.org/10.1038/ncb3257

Horton, E. R., Humphries, J. D., Stutchbury, B., Jacquemet, G., Ballestrem, C., Barry, S. T., & Humphries, M. J. (2016). Modulation of FAK and Src adhesion signaling occurs independently of adhesion complex composition. *Journal of Cell Biology*, *212*(3), 349–364. https://doi.org/10.1083/jcb.201508080

Huang, D., Guo, G., Yuan, P., Ralston, A., Sun, L., Huss, M., Mistri, T., Pinello, L., Ng, H. H., Yuan, G., Ji, J., Rossant, J., Robson, P., & Han, X. (2017). The role of Cdx2 as a lineage specific transcriptional repressor for pluripotent network during the first developmental cell lineage segregation. *Scientific Reports*, *7*(1), 17156. https://doi.org/10.1038/s41598-017-16009-w

Huelsken, J., Vogel, R., Brinkmann, V., Erdmann, B., Birchmeier, C., & Birchmeier, W. (2000). Requirement for β-catenin in anterior-posterior axis formation in mice. *Journal of Cell Biology*, *148*(3), 567–578. https://doi.org/10.1083/jcb.148.3.567

Humphries, J. D., Wang, P., Streuli, C., Geiger, B., Humphries, M. J., & Ballestrem, C. (2007). Vinculin controls focal adhesion formation by direct interactions with talin and actin. *Journal of Cell Biology*, *179*(5), 1043–1057.

https://doi.org/10.1083/jcb.200703036

Inaba, M., & Yamashita, Y. M. (2012). Asymmetric stem cell division: Precision for robustness. In *Cell Stem Cell* (Vol. 11, Issue 4, pp. 461–469). Cell Stem Cell. https://doi.org/10.1016/j.stem.2012.09.003

Irion, S., Luche, H., Gadue, P., Fehling, H. J., Kennedy, M., & Keller, G. (2007). Identification and targeting of the ROSA26 locus in human embryonic stem cells. *Nature Biotechnology*, *25*(12), 1477–1482. https://doi.org/10.1038/nbt1362

Ishibe, S., Karihaloo, A., Ma, H., Zhang, J., Marlier, A., Mitobe, M., Togawa, A., Schmitt, R., Czyczk, J., Kashgarian, M., Geller, D. S., Thorgeirsson, S. S., & Cantley, L. G. (2009). Met and the epidermal growth factor receptor act cooperatively to regulate final nephron number and maintain collecting duct morphology. *Development*, *136*(2), 337–345. https://doi.org/10.1242/dev.024463

Ising, H., Bertschat, F., Gunther, T., Jeremias, E., Jeremias, A., & Ising, H. (1995). Measurement of Free Magnesium in Blood, Serum and Plasma with an Ion-Sensitive Electrode. *Clinical Chemistry and Laboratory Medicine*, *33*(6), 365–372. https://doi.org/10.1515/cclm.1995.33.6.365

Jiao, Y., Lau, T., Hatzikirou, H., Meyer-Hermann, M., Corbo, J. C., & Torquato, S. (2014). Avian photoreceptor patterns represent a disordered hyperuniform solution to a multiscale packing problem. *Physical Review E - Statistical, Nonlinear, and Soft Matter Physics*, *89*(2), 22721. https://doi.org/10.1103/PhysRevE.89.022721

Johnson, M. H., & Ziomek, C. A. (1981). The foundation of two distinct cell lineages within the mouse morula. *Cell*, *24*(1), 71–80. https://doi.org/10.1016/0092-8674(81)90502-X

Kalappurakkal, J. M., Anilkumar, A. A., Patra, C., van Zanten, T. S., Sheetz, M. P., & Mayor, S. (2019). Integrin Mechano-chemical Signaling Generates Plasma Membrane Nanodomains that Promote Cell Spreading. *Cell*, *177*(7), 1738-1756.e23. https://doi.org/10.1016/j.cell.2019.04.037

Kang, M., Garg, V., & Hadjantonakis, A. K. (2017). Lineage Establishment and Progression within the Inner Cell Mass of the Mouse Blastocyst Requires FGFR1 and FGFR2. *Developmental Cell*, *41*(5), 496-510.e5. https://doi.org/10.1016/j.devcel.2017.05.003

Karig, D., Michael Martini, K., Lu, T., DeLateur, N. A., Goldenfeld, N., & Weiss, R. (2018). Stochastic Turing patterns in a synthetic bacterial population. *Proceedings of the National Academy of Sciences of the United States of America*, *115*(26), 6572–6577. https://doi.org/10.1073/pnas.1720770115

Karner, C. M., Chirumamilla, R., Aoki, S., Igarashi, P., Wallingford, J. B., & Carroll, T. J. (2009). Wnt9b signaling regulates planar cell polarity and kidney tubule morphogenesis. *Nature Genetics*, *41*(7), 793–799. https://doi.org/10.1038/ng.400

Karner, C. M., Das, A., Ma, Z., Self, M., Chen, C., Lum, L., Oliver, G., & Carroll, T. J. (2011). Canonical Wnt9b signaling balances progenitor cell expansion and differentiation during kidney development. *Development*, *138*(7), 1247–1257. https://doi.org/10.1242/dev.057646

Karwacki-Neisius, V., Göke, J., Osorno, R., Halbritter, F., Ng, J. H., Weiße, A. Y., Wong, F. C. K., Gagliardi, A., Mullin, N. P., Festuccia, N., Colby, D., Tomlinson, S. R., Ng, H. H., & Chambers, I. (2013). Reduced Oct4 expression directs a robust pluripotent state with distinct signaling activity and increased enhancer occupancy by Oct4 and Nanog. *Cell Stem Cell*, *12*(5), 531–545. https://doi.org/10.1016/j.stem.2013.04.023

Kauts, M. L., De Leo, B., Rodríguez-Seoane, C., Ronn, R., Glykofrydis, F., Maglitto, A., Kaimakis, P., Basi, M., Taylor, H., Forrester, L., Wilkinson, A. C., Göttgens, B., Saunders, P., & Dzierzak, E. (2018). Rapid Mast Cell Generation from Gata2

Reporter Pluripotent Stem Cells. *Stem Cell Reports*, *11*(4), 1009–1020. https://doi.org/10.1016/j.stemcr.2018.08.007

Kechagia, J. Z., Ivaska, J., & Roca-Cusachs, P. (2019). Integrins as biomechanical sensors of the microenvironment. *Nature Reviews Molecular Cell Biology*, *20*(8), 457–473. https://doi.org/10.1038/s41580-019-0134-2

Kelly, O. G., Pinson, K. I., & Skarnes, W. C. (2004). The Wnt co-receptors Lrp5 and Lrp6 are essential for gastrulation in mice. *Development*, *131*(12), 2803–2815. https://doi.org/10.1242/dev.01137

Kicheva, A., & Briscoe, J. (2015). Developmental Pattern Formation in Phases. In *Trends in Cell Biology* (Vol. 25, Issue 10, pp. 579–591). Elsevier Ltd. https://doi.org/10.1016/j.tcb.2015.07.006

Kimura-Yoshida, C., Nakano, H., Okamura, D., Nakao, K., Yonemura, S., Belo, J. A., Aizawa, S., Matsui, Y., & Matsuo, I. (2005). Canonical Wnt signaling and its antagonist regulate anterior-posterior axis polarization by guiding cell migration in mouse visceral endoderm. *Developmental Cell*, *9*(5), 639–650. https://doi.org/10.1016/j.devcel.2005.09.011

Kobayashi, A., Valerius, M. T., Mugford, J. W., Carroll, T. J., Self, M., Oliver, G., & McMahon, A. P. (2008). Six2 Defines and Regulates a Multipotent Self-Renewing Nephron Progenitor Population throughout Mammalian Kidney Development. *Cell Stem Cell*, *3*(2), 169–181. https://doi.org/10.1016/j.stem.2008.05.020

Komekado, H., Yamamoto, H., Chiba, T., & Kikuchi, A. (2007). Glycosylation and palmitoylation of Wnt-3a are coupled to produce an active form of Wnt-3a. *Genes to Cells*, *12*(4), 521–534. https://doi.org/10.1111/j.1365-2443.2007.01068.x

Korotkevich, E., Niwayama, R., Courtois, A., Friese, S., Berger, N., Buchholz, F., & Hiiragi, T. (2017). The Apical Domain Is Required and Sufficient for the First Lineage Segregation in the Mouse Embryo. *Developmental Cell*, *40*(3), 235-247.e7. https://doi.org/10.1016/j.devcel.2017.01.006

Kram, Y. A., Mantey, S., & Corbo, J. C. (2010). Avian cone photoreceptors tile the retina as five independent, self-organizing mosaics. *PLoS ONE*, *5*(2), e8992. https://doi.org/10.1371/journal.pone.0008992

Lander, A. D. (2011). Pattern, growth, and control. In *Cell* (Vol. 144, Issue 6, pp. 955–969). Cell. https://doi.org/10.1016/j.cell.2011.03.009

Lavial, F., Bessonnard, S., Ohnishi, Y., Tsumura, A., Chandrashekran, A., Fenwick, M. A., Tomaz, R. A., Hosokawa, H., Nakayama, T., Chambers, I., Hiiragi, T., Chazaud, C., & Azuara, V. (2012). Bmi1 facilitates primitive endoderm formation by stabilizing Gata6 during early mouse development. *Genes and Development*, *26*(13), 1445–1458. https://doi.org/10.1101/gad.188193.112

Lawson, C., Lim, S. T., Uryu, S., Chen, X. L., Calderwood, D. A., & Schlaepfer, D. D. (2012). FAK promotes recruitment of talin to nascent adhesions to control cell motility. *Journal of Cell Biology*, *196*(2), 223–232. https://doi.org/10.1083/jcb.201108078

Lee, H. S., Lim, C. J., Puzon-McLaughlin, W., Shattil, S. J., & Ginsberg, M. H. (2009). RIAM activates integrins by linking talin to Ras GTPase membrane-targeting sequences. *Journal of Biological Chemistry*, *284*(8), 5119–5122. https://doi.org/10.1074/jbc.M807117200

Lee, J. O., Rieu, P., Arnaout, M. A., & Liddington, R. (1995). Crystal structure of the A domain from the a subunit of integrin CR3 (CD11 b/CD18). *Cell*, *80*(4), 631–638. https://doi.org/10.1016/0092-8674(95)90517-0

Levinson, R. S., Batourina, E., Choi, C., Vorontchikhina, M., Kitajewski, J., & Mendelsohn, C. L. (2005). Foxd1-dependent signals control cellularity in the renal

capsule, a structure required for normal renal development. *Development*, *132*(3), 529–539. https://doi.org/10.1242/dev.01604

Lewis, E. B. (1978). A gene complex controlling segmentation in Drosophila. *Nature*, *276*(5688), 565–570. https://doi.org/10.1038/276565a0

Lewis, S. L., Khoo, P. L., de Young, R. A., Steiner, K., Wilcock, C., Mukhopadhyay, M., Westphal, H., Jamieson, R. V., Robb, L., & Tam, P. P. L. (2008). Dkk1 and Wnt3 interact to control head morphogenesis in the mouse. *Development*, *135*(10), 1791–1801. https://doi.org/10.1242/dev.018853

Li, N., Yang, H., Wang, M., Lü, S., Zhang, Y., & Long, M. (2018). Ligand-specific binding forces of LFA-1 and Mac-1 in neutrophil adhesion and crawling. *Molecular Biology of the Cell*, *29*(4), 408–418. https://doi.org/10.1091/mbc.E16-12-0827

Lin, C. D., Zhang, Y. H., Zhang, K., Zheng, Y. J., Lu, L., Chang, H. S., Yang, H., Yang, Y. R., Wan, Y. Y., Wang, S. H., Yuan, M. Y., Yan, Z. J., Zhang, R. G., He, Y. N., Ge, G. X., Wu, D., & Chen, J. F. (2019). Fever Promotes T Lymphocyte Trafficking via a Thermal Sensory Pathway Involving Heat Shock Protein 90 and α4 Integrins. *Immunity*, *50*(1), 137-151.e6. https://doi.org/10.1016/j.immuni.2018.11.013

Lindström, N. O., De Sena Brandine, G., Tran, T., Ransick, A., Suh, G., Guo, J., Kim, A. D., Parvez, R. K., Ruffins, S. W., Rutledge, E. A., Thornton, M. E., Grubbs, B., McMahon, J. A., Smith, A. D., & McMahon, A. P. (2018). Progressive Recruitment of Mesenchymal Progenitors Reveals a Time-Dependent Process of Cell Fate Acquisition in Mouse and Human Nephrogenesis. *Developmental Cell*, *45*(5), 651-660.e4. https://doi.org/10.1016/j.devcel.2018.05.010

Lindström, N. O., Lawrence, M. L., Burn, S. F., Johansson, J. A., Bakker, E. R. M., Ridgway, R. A., Chang, C. H., Karolak, M. J., Oxburgh, L., Headon, D. J., Sansom, O. J., Smits, R., Davies, J. A., & Hohenstein, P. (2014). Integrated β-catenin, BMP, PTEN, and Notch signalling patterns the nephron. *ELife*, *3*, e04000. https://doi.org/10.7554/eLife.04000

Liu, C., Fu, X., Liu, L., Ren, X., Chau, C. K. L., Li, S., Xiang, L., Zeng, H., Chen, G., Tang, L. H., Lenz, P., Cui, X., Huang, W., Hwa, T., & Huang, J. D. (2011). Sequential establishment of stripe patterns in an expanding cell population. *Science*, *334*(6053), 238–241. https://doi.org/10.1126/science.1209042

Liu, P., Wakamiya, M., Shea, M. J., Albrecht, U., Behringer, R. R., & Bradley, A. (1999). Requirement for Wnt3 in vertebrate axis formation. *Nature Genetics*, *22*(4), 361–365. https://doi.org/10.1038/11932

Lowndes, M., Rotherham, M., Price, J. C., El Haj, A. J., & Habib, S. J. (2016). Immobilized WNT Proteins Act as a Stem Cell Niche for Tissue Engineering. *Stem Cell Reports*, *7*(1), 126–137. https://doi.org/10.1016/j.stemcr.2016.06.004

MacDonald, B. T., Tamai, K., & He, X. (2009). Wnt/β-Catenin Signaling: Components, Mechanisms, and Diseases. *Developmental Cell*, *17*(1), 9–26. https://doi.org/10.1016/j.devcel.2009.06.016

Majumdar, A., Vainio, S., Kispert, A., McMahon, J., & McMahon, A. P. (2003). Wnt11 and Ret/Gdnf pathways cooperate in regulating ureteric branching during metanephric kidney development. *Development*, *130*(14), 3175–3185. https://doi.org/10.1242/dev.00520

Malinauskas, T., Aricescu, A. R., Lu, W., Siebold, C., & Jones, E. Y. (2011). Modular mechanism of Wnt signaling inhibition by Wnt inhibitory factor 1. *Nature Structural and Molecular Biology*, *18*(8), 886–893. https://doi.org/10.1038/nsmb.2081

Manfrin, A., Tabata, Y., Paquet, E. R., Vuaridel, A. R., Rivest, F. R., Naef, F., & Lutolf, M. P. (2019). Engineered signaling centers for the spatially controlled patterning of human pluripotent stem cells. *Nature Methods*, *16*(7), 640–648.

https://doi.org/10.1038/s41592-019-0455-2

Mao, B., Wu, W., Davidson, G., Marhold, J., Li, M., Mechler, B. M., Dellus, H., Hoppe, D., Stannek, P., Walter, C., Glinka, A., & Niehrs, C. (2002). Kremen proteins are Dickkopf receptors that regulate Wnt/β-catenin signalling. *Nature*, *417*(6889), 664–667. https://doi.org/10.1038/nature756

Martin, B. L., & Kimelman, D. (2012). Canonical Wnt Signaling Dynamically Controls Multiple Stem Cell Fate Decisions during Vertebrate Body Formation. *Developmental Cell*, *22*(1), 223–232. https://doi.org/10.1016/j.devcel.2011.11.001

Matsuda, M., Koga, M., Woltjen, K., Nishida, E., & Ebisuya, M. (2015). Synthetic lateral inhibition governs cell-type bifurcation with robust ratios. *Nature Communications*, *6*. https://doi.org/10.1038/ncomms7195

Matzuk, M. M., Kumar, T. R., & Bradley, A. (1995). Different phenotypes for mice deficient in either activins or activin receptor type II. *Nature*, *374*(6520), 356–360. https://doi.org/10.1038/374356a0

McCulloch, E. A., & Till, J. E. (1960). The Radiation Sensitivity of Normal Mouse Bone Marrow Cells, Determined by Quantitative Marrow Transplantation into Irradiated Mice. *Radiation Research*, *13*(1), 115. https://doi.org/10.2307/3570877

McDole, K., Guignard, L., Amat, F., Berger, A., Malandain, G., Royer, L. A., Turaga, S. C., Branson, K., & Keller, P. J. (2018). In Toto Imaging and Reconstruction of Post-Implantation Mouse Development at the Single-Cell Level. *Cell*, *175*(3), 859-876.e33. https://doi.org/10.1016/j.cell.2018.09.031

Meinhardt, H., & Gierer, A. (2000). Pattern formation by local self-activation and lateral inhibition. *BioEssays*, *22*(8), 753–760. https://doi.org/10.1002/1521-1878(200008)22:8<753::AID-BIES9>3.0.CO;2-Z

Michos, O., Cebrian, C., Hyink, D., Grieshammer, U., Williams, L., D'Agati, V., Licht, J. D., Martin, G. R., & Costantini, F. (2010). Kidney development in the absence of Gdnf and Spry1 requires Fgf10. *PLoS Genetics*, *6*(1). https://doi.org/10.1371/journal.pgen.1000809

Michos, O., Gonçalves, A., Lopez-Rios, J., Tiecke, E., Naillat, F., Beier, K., Galli, A., Vainio, S., & Zeller, R. (2007). Reduction of BMP4 activity by gremlin 1 enables ureteric bud outgrowth and GDNF/WNT11 feedback signalling during kidney branching morphogenesis. *Development*, *134*(13), 2397–2405. https://doi.org/10.1242/dev.02861

Mii, Y., & Taira, M. (2009). Secreted Frizzled-related proteins enhance the diffusion of Wnt ligands and expand their signalling range. *Development*, *136*(24), 4083–4088. https://doi.org/10.1242/dev.032524

Mii, Y., Yamamoto, T., Takada, R., Mizumoto, S., Matsuyama, M., Yamada, S., Takada, S., & Taira, M. (2017). Roles of two types of heparan sulfate clusters in Wnt distribution and signaling in Xenopus. *Nature Communications*, *8*(1). https://doi.org/10.1038/s41467-017-02076-0

Miller, E., Vikram, A., Agga, G. E., Arthur, T. M., & Schmidt, J. W. (2018). Effects of in-feed chlortetracycline prophylaxis in beef cattle on antimicrobial resistance genes. *Foodborne Pathogens and Disease*, *15*(11), 689–697. https://doi.org/10.1089/fpd.2018.2475

Mills, C. G., Lawrence, M. L., Munro, D. A. D., Elhendawi, M., Mullins, J. J., & Davies, J. A. (2017). Asymmetric BMP4 signalling improves the realism of kidney organoids. *Scientific Reports*, *7*(1). https://doi.org/10.1038/s41598-017-14809-8

Mistri, T. K., Arindrarto, W., Ng, W. P., Wang, C., Lim, L. H., Sun, L., Chambers, I., Wohland, T., & Robson, P. (2018). Dynamic changes in Sox2 spatio-temporal expression promote the second cell fate decision through Fgf4/Fgfr2 signaling in

preimplantation mouse embryos. *Biochemical Journal*, *475*(6), 1075–1089. https://doi.org/10.1042/BCJ20170418

Miura, S., Singh, A. P., & Mishina Yuji, Y. (2010). Bmpr1a is required for proper migration of the AVE through regulation of Dkk1 expression in the pre-streak mouse embryo. *Developmental Biology*, *341*(1), 246–254. https://doi.org/10.1016/j.ydbio.2010.02.038

Moris, N., Anlas, K., van den Brink, S. C., Alemany, A., Schröder, J., Ghimire, S., Balayo, T., van Oudenaarden, A., & Martinez Arias, A. (2020). An in vitro model of early anteroposterior organization during human development. *Nature*, *582*(7812), 1–6. https://doi.org/10.1038/s41586-020-2383-9

Morkel, M., Huelsken, J., Wakamiya, M., Ding, J., van de Wetering, M., Clevers, H., Taketo, M. M., Behringer, R. R., Shen, M. M., & Birchmeier, W. (2003). β-Catenin regulates Cripto- and Wnt3-dependent gene expression programs in mouse axis and mesoderm formation. *Development*, *130*(25), 6283–6294. https://doi.org/10.1242/dev.00859

Morsut, L., Roybal, K. T., Xiong, X., Gordley, R. M., Coyle, S. M., Thomson, M., & Lim, W. A. (2016). Engineering Customized Cell Sensing and Response Behaviors Using Synthetic Notch Receptors. *Cell*, *164*(4), 780–791. https://doi.org/10.1016/j.cell.2016.01.012

Moser, M., Bauer, M., Schmid, S., Ruppert, R., Schmidt, S., Sixt, M., Wang, H. V., Sperandio, M., & Fässler, R. (2009). Kindlin-3 is required for β2 integrin-mediated leukocyte adhesion to endothelial cells. *Nature Medicine*, *15*(3), 300–305. https://doi.org/10.1038/nm.1921

Mugford, J. W., Yu, J., Kobayashi, A., & McMahon, A. P. (2009). High-resolution gene expression analysis of the developing mouse kidney defines novel cellular compartments within the nephron progenitor population. *Developmental Biology*, *333*(2), 312–323. https://doi.org/10.1016/j.ydbio.2009.06.043

Mukhopadhyay, M., Shtrom, S., Rodriguez-Esteban, C., Chen, L., Tsukui, T., Gomer, L., Dorward, D. W., Glinka, A., Grinberg, A., Huang, S. P., Niehrs, C., Belmonte, J. C. I., & Westphal, H. (2001). Dickkopf1 Is Required for Embryonic Head Induction and Limb Morphogenesis in the Mouse. *Developmental Cell*, *1*(3), 423–434. https://doi.org/10.1016/S1534-5807(01)00041-7

Mulligan, K. A., Fuerer, C., Ching, W., Fish, M., Willert, K., & Nusse, R. (2012). Secreted Wingless-interacting molecule (Swim) promotes long-range signaling by maintaining Wingless solubility. *Proceedings of the National Academy of Sciences of the United States of America*, *109*(2), 370–377. https://doi.org/10.1073/pnas.1119197109

Nagy, A., Rossant, J., Nagy, R., Abramow-Newerly, W., & Roder, J. C. (1993). Derivation of completely cell culture-derived mice from early-passage embryonic stem cells. *Proceedings of the National Academy of Sciences of the United States of America*, *90*(18), 8424–8428. https://doi.org/10.1073/pnas.90.18.8424

Nakamura, H., Cook, R. N., & Justice, M. J. (2013). Mouse Tenm4 is required for mesoderm induction. *BMC Developmental Biology*, *13*(1), 9. https://doi.org/10.1186/1471-213X-13-9

Nakano, T., Ando, S., Takata, N., Kawada, M., Muguruma, K., Sekiguchi, K., Saito, K., Yonemura, S., Eiraku, M., & Sasai, Y. (2012). Self-formation of optic cups and storable stratified neural retina from human ESCs. *Cell Stem Cell*, *10*(6), 771–785. https://doi.org/10.1016/j.stem.2012.05.009

Neagu, A., van Genderen, E., Escudero, I., Kurek, D., Lehmann, J., Stel, J., René, A. M., Mierlo, G. Van, Maas, A., Eleveld, C., Ge, Y., Dekker, A. T. Den, Rutger, W.,

Brouwer, W., Ijcken, W. F. J. Van, Modic, M., Drukker, M., & Jansen, J. H. (2020). In vitro capture and characterization of embryonic rosette-stage pluripotency between naïve and primed states. *Nature Cell BIology*, *22*(5), 534–545. https://doi.org/10.1038/s41556-020-0508-x

Nichols, J., Zevnik, B., Anastassiadis, K., Niwa, H., Klewe-Nebenius, D., Chambers, I., Schöler, H., & Smith, A. (1998). Formation of pluripotent stem cells in the mammalian embryo depends on the POU transcription factor Oct4. *Cell*, *95*(3), 379–391. https://doi.org/10.1016/S0092-8674(00)81769-9

Nie, X., Xu, J., El-Hashash, A., & Xu, P. X. (2011). Six1 regulates Grem1 expression in the metanephric mesenchyme to initiate branching morphogenesis. *Developmental Biology*, *352*(1), 141–151. https://doi.org/10.1016/j.ydbio.2011.01.027

Nieuwkoop, P. D. (1967). The “Organization centre” - II. Field phenomena, their origin and significance. *Acta Biotheoretica*, *17*(4), 151–177. https://doi.org/10.1007/BF01601986

Nieuwkoop, P. D. (1973). The organization center of the amphibian embryo: its origin, spatial organization, and morphogenetic action. *Advances in Morphogenesis*, *10*, 1–39. https://doi.org/10.1016/b978-0-12-028610-2.50005-8

Nishioka, N., Inoue, K. ichi, Adachi, K., Kiyonari, H., Ota, M., Ralston, A., Yabuta, N., Hirahara, S., Stephenson, R. O., Ogonuki, N., Makita, R., Kurihara, H., Morin-Kensicki, E. M., Nojima, H., Rossant, J., Nakao, K., Niwa, H., & Sasaki, H. (2009). The Hippo Signaling Pathway Components Lats and Yap Pattern Tead4 Activity to Distinguish Mouse Trophectoderm from Inner Cell Mass. *Developmental Cell*, *16*(3), 398–410. https://doi.org/10.1016/j.devcel.2009.02.003

Niwa, H., Miyazaki, J. I., & Smith, A. G. (2000). Quantitative expression of Oct-3/4 defines differentiation, dedifferentiation or self-renewal of ES cells. *Nature Genetics*, *24*(4), 372–376. https://doi.org/10.1038/74199

Niwa, H., Toyooka, Y., Shimosato, D., Strumpf, D., Takahashi, K., Yagi, R., & Rossant, J. (2005). Interaction between Oct3/4 and Cdx2 determines trophectoderm differentiation. *Cell*, *123*(5), 917–929. https://doi.org/10.1016/j.cell.2005.08.040

Nomura, M., & Li, E. (1998). Smad2 role in mesoderm formation, left-right patterning and craniofacial development. *Nature*, *393*(6687), 786–790. https://doi.org/10.1038/31693

Nordenfelt, P., Elliott, H. L., & Springer, T. A. (2016). Coordinated integrin activation by actin-dependent force during T-cell migration. *Nature Communications*, *7*. https://doi.org/10.1038/ncomms13119

Nose, A., Nagafuchi, A., & Takeichi, M. (1988). Expressed recombinant cadherins mediate cell sorting in model systems. *Cell*, *54*(7), 993–1001. https://doi.org/10.1016/0092-8674(88)90114-6

O’brien, L. L., Combes, A. N., Short, K. M., Lindström, N. O., Whitney, P. H., Cullen-McEwen, L. A., Ju, A., Abdelhalim, A., Michos, O., Bertram, J. F., Smyth, I. M., Little, M. H., & McMahon, A. P. (2018). Wnt11 directs nephron progenitor polarity and motile behavior ultimately determining nephron endowment. *ELife*, *7*. https://doi.org/10.7554/eLife.40392

Ordak, M., Maj-Zurawska, M., Matsumoto, H., Bujalska-Zadrozny, M., Kieres-Salomonski, I., Nasierowski, T., Muszynska, E., & Wojnar, M. (2017). Ionized magnesium in plasma and erythrocytes for the assessment of low magnesium status in alcohol dependent patients. *Drug and Alcohol Dependence*, *178*, 271–276. https://doi.org/10.1016/j.drugalcdep.2017.04.035

Panáková, D., Sprong, H., Marois, E., Thiele, C., & Eaton, S. (2005). Lipoprotein particles are required for Hedgehog and Wingless signalling. *Nature*, *435*(7038), 58–65.

https://doi.org/10.1038/nature03504

Pani, A. M., & Goldstein, B. (2018). Direct visualization of a native wnt in vivo reveals that a long-range Wnt gradient forms by extracellular dispersal. *ELife*, *7*. https://doi.org/10.7554/eLife.38325

Park, J. S., Ma, W., O'Brien, L. L., Chung, E., Guo, J. J., Cheng, J. G., Valerius, M. T., McMahon, J. A., Wong, W. H., & McMahon, A. P. (2012). Six2 and Wnt Regulate Self-Renewal and Commitment of Nephron Progenitors through Shared Gene Regulatory Networks. *Developmental Cell*, *23*(3), 637–651. https://doi.org/10.1016/j.devcel.2012.07.008

Park, J. S., Valerius, M. T., & McMahon, A. P. (2007). Wnt/β-catenin signaling regulates nephron induction during mouse kidney development. *Development*, *134*(13), 2533–2539. https://doi.org/10.1242/dev.006155

Pepicelli, C. V., Kispert, A., Rowitch, D. H., & McMahon, A. P. (1997). Rapid communication: GDNF induces branching and increased cell proliferation in the ureter of the mouse. *Developmental Biology*, *192*(1), 193–198. https://doi.org/10.1006/dbio.1997.8745

Perea-Gomez, A., Vella, F. D. J., Shawlot, W., Oulad-Abdelghani, M., Chazaud, C., Meno, C., Pfister, V., Chen, L., Robertson, E., Hamada, H., Behringer, R. R., & Ang, S. L. (2002). Nodal antaginists in the anterior visceral endoderm prevent the formation of multiple primitive streaks. *Developmental Cell*, *3*(5), 745–756. https://doi.org/10.1016/S1534-5807(02)00321-0

Pijuan-Sala, B., Griffiths, J. A., Guibentif, C., Hiscock, T. W., Jawaid, W., Calero-Nieto, F. J., Mulas, C., Ibarra-Soria, X., Tyser, R. C. V., Ho, D. L. L., Reik, W., Srinivas, S., Simons, B. D., Nichols, J., Marioni, J. C., & Göttgens, B. (2019). A single-cell molecular map of mouse gastrulation and early organogenesis. *Nature*, *566*(7745), 490–495. https://doi.org/10.1038/s41586-019-0933-9

Qu, A., & Leahy, D. J. (1996). The role of the divalent cation in the structure of the I domain from the CD11a/CD18 integrin. *Structure*, *4*(8), 931–942. https://doi.org/10.1016/S0969-2126(96)00100-1

Ramalingam, H., Fessler, A. R., Das, A., Valerius, M. T., Basta, J., Robbins, L., Brown, A. C., Oxburgh, L., McMahon, A. P., Rauchman, M., & Carroll, T. J. (2018). Disparate levels of beta-catenin activity determine nephron progenitor cell fate. *Developmental Biology*, *440*(1), 13–21. https://doi.org/10.1016/j.ydbio.2018.04.020

Ran, F. A., Hsu, P. D., Wright, J., Agarwala, V., Scott, D. A., & Zhang, F. (2013). Genome engineering using the CRISPR-Cas9 system. *Nature Protocols*, *8*(11), 2281–2308. https://doi.org/10.1038/nprot.2013.143

Renner, M., Lancaster, M. A., Bian, S., Choi, H., Ku, T., Peer, A., Chung, K., & Knoblich, J. A. (2017). Self-organized developmental patterning and differentiation in cerebral organoids. *The EMBO Journal*, *36*(10), 1316–1329. https://doi.org/10.15252/embj.201694700

Rivera-Pérez, J. A., & Magnuson, T. (2005). Primitive streak formation in mice is preceded by localized activation of Brachyury and Wnt3. *Developmental Biology*, *288*(2), 363–371. https://doi.org/10.1016/j.ydbio.2005.09.012

Rosetti, F., Chen, Y., Sen, M., Thayer, E., Azcutia, V., Herter, J. M., Luscinskas, F. W., Cullere, X., Zhu, C., & Mayadas, T. N. (2015). A Lupus-Associated Mac-1 Variant Has Defects in Integrin Allostery and Interaction with Ligands under Force. *Cell Reports*, *10*(10), 1655–1664. https://doi.org/10.1016/j.celrep.2015.02.037

Sadelain, M., Papapetrou, E. P., & Bushman, F. D. (2012). Safe harbours for the integration of new DNA in the human genome. *Nature Reviews Cancer*, *12*(1), 51–58. https://doi.org/10.1038/nrc3179

Sagy, N., Slovin, S., Allalouf, M., Pour, M., Savyon, G., Boxman, J., & Nachman, I. (2019). Prediction and control of symmetry breaking in embryoid bodies by environment and signal integration. *Development (Cambridge)*, *146*(20). https://doi.org/10.1242/dev.181917

Sakurai, H., Bush, K. T., & Nigam, S. K. (2005). Heregulin induces glial cell line-derived neurotrophic growth factor-independent, non-branching growth and differentiation of ureteric bud epithelia. *Journal of Biological Chemistry*, *280*(51), 42181–42187. https://doi.org/10.1074/jbc.M507962200

Salazar-Ciudad, I., Jernvall, J., & Newman, S. A. (2003). Mechanisms of pattern formation in development and evolution. *Development*, *130*(10), 2027–2037. https://doi.org/10.1242/dev.00425

Sato, T., van Es, J. H., Snippert, H. J., Stange, D. E., Vries, R. G., van den Born, M., Barker, N., Shroyer, N. F., van de Wetering, M., & Clevers, H. (2011). Paneth cells constitute the niche for Lgr5 stem cells in intestinal crypts. *Nature*, *469*(7330), 415–418. https://doi.org/10.1038/nature09637

Sato, T., Vries, R. G., Snippert, H. J., Van De Wetering, M., Barker, N., Stange, D. E., Van Es, J. H., Abo, A., Kujala, P., Peters, P. J., & Clevers, H. (2009). Single Lgr5 stem cells build crypt-villus structures in vitro without a mesenchymal niche. *Nature*, *459*(7244), 262–265. https://doi.org/10.1038/nature07935

Scharffetter-Kochanek, K., Lu, H., Norman, K., Van Nood, N., Munoz, F., Grabbe, S., McArthur, M., Lorenzo, I., Kaplan, S., Ley, K., Smith, C. W., Montgomery, C. A., Rich, S., & Beaudet, A. L. (1998). Spontaneous skin ulceration and defective T cell function in CD18 null mice. *Journal of Experimental Medicine*, *188*(1), 119–131. https://doi.org/10.1084/jem.188.1.119

Schmittgen, T. D., & Livak, K. J. (2008). Analyzing real-time PCR data by the comparative CT method. *Nature Protocols*, *3*(6), 1101–1108. https://doi.org/10.1038/nprot.2008.73

Schofield, R. (1978). The relationship between the spleen colony-forming cell and the haemopoietic stem cell. *Blood Cells*, *4*(1–2), 7–25.

Scialdone, A., Tanaka, Y., Jawaid, W., Moignard, V., Wilson, N. K., Macaulay, I. C., Marioni, J. C., & Göttgens, B. (2016). Resolving early mesoderm diversification through single-cell expression profiling. *Nature*, *535*(7611), 289–293. https://doi.org/10.1038/nature18633

Sekine, R., Shibata, T., & Ebisuya, M. (2018). Synthetic mammalian pattern formation driven by differential diffusivity of Nodal and Lefty. *Nature Communications*, *9*(1), 5456. https://doi.org/10.1038/s41467-018-07847-x

Self, M., Lagutin, O. V., Bowling, B., Hendrix, J., Cai, Y., Dressler, G. R., & Oliver, G. (2006). Six2 is required for suppression of nephrogenesis and progenitor renewal in the developing kidney. *EMBO Journal*, *25*(21), 5214–5228. https://doi.org/10.1038/sj.emboj.7601381

Sen, M., Koksal, A. C., Yuki, K., Wang, J., & Springer, T. A. (2018). Ligand- and cation-induced structural alterations of the leukocyte integrin LFA-1. *Journal of Biological Chemistry*, *293*(17), 6565–6577. https://doi.org/10.1074/jbc.RA117.000710

Serra, D., Mayr, U., Boni, A., Lukonin, I., Rempfler, M., Challet Meylan, L., Stadler, M. B., Strnad, P., Papasaikas, P., Vischi, D., Waldt, A., Roma, G., & Liberali, P. (2019). Self-organization and symmetry breaking in intestinal organoid development. *Nature*, *569*(7754), 66–72. https://doi.org/10.1038/s41586-019-1146-y

Shen, Q., Rahn, J. J., Zhang, J., Gunasekera, N., Sun, X., Shaw, A. R. E., Hendzel, M. J., Hoffman, P., Bernier, A., & Hugh, J. C. (2008). MUC1 initiates Src-CrkL-Rac1/Cdc42-mediated actin cytoskeletal protrusive motility after ligating

intercellular adhesion molecule-1. *Molecular Cancer Research*, *6*(4), 555–567. https://doi.org/10.1158/1541-7786.MCR-07-2033

Shimaoka, M., Xiao, T., Liu, J. H., Yang, Y., Dong, Y., Jun, C. D., McCormack, A., Zhang, R., Joachimiak, A., Takagi, J., Wang, J. H., & Springer, T. A. (2003). Structures of the αL I domain and its complex with ICAM-1 reveal a shape-shifting pathway for integrin regulation. In *Cell* (Vol. 112, Issue 1, pp. 99–111). Cell Press. https://doi.org/10.1016/S0092-8674(02)01257-6

Sims-Lucas, S., Caruana, G., Dowling, J., Kett, M. M., & Bertram, J. F. (2008). Augmented and accelerated nephrogenesis in TGF-β2 heterozygous mutant mice. *Pediatric Research*, *63*(6), 607–612. https://doi.org/10.1203/PDR.0b013e31816d9130

Skamagki, M., Wicher, K. B., Jedrusik, A., Ganguly, S., & Zernicka-Goetz, M. (2013). Asymmetric Localization of Cdx2 mRNA during the First Cell-Fate Decision in Early Mouse Development. *Cell Reports*, *3*(2), 442–457. https://doi.org/10.1016/j.celrep.2013.01.006

Smith, C. W., Marlin, S. D., Rothlein, R., Toman, C., & Anderson, D. C. (1989). Cooperative interactions of LFA-1 and Mac-1 with intracellular adhesion molecule-1 in facilitating adherence and transendothelial migration of human neutrophils in vitro. *Journal of Clinical Investigation*, *83*(6), 2008–2017. https://doi.org/10.1172/JCI114111

Soriano, P. (1999). Generalized lacZ expression with the ROSA26 Cre reporter strain [1]. *Nature Genetics*, *21*(1), 70–71. https://doi.org/10.1038/5007

Spemann, H., & Mangold, H. (1924). über Induktion von Embryonalanlagen durch Implantation artfremder Organisatoren. *Archiv Für Mikroskopische Anatomie Und Entwicklungsmechanik*, *100*(3–4), 599–638. https://doi.org/10.1007/BF02108133

Springer, T. A., Scott Thompson, W., Miller, L. J., Schmalstieg, F. C., & Anderson, D. C. (1984). Inherited deficiency of the Mac-l, LFA-1, p150,95 glycoprotein family and its molecular basis. *Journal of Experimental Medicine*, *160*(6), 1901–1918. https://doi.org/10.1084/jem.160.6.1901

Stanganello, E., Hagemann, A. I. H., Mattes, B., Sinner, C., Meyen, D., Weber, S., Schug, A., Raz, E., & Scholpp, S. (2015). Filopodia-based Wnt transport during vertebrate tissue patterning. *Nature Communications*, *6*. https://doi.org/10.1038/ncomms6846

Strazza, M., Azoulay-Alfaguter, I., Pedoeem, A., & Mor, A. (2014). Static adhesion assay for the study of integrin activation in T lymphocytes. *Journal of Visualized Experiments*, *88*. https://doi.org/10.3791/51646

Strohmeyer, N., Bharadwaj, M., Costell, M., Fässler, R., & Müller, D. J. (2017). Fibronectin-bound α5β1 integrins sense load and signal to reinforce adhesion in less than a second. *Nature Materials*, *16*(12), 1262–1270. https://doi.org/10.1038/nmat5023

Strumpf, D., Mao, C. A., Yamanaka, Y., Ralston, A., Chawengsaksophak, K., Beck, F., & Rossant, J. (2005). Cdx2 is required for correct cell fate specification and differentiation of trophectoderm in the mouse blastocyst. *Development*, *132*(9), 2093–2102. https://doi.org/10.1242/dev.01801

Surendran, K., Selassie, M., Liapis, H., Krigman, H., & Kopan, R. (2010). Reduced notch signaling leads to renal cysts and papillary microadenomas. *Journal of the American Society of Nephrology*, *21*(5), 819–832. https://doi.org/10.1681/ASN.2009090925

Svensson, L., Howarth, K., McDowall, A., Patzak, I., Evans, R., Ussar, S., Moser, M., Metin, A., Fried, M., Tomlinson, I., & Hogg, N. (2009). Leukocyte adhesion

deficiency-III is caused by mutations in KINDLIN3 affecting integrin activation. *Nature Medicine*, *15*(3), 306–312. https://doi.org/10.1038/nm.1931

Sweeney, D., Lindström, N., & Davies, J. A. (2008). Developmental plasticity and regenerative capacity in the renal ureteric bud/collecting duct system. *Development*, *135*(15), 2505–2510. https://doi.org/10.1242/dev.022145

Tadokoro, S., Shattil, S. J., Eto, K., Tai, V., Liddington, R. C., De Pereda, J. M., Ginsberg, M. H., & Calderwood, D. A. (2003). Talin binding to integrin β tails: A final common step in integrin activation. *Science*, *302*(5642), 103–106. https://doi.org/10.1126/science.1086652

Takada, R., Mii, Y., Krayukhina, E., Maruyama, Y., Mio, K., Sasaki, Y., Shinkawa, T., Pack, C. G., Sako, Y., Sato, C., Uchiyama, S., & Takada, S. (2018). Assembly of protein complexes restricts diffusion of Wnt3a proteins. *Communications Biology*, *1*(1). https://doi.org/10.1038/s42003-018-0172-x

Takada, R., Satomi, Y., Kurata, T., Ueno, N., Norioka, S., Kondoh, H., Takao, T., & Takada, S. (2006). Monounsaturated Fatty Acid Modification of Wnt Protein: Its Role in Wnt Secretion. *Developmental Cell*, *11*(6), 791–801. https://doi.org/10.1016/j.devcel.2006.10.003

Takahashi, K., & Yamanaka, S. (2006). Induction of Pluripotent Stem Cells from Mouse Embryonic and Adult Fibroblast Cultures by Defined Factors. *Cell*, *126*(4), 663–676. https://doi.org/10.1016/j.cell.2006.07.024

Takata, N., Sakakura, E., Eiraku, M., Kasukawa, T., & Sasai, Y. (2017). Self-patterning of rostral-caudal neuroectoderm requires dual role of Fgf signaling for localized Wnt antagonism. *Nature Communications*, *8*(1). https://doi.org/10.1038/s41467-017-01105-2

Tamai, K., Zeng, X., Liu, C., Zhang, X., Harada, Y., Chang, Z., & He, X. (2004). A Mechanism for Wnt Coreceptor Activation. *Molecular Cell*, *13*(1), 149–156. https://doi.org/10.1016/S1097-2765(03)00484-2

ten Berge, D., Koole, W., Fuerer, C., Fish, M., Eroglu, E., & Nusse, R. (2008). Wnt Signaling Mediates Self-Organization and Axis Formation in Embryoid Bodies. *Cell Stem Cell*, *3*(5), 508–518. https://doi.org/10.1016/j.stem.2008.09.013

Tewary, M., Ostblom, J., Prochazka, L., Zulueta-Coarasa, T., Shakiba, N., Fernandez-Gonzalez, R., & Zandstra, P. W. (2017). A stepwise model of reaction-diffusion and positional information governs self-organized human peri-gastrulation-like patterning. *Development (Cambridge)*, *144*(23), 4298–4312. https://doi.org/10.1242/dev.149658

Thompson, D. W. (1992). On Growth and Form. In *On Growth and Form*. Cambridge University Press. https://doi.org/10.1017/cbo9781107325852

Thomson, J. A. (1998). Embryonic stem cell lines derived from human blastocysts. *Science*, *282*(5391), 1145–1147. https://doi.org/10.1126/science.282.5391.1145

Tiwari, S., Askari, J. A., Humphries, M. J., & Bulleid, N. J. (2011). Divalent cations regulate the folding and activation status of integrins during their intracellular trafficking. *Journal of Cell Science*, *124*(10), 1672–1680. https://doi.org/10.1242/jcs.084483

Toda, S., Blauch, L. R., Tang, S. K. Y., Morsut, L., & Lim, W. A. (2018). Programming self-organizing multicellular structures with synthetic cell-cell signaling. *Science*, *361*(6398), 156–162. https://doi.org/10.1126/science.aat0271

Tortelote, G. G., Hernández-Hernández, J. M., Quaresma, A. J. C., Nickerson, J. A., Imbalzano, A. N., & Rivera-Pérez, J. A. (2013). Wnt3 function in the epiblast is required for the maintenance but not the initiation of gastrulation in mice. *Developmental Biology*, *374*(1), 164–173.

https://doi.org/10.1016/j.ydbio.2012.10.013

Turing, A. M. (1990). The chemical basis of morphogenesis. *Bulletin of Mathematical Biology*, *52*(1–2), 153–197. https://doi.org/10.1007/BF02459572

Turner, D. A., Girgin, M., Alonso-Crisostomo, L., Trivedi, V., Baillie-Johnson, P., Glodowski, C. R., Hayward, P. C., Collignon, J., Gustavsen, C., Serup, P., Steventon, B., Lutolf, M. P., & Arias, A. M. (2017). Anteroposterior polarity and elongation in the absence of extraembryonic tissues and of spatially localised signalling in gastruloids: Mammalian embryonic organoids. *Development (Cambridge)*, *144*(21), 3894–3906. https://doi.org/10.1242/dev.150391

Tuÿsüz, N., Van Bloois, L., Van Den Brink, S., Begthel, H., Verstegen, M. M. A., Cruz, L. J., Hui, L., Van Der Laan, L. J. W., De Jonge, J., Vries, R., Braakman, E., Mastrobattista, E., Cornelissen, J. J., Clevers, H., & Ten Berge, D. (2017). Lipid-mediated Wnt protein stabilization enables serum-free culture of human organ stem cells. *Nature Communications*, *8*, 14578. https://doi.org/10.1038/ncomms14578

Uff, C. R., Neame, S. J., & Isacke, C. M. (1995). Hyaluronan binding by CD44 is regulated by a phosphorylation-independent mechanism. *European Journal of Immunology*, *25*(7), 1883–1887. https://doi.org/10.1002/eji.1830250714

Vainio, S., Lin, Y., & Pihlajaniemi, T. (2003). Induced repatterning of type XVIII collagen associates with ectopic sonic hedgehog and lung surfactant C gene expression and changes in epithelial epigenesis in the ureteric bud. *Journal of the American Society of Nephrology*, *14*(SUPPL. 1). https://doi.org/10.1097/01.asn.0000068682.41378.c4

van den Brink, S. C., Alemany, A., van Batenburg, V., Moris, N., Blotenburg, M., Vivié, J., Baillie-Johnson, P., Nichols, J., Sonnen, K. F., Martinez Arias, A., & van Oudenaarden, A. (2020). Single-cell and spatial transcriptomics reveal somitogenesis in gastruloids. *Nature*. https://doi.org/10.1038/s41586-020-2024-3

Van Den Brink, S. C., Baillie-Johnson, P., Balayo, T., Hadjantonakis, A. K., Nowotschin, S., Turner, D. A., & Arias, A. M. (2014). Symmetry breaking, germ layer specification and axial organisation in aggregates of mouse embryonic stem cells. *Development (Cambridge)*, *141*(22), 4231–4242. https://doi.org/10.1242/dev.113001

Varelas, X., Miller, B. W., Sopko, R., Song, S., Gregorieff, A., Fellouse, F. A., Sakuma, R., Pawson, T., Hunziker, W., McNeill, H., Wrana, J. L., & Attisano, L. (2010). The Hippo Pathway Regulates Wnt/β-Catenin Signaling. *Developmental Cell*, *18*(4), 579–591. https://doi.org/10.1016/j.devcel.2010.03.007

Waddington, C. H. (1940). Organisers and genes. *Organisers and Genes.*

Waites, W., & Davies, J. A. (2019). Emergence of structure in mouse embryos: Structural Entropy morphometry applied to digital models of embryonic anatomy. *Journal of Anatomy*, *235*(4), 706–715. https://doi.org/10.1111/joa.13031

Waldrip, W. R., Bikoff, E. K., Hoodless, P. A., Wrana, J. L., & Robertson, E. J. (1998). Smad2 signaling in extraembryonic tissues determines anterior-posterior polarity of the early mouse embryo. *Cell*, *92*(6), 797–808. https://doi.org/10.1016/S0092-8674(00)81407-5

Wang, Y., Wang, F., Wang, R., Zhao, P., & Xia, Q. (2015). 2A self-cleaving peptide-based multi-gene expression system in the silkworm Bombyx mori. *Scientific Reports*, *5*. https://doi.org/10.1038/srep16273

Warmflash, A., Sorre, B., Etoc, F., Siggia, E. D., & Brivanlou, A. H. (2014). A method to recapitulate early embryonic spatial patterning in human embryonic stem cells. *Nature Methods*, *11*(8), 847–854. https://doi.org/10.1038/nMeth.3016

Willert, K., Brown, J. D., Danenberg, E., Duncan, A. W., Weissman, I. L., Reya, T., Yates,

J. R., & Nusse, R. (2003). Wnt proteins are lipid-modified and can act as stem cell growth factors. *Nature*, *423*(6938), 448–452. https://doi.org/10.1038/nature01611

Wolpert, L. (1969). Positional information and the spatial pattern of cellular differentiation. *Journal of Theoretical Biology*, *25*(1), 1–47. https://doi.org/10.1016/S0022-5193(69)80016-0

Xie, M., & Fussenegger, M. (2018). Designing cell function: assembly of synthetic gene circuits for cell biology applications. *Nature Reviews Molecular Cell Biology*, *19*(8), 507–525. https://doi.org/10.1038/s41580-018-0024-z

Yamaguchi, T. P., Bradley, A., McMahon, A. P., & Jones, S. (1999). A Wnt5a pathway underlies outgrowth of multiple structures in the vertebrate embryo. *Development*, *126*(6), 1211–1223.

Yamaguchi, T. P., Harpal, K., Henkemeyer, M., & Rossant, J. (1994). Fgfr-1 Is Required for Embryonic Growth and Mesodermal Patterning During Mouse Gastrulation. *Genes and Development*, *8*(24), 3032–3044. https://doi.org/10.1101/gad.8.24.3032

Yamaguchi, T. P., Takada, S., Yoshikawa, Y., Wu, N., & McMahon, A. P. (1999). T (Brachyury) is a direct target of Wnt3a during paraxial mesoderm specification. *Genes and Development*, *13*(24), 3185–3190. https://doi.org/10.1101/gad.13.24.3185

Yamamoto, M., Saijoh, Y., Perea-Gomez, A., Shawiot, W., Behringer, R. R., Ang, S. L., Hamada, H., & Meno, C. (2004). Nodal antagonists regulate formation of the anteroposterior axis of the mouse embryo. *Nature*, *428*(6981), 387–392. https://doi.org/10.1038/nature02418

Yokomizo, T., Yamada-Inagawa, T., Yzaguirre, A. D., Chen, M. J., Speck, N. A., & Dzierzak, E. (2012). Whole-mount three-dimensional imaging of internally localized immunostained cells within mouse embryos. *Nature Protocols*, *7*(3), 421–423. https://doi.org/10.1038/nprot.2011.441

Zaikin, A. N., & Zhabotinsky, A. M. (1970). Concentration wave propagation in two-dimensional liquid-phase self-oscillating system. *Nature*, *225*(5232), 535–537. https://doi.org/10.1038/225535b0

Zehtabchi, S., Sinert, R., Rinnert, S., Chang, B., Heinis, C., Altura, R. A., Altura, B. T., & Altura, B. M. (2004). Serum ionized magnesium levels and ionized calcium-to-magnesium ratios in adult patients with sickle cell anemia. *American Journal of Hematology*, *77*(3), 215–222. https://doi.org/10.1002/ajh.20187

Zeng, L., Fagotto, F., Zhang, T., Hsu, W., Vasicek, T. J., Perry, W. L., Lee, J. J., Tilghman, S. M., Gumbiner, B. M., & Costantini, F. (1997). The mouse Fused locus encodes axin, an inhibitor of the Wnt signaling pathway that regulates embryonic axis formation. *Cell*, *90*(1), 181–192. https://doi.org/10.1016/S0092-8674(00)80324-4

Zeng, X., Huang, H., Tamai, K., Zhang, X., Harada, Y., Yokota, C., Almeida, K., Wang, J., Doble, B., Woodgett, J., Wynshaw-Boris, A., Hsieh, J. C., & He, X. (2008). Initiation of Wnt signaling: Control of Wnt coreceptor Lrp6 phosphorylation/activation via frizzled, dishevelled and axin functions. *Development*, *135*(2), 367–375. https://doi.org/10.1242/dev.013540

Zhou, X., Sasaki, H., Lowe, L., Hogan, B. L. M., & Kuehn, M. R. (1993). Nodal is a novel TGF-β-like gene expressed in the mouse node during gastrulation. *Nature*, *361*(6412), 543–547. https://doi.org/10.1038/361543a0